From Brownian motion to supercooled water in confinements - a molecular dynamics simulation study

Von Brownscher Bewegung zu unterkühltem Wasser in Confinements - eine molekular-dynamische Studie

Zur Erlangung des Grades eines Doktors der Naturwissenschaften (Dr. rer. nat.) genehmigte Dissertation von Felix Klameth, M.Sc. geboren in Erlenbach am Main
Tag der Einreichung: 12.11.2014, Tag der Prüfung: 08.12.2014

Januar 2015
Darmstadt — D 17

1. Gutachten: Prof. Dr. Michael Vogel
2. Gutachten: Prof. Dr. Barbara Drossel

TECHNISCHE UNIVERSITÄT DARMSTADT

Fachbereich Physik
Institut für Festkörperphysik

From Brownian motion to supercooled water in confinements - a molecular dynamics simulation study
Von Brownscher Bewegung zu unterkühltem Wasser in Confinements - eine molekulardynamische Studie

Genehmigte Dissertation von Felix Klameth, M.Sc. geboren in Erlenbach am Main

1. Gutachten: Prof. Dr. Michael Vogel
2. Gutachten: Prof. Dr. Barbara Drossel

Tag der Einreichung: 12.11.2014

Tag der Prüfung: 08.12.2014

Januar 2015

Darmstadt — D 17

Erklärung zur Dissertation

Hiermit versichere ich, die vorliegende Dissertation ohne Hilfe Dritter nur mit den angegebenen Quellen und Hilfsmitteln angefertigt zu haben. Alle Stellen, die aus Quellen entnommen wurden, sind als solche kenntlich gemacht. Diese Arbeit hat in gleicher oder ähnlicher Form noch keiner Prüfungsbehörde vorgelegen.

Darmstadt, den 12.11.2014

_____

(Felix Klameth)

Abstract

In biological cells, water is confined by macromolecules. Additionally, huge amounts of water are confined in minerals in the lower Earth mantle, so, water in narrow confinements is important in technology and nature. Therefore, it is relevant to examine how the surfaces affect the properties of water, e.g., to understand the role of water in biological processes. The aim of the present study is to investigate supercooled water in confinements using molecular dynamics simulations. For this purpose, structure and dynamics are ascertained for the water model SPC/E in silica pores and amorphous ice pores.

Water appears to be a simple liquid, but it shows many anomalies which are not understood. Popular approaches propose a liquid-liquid phase transition to explain the anomalies. This phase transition is located at supercooled temperatures. However, water starts to crystallize at low temperatures, thus, experimentalists employ narrow confinements to prevent the crystallization. As those systems are very complex, the goal of this study is to systematically vary the surface, the confinement geometry, the size of the confinements, and the density of confined water to distinguish between finite-size, density, and surface effects.

It is found that the surface strongly affects the structure of water. Water in silica confinements exhibits an induced disorder, in contrast to the amorphous ice confinements, where the structure of water is not changed compared to that of the bulk liquid. Despite this difference, it turns out that using these pores yields a similar change of the relaxation mechanism of water molecules near the wall, accompanied by a tremendous slowdown of dynamics. Furthermore, comparing the sizes of the confinements suggests that the recently proposed phase transition of water in silica confinements, observed in molecular dynamics simulations, can be presumably attributed to a finite-size effect.

The amorphous ice pores are additionally used to obtain information on intrinsic length scales of water. Recently proposed theories which attempt to elucidate the still unresolved issue about the dynamic behavior of supercooled liquids, like the random first-order transition theory (RFOT) or the elastically non-linear Langevin equation (ECNLE) approach, attribute the non-Arrhenius temperature dependence of dynamics of supercooled liquids to an increasing intrinsic length. In this study, two length scales are obtained. Both increase as a linear function of inverse temperature and both show a simple relation to the structural correlation times of the bulk liquid, implying fragile behavior. However, it is not clear which of the length scales dominates. This point is crucial for the RFOT theory, thus, the ECNLE approach was used. It was possible to de-

scribe the tremendous slowdown of dynamics within the amorphous ice pores by using the vibrational short time dynamics on a picosecond timescale. Furthermore, it was possible to transfer the findings from the pore system to the bulk and obtain a detailed understanding of the mechanism of motion, e.g., explaining the Stokes-Einstein breakdown. Thus, a striking relation between short time dynamics and structural correlation times up to several hundred nanoseconds is observed. The presented approach appears to be not only restricted to the specific water model used for this study, therefore, this might be of great interest for the understanding of supercooled liquids in general.

Next, a specific motion of water, the π-flip, is found for molecules near the walls. An idea was proposed to quantify this effect for the bulk system, so, correlation times and the activation energy ($E_A = 0.44$ eV) of this process can be estimated. Owing to the Arrhenius-like temperature dependence, it is argued that this process should become relevant at temperatures near the glass transition temperature of water.

Finally, internal protein motion is ascertained. Subdiffusive behavior is observed, thus, a complex mathematical treatment to account for this motion is applied. This approach uses power-law waiting time distributions to describe motion in a harmonic potential. The calculations give a good approximation of dynamics.

Zusammenfassung

In biologischen Zellen liegt Wasser in Confinement durch verschiedene Makromoleküle vor. Weiterhin wird vermutet dass der größte Anteil von Wasser auf der Erde eingeschlossen in Mineralien im Erdmantel vorliegt. Daher ist Wasser in Nanoconfinements von großer Relevanz in Technologie und Natur, und es ist wichtig zu verstehen wie das jeweilige Confinement Wassereigenschaften beeinflusst und verändert. Die vorliegende Arbeit beschäftigt sich mit der Charakterisierung von unterkühltem Wasser in verschiedenen Confinements um die Auswirkungen auf das Wasser zu verstehen. Zur Untersuchung werden molekular-dynamische Simulationen des Wassermodells SPC/E in zylindrischen Siliziumdioxid-Poren und in amorphen Eis-Poren verwendet.

Aufgrund der Alltäglichkeit von Wasser erscheint es als eine einfache Flüssigkeit, jedoch zeigt es viele Anomalien die bislang nicht vollständig verstanden sind. Verschiedene Ansätze zur Erklärung dieser Anomalien schlagen einen flüssig-flüssig Phasenübergang bei sehr niedrigen, unterkühlten Temperaturen vor. Da Wasser jedoch aufgrund von homogener Nukleation kristallisiert wird in Experimenten ausgenutzt, dass für Wasser in sehr kleinen Confinements keine Anzeichen für Kristallisation gefunden werden. Diese Systeme sind jedoch sehr komplex, daher ist das Ziel dieser Studie systematisch die Confinementparameter zu variieren um Dichte-, finite-size und Oberflächeneffekte zu unterscheiden.

Die Oberflächenbeschaffenheit beeinflusst die Wasserstruktur in den Poren. Wasser in Siliziumdioxid zeigt induzierte Unordnung nahe der Porenwand. Dies steht im Gegensatz zu Wasser in amorphen Eisporen, für die keine Veränderung der Struktur des eingeschlossenen Wassers im Vergleich mit der Bulkflüssigkeit gefunden wird. Trotz dieser Unterschiede ist die Dynamik nahe den Oberflächen ähnlich. Es wird ein stark veränderter Relaxationsmechanismus beobachtet, der mit einer enormen Verlangsamung der Dynamik einhergeht. Weiter war es durch Vergleiche von Poren mit verschiedenen Durchmessern möglich, den kürzlich postulierten flüssig-flüssig Phasenübergang von Wasser in Siliziumdioxid-Poren, welcher in molekular-dynamischen Simulationen gefunden wurde, auf einen finite-size-Effekt zurückzuführen.

Die amorphen Eis-Poren wurden darüber hinaus auch verwendet um Informationen über intrinsische Längenskalen von Wasser zu erhalten. In verschiedenen, neuen, theoretischen Ansätzen zur Beschreibung der immernoch unverstandenen Dynamik unterkühlter Flüssigkeiten sind diese Längenskalen von großer Bedeutung, z.b. der random first-order transition Theorie (RFOT)

oder bei dem elastically non-linear Langevin equation (ECNLE) Ansatz. Es wurden zwei Längenskalen ausgewertet, und für beide wird ein linearer Anstieg mit inverser Temperatur beobachtet. Auch eine einfache Relation zu den strukturellen Korrelationszeiten der Bulkflüssigkeit lässt sich herstellen, jedoch ist nicht klar welche der Längenskalen die Verlangsamung dominiert. Dies ist von größter Wichtigkeit für die RFOT Theorie. Deshalb wurde im weiteren die ECNLE verwendet. Mit diesem Ansatz ist es möglich die Verlangsamung der Dynamik in den amorphen Eis-Poren sehr gut zu beschreiben. Es wird somit ein signifikanter Zusammenhang zwischen der Vibrationsbewegung zu sehr kurzen Zeiten (1 ps) und den strukturellen Korrelationszeiten bis zu hunderten von Nanosekunden gefunden. Diese Ergebnisse lassen sich auch auf die Bulkflüssigkeit übertragen und erlauben es die Fragilität des Systems sowie verwandte typische Eigenschaften unterkühlter Flüssigkeiten exakt zu erklären. Da das verwendete Wassermodell als typische unterkühlte Flüssigkeit angesehen werden kann, ist dieser Ansatz möglicherweise von sehr großer Relevanz um die Dynamik unterkühlter Flüssigkeiten im Allgemeinen zu verstehen.

Die letzten beiden Kapitel dieser Arbeit behandeln einerseits eine spezielle Wasserbewegung, den π-flip Prozess, der für Wasser nahe der Porenwand beobachtet wurde. Ein Methode wird vorgestellt diesen Prozess für die Bulkflüssigkeit zu quantifizieren. Andererseits eine interne Proteinrückgratbewegung, für die subdiffusives Verhalten gefunden wurde. Hier wird ein fraktaler Ornstein-Uhlenbeck-Prozess eingeführt und verwendet, der die Ergebnisse sehr gut beschreibt.

Contents

Acronyms

BM Brownian motion

CC Cole-Cole

CD Cole-Davidson

CP cylindrical pores

CPF conditional probability functions

CRRs cooperatively rearranging regions

DS dielectric spectroscopy

DSC differential scanning calorimetry

ECNLE elastically collective nonlinear Langevin equation

fFPE fractional Fokker-Planck equation

FPE Fokker-Planck equation

FST *fragile-to-strong* transition

HB hydrogen bonds

HDL high-density liquid

KWW Kohlrausch-Williams-Watts

LDL low-density liquid

LE Langevin equation

LLCP liquid-liquid critical point

LSP large silica pore

MC Monte Carlo

MCT mode-coupling theory

MD molecular dynamics

MSD mean square displacement

NGP non-Gaussian parameter

NMR neutron magnetic resonance

PME particle-mesh Ewald

RFOT random first-order transition theory

RP random pinning

SHD spatially heterogeneous dynamics

SL slit geometry

SPC/E “simple point charge extended”

SSP small silica pore

TTS time-temperature superposition

VAC velocity autocorrelation function

VFT Vogel-Fulcher-Tammann

VHF van Hove correlation function

VDOS vibrational density of states

1 Introduction

This thesis is about supercooled water in confinements. Water is the origin of life on Earth, and it is also found on other planets and in the universe as supercooled liquid, as ice, or as aqueous vapor. Two-third of Earth´s surface is water-covered. Water is important in nature, medicine, biology, geology and technology. Recently, it was proposed that most of the water on Earth is located in the lower Earth mantle confined by minerals [1]. In biological cells, water is confined by macromolecules like proteins, therefore, water in confinements is important. Further, water appears to be a simple liquid, but in fact, it exhibits many anomalies, like the density maximum at 4 °C.

Despite the presence of water in daily life and despite the common knowledge, e.g., that ice is on the top of a freezing lake, the various anomalies of bulk water are not understood. Further, it was pointed out above that water in confinements is a very usual occurrence on Earth, thus, the behavior of water near surfaces is important and is subject to an abundance of studies, which try to answer the questions about the role of water in biological processes in cells, and, how structure and dynamics are changed in the vicinity of surfaces [2, 3].

Several hypotheses have been proposed to explain the anomalies of bulk water. Popular approaches suggest a phase transition between two liquid phases of water, a high density liquid and a low density liquid, at very low, supercooled temperatures [4, 5]. Also, the existence of an additional critical point, the liquid-liquid critical point was proposed [4]. However, there are also other suggestions, only based on the hydrogen-bond network of water [6]. Thus, it is an ongoing debate for more than a decade which of the hypotheses is appropriate to explain the anomalies.

Numerous experimental, simulation, and theoretical studies tried to check the outlined hypotheses for the water anomalies [7–9]. However, there is an obstacle when investigating water at very low temperatures: homogeneous nucleation. Therefore, experimentalists sought for ways to circumvent the problem of crystallization. They exploit that water in narrow confinements shows no indication of crystallization in a wide (supercooled) temperature range [10–12]. This relates supercooled water to water in confinements. Confined water is a very complex system due to several effects like finite-size effects, density effects, and surface effects. This is highlighted by the fact that various experiments and simulation studies observed a sudden change of the temperature dependence of water dynamics in narrow confinements [7–9]. However, the interpretations of the results are diverse. Some workers claimed that this change is attributable to

the proposed phase transition behavior of water at low temperatures, whereas others refuse this interpretation.

For this study, molecular dynamics simulations are performed. As the focus is on investigating water in confinements, one goal is to precisely characterize how structure and dynamics of water are affected by the presence of surfaces. Therefore, position resolved analyses are conducted, which for the desired accuracy and trajectory lengths are only possible by applying molecular dynamics simulations. The water model SPC/E is used, which is commonly employed in simulations due to a computational simplicity while still reproducing many essential features of water [13, 14]. Several studies found interesting effects for SPC/E confined in various materials, like distorted structure near the surface [15], strongly changed dynamics [16] and even claim to find evidence for the proposed phase transition behavior of water [17].

The goal of this study is to systematically vary the confinement parameters in order to distinguish between finite-size, density, and surface effects. For this purpose, two kinds of confinements, several confinement lengths, and water densities are used. The first class of confinements examined in this study mimics narrow cylindrical silica pores used in many experimental approaches. These analyses are meant to guide experimental observations in these confinements. Three pore fillings and a pore with twice the radius of the other silica pores are used to unravel finite-size and density effects in silica confinements. The second type of confinements are neutral pores or amorphous ice pores. For these pores, the water-water and the water-wall interactions are identical. Several confinement geometries are used and the softness of the walls is changed. Thus, comparison with the results from the silica pores reveals surface effects and finite-size effects.

Additionally, previous simulation studies on other supercooled liquids in neutral confinements were used to obtain information about intrinsic length scales [18–20]. It was proposed that knowledge on these lengths is crucial for understanding the still unresolved issues about the features of supercooled liquids [21]. Therefore, studies on neutral pores are used to investigate intrinsic length scales of water. Based on these studies, a recently proposed theory which aims at describing dynamics of supercooled liquids will be used to obtain a detailed understanding of the dynamics within the pores and of the bulk dynamics.

The structure of the thesis is the following: In chapter 2, typical features of supercooled liquids and relevant theories describing dynamics are introduced, as they will be important thereafter. In chapter 3, molecular dynamics simula-

tions are compared with other simulation methods and experiments. Then, the method is detailed and important simulation aspects are given. In chapter 4, the water model and the steps for the production of the confinement systems are detailed. Chapter 5, gives a technical description of quantities, probing structure and dynamics, used in this thesis. In chapter 6, dynamics and structure of the bulk system will be characterized. The proposed phase transition of water in the bulk is investigated and it will be shown that SPC/E water exhibits several properties of typical supercooled liquids, like spatially heterogeneous dynamics. This is important as it lays the ground for the investigation of the confinement systems. Chapter 7 deals with water in silica confinements. Structure and dynamics of water in silica pores are examined. Averages over the entire water in the pores are compared to that of spatially resolved analyses and the claimed phase transition of water in silica pores is addressed. In chapter 8, water in neutral confinements is scrutinized. The structure is checked to be unperturbed when compared to that of the bulk. Two new theoretical approaches to describe dynamics of supercooled liquids are used to rationalize the findings for dynamics in the pores. The elastically non-linear Langevin equation approach turns out to give a valuable description of the dynamics in the neutral confinement and in the bulk. The last two chapters are minor topics: In chapter 9, a particular motion, the π-flip reorientation is investigated for the confined water and for the bulk. In chapter 10, internal motion of protein backbone atoms is described by employing a fractional Ornstein-Uhlenbeck process.

2 State of research and theories

As pointed out in the introduction, the present study deals with molecular-dynamics simulations of water due to two reasons:

First, water appears to be a simple liquid owing to the small number of atoms per molecule, but in fact, water exhibits many anomalies which are currently not fully understood.
Second, water can be supercooled, in experiments and in simulations, and is thus a system, among many others, which can improve the general understanding of supercooled liquids.

Molecular-dynamics simulations enable investigations of both aspects of water and it will be shown that these two aspects are intertwined. Therefore, it is at hand to introduce basic principles and key features of supercooled liquids in general and afterwards this knowledge will be used to detail theories, which strive for an explanation of water anomalies.

To do so, data from bulk simulations of a specific water model, called "simple point charge extended" (SPC/E) are shown. This model is commonly used in many simulation studies, due to the computational simplicity combined with the possibility to obtain reliable and decent results compared to that of real water. The model is specified in chapter 4.1. It is emphasized that employing a different water model, which, e.g., may more accurately describe the structure of real water, does not change the key assertions in this chapter.

2.1 Supercooled liquids

First, what is a supercooled liquid? It is a liquid at temperatures below its melting temperature T_m. Thus supercooled liquids are in a metastable state. Experimentalists can use techniques like differential scanning calorimetry (DSC) to determine the melting temperature of liquids [22]. Real water starts to crystallize at $T_\mathrm{m} = 273.15$ K ($p = 1$ bar). Hence, supercooling liquids requires to avoid crystallization, which is either driven by homogeneous or by heterogeneous crystallization. Homogeneous means that due to thermal fluctuations, molecules statistically form a small crystal nucleus and if the size is larger than a threshold size, it will grow and the entire system will crystallize. On the contrary, heterogeneous means that impurities drive the emergence of crystallization seeds. In molecular dynamics (MD) simulations of bulk water, the system is by definition without any impurity but homogeneous crystallization is possible. However, this does not imply that the melting temperature is identical to that of real water. Exploiting different water-specific temperatures, for in-

stance, the density maximum of real water at 277.15 K (p = 1 bar) [23], which is attained in simulations of SPC/E at $T \approx (230 - 250)$ K ($p = 1$ bar) [24, 25], yields evidence that the temperature scale of simulations and experiments are not identical. This is valid for MD simulations in general, therefore, T_m depends on simulation details like the water model. For the present SPC/E system, one can conclude that upon cooling it enters the supercooled regime at $T \approx 250$ K [1].

The next question is how to characterize a liquid? In general, one can distinguish between dynamics and structure. Liquids exhibit short-range order but no long-range order like crystals. A typical quantity to probe the structure of liquids is the radial pair distribution function, cf. equation (5.4), which is commonly obtained from neutron-scattering experiments. Using the example of SPC/E, the oxygen-oxygen radial distribution function, $g_{OO}(r)$, see Figure 2.1, exhibits next-neighbor peaks which become more pronounced upon cooling. However, the peak positions hardly change and strikingly, translation symmetry is not observed. Hence, no long-range order is present.

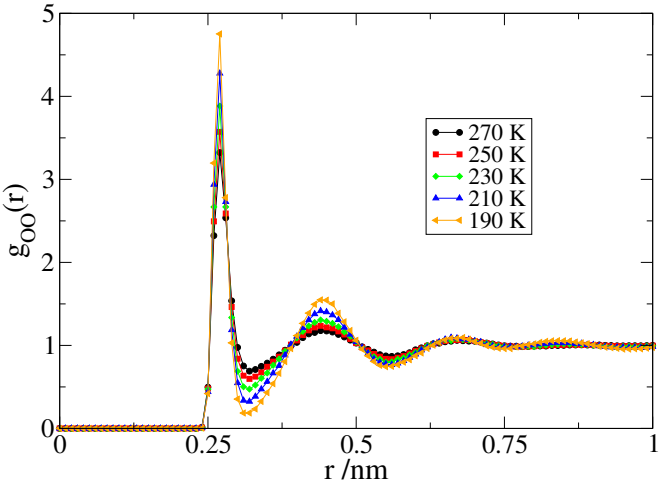

Figure 2.1: Radial pair distribution function illustrating the local order and the absence of long-range order for liquids. The data are from simulations of SPC/E water and show the oxygen-oxygen radial distribution function $g_{OO}(r)$ at various temperatures.

It is known for supercooled liquids that as temperature is lowered dynamics slow down drastically, while the structure changes modestly [27–29]. Therefore, a measure for dynamics is needed.

[1] It was assured that crystallization did not take place during the simulations by investigating the potential energy as time series. Crystallization should give a pronounced trend to lower values for the potential energy [26].

There are various techniques for probing dynamics, the most prominent ones are dielectric spectroscopy (DS), neutron scattering, and neutron magnetic resonance (NMR). They can be used to obtain correlation functions in the time domain or susceptibilities in the frequency domain, however, the detected motion differs as the methods are sensitive to different particles, translational or rotational motion, weight the motion in different ways and use different length scales. In the case of water, DS probes the dipole reorientation of the nuclear dipole moment, NMR can be used to detect bond reorientation, and neutron scattering mainly measures the motion of hydrogen atoms (the total scattering cross section is significantly dominated by the incoherent cross section for hydrogen atoms) [30–32]. Further, NMR and DS use external fields to disturb the system and gather information on how the system relaxes to equilibrium. On the other hand, neutron scattering makes no use of external fields and thus probes *internal* fluctuations. With reference to these methods, MD simulations can be employed to calculate all of the previously mentioned quantities, however, also probe *internal* fluctuations [2]. Hence, the final step to establish a proper connection between NMR or DS and MD simulations is based on the very meaning of the fluctuation-dissipation theorem, stating that internal fluctuations and external disturbances are intrinsically related [34].

A typical correlation function $C(t)$ and the imaginary part of the corresponding susceptibility $\chi''(\omega) = \pi\omega \cdot \frac{1}{2\pi}\int_{-\infty}^{\infty} C(t)e^{-i\omega t}dt$ (see also equations (5.8) and (5.15)) for a liquid in the supercooled regime are depicted in Figure 2.2, panel a) and b) respectively [28, 29, 31, 35].

Starting at high temperatures, a single decay for the correlation function can be observed. As the temperature is reduced, a two-step decay emerges and becomes increasingly more pronounced below $T \approx 240$ K. This is accompanied by a shift of the curves to longer times, corresponding to slower dynamics. Usually, the Kohlrausch-Williams-Watts (KWW) function is employed to describe the long-time decay of correlation functions, see the solid lines in a) [29]. Mathematically, a KWW function corresponds to a stretched-exponential form, reading

$$C(t) = A \cdot e^{-\left(t/\tau_{\mathrm{KWW}}\right)^{\beta_{\mathrm{KWW}}}} \tag{2.1}$$

with values β_{KWW} between 0 and 1. For the curves from panel a), β_{KWW} changes from 0.8 at high temperatures to ≈ 0.6 at low temperatures, where it levels off, cf. Figure 6.8 in chapter 6.4. Thus, decorrelation is clearly non-exponential.

[2] At least in this work. Basically it is also possible to use external electric fields [33].

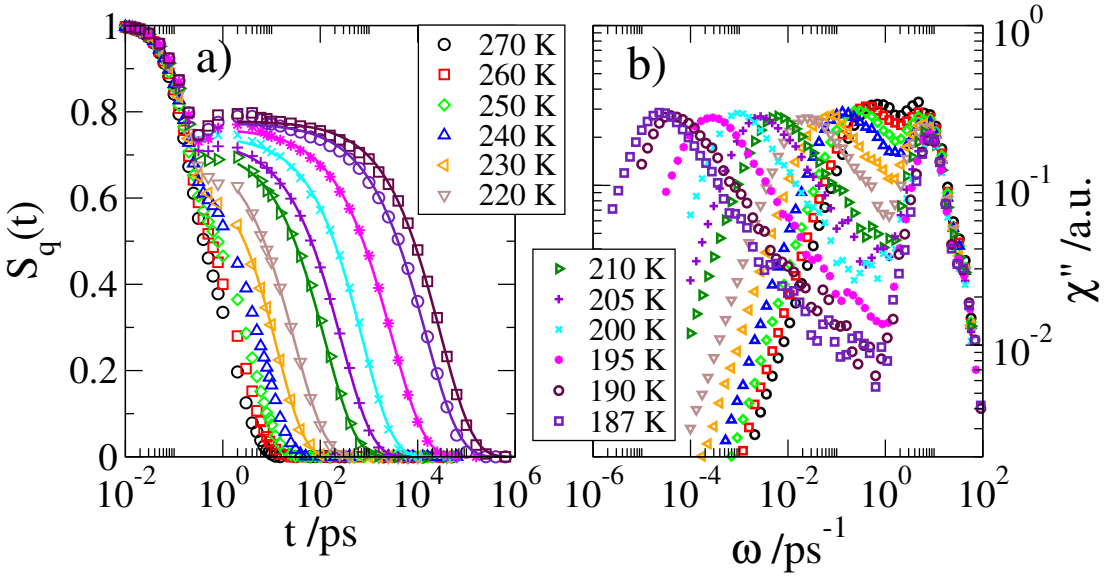

Figure 2.2: Typical decay of a correlation function, a), and the imaginary part of the corresponding susceptibility, b), probing local motion of a liquid in the supercooled regime. The data are from simulations of SPC/E and depict the incoherent intermediate scattering function, $S_q(t)$ ($q = 22.7\,\mathrm{nm}^{-1}$), for oxygen atoms and the corresponding susceptibility.

Due to the two-step decay, the susceptibility χ'' exhibits two distinct peaks at lower temperatures. A vibrational peak is located at high frequencies. While the position of the maximum of this peak changes weakly with decreasing temperature, the location of the other peak is strongly temperature dependent. The latter peak is typically interpreted as relaxation process and denoted α- or structural relaxation process, when probed on sufficiently large length scales [31, 35].

In general, the introduced KWW functions are not the only possible way to describe the decay of correlation functions. Another more rarely used approach to describe the data in the time domain is given by Mittag-Leffler functions[3],

$$C(t) = A \cdot E_\alpha \left(-(t/\tau_{\mathrm{MLF}})^\alpha\right), \tag{2.2}$$

with $E_\alpha(z) = \sum_{n=0}^{\infty} \frac{z^n}{\Gamma(1+n\alpha)}$ [37]. Mittag-Leffler functions are generalized exponential functions. Choosing $\alpha = 1$ yields a simple exponential function, whereas $\alpha < 1$ gives first a KWW-like decay which is followed by a power-law [38, 39].

[3] The Mittag-Leffler fits were performed by using a modified Matlab code available on this website [36].

The crossover from one regime to the other is determined by τ_{MLF}. In DS experiments, susceptibilities are detected directly, and usually the data is not transformed to the time domain. Therefore, it is very important to know how KWW functions and Mittag-Leffler functions are related to functions which are typically used to describe data in the frequency domain.

There, two functions are typically employed, the so-called Cole-Cole (CC) functions

$$\chi''_{\mathrm{CC}} = A \cdot \frac{(\omega\tau_0)^{\beta_{\mathrm{CC}}} \sin(\pi\beta_{\mathrm{CC}}/2)}{1 + 2(\omega\tau_0)^{\beta_{\mathrm{CC}}} \cos(\pi\beta_{\mathrm{CC}}/2) + (\omega\tau_0)^{2\beta_{\mathrm{CC}}}} \tag{2.3}$$

and the Cole-Davidson (CD) functions

$$\chi''_{\mathrm{CD}} = A \cdot \left[\cos\left(\frac{1}{\tan(\omega\tau_0)} \right)^{\beta_{\mathrm{CD}}} \sin\left(\beta_{\mathrm{CD}} \frac{1}{\tan(\omega\tau_0)} \right) \right] \tag{2.4}$$

with τ_0, A, and $\beta_{\mathrm{CC;CD}}$ as free parameters [40]. Remarkably, the rarely used Mittag-Leffler approach, see equation (2.2), yields for the imaginary part of the susceptibility the very often used CC approach, equation (2.3), which describes a symmetrical peak behavior in frequency space [38]. In contrast to this, KWW functions do not exactly correspond to the CD relaxation patterns, but they are similar [41, 42]. Both yield asymmetrical behavior in frequency space and exhibit a low frequency flank which decreases as $\propto \omega^1$, though, they are not identical, in particular with respect to the distribution of correlation times [41, 42]. For this thesis, both are used as synonyms referring to the time domain or frequency domain respectively.

So far, it was stated that dynamics slow down upon cooling, because the correlation functions depicted in Figure 2.2 shift to longer times. Quantifying this shift can be done by employing the characteristic times τ_{KWW} or τ_{MLF}, or by manually specifying a correlation time using the condition $C(\tau) = 1/e$. The methods are not identical due to the prefactor A, see (2.1), which can be temperature dependent. However, the general behavior is not altered and the correlation times are denoted as structural correlation time τ_α either way (or relaxation time for experiments using external fields). Relating to the temperature dependence of the correlation times, two characteristic behaviors can be distinguished [43]. First, *strong* or *Arrhenius-like* behavior, corresponding to crossings of energy barriers of constant height

$$\tau_\alpha = \tau_0 \cdot e^{\frac{\Delta F}{k_{\mathrm{B}} T}} \tag{2.5}$$

with, in this particular case, ΔF referring to a constant free-energy barrier. Second, *fragile* or *non-Arrhenius* behavior, where often the empirical Vogel-Fulcher-Tammann (VFT) relationship is applied [27, 29, 44–46],

$$\tau_\alpha = \tau_0 \cdot e^{\frac{B}{T-T_\infty}}. \tag{2.6}$$

Figure 2.3 illustrates *strong* and *fragile* behavior. In this Figure, *strong* behavior appears as straight line whereas *fragile* behavior yields a bended curve. The extent of curvature, also called fragility, depends on the material. A common measure of fragility is the ratio B/T_∞ [47, 48]. The black circles show the correlation times obtained from the curves in Figure 2.2 consistent with the definition $C(\tau_\alpha) = 1/e$. A VFT function (red curve) describes the data with the parameters $T_\infty = 156$ K and $B = 451$ K, whereas a *strong* behavior is not appropriate in this case. The ratio $B/T_\infty = 2.9$ indicates that SPC/E water is a very fragile liquid.

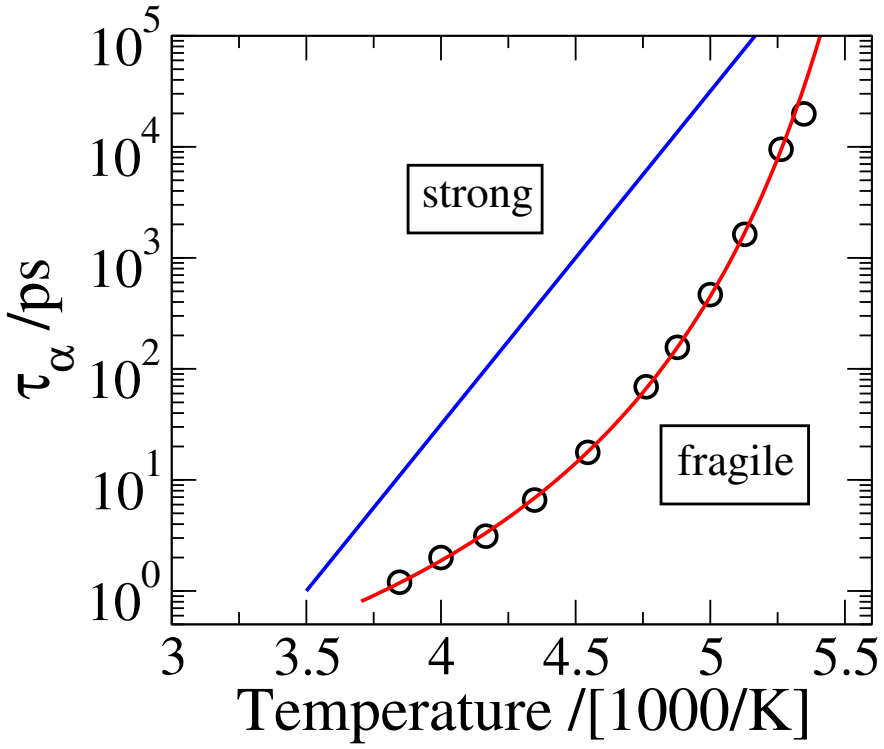

Figure 2.3: Structural correlation time τ_α dependent on temperature. The black circles are correlation times obtained from the curves in Figure 2.2 a) using the definition $C(\tau_\alpha) = 1/e$. The red line depicts a Vogel-Fulcher-Tammann function, which well describes the data, and the blue line is an Arrhenius function for comparison.

By definition, a supercooled liquid enters a state called *glassy* when the structural relaxation time is on the order of $\tau_\alpha = 100$ s [27]. At that point, ergodicity is broken and the system appears as a solid and not as a liquid [29]. This highlights the relevance of time scales on which dynamics is probed, as the prior definition does not correspond to a thermodynamic phase transition. Using the parameters of the VFT fit in the studied temperature range, the glass transition temperature for SPC/E should be roughly 160 K.[4]

In conclusion, typical properties of supercooled liquids have been introduced, namely, two-step decays of correlation functions, non-exponential decorrelation, non-Arrhenius or fragile behavior for slowing of dynamics, whereas structure changes only on a local scale, and non-ergodicity at the glass transition temperature. This was illustrated using the example of bulk simulations of SPC/E which is therefore a typical supercooled liquid. Those findings are in agreement with various MD studies on SPC/E [25, 49–51].

In order to explain the results, the next subsections will shed light on some selected theories and additional properties of supercooled liquids.

2.2 Spatially heterogeneous dynamics

In this part of the thesis, a key feature of supercooled liquids called spatially heterogeneous dynamics (SHD) will be detailed. The interested reader is referred to the reviews by *Ediger* and *Sillescu* for more information relating to SHD [52, 53].

In chapter 2.1, a slowing of dynamics was observed as the temperature was reduced. In order to quantify this, structural correlation times τ_α have been defined based on correlation functions. In experiments and simulations, correlation functions (or susceptibilities) are usually obtained as an average over the particles in the system. For example, conducting DS experiments with a common setup probes the dipole reorientation as average over all water molecules in the sample. Therefore, correlation functions and derived parameters like τ_α are ensemble averaged quantities. This brings up the question about the origin of the non-exponential decays and relates to an underlying distribution of correlation times $G(\tau)$. In general, there are two possible scenarios. First, rele-

[4] In fact, the glass-transition temperature is even more baffling as it depends not only on an ad-hoc definition for the relaxation times, but also on the cooling rate. The latter feature of glasses will not be detailed in the following.

vant particles relax in the same, in the case of supercooled liquids, intrinsically non-exponential way. This scenario is called ideal *homogeneous* [29, 52–55]. Second, there may exist a broad distribution of correlation times $G(\tau)$ yielding a non-exponential decay due to the superposition of many exponential decays. This scenario is called ideal *heterogeneous* [29, 52–55].

On the one hand, MD simulation studies analyzing different quantities like dynamic clusters, see equations (5.22) or (5.24), [56, 57], the non-Gaussian parameter, equation (5.10) [57–59], and susceptibilities derived from four-point density correlations, see equation (5.18), [56, 60–62] make a compelling case for the evidence of heterogeneous dynamics and the clustering of fast or slow particles. This feature is called spatially heterogeneous dynamics (SHD).

On the other hand, dynamic hole-burning experiments found evidence for the heterogeneous case at the glass transition temperature, while MD simulations are restricted to the weakly supercooled regime [52, 53]. The principle idea of these methods is to chose e.g. slow particles and then monitor the time scale on which those particles relax to the average equilibrium correlation time. Selecting slow particles can be done by employing dynamical filters, see equation (5.20). In essence, four-dimensional NMR and DS experiments settled the lifetime of dynamic heterogeneities on the order of τ_α and three-dimensional NMR experiments provided access to the relevance of homogeneous and heterogeneous contributions [55, 63].

In the present study, three-time correlations will be also investigated. Following the idea proposed above, a filter must be chosen to weight the motion in the first time interval. Here, an ideal binary filter $K_i(t_f,R)$ which weights the motion of the i-th particle in the first time interval t_f will be used, with $K_i(t_f,R) = 1$ if $|\vec{r}_i(t_f) - \vec{r}_i(0)| < R$ and $K_i(t_f,R) = 0$ if $|\vec{r}_i(t_f) - \vec{r}_i(0)| \geq R$. It is strongly emphasized that only for this particular filter, the limiting cases of ideal homogeneous or ideal heterogeneous dynamics given below are correct [55]. For the ideal homogeneous case, motion in the first interval is by definition entirely uncorrelated from motion during the second time interval [55]. This yields a simple factorization,

$$C^{\mathrm{hom}}_{\mathrm{bin},3}(t;t_f) = 1 \cdot C(t) + 0 \cdot C(t), \tag{2.7}$$

with $C^{\mathrm{hom}}_{\mathrm{bin},3}(t;t_f)$ a three-point correlation function using a binary filter in the ideal homogeneous case and $C(t)$ a two-point correlation function, e.g. the incoherent intermediate scattering function $S_q(t)$. For the ideal heterogeneous case, the system consists of several exponentially relaxing subensembles and

particles belonging to the same subemsemble are assumed to show ideal homogeneous behavior [55]. After some calculus, the ideal heterogeneous case is

$$C^{\text{het}}_{\text{bin},3}(t;t_f) = C(t+t_f). \tag{2.8}$$

In chapter 6.2, the mentioned methods are used to thoroughly characterize bulk SPC/E, before moving to much more complex systems like water in silica or neutral confinements.

The connection of SHD to the slowing of dynamics is an ongoing discussion, see also chapter 2.6.

The following part will deal with theoretical approaches for describing dynamics of liquids. The starting point for this are high temperatures (not supercooled).

2.3 Brownian motion

The concept of Brownian motion (BM) is introduced, due to its transferability to real systems and the physical insights into the dynamics of liquids. Afterwards, slow dynamics of supercooled liquids is addressed. All equations and explanations for the following part dealing with BM are based on the textbooks of *H. Risken* and *R. Zwanzig* (see [64, 65]), otherwise literature is explicitly mentioned.

A description of BM is possible by applying the one-dimensional Langevin equation (LE),

$$\dot{v} + \gamma \cdot v = \Gamma(t), \tag{2.9}$$

with v the velocity, γ the friction coefficient and $\Gamma(t) = F_{\text{fluc}}/m$ the fluctuating force per mass (Langevin force). The basic idea of equation (2.9) is to separate the total force into two parts: a systematic part, the friction term, and an extremely fast fluctuating part or noise, which gives rise to the Langevin force. Γ is often assumed to obey a Gaussian distribution with zero mean and a δ-correlation in time, called white noise,

$$\langle \Gamma(t)\Gamma(t')\rangle = \delta(t-t') \cdot 2\gamma k_{\text{B}} T/m, \quad \langle \Gamma(t)\rangle = 0. \tag{2.10}$$

Solutions of (2.9) are then usually obtained by integration.

Another approach is to use a Fokker-Planck equation (FPE). Those equations can be deduced when starting from a master equation and performing a Kramers-Moyal expansion. Given the conditions of (2.10) one can proof that only the first two terms of the expansion do not vanish and the FPE follows,

$$\frac{\partial W(x,t)}{\partial t} = \left[-\frac{\partial}{\partial x} D^{(1)}(x,t) + \frac{\partial^2}{\partial x^2} D^{(2)}(x,t) \right] W(x,t), \tag{2.11}$$

with x denoting the position in this case, but similar formulations are valid for any macroscopic variable like the velocity. Further, $D^{(1)}(x,t)$ designates the drift coefficient, $D^{(2)}(x,t)$ the diffusion coefficient and $W(x,t)$ the probability density. If drift and diffusion coefficient are independent of time, the process which yields the distribution W is a Markov process. For the BM process described by equation (2.9) drift and diffusion are determined by

$$D_v^{(1)} = -\gamma \cdot v, \quad D_v^{(2)} = \frac{\gamma k_B T}{m}. \tag{2.12}$$

The subscripts v are intended to explicitly highlight that this is valid for the velocities as the macroscopic variable. Large friction yields rapidly diffusing velocities, whereas a description for the position would yield exactly the opposite.

Equation (2.11) also holds for transition probability densities $P(x,t|x',0) = \frac{W(x,t;x',0)}{W(x',0)}$ given the special initial condition $W(x,t') = \delta(x-x')$ [5]. Assuming a process with drift coefficient $D^{(1)} = 0$ and constant diffusion coefficient like $D(x,t) = D$, a so-called Wiener process, yields for $t > 0$

$$P(x,t|x',0) = \frac{1}{\sqrt{4\pi D \cdot t}} e^{\left(-\frac{(x-x')^2}{4D\cdot t}\right)}. \tag{2.13}$$

By using equation (2.13) it is possible to calculate typical quantities like the mean square displacement (MSD), see equation (5.7), or the incoherent intermediate scattering function $S_q(t)$. For the MSD a linear dependence on t is obtained,

$$\langle x^2 \rangle = 2D \cdot t, \tag{2.14}$$

or using three dimensions

$$\langle \Delta r^2 \rangle = 6D \cdot t \tag{2.15}$$

[5] For a Markov process, $W(x,t;x',t')$ contains the full information to characterize the process.

and $S_q(t)$ shows a single-exponential decay for the freely diffusing particle [66, 67]

$$S_q(t) \equiv \int\int dx' dx e^{-iq(x-x')} P(x,t|x',0) W_{\mathrm{st}}(x') = e^{-Dq^2 \cdot t}, \tag{2.16}$$

with $\tau_\alpha = \frac{1}{Dq^2}$, $W_{\mathrm{st}}(x)$ denoting a general stationary probability density [6], and stretching parameter $\beta_{\mathrm{KWW}} = 1$. The temperature dependence is given as $\tau_\alpha(q,T) = \frac{1}{D(T)q^2} = \frac{\gamma m}{k_{\mathrm{B}}T}\frac{1}{q^2}$.

It is sometimes useful to associate a distribution of correlation times $G(\tau)$ with the decay of a correlation function $C(t)$, see the discussion on heterogeneous and homogeneous behavior in chapter 2.2. This can be achieved by a Laplace transformation,

$$C(t) = \int_0^\infty G(\tau) e^{-t/\tau} d\tau. \tag{2.17}$$

The single-exponential decay of $S_q(t)$ given by equation (2.16) yields a correlation times distribution $G(\tau) = \delta(\tau - \tau_\alpha)$ and trivially homogeneous behavior (see the discussion of heterogeneity for the bulk system in chapter 6.2) [39, 52].

During chapter 2.1, the temperature dependence of correlations times had been distinguished into strong and fragile behavior. The framework of BM is also suitable to give some basic insights relating to this. First, diffusion within a harmonic potential with the force $f(x) = -\kappa \cdot x$ is investigated. The one-dimensional Fokker-Planck equation is then dependent on the variables x, v, t,

$$\frac{\partial W(x,v,t)}{\partial t} = \left\{ -\frac{\partial}{\partial x} v + \frac{\partial}{\partial v}[\gamma v + f(x)] + \frac{\gamma k_{\mathrm{B}} T}{m} \frac{\partial^2}{\partial v^2} \right\} W(x,v,t) \tag{2.18}$$

and is called Kramers equation. In the high-friction limit, the Kramers equation can be transformed to the Smoluchowski equation,

$$\frac{\partial W(x,t)}{\partial t} = \frac{1}{m\gamma} \left[-\frac{\partial}{\partial x} f(x) + k_{\mathrm{B}} T \frac{\partial^2}{\partial x^2} \right] W(x,t). \tag{2.19}$$

[6] For the freely diffusing particle, there is a stationary state for the velocities but not for the coordinates. For a harmonically bound particle, there exists a stationary probability in the coordinate space, see below, and the solution for the freely diffusing particle can be obtained as limit for a vanishing potential.

For particles trapped in a harmonic potential the stationary solution is

$$W_{\mathrm{st}}(x) = \sqrt{\frac{\kappa}{m\gamma \cdot 2\pi D}} e^{-\frac{\kappa x^2}{m\gamma \cdot 2D}} \tag{2.20}$$

and therefore the MSD is finite for $t \to \infty$

$$\langle x^2 \rangle = \frac{2Dm\gamma}{\kappa} = \frac{k_{\mathrm{B}}T}{\kappa}. \tag{2.21}$$

On the other hand, for particles in the high-friction limit diffusing over a barrier $\Delta F = F(x_{\mathrm{max}}) - F(x_{\mathrm{min}})$ with the necessary condition $\frac{\Delta F}{k_{\mathrm{B}}T} \gg 1$, the Smoluchowski equation yields

$$\tau = \frac{2\pi k_{\mathrm{B}}T}{D} \cdot \frac{1}{\sqrt{F''(x_{\mathrm{min}})|F''(x_{\mathrm{max}})|}} e^{\frac{F(x_{\mathrm{max}}) - F(x_{\mathrm{min}})}{k_{\mathrm{B}}T}}. \tag{2.22}$$

In the case of $\Delta F = \mathrm{const}$, the result is identical to equation (2.5), thus giving a possible explanation for Arrhenius behavior.

At the beginning of this subsection, BM was introduced as possible high temperature description of dynamics. In fact the framework is more general. This can be illustrated using the typical MSD of supercooled liquids, see Figure 2.4. The dynamical behavior can be separated into three different regimes, namely ballistic, subdiffusive and diffusive behaviors [51]. The framework discussed so far is only valid in the limit of long times or equivalently large length scales (small $|\vec{q}|$), the diffusive regime. For very long times, supercooled liquids exhibit *simple* diffusive behavior and the description of freely diffusing particles applies. This is shown for oxygen atoms of SPC/E where a diffusive regime is visible for all temperatures, even at deeply supercooled temperatures like $T = 187$ K. Therefore, the focus of this work is on intermediate time scales relative to the diffusive and ballistic regimes and thus on internal length scales, e.g. next-neighbor distances. In chapter 10, a generalized version of equation (2.11) is discussed and employed to characterize subdiffusive behavior found for backbone atoms of proteins. It should be noticed that it is not possible to describe ballistic motion with the presented approach of BM. For instance, the LE corresponding to equation (2.19) is given by

$$\dot{x} = \frac{1}{m\gamma} f(x) + \frac{1}{\gamma} \Gamma(t), \tag{2.23}$$

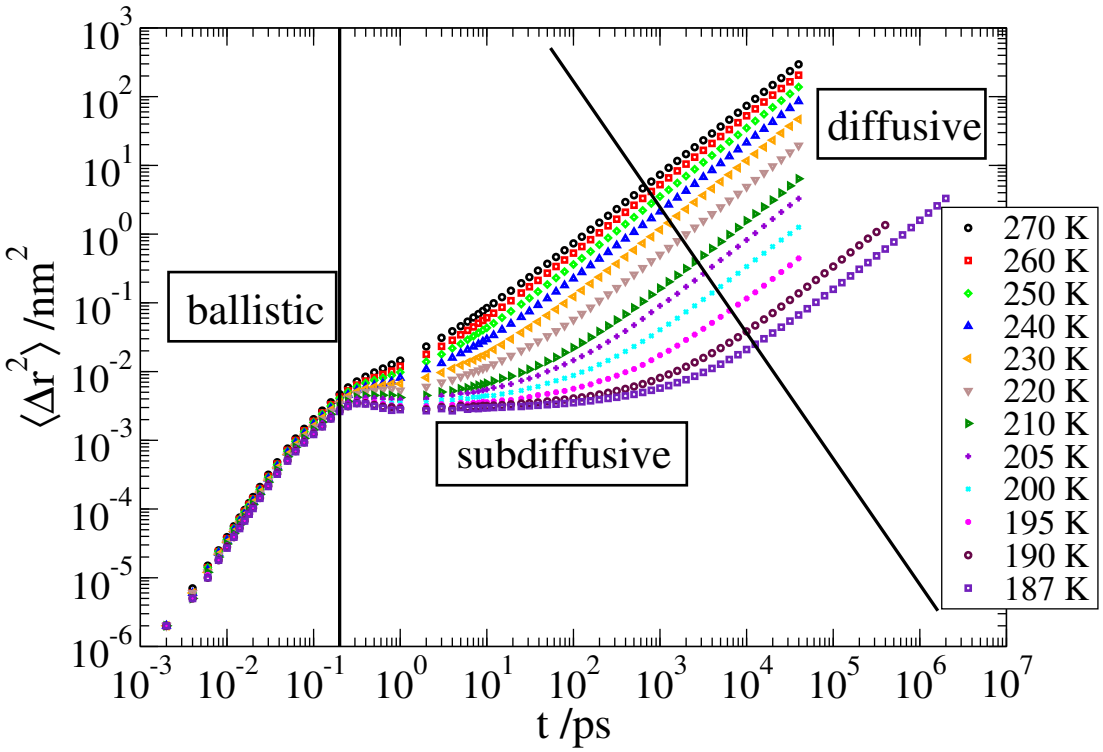

Figure 2.4: Mean square displacements (MSD) of a supercooled liquid. The MSD was calculated for the oxygen atoms of bulk water. Three regimes of dynamics are separated by the black lines [51].

similar to equation (2.9). Owing to $\Gamma(t)$, see equation (2.10), random distances can be passed in finite time intervals, hence, the speed of particles is infinite [68] [7].

2.4 The random first-order transition theory

The random first-order transition theory (RFOT) is a theory which attempts to explain dynamics of supercooled liquids. The following equations and explanations can be found in the reviews by *Cavagna*, *Biroli&Bouchaud*, the textbooks by *Zwanzig* and *Götze* [27, 65, 70, 71] or the literature is explicitly mentioned.

The theory is based on calculations for spin models and essentially consists of two parts, a high temperature and a low temperature description of dynam-

[7] A possible solution for this is the telegraph equation $t_c \frac{\partial^2 W(x,t)}{\partial t^2} + \frac{\partial W(x,t)}{\partial t} = D \frac{\partial^2 W(x,t)}{\partial x^2}$ with t_c the length of time for an averaged free path and c the velocity, what can be verified to be a special case for time-nonlocal Fokker-Planck equations [68, 69].

ics.

Starting at high temperatures the mode-coupling theory (MCT) approach is adopted, which contains BM as limiting case. MCT is a theory which intends to describe structural relaxation. To do this, a Hilbert space picture is employed, distinguishing between relevant and irrelevant variables, similar to the introduction of BM in chapter 2.3. A projection approach is chosen to separate the subspace of *slow* variables from an orthogonal subspace of *fast* variables. Following the *Mori-Zwanzig* projection operator formalism, a generalized Langevin equation can be obtained,

$$\frac{dA}{dt} = i\Omega A(t) - \int_0^t d\tau K(\tau) \cdot A(t-\tau) + \Gamma(t), \tag{2.24}$$

with K as memory function, Ω as a frequency and the fluctuation-dissipation theorem $\langle \Gamma(t)\Gamma(t')\rangle = K(t-t') \cdot \langle AA\rangle_{\mathrm{eq}}$ (e.g. $\langle AA\rangle_{\mathrm{eq}} = \frac{k_B T}{\gamma m}$ for the position $A = x$ in the case of a particle trapped in a harmonic potential and large friction (see equation (2.21)). This equation is a generalization of equation (2.9) because it allows for different than harmonic-oscillator heat baths and is thus in general non-Markovian. However, it is crucial that for the derivation only potentials up to harmonic can be used, this property is called linear.

Equation (2.24) can be transformed to directly account for correlation functions $C(t)$ [72],

$$\frac{dC}{dt} = i\Omega C(t) - \int_0^t d\tau K(\tau) \cdot C(t-\tau). \tag{2.25}$$

The key idea of the theory is to employ a certain *relevant* subspace which is spanned by orthonormal functions, the longitudinal currents $\vec{j}^{\mathrm{L}}(\vec{q}) = \frac{1}{m}\sum_{i=1}^{N} \vec{p}_i^{\mathrm{L}} e^{i\vec{q}\vec{r}_i}$ and number densities $\partial\rho(\vec{q}) = \sum_{i=1}^{N} e^{i\vec{q}\vec{r}_i} - (2\pi)^3 \rho\, \partial(\vec{q})$, as only pairs of these contribute to density correlations [8] [72, 73]. All possible combinations of modes $\vec{q}$ for the product variables have to be considered to describe the system in Hilbert space, and that is the reason to name the theory *mode-coupling*. Due to the choice of orthonormal functions, $A = \begin{Bmatrix} \partial\rho(\vec{q}) \\ \vec{j}^{\mathrm{L}}(\vec{q}) \end{Bmatrix}$ and C becomes a matrix and the Langevin equation is nonlinear. After some arith-

[8] Only the number densities or the currents do not contribute to the density correlations, as, e.g., the number density is position dependent, whereas the density correlations are not.

metics and using several assumptions for the memory kernel, an equation of motion for the isotropic ($\vec{q} \to |\vec{q}| = q$) density correlations is given as,

$$0 = \frac{d^2F(q,t)}{dt^2} + \frac{q^2 k_B T}{mS(q)} F(q,t) + \int_0^t d\tau K(q, t-\tau) \frac{\partial F(q,t)}{\partial \tau} \tag{2.26}$$

with $F(q,t) = \left\langle \sum_i \sum_j \frac{\sin[q\cdot(r_i(t) - r_j(0))]}{q\cdot(r_i(t) - r_j(0))} \right\rangle$ the intermediate scattering function and $S(q)$ the static structure factor. The only input needed to solve the equation is $S(q)$.

In essence, mode-coupling theory derives nonlinear Langevin equations by expanding the subspace to product variables. This leads to a separation of time scales for the memory, a fast Markovian part and a non-Markovian contribution due to the nonlinearity [9]. Solutions of equation (2.26) yield a two-step decay and a stretched-exponential form for the long-time decay, consistent with the typical features of supercooled liquids discussed in chapter 2.1 [10].

Upon cooling, the theory predicts an increasing correlation length ξ_{MCT}, which is referred to as *dynamic* correlation length hereafter [61, 72, 75, 76] [11]. At a certain temperature T_C the length scale diverges and RFOT suggests a transition for the mechanism of relaxation from non-activated, MCT-like, to activated events. MCT is usually assumed to be unable to account for activated barrier crossing as a system of infinite dimensionality (all combinations of product modes, see above) is never able to surmount any barrier. This transition within RFOT is accompanied by a discontinuous order parameter, the configurational entropy, but without any thermodynamic sign (no latent heat) [77], rationalizing the name *random first order*. The idea is that MCT describes motion within a large single minimum in the energy landscape, but at T_C, this minimum splits up into many disconnected minima and leads to the definition of the configurational entropy, which is therefore discontinuous.

[9] This is basically the idea why to use a product variable approach. Equation (2.25) is based on separating fast and slow variables into orthogonal spaces. Now, the point is that the subtle choice of number densities and currents as basis yields slow contributions from the products of slow density modes for the random force [72]. Thus, the random force is itself not strictly *fast*. This immediately yields long-time tails for the memory and correlation functions.

[10] A similar approach appears promising to describe the so-called *Debye process* found for water and various liquids which form hydrogen bonds (HB) [74]. Of course in this case, the basis must be chosen differently than for the *usual* MCT which attempts to describe density fluctuations.

[11] Therefore, the theory is no *simple* mean-field theory, because in this case it would not be possible to define this kind of a length scale [61].

Figure 2.5 illustrates the idea in terms of the free energy of the system. The dashed line corresponds to the free energy of the liquid state f_{L}. Below T_0 the first and thus most stable minimum, f_{min}, in the free-energy landscape is present. At T_C the dynamical transition occurs. This means that each of the minima exhibits a large free energy f_{th}, but the idea is that there are exponentially many of them. This gives rise to the configurational entropy, with $T \cdot S_C$ the difference between f_{L} and the marginally stable states f_{th}. Further lowering the temperature yields a reduction of $T \cdot S_C$ and at T_K (Kauzmann temperature) the configuration entropy vanishes. It is important to notice that methods tracking f_{L} do not observe the dynamic transition.

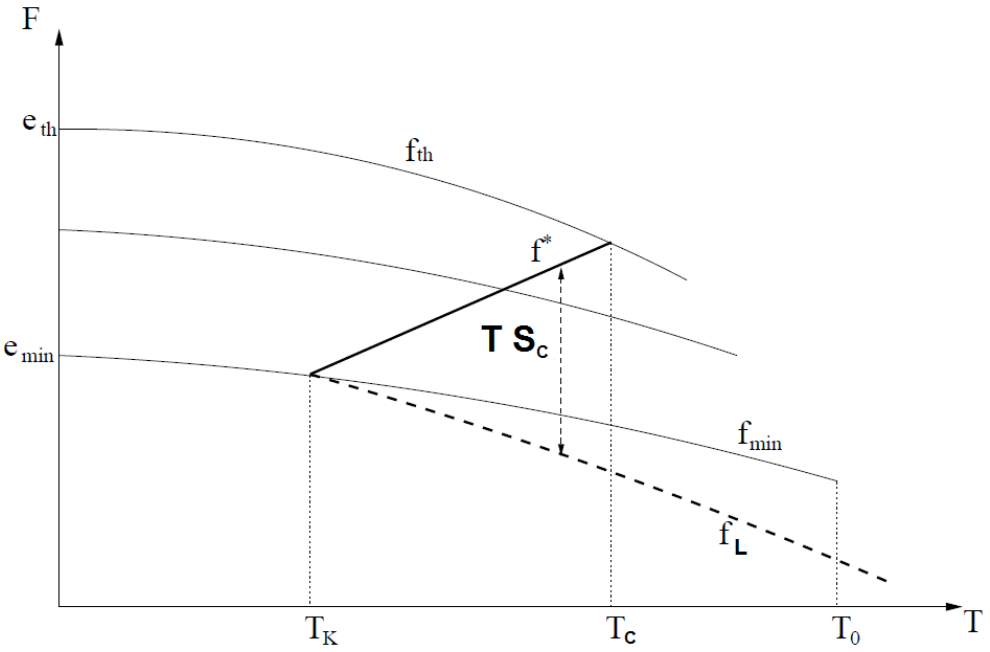

Figure 2.5: Schematic illustration of the random first-order transition theory in terms of free energies. See text for explanation. The figure was adapted from [70].

The next step for the theory is to calculate S_C, which can be regarded as entropic difference to the crystalline state. In the latter state, the system is trapped in a single minimum and only vibrations are possible. In contrast, RFOT proposes that there are exponentially many states for the supercooled liquid, thus, $S_C \approx S_{\mathrm{liquid}} - S_{\mathrm{crystal}}$. The point is to transfer S_C from the energy landscape to real space. This is done by using cooperatively rearranging regions (CRRs). Different from the older Adam-Gibbs approach, where S_C is based on a combinatorial argument, which neglects any interaction between

CRRs, RFOT suggests a nucleation-theory approach for the size of these CRRs and accounts for interaction. Following the nucleation spirit, there exists a surface-tension term and a volume entropy-gain term, see also [78], reading

$$\Delta F_{\text{surf}} = Y(T) \cdot L^{\theta} \tag{2.27}$$

with Y a surface tension and L the size of the object. The exponent θ must satisfy the condition $\theta \leq d - 1$, with d the dimensionality of the system. For the volume term the definition reads

$$\Delta F_{\text{vol}} = -TS_C(T) \cdot L^{d} \tag{2.28}$$

The size of *droplets* ξ_S is given by the condition $\Delta F_{\text{surf}} = \Delta F_{\text{vol}}$. This yields

$$\xi_{\text{S}} = \left(\frac{Y(T)}{TS_C(T)} \right)^{\frac{1}{d-\theta}}. \tag{2.29}$$

ξ_{S} denotes the minimum length scale for which the entropy gain balances the surface tension costs and increases upon cooling. The idea is that the entire liquid is build up by droplets of size ξ_{S} and thermally induced fluctuations drive the droplets to rearrange and explore different configurations. In the following, ξ_{S} will be denoted as *static* length scale to distinguish it from the *dynamical* length scale of MCT. The derivations in chapter 2.3 revealed for *strong* behavior a constant free-energy barrier. In the RFOT scenario the barrier scales as

$$\Delta F_{\text{barrier}} \propto \xi_S^{\psi}, \tag{2.30}$$

with ψ an additional exponent with $\psi \geq \theta$. The barrier increases with increasing length scale or when the temperature is lowered and VFT behavior is found for the specific choice $\psi = d/2$ [79][12]. Consistent with equation 2.30, larger regions $\xi > \xi_S$ can rearrange too, but it will take them an exponentially longer time, thus justifying the idea that systems consist of rearranging regions or patches of amorphous order of size ξ_S.

But how to probe ξ_{S}? *Bouchaud* and *Biroli* proposed a solution for this issue [77]. The first step is to confine a liquid in a confinement which forms a sphere of radius R. It is crucial that this is done without changing the structural properties of the confined liquid, thus, the wall must consist of the same material and structure as the liquid, therefore the name *neutral* confinement.

[12] For $\psi = d/2$, RFOT and Adam-Gibbs give the same results, despite the grave difference regarding the surface tension.

The basic idea is to assume the wall to be in state or configuration α. It is supposed that the wall imposes a static contribution to the energy landscape of the confined liquid, therefore, the liquid is in the same state α or in a different state. If the liquid is in a different state than prescribed by the wall there must be some kind of penalty by the wall. This mismatch was previously introduced as surface tension. This means, as the structural properties of the confined liquid and the wall are assumed to be identical, that the wall consists of frozen patches of amorphous order. Thus, the sampling of different configurations of the confined liquid should yield exactly the information about the interaction of droplets in the bulk. However, employing this procedure yields the issue how to probe configurations or states. RFOT suggests a new overlap function, sometimes referred to as *point-to-set* to probe the overlap between the configuration of the wall and the confined liquid, see (5.19). Recent theoretical considerations found the long-time overlap Q_∞ to decrease exponentially with the pore radius R [80], explicitly

$$Q_\infty(R) \propto e^{-(R/\xi_S)^{\nu(d-\theta)}}. \tag{2.31}$$

It is emphasized that the overlap is obtained for $\lim_{t\to\infty}$, thus the notion of a *static* length scale. Additionally, a new exponent ν appears which relates the simple surface tension Y to a distribution of surface tensions $P(Y)$ and leads to a distinct compressed-exponential decay.

Several studies used the discussed framework to obtain ξ_S [18–20, 80–82]. The main results are a static length scale which increases upon lowering the temperature and a scaling of τ_α with ξ_S. Further, *Kob* claims to find evidence for a dynamical transition by analyzing dynamic length scales which exhibit a maximum, whereas static lengths increase monotonically in the investigated temperature range. The findings are interpreted as change from MCT-like dynamics to dynamics governed by droplets of size ξ_S. However, there are also critical assessments of the theory, claiming no striking evidence for the relation between relaxation time and static length scale [83]. Some studies focus on random pinning (RP) geometries and reveal trivial reasons for the increase of static length scales [84, 85]. It is stated that the trivial contribution comes from the presence of the surface itself, which mediates a simple interaction between liquid particles and gives contributions regardless of the geometry.

The proposed procedure to obtain the static length scales is one of the main reasons for examining water in neutral confinements. The results are discussed in chapter 8.

In general, the RFOT theory is inspired by calculations for p-spin models with infinite dimensions. In finite dimensions, the sharp transition from non-activated to activated dynamics is assumed to smear out.

2.5 Elastically collective nonlinear Langevin equation approach

The literature for this chapter can be found in [21, 86–91].
The elastically collective nonlinear Langevin equation (ECNLE) approach was recently proposed by *Mirigian* and *Schweizer*. The starting point is a MCT description of dynamics. The idea is to derive a non-ensemble averaged equation-of-motion for the single-particle position where surmounting of barriers is possible. This is not possible in the usual MCT approach, and therefore, the goal of the theory is to go beyond the MCT limits, but in a different way than RFOT.

This is achieved by constructing an effective potential $V_{\mathrm{dyn}}(r(t))$ from the MCT equations. $V_{\mathrm{dyn}}(r(t))$ is build in a manner to obtain a localization of the particles, which is identical to the result of the MCT at or below T_C, if no thermal noise is assumed. Then, noise is added and the particles can cross the barriers in an activated way. It is important to understand that no local minimum for $V_{\mathrm{dyn}}(r(t))$ and therefore no barriers are present at temperatures $T > T_C$ (or equivalently low densities), because there is no localization in MCT at these temperatures.

The equation-of-motion in the overdamped case yields a nonlinear Langevin equation for the modulus of the particle displacement $r(t) = |\vec{r}_i(t) - \vec{r}_i(0)|$,

$$0 = -\gamma \frac{dr(t)}{dt} - \frac{1}{m}\frac{\partial V_{\mathrm{dyn}}(r(t))}{\partial r(t)} + \Gamma(t), \tag{2.32}$$

with m the mass of the particle, γ the friction coefficient, $\Gamma(t)$ satisfying the fluctuation-dissipation condition $\langle \Gamma(t)\Gamma(t')\rangle = 2\frac{k_B T\gamma}{m}\delta(t-t')$ and

$$V_{\mathrm{dyn}}(r) = k_B T \cdot [-3\ln(r) + \int \frac{d\vec{k}}{(2\pi)^3}\frac{\rho C^2(k)S(k)}{1+S^{-1}(k)} \cdot e^{-\frac{k^2r^2}{6}(1+S^{-1}(k))}], \tag{2.33}$$

where ρ is the density, S denotes the structure factor and C the direct part of the Ornstein-Zernike relation [71]. The potential $V_{\mathrm{dyn}}(r)$ is illustrated in Figure 2.6 for temperatures below T_C, as there is a local energy minimum. $V_{\mathrm{dyn}}(r)$ consists of two terms. The term $\int \frac{d\vec{k}}{(2\pi)^3}\frac{\rho C^2(k)S(k)}{1+S^{-1}(k)} \cdot e^{-\frac{k^2r^2}{6}(1+S^{-1}(k))}$ yields the MCT localization, whereas the term $-3\ln(r)$ counteracts this contribution and strongly

favors the *liquid* state (no localization). The latter contribution is motivated by the idea that the localization within the MCT framework is an artifact due to the particular way of constructing the theory. The term which favors the liquid state is obtained from density functional theory, which gives an estimate of the free energy of an amorphous solid due to vibrations [92]. It is emphasized that this is no *real* free energy description in an equilibrium sense, as this approach is based on an Einstein oscillator picture of an aperiodic crystal, which is clearly not valid for freely diffusing particles [92]. In the diffusive regime, particles do not recall any initial local potential, thus this approach can be only used on time scales before the entire energy landscape relaxes.

The barrier-crossing scheme, set out in the BM part of this chapter, can be used to describe hopping motion at temperatures where barriers are present,

$$\tau \propto e^{\frac{F_\mathrm{B}}{k_\mathrm{B}T}}, \tag{2.34}$$

and F_B denotes the barrier height. F_B is not temperature independent but this term is still assumed to give an Arrhenius-like behavior. It can be shown that if F_B is in the region of several $k_\mathrm{B}T$, the second part in equation (2.33) dominates and yields

$$F_\mathrm{B} \approx A \cdot \sqrt{\frac{1}{\langle \Delta r^2 \rangle}}, \tag{2.35}$$

with $\langle \Delta r^2 \rangle$ the mean squared displacement, and A a constant.

So far, only single-particle dynamics was addressed where the local potential comes from the local environment, but a collective behavior was not assumed. The second part of the model is based on an elastic coupling between particles. Figuratively, the motion of an atom in the local potential yields small displacements for neighboring particles, which are themselves trapped in a local potential. Due to the small displacements, a harmonic approximation for the local potentials is employed, thus the name *elastic* contribution. The idea is to describe the particles as coupled through an elastic distortion field. The process of disturbing the environment is treated as expanding the local cage. The elastic contribution is then given as sum over all elastic displacements which decay with r^{-2} due to the assumed spherical symmetry. This calculation yields

$$\frac{F_\mathrm{elastic}}{k_\mathrm{B}T} \propto \xi^2_\mathrm{elastic}(T) \left(\frac{r_\mathrm{cage}}{d}\right)^3 \cdot \kappa, \tag{2.36}$$

with $\xi_\mathrm{elastic}(T)$ as the effective cage expansion length, $\left(\frac{r_\mathrm{cage}}{d}\right)^3$ the cage volume per particle volume d^3, and κ the force constant for the harmonic approximation.

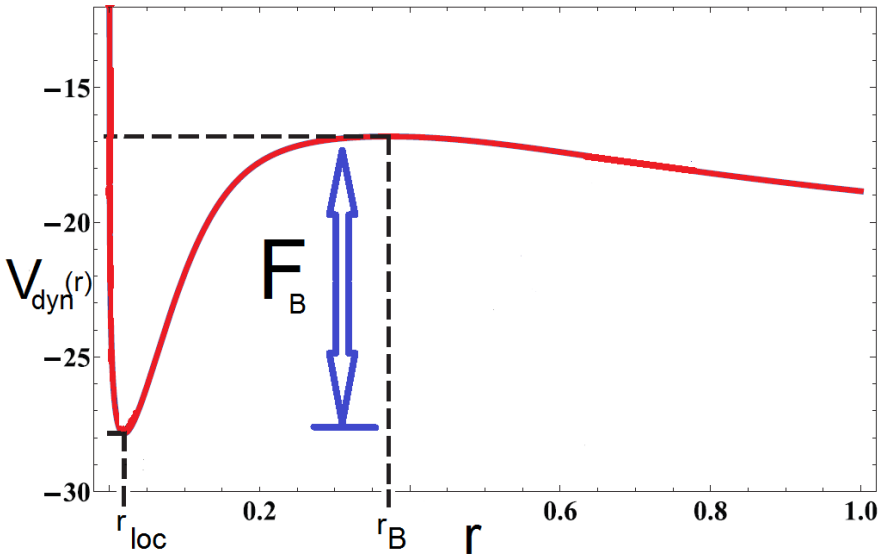

Figure 2.6: Illustration of the potential $V_{\text{dyn}}(r)$. See text for explanation. The figure is adapted from [21].

One can define a cooperative volume, where an elastic interaction is significant. The motivation for this contribution is similar to models like the Shoving-model proposed by *Dyre* [28]. However, it substantially differs in some points, which will be discussed at the end of this part. In a Shoving-model spirit, the elastic contribution can be written as

$$\frac{F_{\text{elastic}}}{k_{\text{B}}T} \propto \xi^2_{\text{elastic}}(T)\left(\frac{r_{\text{cage}}}{d}\right)^3 \cdot \kappa \equiv H(T)\cdot G(T), \tag{2.37}$$

with

$$H \propto \xi^2_{\text{elastic}}(T)\frac{r^3_{\text{cage}}}{d^2} \tag{2.38}$$

as cooperative volume. The main dependence of $H(T)$ on T is expected to result from $\xi_{\text{elastic}}(T)$. Further,

$$G \propto \frac{\kappa}{d} \propto \frac{1}{d}\cdot\frac{k_{\text{B}}T}{\langle\Delta r^2\rangle} \tag{2.39}$$

the glassy shear modulus (or plateau modulus [13]).

[13] This is not identical to the infinite frequency shear modulus [93].

Basically, the shear modulus relates the stress σ in the system to a shear displacement x/d [27, 28]. The previous transformations are only valid if a single force constant for the elastic coupling is assumed [28]. Only for this case, the shear modulus, which is related to shear waves, can be expressed using the force constant $\kappa = \frac{k_B T}{\langle \Delta r^2 \rangle}$, see equation (2.21), because the fraction of longitudinal modes to transversal modes is constant [28]. It should be clear that $\langle \Delta r^2 \rangle$ must be calculated on very short time scales, as the particles always leave the local cage due to hopping motion which preserves ergodicity.

In the framework of the model, F_{elastic} yields the non-Arrhenius behavior and dominates at low temperatures. It is important to notice that F_B and F_{elastic} are not independent, as the distortion due to the elastic coupling is dependent on the force constant at the minimum of $V_{\text{dyn}}(r)$.

The total non-equilibrium free energy barrier is finally,

$$F_{\text{total}} = F_B + F_{\text{elastic}} \tag{2.40}$$

and yields for the barrier crossing

$$\tau_\alpha \propto e^{\frac{F_B + F_{\text{elastic}}}{k_B T}}. \tag{2.41}$$

Using equations (2.35), (2.38), and (2.39) gives for the barrier crossing,

$$\tau_\alpha \propto e^{\frac{F_B + F_{\text{elastic}}}{k_B T}} \approx e^{\frac{A}{\sqrt{\langle \Delta r^2 \rangle}} + \frac{B \cdot H(T)}{\langle \Delta r^2 \rangle}} \approx e^{\frac{A}{\sqrt{\langle \Delta r^2 \rangle}} + \frac{B \cdot \xi^2_{\text{elastic}}(T)}{\langle \Delta r^2 \rangle}}. \tag{2.42}$$

The constants A and B weight the non-collective single particle *jump* contribution and the collective elastic part of the total barrier, respectively. The important aspect of the latter equation is the relation of short time dynamics, $\langle \Delta r^2 \rangle$ must be obtained at times where a localization is present, and correlation times τ_α at several nanoseconds.

Similar to the RFOT approach, a length scale is important to describe fragile behavior, as it was stated that the main temperature dependence of the elastic part is owing to ξ_{elastic}, which is the dominating contribution at low temperatures. Therefore, it is tempting to associate the length scales ξ_{MCT} or ξ_S, see chapter 2.4, with ξ_{elastic}. But, there are severe differences. First, ξ_{MCT} is obtained in a temperature regime where according to ECNLE no barrier crossings are present. Therefore, the elastic coupling, which is important at low temperatures, is negligible. This rules out ξ_{MCT}. Second, the ECNLE approach is

intended to go beyond MCT but in a very different way compared with the RFOT approach. The static length scale in the RFOT theory is an equilibrium length scale, whereas the entire ECNLE is based on non-equilibrium free-energy barriers. Therefore, there might be a connection, but this is far from obvious.

Niss and co-workers performed neutron scattering experiments on liquids and used the Shoving-model, which is similar to equation (2.37), to describe dynamics. They found a connection between short time dynamics and relaxation times [94]. However, the approaches revealed no universal behavior when comparing various liquids. One can speculate that this is rooted in two of the main differences between the ECNLE approach and the Shoving-model. First, the ECNLE approach consists of two parts, whereas the Shoving-model only consists of an elastic part. Second, the cooperative volume is clearly supposed to be temperature dependent in ECNLE, in contrast to the Shoving-model, where only the shear modulus is temperature dependent. A warning is appropriate at that point. The cooperative volume has a different meaning for the ECNLE approach, as it is directly related to collective behavior, whereas for the Shoving-model, it is more related to a jump length times the effective potential.

It will be shown in chapter 8.4 that $\xi^2_{\text{elastic}}(T)$ depends on temperature. Characterizing the presumed temperature dependence of $\xi^2_{\text{elastic}}(T)$ is one of the main new scientific results of this study. Furthermore, it will be shown that the presented approach is suitable to describe the correlation times of water in the neutral pores and for bulk water. Therefore, a very clear relation between short time dynamics and dynamics on up to several hundreds of nanoseconds will be given, together with a very precise picture of the relevant mechanisms of motion in supercooled liquids in general.

2.6 Open questions related to supercooled liquids

Several important properties of supercooled liquids have been introduced, like non-exponential decays, non-Arrhenius temperature dependence of τ_α, and the concept of spatially heterogeneous dynamics. In addition, the Brownian motion concept, the RFOT approach, and the ECNLE theory were discussed. This may look like a conclusive picture of dynamics in supercooled liquids, however, the discussed theories are subject of an ongoing debate. In the following, some examples for this discussion are given [21, 95].

The choice of theories is dependent on the correlations one wants to describe, as they provide answers to specific phenomena and there are still many open

questions. Following *Tarjus*,[21, 95], one of the most pressing ones is related to SHD: Is dynamic heterogeneity the driver of vitrification or instead a side effect of the slowing? Further, the point of view matters for the starting point of theories, as it might be more useful to imagine a supercooled liquid as a slowly flowing solid, like in some sense the ECNLE theory does. Opposite to this is the description on the RFOT approach, which was given above. Relating to the latter approach, it is not clear whether in finite dimensions critical points like the MCT divergence are smeared out or non-existent at all? Additionally, the introduced theories are based on length scales. It is not known whether these length scales are clearly related to a collective motion or do they point towards a coarse grained description of dynamics?

In chapter 8, the neutral confinements will be used to obtain both dynamic and static length scales, as investigating water in these confinements is very similar to the proposed procedure on how to get information on static length scales in chapter 2.4. Therefore, the goal of chapter 8 is to give further insights to some of the fundamental questions raised above.

2.7 The quest for a liquid-liquid phase transition of water

Up to now, phenomena of supercooled liquids have been discussed. This part will elaborate the importance of this knowledge with respect to water.

Water shows several remarkable effects, if compared with other liquids. Those effects are usually called *anomalies*. The probably best known anomalies are the density maximum at roughly 277.15 K ($p = 1$ bar), the minimum of the isothermal compressibility at 319.15 K, the constant-pressure specific heat minimum at 308.15 K and the thermal expansivity, which is positive above the density maximum and negative below [23, 96]. In order to explain the anomalies several theories have been proposed, and some of them are discussed in the following. All have in common that they are based on the specific hydrogen-bond structure found for water [6, 97].

In 1992, *Poole* proposed the hypothesis of a second critical point, the so-called liquid-liquid critical point (LLCP), based on MD simulations of the ST2 water model [4]. The LLCP is claimed to be located at low temperatures, in the supercooled regime, and at high pressures. *Poole* asserts that there is a first-order phase transition between a high-density liquid (HDL) and a low-density liquid (LDL), similar to high and low-density amorphous ice phases (HDA/LDA), which were found in experiments. The ending point of this phase transition is marked by the LLCP. The theory suggests that the density-maximum anomaly is attributable to fluctuations when crossing the Widom line. Due to the fluctuations, it is possible to achieve an increase in pressure by lowering the temperature, what is related to the density anomaly.

A different approach, which was suggested by *Angell*, is called critical point-free scenario [5]. In this case, there exists no LLCP, or only at negative pressures, but there is still a phase transition of first-order, in the sense of an order-disorder transition, separating HDL from LDL in the supercooled regime.

The last scenario addressed in this framework is the singularity-free scenario proposed by *Sastry* in 1996 [6]. He employed a lattice model designed to resemble typical behavior of water like the density anomaly, but this model did not exhibit any phase transitions or critical points at low temperatures. Thus, *Sastry* stated that singularities are not necessary to describe water appropriately.
The predictions of the proposed hypotheses are summarized in Figure 2.7.

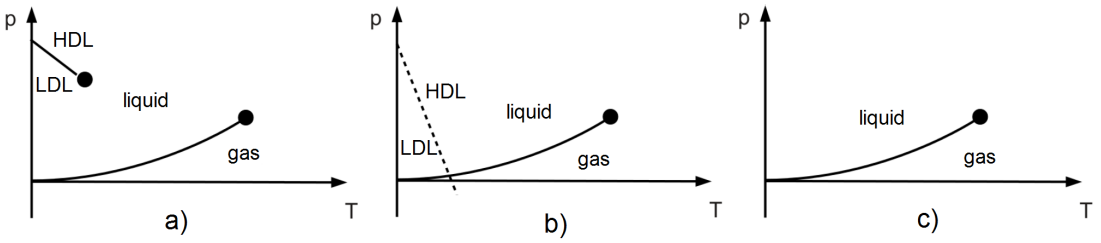

Figure 2.7: Schematic phase diagrams juxtaposing different hypotheses for the low temperature phase behavior of water. a) Corresponding to the liquid-liquid critical point scenario [4]. b) The critical point-free scenario [5]. c) The singularity-free scenario [6]. The Figure was adapted from [98].

In order to rule out or find evidence for these conjectures, it is mandatory to supercool water as the LLCP or the HDL/LDL phase transition occur at very low temperatures, see the red dot and the dashed red line in Figure 2.8 [99]. Unfortunately, the temperature regime accessible for supercooling water is limited in experiments. Starting from ambient conditions and cooling the system, there is a temperature T_H where water starts to crystallize due to homogeneous nucleation. Quenching the system to very low temperatures to obtain HDA or LDA and then heating up, water starts to crystallize at T_X. Therefore, the region enclosed by T_H and T_X is known as *No man's land* [96] and this is the putative location for the HDL/LDL phase transition. This led to the idea that if crystallization of water can be avoided or at least T_H pushed to lower temperatures, the *No man's land* becomes accessible to experiments. Even if the achievable temperatures are not low enough to cross the hypothetical phase transition line, the imprints of a critical point should be traceable, as it affects a larger area in the phase diagram [96].

Several experimental studies on water in various sorts of confinements found that water exhibits a reduced crystallization temperature [10–12] or lacks any sign of crystallization if the confinement is sufficiently small (confinement radius $r < 1.1$ nm) [100]. Using confinements, there is still the problem of what to investigate, structure or dynamics. By examining the structure, it seems reasonable to assume that the differences between HDL and LDL may not be large. Thus, studies on dynamics promise more insights. Therefore, the problem of how to track the structural phase transition is transformed to distinguish dynamics for the HDL and LDL.

Usually, the HDL is supposed to obey fragile behavior and the LDL strong behavior [101, 102]. This is derived following the ideas proposed by *Adam* and

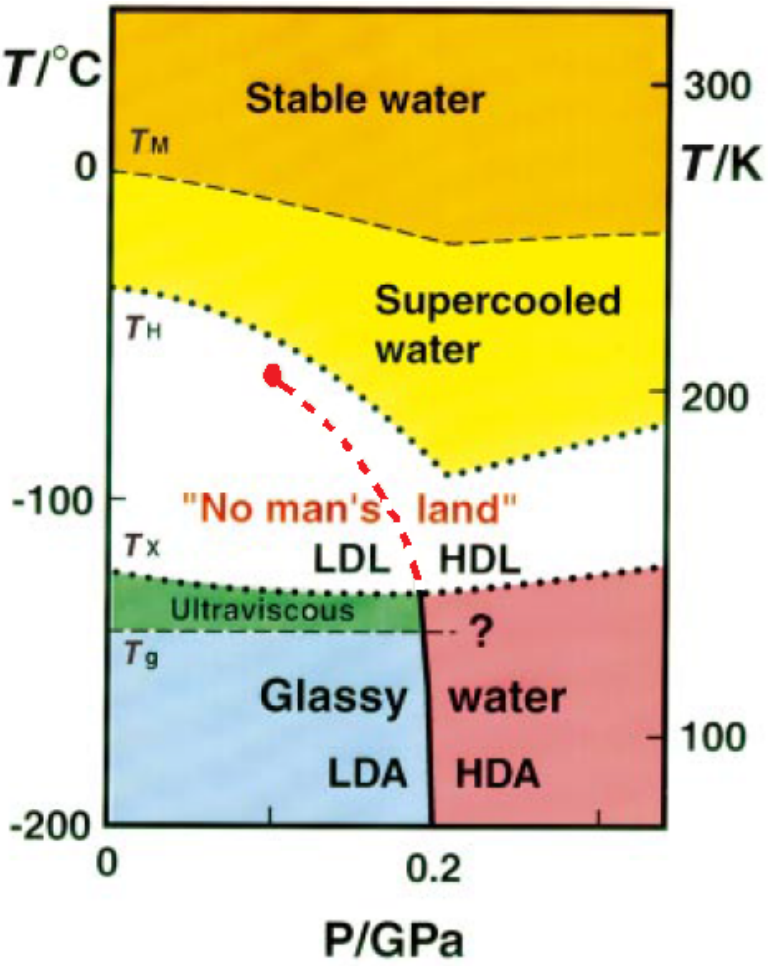

Figure 2.8: Phase diagram for water, adapted from [96].

Gibbs or the RFOT approach below T_C (which are identical on this quantitative level) to explain fragile behavior [102]. As discussed in chapter 2.4, the theory is based on the conception that the time scale of relaxation events depends on the size of the involved regions and this is related to the configurational entropy $S_c(T)$ of the system [103], which is approximated by [27]

$$\frac{S_c(T)}{dT} \approx \frac{(c_p^{\mathrm{LQ}} - c_p^{\mathrm{CR}})}{T} = \frac{\Delta c_p}{T}, \tag{2.43}$$

with c_p^{LQ} as the specific heat capacity at constant pressure for the liquid and c_p^{CR} for the crystal. The relaxation time is, thus, given by

$$\tau_{\mathrm{AG}} = \tau_0 \cdot e^{\frac{B}{T \cdot S_c(T)}}, \tag{2.44}$$

where B is a constant. According to the *Adam-Gibbs* theory, a liquid is more fragile for larger Δc_p. Reversed, the theory claims $S_c(T)$ to be a constant for

strong liquids. Consistent with the latter statement, LDL is more ice-like due to the lower density, and thus, Δc_p and the change of $S_c(T)$ with temperature are small, yielding a strong liquid, whereas the opposite applies to HDL.

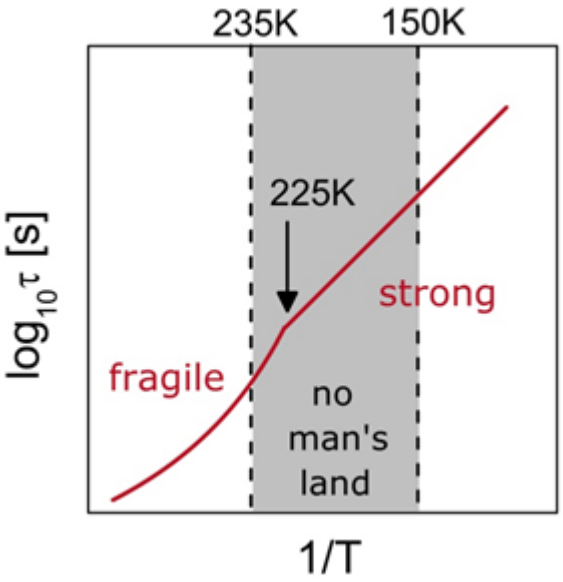

Figure 2.9: Schematic representation of the *fragile-to-strong* transition for bulk-water dynamics at ambient pressure [104]. This figure is courtesy of Prof. Dr. M. Vogel.

In fact, bulk water is one of the most fragile liquids in the mildly supercooled regime, whereas quenched to the deeply supercooled regime, near the glass transition temperature, the relaxation behavior seems to be strong. Hence, there may be a crossover called *fragile-to-strong* transition (FST) at roughly 225 K [102], see Figure 2.9. It is emphasized that the idea of the FST is based on an abrupt change of the water structure at the transition temperature and it is thus related to thermodynamics. Therefore and given the derivation of dynamical behavior for water in the HDL and LDL phases, the HDL/LDL scenario and the FST are used as synonyms.

Early studies on water in confinement observed a crossover in the temperature dependence of correlation times and attributed it to a FST [105, 106]. More recently, various experimental results for water in confinement have been published, which have in common that a kink is found for the correlation times upon cooling, but the interpretations differ and are often not attributed to a HDL-LDL transition. Some are listed in the following and Figure 2.10 summarizes the diverse interpretations.

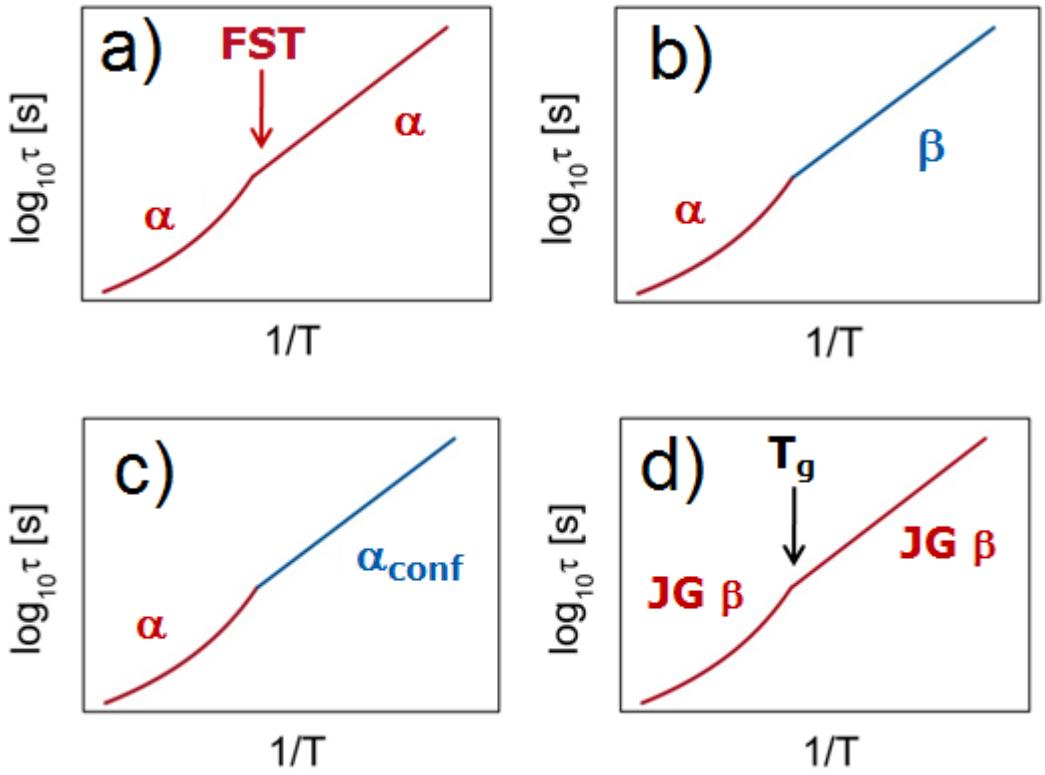

Figure 2.10: Summary of interpretations for results obtained from water in confinement. a) HDL/LDL transition [7, 101]. b) Structural to local relaxation processes [8, 107, 108]. c) Structural to confinement related relaxation processes [109]. d) Crossover due to glass transition at T_g [9, 110]. This figure is courtesy of Prof. Dr. M. Vogel.

First, a group around *Chen* and co-workers conducted neutron scattering experiments on water in silica confinements and NMR spectroscopy on water in proteins [7, 101]. They explain the results with the presence of a LLCP and FST, see Figure 2.10 a).

A second group, mainly *Swenson* and co-workers, used dielectric spectroscopy (DS) and neutron scattering experiments to investigate water in confinements [8, 107, 108]. They claim that the glass transition temperature of water is located at higher temperatures than assumed by the first group. Further, referring to the *Adam-Gibbs* theory, they suggest that confinements restrict the growth of inherent length scales and thus of the size of rearranging regions. By putting both arguments together, the kink in the dynamical behavior is attributed to a crossover from structural relaxation processes (α-processes) to local ones de-

noted as β, see Figure 2.10 b).

A third idea was brought forward by *Cerveny* [109]. Based on DS experiments of water in various confinements, the kink was ascribed to emerging confinement effects, see Figure 2.10 c).

Ngai and co-workers investigated several water-mixtures employing DS and attributed the crossover in dynamics to the behavior of a specific local process the so-called *Johari-Goldstein* β-process at the glass transition temperature, see Figure 2.10 d) [9, 110][14].

In contrast to experiments, MD simulations produce trajectories that are usually too short or the models show too little structuring of atoms beyond the next-neighbor shell to obtain crystallization. Therefore, the *No man's land* is accessible also without using techniques to explicitly prevent the system from crystallization. Bulk simulations, performed for several water models, suggest a phase transition from HDL to LDL upon cooling [111–116]. This is also concluded from MD simulations of water in confinements [17, 117], but as is the case for the experimental studies, there are deviating interpretations. For instance, *Chandler* and co-workers assign the putative phase transitions and critical points found in MD simulations to a precursor behavior for an ice-like phase [118, 119].

In general, water in confinement is a very complex system. There are finite-size, surface and density effects. Hence, chapter 7 characterizes water in silica confinements and is intended to give guidance to experimentalists. Further, the allegedly observed FST in silica confinements, see [17], is discussed.

[14] This process is not detailed in the following. For further explanations see the cited literature.

3 Molecular dynamics simulations

Molecular dynamics (MD) simulations will be introduced in this chapter. The first part will give an overview of simulation methods and compare it to experiments. The second part will give technical details about MD simulations.

3.1 Accessing simulations

This study is based on MD simulations. The present chapter aims at introducing MD simulations and comparing it with other simulation methods and experiments.

There are several simulation techniques, see Figure 3.1. The probably most frequently used ones are Monte Carlo (MC) and *classical* MD simulations. In the following, MD simulations are used as synonym for classical MD simulations. Non-classical MD simulations are referred to as *ab-initio* simulations. There also exist many hybrids combining some of the simulation aspects, which will be not discussed here [120].

MD and MC simulations are based on common assumptions. They suppose that the De Broglie wavelength is very small compared to next-neighbor lengths [121]. Further, electrons adjust instantaneously to the motion of atoms and effective potentials are employed [122, 123]. Combining these aspects yields a classical description on a particle level.

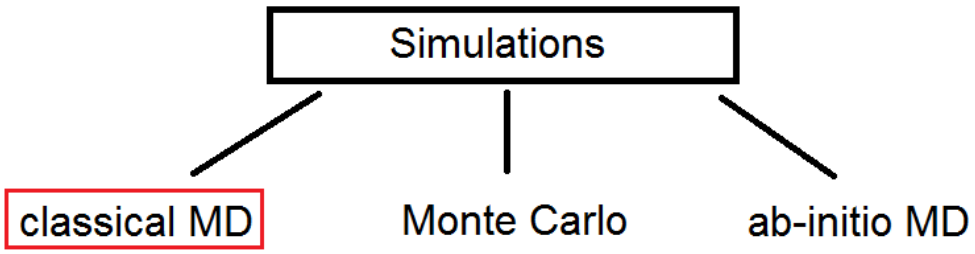

Figure 3.1: Simulation methods

The main difference between MD and MC is that MD is based on solving Newton's equations of motion and is, thus, deterministic. In contrast, MC is a stochastic method and yields different configurations of the system [122]. In MC simulations, particles are moved to different locations and the new position is accepted or discarded. If the system evolves towards lower energies the moves are always accepted. However, moves to higher energies are not gener-

ally discarded as there are thermal fluctuations. So those steps are compared with the thermal energy of the system and, if too large, they are discarded [122].

MD simulations directly yield the time evolution of the system according to Newton's equations, in contrast with MC simulations. In terms of thermodynamics, MC and MD can yield the same results as far as the same ensembles are used.

Ab-initio simulations also solve Newton's equations of motion, but they are based on calculating proper forces between atoms for the respective electronic structure [124]. These approaches circumvent the problem of developing effective potentials for MD simulations, though, the computational costs are huge and limit the accessible time scale to several picoseconds.

As the focus of this study is on dynamics of supercooled water and also to provide information for experiments on confined liquids/water, an objective definition of time (not provided in MC simulations) and trajectories up to several hundred nanoseconds (not provided in ab-initio simulations) are mandatory. Therefore, MD simulations are used.

The main advantage of MD simulations is to provide a trajectory for every atom, enabling comparison with the results from experiments like DS, NMR, or neutron scattering. MD simulations give insights into a microscopic description of dynamics and structure for a variety of systems. From biological systems including water at protein surfaces to polymers, ionic liquids and supercooled liquids in general, MD simulations are employed to unravel microscopic properties [57, 58, 125, 126] [15]. They also yield important tests for theories, see chapter 2, which are not always possible in experiments. This study is an example for employing MD simulations in order to get insights into spatial heterogeneity of confined liquids, which is impossible for most experiments apart from solvation dynamics experiments [127].

The main limit for comparing experiments and MD simulations is the time scale and the system size. There exist highly sophisticated algorithms to push the time limit as far as possible, but for small systems and using usual CPU-clusters, the limit should be at several hundred nanoseconds given nowadays computer performance. On a quantitative level, the time scales for selected experiments and for MD simulations are depicted in Figure 3.2.

[15] For the ionic liquids, the effective potential is more complex than in other MD simulations, as the potential should account for dynamical polarization effects.

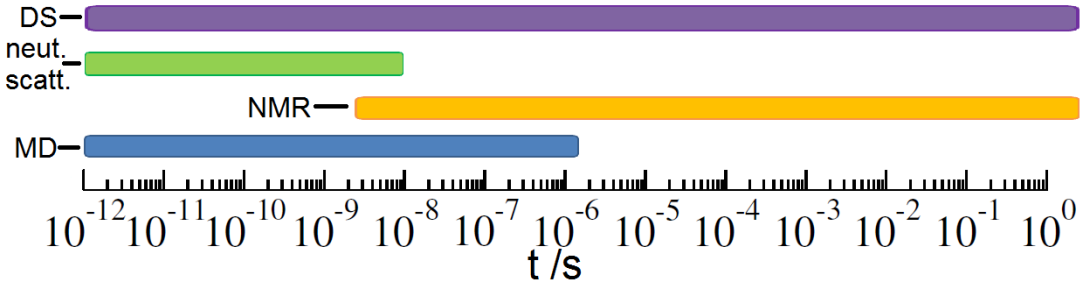

Figure 3.2: Rough comparison of time scales of experiments and MD simulations.

There are some drawbacks of MD simulations. First, the system size is usually very small (<100,000 atoms) compared to that of experiments. However, 13 years ago, MD simulations of water comprised roughly 300 molecules [128], so there is a huge progress due to the increasing computational power. Currently, very large biological objects, like a virus, are still beyond the scope of most approaches, but they have become available on supercomputers or machines like *Anton* [129]. The small system size brings up the question about boundary effects. The latter problem is mitigated by introducing periodic images, however, if phase transitions are investigated critical length scales can grow to larger values than the box size (see for example the discussion on the growing length scale in the context of the MCT in chapter 2.4) rendering the idea of periodic images obsolete [122].

Second, chemical reactions and other quantum effects, like tunneling, cannot be parametrized. If such effects are important, as for deeply cooled helium [122], MD simulations do not provide a good description. An important aspect of real water is that it can dissociate into hydronium ions H_3O^+ and hydroxide ions OH^- [130]. However, chemical processes cannot be modeled by MD simulations. Because of this, it is not possible to obtain a meaningful pH-value from MD simulations of water, as, if simply taking the hydronium ions as measure of the H^+ concentration, the pH-value is ∞. A neutral pH-value $pH = 7$ implies a concentration of one H^+ out of 10 million molecules. Thus, taking into account the usual system sizes in MD simulations, and in particular the 895 molecules for the present bulk simulations, the probability to find one dissociated molecule is negligible.

In conclusion, the goal of this study is to unravel dynamical and structural aspects of supercooled water confined in diverse confinements. For this pur-

pose, MD simulations are a powerful tool as they provide access to an amazing variety of dynamical and structural analyses.

3.2 Technical details on molecular dynamics simulations

All simulations of this work were conducted using the software *Gromacs*, version 4.5.3 [33]. The following explanations are mainly based on the *Gromacs* manual, see [123]. Different sources are explicitly mentioned.

As stated in the previous section, MD simulations are an extremely powerful tool when dealing with systems where quantum effects can be well parametrized and then treated in a classical way. Thus neither chemical reactions or processes nor tunneling effects can be modeled. But if a reasonable parametrization is possible MD simulations provide the trajectory of every single atom in the system, and thus allow for very detailed analyses of dynamics and structure.

The starting point of MD simulations are Newton's equations of motion, describing the force on the i-th out of N particles,

$$\vec{F}_i(t) = m_i \frac{d^2\vec{r}_i}{dt^2} = -\frac{\partial V\{\vec{r}_1, ..., \vec{r}_N\}}{\partial \vec{r}_i}, \tag{3.1}$$

with m_i as the mass of the respective particle and V a potential function. MD simulations aim at solving the latter equation. This is not possible in an analytic way due to the interaction of many particles. Therefore, the chosen integrator solves equation (3.1) using discrete time steps Δt for integration, usually in the femtosecond regime. Notice that the potential function V considers the positions of atoms only, thus, electrons are assumed to be in the ground state and, owing to the *Born-Oppenheimer* approximation, to instantaneously adjust for center of mass motions of the atom. The potential consists of two parts, the bonded and the non-bonded interactions.

In order to describe bonds, a harmonic oscillator with quantum corrections is used to obtain appropriate energies. This approach is applied to bond-angle and bond-stretching motion. Further, constraints are used to handle motion of bonded particles. This effectively cuts off very high frequencies, enabling the use of larger time steps Δt. Here, the SETTLE algorithm was applied to specifically account for the constraints of water [131], otherwise the LINCS algorithm was used [132]. Non-bonded interactions comprise a repulsive and a

dispersive term and additionally the Coulomb term. They are treated by employing a conservative force field which is pair-additive except for Coulomb forces. *Gromacs* provides two kinds of potentials for describing the repulsive and dispersive term, the Lennard-Jones interaction and the Buckingham interaction [133, 134]. The first one reads,

$$V_{\mathrm{LJ}}(r_{ij}) = \frac{C_{ij}^{(12)}}{r_{ij}^{12}} - \frac{C_{ij}^{(6)}}{r_{ij}^{6}} \tag{3.2}$$

and the second one,

$$V_{\mathrm{B}}(r_{ij}) = A_{ij} e^{-B_{ij} r_{ij}} - \frac{C_{ij}}{r_{ij}^{6}} \tag{3.3}$$

with the coefficients $C_{ij}^{(12)}$, $C_{ij}^{(6)}$, A_{ij}, B_{ij} and C_{ij} determined when developing the force field. This simple description is only valid if particles of the same atom type interact with each other. The coefficients are modified when calculating the interactions between different atom types, using the following mixing rules [16]

$$C_{ij}^{(6)} = \left(C_{ii}^{(6)} C_{jj}^{(6)} \right)^{1/2} \tag{3.4}$$

$$C_{ij}^{(12)} = \left(C_{ii}^{(12)} C_{jj}^{(12)} \right)^{1/2}. \tag{3.5}$$

For the calculation of the Lennard-Jones forces, the interaction is truncated at 1.2 nm. Long-range electrostatic interactions are calculated with the help of the particle-mesh Ewald (PME) algorithm. The Ewald summation separates the total electrostatic energy into a term in direct space and a term in reciprocal space, avoiding the slow convergence of the sum if only direct space is considered. In essence, PME is an advanced algorithm to accomplish the calculation of the sum in reciprocal space as swiftly as possible. It scales like $N \log(N)$. In order to use PME and to avoid boundaries, periodic images are used for all simulations of this work.

The default integrator of *Gromacs*, the *leap-frog* algorithm, was employed to perform the simulations. This integrator is remarkable for evaluating positions

[16] *Gromacs* supports further mixing rules or it is possible to specify the parameters directly by way of a matrix.

and velocities at different times. This means that positions are calculated at time t, whereas velocities are evaluated at time $t - \frac{1}{2}\Delta t$, reading

$$\vec{v}(t + \frac{1}{2}\Delta t) = \vec{v}(t - \frac{1}{2}\Delta t) + \frac{\Delta t}{m}\vec{F}(t) \tag{3.6}$$

and

$$\vec{r}(t + \Delta t) = \vec{r}(t) + \Delta t\,\vec{v}(t + \frac{1}{2}\Delta t). \tag{3.7}$$

The precision of the *leap-frog* algorithm is up to third-order in the position for an expansion in a Taylor series. The advantage of this particular algorithm is the possibility to easily couple the system to a heat bath due to the explicit equation for velocities, which is not provided by, e.g., the Verlet algorithm [135].

MD simulations provide the opportunity to use different thermodynamic ensembles. Only two have been used for this work, namely NpT, constant number of particles, pressure, and temperature, and NVT, constant number of particles, volume, and temperature. Usually the NpT ensemble is used for equilibration and the NVT ensemble for data production runs, except for water confined in silica pores, see chapter 4. In order to sustain constant temperatures the *Nosé-Hoover* temperature coupling was applied [136, 137]. This algorithm modifies the equation of motion given by equation (3.1) and adds a coupling to a heat bath, reading

$$\frac{d^2\vec{r}_i}{dt^2} = \frac{\vec{F}_i}{m_i} - \frac{p_\xi}{Q}\frac{d\vec{r}_i}{dt} \tag{3.8}$$

with $Q = \frac{\tau_T^2 T_0}{4\pi^2}$ and the heat-bath parameter determined by the equation of motion

$$\frac{dp_\xi}{dt} = (T - T_0). \tag{3.9}$$

The actual instantaneous temperature of the system is given by T and T_0 denotes the desired temperature. The coupling strength Q depends on the oscillation period τ_T between the system and the heat bath, which is set to a fixed value for all simulations $\tau_T = 0.4$ ps. These equations allow the temperature to fluctuate while on average, and for long times if starting from a very different initial temperature than the desired one, T_0 is obtained. The drawback of the *Nosé-Hoover* scheme is that phase space is maybe only partially sampled even for infinitely long times. Extensions, which attempt to solve this problem by coupling many heat baths, could not be used, as these so-called *Nosé-Hoover* chains are not supported by the *leap-frog* algorithm.

Constant-pressure simulations employed the coupling scheme by *Parrinello-Rahman* [138, 139]. It resembles the *Nosé-Hoover* temperature coupling and adds an additional term to equation (3.8)

$$\frac{d^2\vec{r}_i}{dt^2} = \frac{\vec{F}_i}{m_i} - \frac{p_\xi}{Q}\frac{d\vec{r}_i}{dt} - \vec{\mathbf{M}}\frac{d\vec{r}_i}{dt}, \tag{3.10}$$

with the *Nosé-Hoover* contribution included. Here, the explicit equations for the matrix $\vec{\mathbf{M}}$ are not specified. The scheme is similar to the previously discussed *Nosé-Hoover* approach, but much more complex due to several matrix operations. The inputs to the algorithm are a single compressibility $\beta = 4.5 \cdot 10^{-5}$ 1/bar in case of isotropic pressure coupling, and the pressure time constant $\tau_p = 0.5$ ps, which is similar in value and physical meaning to τ_T for the temperature coupling. The main advantage of this kind of pressure coupling is that it is flexible and allows for changing the shape of the box during simulations.

A typical work flow for a simulation starts at an initial configuration. Figuratively, one chooses a box shape, which must be space-filling when periodic boundaries are applied, and puts molecules inside. This is done by a particular algorithm provided by the software package *Gromacs*. The initial velocities are drawn from a Maxwell–Boltzmann distribution given the desired temperature T. In a second step, the entire forces acting on every atom are computed. After that kinetic energies, and if pressure coupling is enabled, the pressure tensor and the potential are calculated. In the third step, the equations of motion, like equation (3.10) are solved by the chosen integrator. This gives new positions and velocities, available for output and the MD algorithm proceeds at the second step. Due to the huge amount of iterations required to investigate structure and dynamics, the output is usually written to a file every 500 iterations. A 1 μs long trajectory with a time step of 2 fs corresponds to 500 million iterations and 1 million written configurations. Considering a system of up to 10000 atoms yields a file size of roughly 50 GB. For this study the production runs range from 1 ns to 4 μs.
Finally, the important settings are compiled in Table 1.

Fact sheet	
Integrator	leap-frog
Temperature coupling	Nosé-Hoover
Pressure coupling	Parrinello-Rahman
Boundary conditions	periodic (x,y,z)
Electrostatics	particle-mesh Ewald
Non-bonded interaction	Lennard-Jones (LJ) potential
LJ long-range contribution	cut-off distance = 1.2 nm
Bonds	harmonic with constraints (SETTLE or LINCS)
Box shape	cuboid
Time step	1 or 2 fs
Simulation length	up to 4 μs

Table 1: Relevant algorithms and simulation aspects.

4 Systems

The simulations for the present study can be split into two kinds of systems:

- The first part concerns water as a liquid which shows many anomalies. In chapter 2.7, it was clearly stated that silica pores with pore radii on the order of 1 to 2 nm (among other confinements) were found to suppress the crystallization of confined water. Therefore, silica pores of the same size will be used to characterize structure and dynamics and, e.g., to unravel why water is prevented from crystallization within these pores.

- Second, neutral confinements are important because they allow the investigation of dynamics without altering the structure of the confined liquid, see chapter 8.1. Thus, comparison of results to that of the silica pores yields generic effects of atomistic pores. Further, the second part is mainly about supercooled liquids, and water as a typical representative. *Biroli* and *Bouchaud* proposed the use of neutral confinements in order to obtain static length scales, allegedly related to the non-Arrhenius temperature dependence of structural relaxation times for various supercooled bulk liquids. It will be shown in chapter 8 that water in neutral confinements is very important for the understanding of dynamics of supercooled liquids as, without changing the structure, dynamics is changed drastically dependent on the distance to the pore wall.

For this study, the water model SPC/E (extended simple point charge) was used. This model is widely employed in the literature, but more important, studies find interesting behavior in various confinements, like disordered structures [15], changed dynamics compared to that of the bulk [16, 140], and it was claimed that a fragile-to-strong transition (FST), related to the putative phase transition of water at low temperatures, was found for SPC/E confined in silica pores at a temperature of ≈ 220 K [17]. It was further pointed out that the goal of this study is to investigate fragile behavior of supercooled liquids. SPC/E is an economical model from a computational point of view, thus, a wide range of correlation times is accessible, in contrast to more sophisticated but also more computationally expensive models like TIP4P or TIP5P. This is relevant for elaborated analyses of fragility. In conclusion, this model shows interesting effects when confined in silica pores and correlation times up to several nanoseconds are achievable with usual CPU-clusters, thus, this model was chosen.

Simulations	
Water model	simple point charge /extended (SPC/E)
Bulk	cubic boxes (V $\approx$ 27 nm^3)
Small silica pores	cylindrical pore, radius $\approx$ 1.1 nm
Large silica pores	cylindrical pore, radius $\approx$ 2 nm
Neutral confinements	various geometries, CL from 0.5 to 2.5 nm

Table 2: Overview over the systems. CL means confining lengths.

Table 2 lists the systems and the water model for this study. Technical details of the simulations are given in the following subsections.

4.1 Bulk simulations

The focus of this work is mainly on water in confinements, though, it is absolutely necessary to compare results to bulk simulations. Therefore, bulk simulations were conducted as reference for the confinement simulations. There are plenty of water models, like ST2, SPC and SPC/E and the TIPxP series, with x = $\{3, 4, 5\}$ and recently TIP4P-05 [13, 14, 141–144]. For this work, the water model of choice is SPC/E.

4.1.1 SPC/E

SPC/E is the abbreviation for *extended simple point charge* and consists of three atoms. Figure 4.1 illustrates the model with the respective angle and bond length [14]. The charge on the oxygen atom is $q_0 = -0.8476$ e and on the hydrogen atoms $q_H = 0.4238$ e [17]. The non-bonded interaction is determined by Lennard-Jones parameters for oxygen atoms only. Hydrogen atoms contribute to the Coulomb interaction but are excluded from the Lennard-Jones interaction. The model was designed to give reasonable results e.g. for the density, potential energy in the system, diffusion constant and radial pair distribution function compared to experimental results at 300 K.

In order to perform the SPC/E simulations, 895 molecules are placed in a cubic box. Then, the systems are always equilibrated in the NpT ensemble

[17] The charges are mentioned as they will be of interest for the neutral confinements.

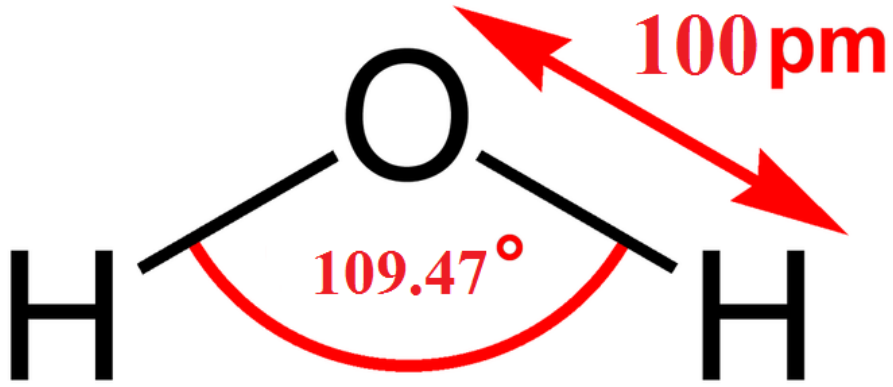

Figure 4.1: Water molecule with bond length and angle referring to the SPC/E model [14], adapted from [145].

with $p = 1$ bar and a time step of 2 fs using the *Parrinello-Rahman* and *Nosé-Hoover* coupling schemes, see the previous chapter for details. The length of the equilibration runs varied substantially as a function of temperature, ranging from 40 ns at 270 K to 2000 ns at 187 K. Determining a reasonable box size for the NVT production runs was ambiguous. The procedure is to visualize the box-size fluctuations, see Figure 4.2. Then, the limits for obtaining the average box size are chosen by hand because it is crucial to account for equilibration at the beginning of the trajectory. For instance, the box fluctuations at a temperature of 187 K are depicted in Figure 4.2 and show such behavior within the first roughly 250 ns. Finally, an algorithm took the frame which was nearest to the average box size and located near the end of the trajectory. At temperatures lower than 187 K a steady-state behavior in the box size or potential energy could not be achieved on time scales even larger than 2000 ns. Hence, data for those simulations is not presented.
The volume obtained by the discussed procedure changes mildly with temperature and is roughly $V \approx 27$ nm^3.

After the equilibration, the simulations in the NVT ensemble are used as production runs, with the temperature controlled by the *Nosé-Hoover* algorithm. Again the time step is set to 2 fs. Production runs mean that only data gathered during those runs is analyzed. The length of trajectories reaches from 100 ns at 270 K to 4000 ns at 187 K.

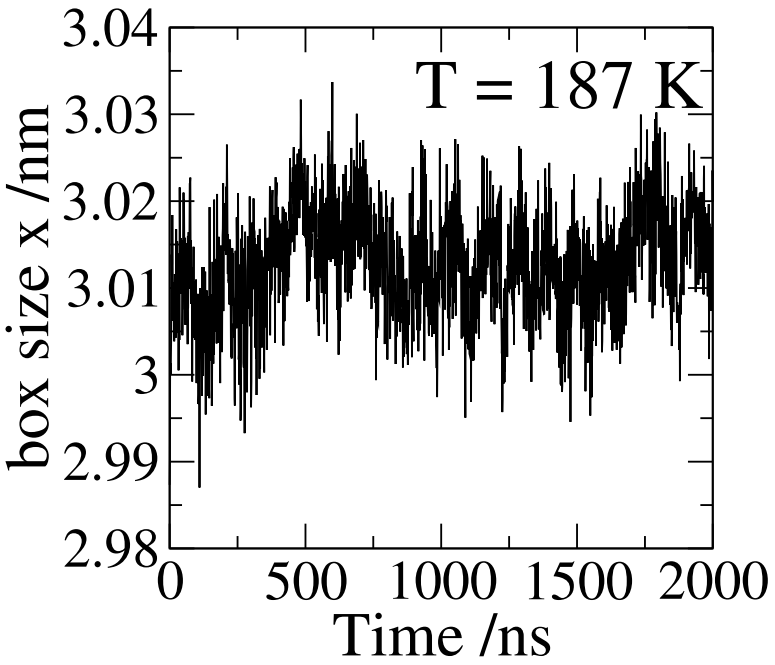

Figure 4.2: Fluctuations of the box size in x direction during NpT equilibration at $T = 187$ K.

4.2 Water confined in pores

As mentioned above, the confinements for this study can be classified in silica pores and neutral pores. It is emphasized that confinement simulations using too small boxes yielded unphysical interactions between particles near walls and their periodic images. It was found that those effects vanished when the pore wall plus the periodic image of the pore wall had been larger than the cut-off length for the Lennard-Jones interaction (here, 1.2 nm)[18]. All confinement simulations make use of walls whose thickness is sufficiently large.

In the following, all pores will be detailed. First, silica pores are introduced. Two kinds of silica pores were used, a small and a large silica pore.

4.2.1 Small silica pore

The small silica pore was obtained from ab-initio simulations combined with reaction force-field simulations[19] performed by *Allolio et al* [148].

[18] This effect was discovered by *Wohlfromm* as part of his bachelor work.

[19] Ab-initio simulations calculate forces relying on the electronic structure obtained from density functional theory [124] and reaction force-field simulations are specifically designed

The starting point was a very high temperature simulation (T = 5655 K, $\rho = 2.41 \frac{\mathrm{g}}{\mathrm{cm}^3}$) of molten silica using the ReaxFF force field for silicon dioxide, [147], to obtain an amorphous silica structure. The system was annealed to a temperature of 200 K within ≈ 35 ps. Then, a part of the system was cut out along the z-axis, resulting in an almost cylindrically shaped pore with a radius of roughly 1.1 nm. Afterwards, the pore was filled with water molecules and the system initially heated up to T = 2100 K and quenched within 70 ps to 100 K. During the quenching, water could react with the silica surface. The resulting configuration was then used as input for the ab-initio simulations and equilibrated for 24 ps. The surface density of silanols is ≈ 3 OH/nm^2, obtained from calculations of the solvent-accessible surface area employing the visualization software VMD [149]. This yields a hydrophilic surface[20].

In order to run the classical MD simulations, an appropriate system had to be obtained from the output of the ab-initio simulations. First, all water molecules were removed, some of them were dissociated, and silanols, Si-O-H and Si-O-H_2 at the pore surface were grouped to form molecules. Afterwards, the pore was duplicated four times[21] along the symmetry axis of the pore (z-axis direction) and filled with SPC/E water yielding three different pore fillings, namely *hi-dens* (high density) corresponding to 712 water molecules, *me-dens* (medium density) with 569 molecules and *lo-dens* (low density) with 529 molecules. The interaction of SPC/E with the wall was calculated according to the mixing rule described in the previous chapter with Lennard-Jones coefficients and charges given by *Bródka* [150]. This parametrization provides Lennard-Jones coefficients only for the oxygen atoms of the wall, whereby hydrogen atoms contribute only via Coulomb interaction. The coefficients had been converted to the *Gromacs* units in the framework of the master thesis by *Janz* [151]. Using the charges by *Bródka* gives a positively charged system and the PME algorithm is not applicable. In order to circumvent this problem, the charges of silicon and oxygen atoms, which are not near the surface and not part of silanol molecules, were adjusted. The charge of those silicon atoms was decreased by roughly 1% and the charge of those so-called bridging oxygen atoms increased by approximately 1%. The resulting pore is shown in Figure 4.3.

It was necessary to freeze the wall, meaning that all motion of wall atoms is

to deal with chemical reactions, but much faster than quantum chemical approaches [146, 147].

[20] Hydrophilic in the sense that there exists a chance to form hydrogen bonds (HB) with the wall and concurrently this does not prevent surface water from having further HB with other water molecules.

[21] The duplication was due to improve statistics as more water molecules are simulated.

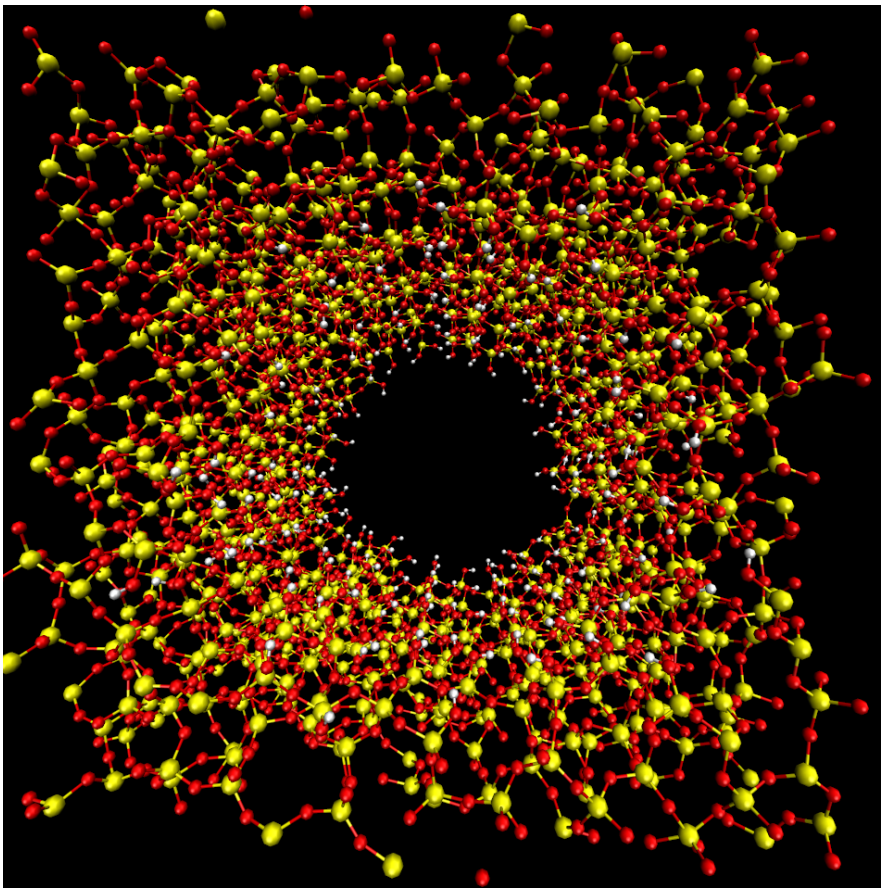

Figure 4.3: Small silica pore (Radius $r \approx 1.1$ nm) with perspective along the z-axis. The shown configuration is the result of ReaxFF and ab-initio simulations performed by *Allolio et al* [148], but already prepared for MD simulations. Silicon atoms are yellow, oxygen red and hydrogen white. The inner surface of the cylindrical pore is coated with silanols (≈ 3 OH/nm^2).

absent. Thus, the wall is not thermalized yielding elastic scattering of particles at the surface. Simulations without freezing the silica wall, which employed the bond parameters for silanols given by *Hill* [152] immediately crashed due to bond-length and bond-angle violations. This is because ab-initio simulations provide a lot of flexibility to bonds as there are no constraints or fixed bond lengths. Therefore, the wall had to be frozen and the time step had to be reduced to 1 fs for conducting MD simulations[22]. Additionally, equilibration was not performed in the NpT ensemble. Due to the frozen walls pressure coupling was impossible, therefore, equilibration was performed in the NVT ensemble yielding simulations at constant density rather than constant pressure, as used

[22] Also energy minimizations did not solve the problem.

Small silica pore	
Dimensions	x=3.931 nm, y = 3.931 nm, z = 4.108 nm
Radius	$\approx$ 1.1 nm
Silanols per surface	$\approx$ 3 OH/nm^2 yields hydrophilic wall [148]
Temperature range	300 K - 195 K
Silica matrix	frozen (no motion)
Equilibration	NVT ensemble
Time step	1 fs
Charges	
Silicon	1.26 e
Oxygen	-0.634 e
Silanol silicon	1.287 e
Silanol oxygen	-0.528 e
Silanol hydrogen	0.210 e
LJ coefficients	
Oxygen	$C_{ij}^{(6)} = (0.37900)^6$ (kJ/mol)nm^6, $C_{ij}^{(12)} = (0.3199)^{12}$ (kJ/mol)nm^{12}
Silanol oxygen	$C_{ij}^{(6)} = (0.42111)^6$ (kJ/mol)nm^6, $C_{ij}^{(12)} = (0.3554)^{12}$ (kJ/mol)nm^{12}

Table 3: Relevant simulation aspects for the small silica pore.

for the bulk simulations. The length of the trajectories varied with temperature, from 1 ns at 300 K to 75 ns at 195 K. Roughly the first 10% of each trajectory were used as equilibration and therefore not considered during data analyses. Table 3 summarizes the charges, Lennard-Jones coefficients and further aspects of the simulation of the small silica pore.

4.2.2 Large silica pore

Further, simulations involving a larger silica pore were performed. This pore is not based on ab-initio or ReaxFF simulations, but on classical MD simulations. It was produced during the master work of *Janz* [151]. However, the procedure for creating the pore is similar to the generation of the ab-initio silica pore. An initial configuration of silicon dioxide was heated and molten in order to have an amorphous structure. For this purpose the simulations employed the Buckingham potential. Then, the system was quenched and a part of it cut out, creating the cylindrical pore. The pore radius in this case is roughly 2 nm. Subsequently, the surface was coated by an algorithm, searching for oxygen atoms with too few silicon atoms surrounding it. For every missing silicon an OH group was attached, forming the silanols at the surface. The surface density for silanols is $\approx 2-3$ OH/nm^2 [23] yielding a hydrophilic wall[24]. It should be noticed that this is very different from the ab-initio/ReaxFF approach, where silanols are formed during a high temperature silica-water simulation, which is not possible in MD simulations, employing intact H_2O molecules.

The slightly different surface density for silanols and the much larger number of wall particles, when compared to the small silica pore, reduces the amount to which the charges for neutralizing the system had to be adjusted within the *Brodka* parametrization, compare Tables 3 and 4. The pore without water is depicted in Figure 4.4.

Simulations for the large silica pore are conducted in a different way than for the small silica pore. Only one pore filling with 3260 SPC/E molecules was used and parts of the matrix were position restrained rather than completely frozen. Owing to the *Brodka* potential, which aims at describing water to wall-surface interactions, Lennard-Jones coefficients for the silicon atoms are not provided and the matrix deforms in an unphysical and artificial way, even at rather low temperatures. The solution for this problem was to pin matrix atoms in space employing position restraints for the simulations [33]. This means that silicon and oxygen atoms were trapped in a 3-dimensional very stiff harmonic potential (force constant $\kappa = 10^6 \frac{\text{kJ}}{\text{mol nm}}$) whereas hydrogen atoms were free to rotate according to the bond parameters for silanols given by *Hill* [152]. Therefore, the wall is supposed to be thermalized as all molecules could be coupled to a heat bath. It will be shown in chapter 7 that structure and dynamics are

[23] Using the same solvent-accessible surface area calculations as for the small silica pore.

[24] Hydrophilic in the sense that there exists a chance to form hydrogen bonds (HB) with the wall and concurrently this does not prevent surface water from having further HB with other water molecules.

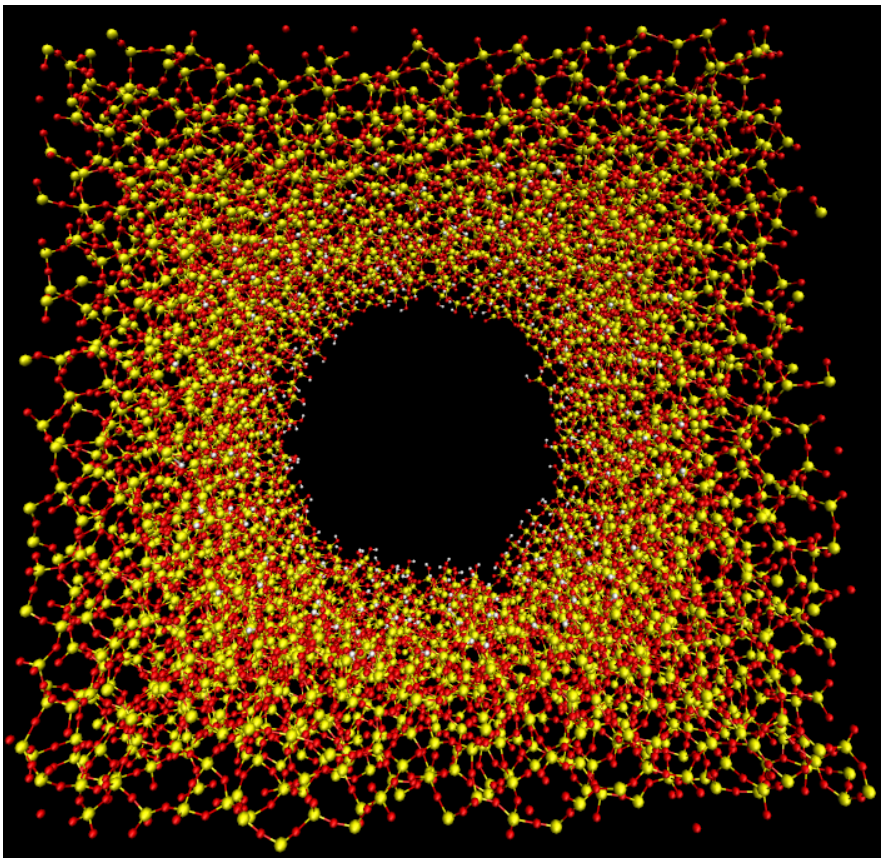

Figure 4.4: Large silica pore (Radius $r \approx 2$ nm) with perspective along the z-axis. Silicon atoms are yellow, oxygen red and hydrogen white. The inner surface of the cylindrical pore is coated with silanols ($\approx 2-3$ OH/nm^2).

very similar for the frozen and position restrained pores with the same density in a broad temperature regime. However, subtle effects due to the different thermostatting cannot be ruled out completely.

Owing to the position-restraint atoms, equilibration in the NpT ensemble was not possible, like for the small silica pore. Thus, equilibration was done in the NVT ensemble by dismissing the first 10% of the trajectories. The length of the trajectories for the data analyses ranged between 1 ns at 300 K and 180 ns at 195 K. Table 4 shows a collection of relevant simulation aspects for the large silica pore.

Large silica pore	
Dimensions	x=6.449 nm, y = 6.449 nm, z = 7.166 nm
Radius	≈ 2 nm
Silanols per surface	$\approx 2-3$ OH/nm^2 yields hydrophilic wall [148]
Temperature range	300 K - 195 K
Silica matrix	Silicon and oxygen atoms position restraint, hydrogen atoms free to rotate
Equilibration	NVT ensemble
Time step	2 fs
Charges	
Silicon	1.287 e
Oxygen	-0.629 e
Silanol silicon	1.287 e
Silanol oxygen	-0.528 e
Silanol hydrogen	0.210 e
LJ coefficients	
Oxygen	$C_{ij}^{(6)} = (0.37900)^6$ (kJ/mol)nm^6, $C_{ij}^{(12)} = (0.3199)^{12}$ (kJ/mol)nm^{12}
Silanol oxygen	$C_{ij}^{(6)} = (0.42111)^6$ (kJ/mol)nm^6, $C_{ij}^{(12)} = (0.3554)^{12}$ (kJ/mol)nm^{12}

Table 4: Relevant simulation aspects for the large silica pore.

4.2.3 Neutral confinement

The last group of systems which was investigated for this work is SPC/E water confined in amorphous ice pores. The goal of this approach is to use a neutral confinement rather than a hydrophilic or hydrophobic one and to investigate which effects are present or lacking compared to that of the silica pores.

The procedure to produce the amorphous-ice (or neutral) pores is fundamentally different from the approaches to obtain the silica pores. NpT ($p = 1$ bar) equilibration runs were conducted, as for the bulk systems of SPC/E, with trajectory lengths of 15 ns at 270 K and 150 ns at 195 K (time step 2 fs), but with much larger systems. The number of water molecules amounts to 11890. The large number was required in order to form cylindrical pores with large radii[25]. The amorphous-ice walls were build using position restraints. After each equi-

[25] Studies ensuing this work should consider different than cubic boxes to reduce the particle number and improve performance.

libration for a given temperature, some fraction of oxygen atoms was chosen to be position restraint, whereas the hydrogen atoms were not affected[26]. This means, as described in the previous subsection, that a fraction of oxygen atoms is trapped in a 3-dimensional harmonic potential.

The oxygen atoms for pinning were selected so as to obtain cylindrical pores (CP) with 2.5 nm, 1.5 nm and 0.5 nm radius. To do so, the z-axis was chosen as symmetry axis of the CP confinements and all oxygen atoms with a perpendicular distance to the symmetry axis larger than 2.5 nm, 1.5 nm or 0.5 nm were position restraint. Additionally, a slit geometry (SL) confinement was produced, where the liquid part of the water is confined by a layer of 2 nm thickness and its periodic image. Finally, a system was generated where different fractions of oxygen atoms were chosen at random, called random pinning (RP).

The force constant was varied but if not explicitly stated otherwise set to $\kappa = 10^6 \frac{\text{kJ}}{\text{mol nm}}$. The major difference to the previous pores is the possibility of equilibration in the NpT ensemble. This yields new pores for every temperature and geometry. The described procedure is also known as *equilibrated mixture protocol* [154].
Figure 4.5 illustrates the amorphous-ice confinements.

Production runs were carried out in the NVT ensemble whereby also for the amorphous-ice pores the first 10% of the trajectories in the NVT ensemble were omitted to account for the instantaneous pinning of the particles. The investigated temperature regime extends from 270 K to 195 K and the length of trajectories varies from 100 ns to 1200 ns.

[26] In fact the procedure is more complex owing to the SETTLE algorithm calculating the position of the hydrogen atoms of water when using constraints, see chapter 3. The employed *Gromacs* version only allows for applying the position restraints to molecules and SETTLE only works with a single definition of water molecules, thus excluding the option to simply define molecules where the oxygen atom should be position restraint and *liquid* ones. The problem was solved by pretending *Gromacs* a large water molecule comprising the whole system, see the master proposal by the author [153]. It was assured to yield the same results as the original definition.

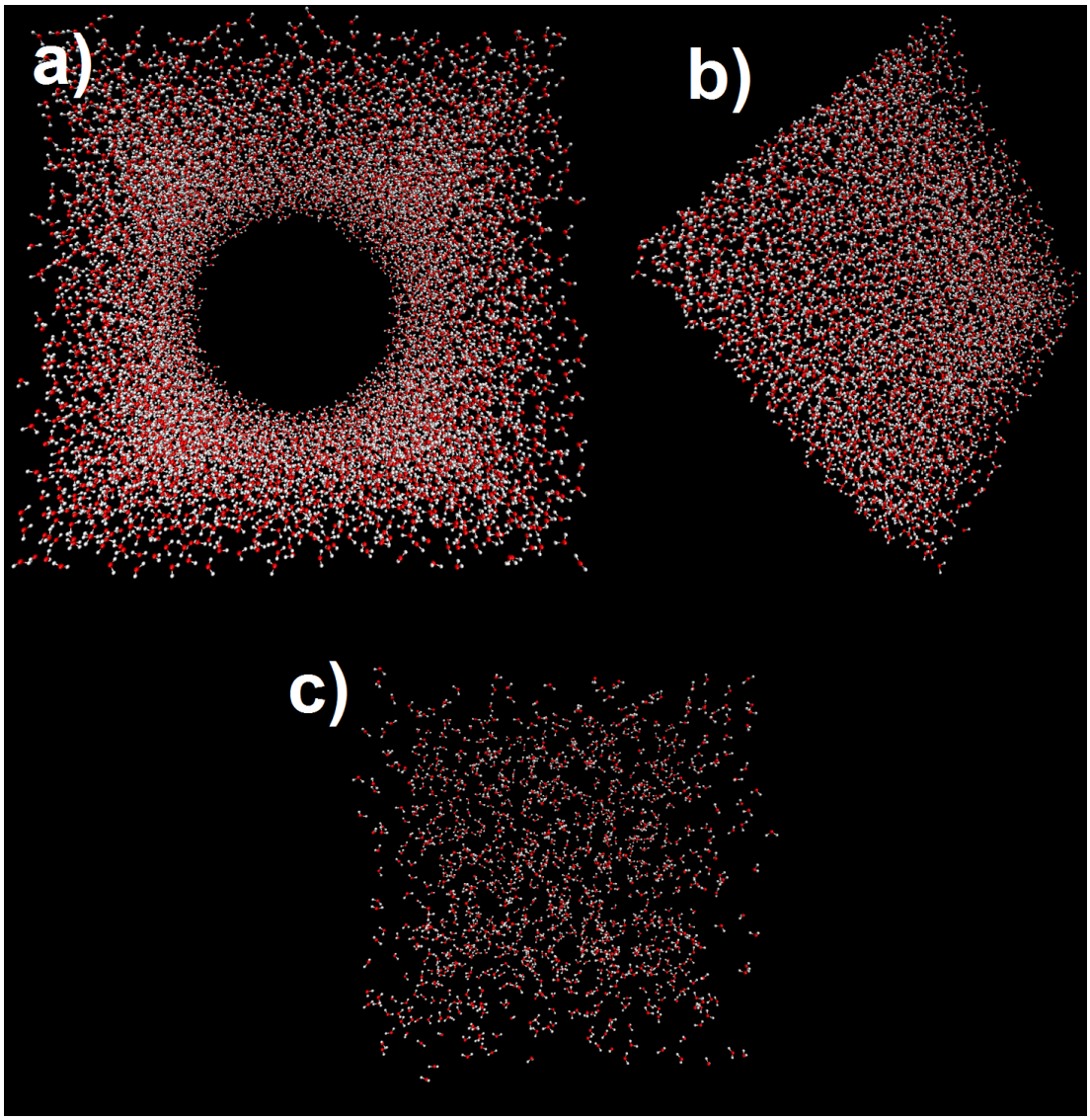

Figure 4.5: Amorphous-ice confinements at $T = 240$ K. a) shows a cylindrical pore (CP) with 2.5 nm radius. b) depicts a slit geometry (SL) with 2 nm of layer thickness. c) illustrates a random pinned (RP) confinement where 10% of the oxygen atoms are pinned.

Amorphous-ice pores	
Dimensions	cubic with $x, y, z \approx 7$ nm depending on temperature
Walls	oxygen atoms position restraint, hydrogen atoms free to rotate
Hydrophilicity	neutral
Equilibration	NpT and NVT ensemble
Time step	2 fs
CP	radii: 0.5 nm, 1.5 nm and 2.5 nm
SL	2 nm layer pinned
RP	randomly pinned fraction, 10% to 50%
Temperature range	270 K - 195 K

Table 5: Relevant simulation aspects for the amorphous-ice pores.

5 Observables

This chapter will give a description of observables which are used in this study. Some of them have already been mentioned in chapter 2, like the radial distribution function, the incoherent intermediate scattering function or three-time correlation functions for detecting heterogeneity. It is clearly stated that this chapter will only give a technical description of the quantities. They will be detailed and explained by means of the bulk system in chapter 6. The reason for evaluating those quantities is related to the motivations to investigate the different confinement systems. For the silica pores, a comparison with quantities which are accessible in experiments, like F_1 or F_2, is conducted. In the neutral confinement chapter, translational motion and overlap functions are important.

Various of the following observables can be modified to account only for subensembles of the system. As already stated, MD simulations provide the trajectory of every atom in the system. This advantage is used as the analyses of the confinement systems are mainly based on distinguishing atoms dependent on their location within the pore, what is usually not possible in experiments. The symbol d denotes the initial average distance of oxygen atoms to wall atoms within an interval of size $\Delta d = 0.05$ nm. For instance, all oxygen atoms having a distance between 0.5 nm to 0.55 nm to the wall are designated by $d = 0.525$ nm, see Figure 5.1. It is important to notice that the assignment to d was done at each initial time when calculating correlation functions.
i designates the i-th out of an ensemble of N particles and $\langle\rangle$ denotes averages over time.

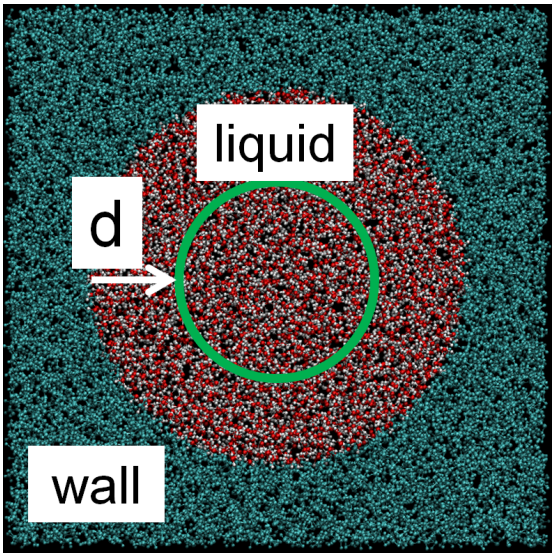

Figure 5.1: Schematic illustration of the distance d to the pore wall.

5.1 Structure

In the following, observables probing structure are introduced.

5.1.1 Radial distribution functions

A typical structural quantity, which can be obtained by neutron scattering experiments, is the structure factor,

$$S(\vec{q}) = \left\langle \frac{1}{N} \sum_{i,j} e^{-i\vec{q}\left[\vec{r}_i(0) - \vec{r}_j(0)\right]} \right\rangle, \tag{5.1}$$

with $\vec{q} = \vec{k}_0 - \vec{k}_f$ the scattering vector [155]. This vector gives the change of the incident wave vector $\vec{k}_0$ compared with the reflected one $\vec{k}_f$, e.g. for neutrons. If the system is isotropic, then equation (5.1) reduces to the formulation

$$S(q) = \left\langle \frac{1}{N} \sum_{i,j} \frac{\sin(q\left[\vec{r}_i(0) - \vec{r}_j(0)\right])}{q\left[\vec{r}_i(0) - \vec{r}_j(0)\right]} \right\rangle, \tag{5.2}$$

with $|\vec{q}| = q$.
In the limit of $N \to \infty$ and if an isotropic system is assumed, the radial pair distribution function is defined as

$$g(r) = \frac{1}{2\pi^2 \rho r} \int_0^\infty q[S(q) - 1] \sin(qr) dq, \tag{5.3}$$

where ρ designates the average density of the system and $r = |\vec{r}|$ [155].
A more convenient way to calculate $g(r)$ is given by

$$n(r)dr = 4\pi\rho \int g(r) r^2 dr, \tag{5.4}$$

with $n(r)$ the number of particles located in a spherical shell with thickness dr [155]. If only oxygen atoms are considered, equation (5.4) yields the oxygen-oxygen distribution function $g_{OO}(r)$. If the center of the spheres is determined by oxygen atoms and only hydrogen atoms are considered for the number of particles in the shells, the oxygen-hydrogen (OH) distribution function $g_{OH}(r)$ results.

5.1.2 Hydrogen bonds

Hydrogen bonds are defined by the following conditions [156, 157]. First, the distance between two oxygen atoms is less than 0.35 nm ($R_{OO} < 0.35$ nm). Second, the hydrogen atom must be located within a cone, whose symmetry axis is the line connecting the oxygen atoms and whose opening angle amounts to 30°, see Figure 5.2.

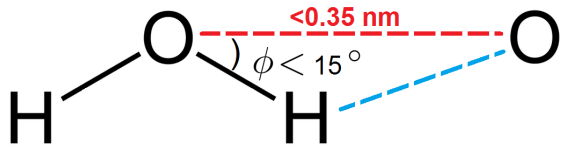

Figure 5.2: Conditions for hydrogen bonds.

5.1.3 Tetrahedral order

To account for the ability of water to form hydrogen bonds with adjacent water molecules and thus, to establish a tetrahedral network, the tetrahedral order parameter is defined [128, 158, 159]

$$Q_i = 1 - \frac{3}{8}\sum_{j=1}^{3}\sum_{k=j+1}^{4}\left[\cos(\psi_{jik}) + \frac{1}{3}\right]^2. \tag{5.5}$$

The index i denotes the considered oxygen atom and j,k the nearest oxygen neighbors (not necessarily hydrogen bonded to the local atom). The average $\left\langle \frac{1}{N}\sum_i Q_i \right\rangle$ is 0 for random configurations and 1 for perfect tetrahedral orientation of all molecules [128].

Kumar derived an entropy per molecule, which is based on the order parameter given in equation (5.5), called tetrahedral entropy [159]. The entropy is calculated according to

$$S_Q(T) \equiv S_0 + \frac{3}{2}k_B\int_{Q_{min}}^{Q_{max}} \ln(1-Q_i)P(Q_i,T)dQ_i. \tag{5.6}$$

S_0 refers to a high-temperature limit and is usually not known. Therefore, the quantity $\frac{2}{3}\left(S_Q(T) - S_0\right)/k_B$ will be discussed, because the distribution $P(Q_i,T)$ and thus the weighted integral over the distribution in equation (5.6) is available. $\frac{2}{3}\left(S_Q(T) - S_0\right)/k_B$ ranges between the limiting cases 0 and $-\frac{2}{3}S_0/k_B$ for random or perfect tetrahedral order, respectively.

5.2 Dynamics

All correlation times τ are obtained from the condition $C(\tau) \equiv 1/e$ with C denoting a correlation function normalized to $C(0) \equiv 1$. In the following, t always refers to a time interval. The correlation time $\tau_{\alpha,\text{trans}}$ is obtained from

the incoherent intermediate scattering function, equation (5.8), τ_{α,F_1} from the nuclear dipole reorientation, equation (5.11), and τ_{α,F_2} from the reorientation of the $\vec{\text{OH}}$ bond vector, see eqation (5.12).

5.2.1 Mean squared displacement

The mean squared displacement (MSD) is important especially with respect to BM, see chapter 2.3, and can be obtained by e.g. neutron scattering experiments. The definition is

$$\langle \Delta r^2(t) \rangle = \left\langle \frac{1}{N} \sum_{i=1}^{N} [\vec{r}_i(t) - \vec{r}_i(0)]^2 \right\rangle \tag{5.7}$$

5.2.2 Translational correlation functions

In analogy to neutron scattering experiments, the incoherent intermediate scattering function is defined as the Fourier-transformed single particle displacement

$$S_{\vec{q}}(t) = \left\langle \frac{1}{N} \sum_{i=1}^{N} e^{-i\vec{q}\cdot\left[\vec{r}_i(t) - \vec{r}_i(0)\right]} \right\rangle \overset{\text{isotropic}}{=} \left\langle \frac{1}{N} \sum_{i=1}^{N} \frac{\sin(|\vec{q}| \cdot |\vec{r}_i(t) - \vec{r}_i(0)|)}{|\vec{q}| \cdot |\vec{r}_i(t) - \vec{r}_i(0)|} \right\rangle . \tag{5.8}$$

It probes translational motion on a length scale determined by the value of the scattering vector $|\vec{q}|$, with $\vec{q} = \vec{k}_0 - \vec{k}_f$ the difference between the incident and final wave vector [125]. For isotropic motion, the conversion to the term on the right hand side is feasible and $\vec{q}$ changes to $q = |\vec{q}|$ [160]. The backward Fourier transformed $\mathfrak{F}\left\{S_q(t)\right\}$ yields the self-part of the van Hove correlation function [161],

$$G(r,t) = \left\langle \frac{1}{N} \sum_{i=1}^{N} \delta\left[|\vec{r}_i(t) - \vec{r}_i(0)| - r\right] \right\rangle , \tag{5.9}$$

with $|\vec{r}| \equiv r$. Deviations from an ideal Gaussian-shaped distribution of displacements are measured with the non-Gaussian parameter,

$$\alpha_2(t) = \left\langle \frac{3}{5} \frac{\sum_{i=1}^{N} \vec{r}_i^{\,4}(t)}{\left(\sum_{i=1}^{N} \vec{r}_i^{\,2}(t)\right)^2} - 1 \right\rangle \tag{5.10}$$

5.2.3 Length scale for probing dynamics

The focus of this thesis is on structural relaxation. $S_q(t)$ can be used to probe this kind of relaxation, however, the length scale $|\vec{q}|$ must be sufficiently large. Therefore, this part is intended to reason the specific choice of q, which is used throughout this study.
In chapter 2.1, the radial pair-distribution function $g_{OO}(r)$, cf. (5.4), depicted in Figure 2.1, revealed local structuring while long-range order is absent, as expected for liquids. Another way to examine structure is given by the structure factor $S(q)$, which is closely related to $g(r)$, cf. equation (5.3). $S_{OO}(q)$ is illustrated for oxygen atoms in Figure 5.3 and is in perfect agreement with previous studies on SPC/E [25]. At high temperatures, only a peak at approximately $q = 30\,\mathrm{nm}^{-1}$ is found. Upon lowering the temperature, this peak becomes more pronounced and a second peak emerges at roughly $q = 17\,\mathrm{nm}^{-1}$, corresponding to voids in the water network [162]. In simple liquids, this doublet of peaks in the mentioned q-regime is missing, there exists only one large peak corresponding to the next-neighbor peak [162]. Therefore, the intermediate region between these peaks, like $q = 22.7\,\mathrm{nm}^{-1}$, seems feasible to characterize α-relaxation probed by e.g. the incoherent intermediate scattering function and is, thus, used as length scale for $S_q(t)$. It should be noticed that very subtle length-scale dependent effects like de Gennes narrowing are not detailed in this study, but are known for SPC/E [49].

5.2.4 Rotational autocorrelation functions

Two rotational autocorrelation functions are studied. The first is used to probe the reorientation of the nuclear dipole vector of water. Neglecting correlations between different dipole terms, F_1 is measured in DS experiments. Therefore, this function is used to probe the reorientation of the dipole vector of water molecules only,

$$F_1(t) = \left\langle \frac{1}{N} \sum_{i=1}^{N} \vec{e}_{i,\mathrm{dipole}}(t) \cdot \vec{e}_{i,\mathrm{dipole}}(0) \right\rangle . \tag{5.11}$$

The second correlation function is employed for detecting the reorientation of the $\vec{\mathrm{OH}}$ bonds only and is probed by NMR,

$$F_2(t) = \left\langle \frac{1}{2N} \sum_{i=1}^{2\cdot N} \frac{1}{2} \left[3 \cdot \left\{ \vec{e}_{i,\mathrm{OH}}(t) \cdot \vec{e}_{i,\mathrm{OH}}(0) \right\}^2 - 1 \right] \right\rangle . \tag{5.12}$$

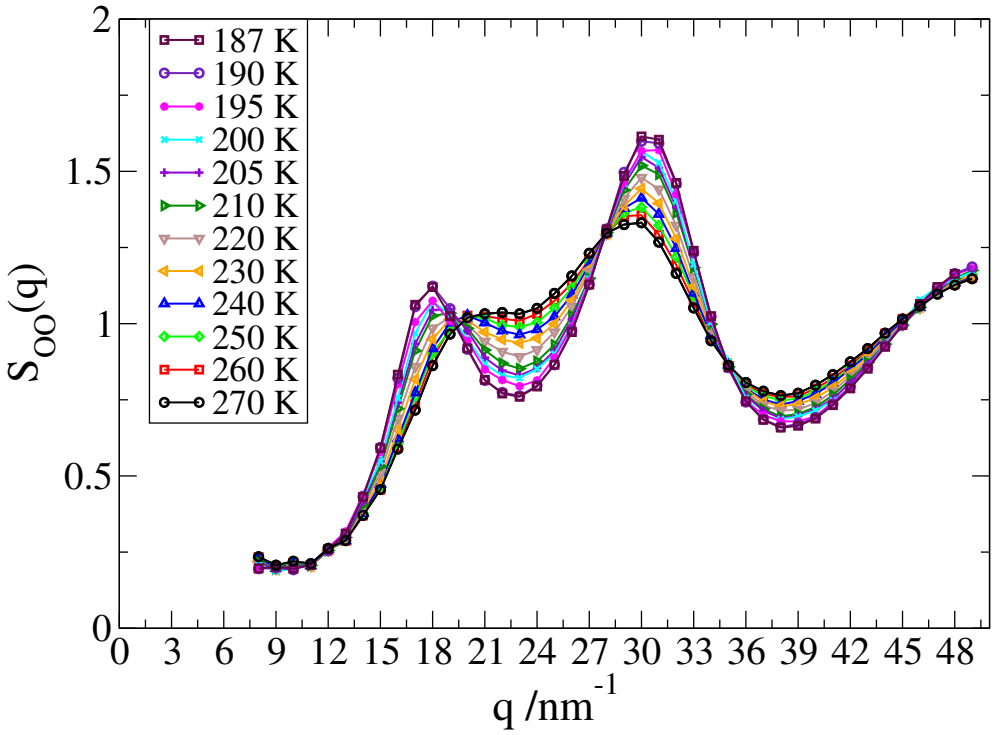

Figure 5.3: Structure factor for oxygen atoms of bulk water.

MD simulations provide the opportunity to swap the definitions and calculate the $\vec{\text{OH}}$ bond reorientation using F_1 and vice versa. But for this study, F_1 and F_2 are employed consistent with experiments.

5.2.5 Velocity autocorrelation function

Similar to $F_1(t)$ a correlation between velocities can be defined [163, 164]

$$C_v(t) = \frac{1}{C_v(0)} \left\langle \sum_{i=1}^{N} \vec{v}_i(t)\vec{v}_i(0) \right\rangle \tag{5.13}$$

with $\vec{v}_i(t)$ the velocity vector for the i-th particle at time t. Related to $C_v(t)$, the so-called vibrational density of states (VDOS) can be defined,

$$Z(\omega) = \frac{1}{2\pi} \int_0^\infty \cos(\omega t) C_v(t). \tag{5.14}$$

Both quantities can be used to determine longitudinal or transversal modes propagating through the systems and $C_v(t)$ allows for specifying the time scale for the crossover from vibrational to, e.g., diffusive motion within a potential. These observables will be used to characterize short time dynamics in chapter 8.4.

5.2.6 Susceptibilities

Following *Kubo* and *Shimizu* [34, 165, 166], the imaginary part of the susceptibility (spectral response function) χ'' can be calculated according to

$$\chi''(\omega) = \pi\omega \cdot J(\omega) = \pi\omega \cdot \frac{1}{2\pi} \int_{-\infty}^{\infty} C(t) e^{-i\omega t} dt, \tag{5.15}$$

with $J(\omega)$ the so-called spectral density. For actual calculation purposes only the cosine transformation was performed, what is equivalent due to $C(t)$ depending solely on the time interval t. Therefore, it is an even function and together with being strictly real, the Fourier transform $\mathfrak{F}\{C(t)\}$ yields a real and even function too [65].

Another kind of response function is based on four-point density correlation functions. The definition reads

$$\chi_4 = \frac{V}{N^2 k_B T} \int d^3r_1 d^3r_2 d^3r_3 d^3r_4 e^{-i\vec{q}(\vec{r}_1 - \vec{r}_2)} e^{-i\vec{q}(\vec{r}_3 - \vec{r}_4)} G_4(\vec{r}_1, \vec{r}_2, \vec{r}_3, \vec{r}_4, t) \tag{5.16}$$

with

$$\begin{aligned} G_4(\vec{r}_1, \vec{r}_2, \vec{r}_3, \vec{r}_4, t) = &\langle \rho(\vec{r}_1, 0) \rho(\vec{r}_2, t) \rho(\vec{r}_3, 0) \rho(\vec{r}_4, t) \rangle \\ &- \langle \rho(\vec{r}_1, 0) \rho(\vec{r}_2, t) \rangle \langle \rho(\vec{r}_3, 0) \rho(\vec{r}_4, t) \rangle. \end{aligned} \tag{5.17}$$

$\rho(\vec{r}, t)$ denotes density fluctuations at the position $\vec{r}$. The idea is that G_4 accounts for correlated density fluctuations [56]. For this thesis, only the self-part of the density fluctuations was considered, in agreement with earlier studies, see [56, 60]. A more convenient formulation yields

$$\chi_4(t) = \frac{V}{N^2 k_B T} \left[\langle S_q(t)^2 \rangle - \langle S_q(t) \rangle^2 \right], \tag{5.18}$$

thus, the response function is obtained by the variance of the incoherent intermediate scattering function.

5.2.7 Overlap functions

Overlap functions are used to probe the overlap of configurations. For a detailed motivation on the use of them, the reader is referred to chapter 2.4. The definition is given as

$$Q(t) = \frac{\sum_i^N \langle n_i(t) n_i(0) \rangle}{\sum_i^N \langle n_i(0) \rangle}. \tag{5.19}$$

Every oxygen atom defines a spherical cell with radius 0.11 nm (chosen to reflect the size of water molecules and to ensure that only one molecule fits in the cells) at time $t = 0$. The sum runs over the cells which are counted as $n_i(t) = 1$ if the cell is occupied and 0 if not. Thus, the overlap function is invariant under pairwise exchange of molecules.

5.3 Probing heterogeneity

Different quantities probing heterogeneity are defined. It will be shown in chapter 6 that in this sense the non-Gaussian parameter also probes heterogeneity.

5.3.1 Three-time correlation functions

It was pointed out in chapter 2.2 that experimental studies used three-time and four-time correlations functions to get information about heterogeneity. In this study, only three-time correlation functions are used. Basically, three-time correlation functions are split in two parts. First, there is a dynamical filter, then, the usual two-time correlation function is calculated for the particles which passed the filter. The dynamic filter weights the contribution of particles by the effects resulting from motion during the filter time t_f. Hence, fast particles relative to t_f are omitted. Additionally, it is necessary to use a binary filter for defining the limiting case of homogeneous behavior in a simple way, see [55] and chapter 6.2 where this is detailed. Unfortunately, it is not appropriate to mix a smooth weighting function like for $S_q(t)$, $\sin(x)/x$, with a binary filter. Hence, a binary correlation function $S_{\text{bin}}(t)$ analogous to $S_q(t)$ is defined. Here, the smooth weighting of $\sin(x)/x$ is replaced by a binary 0,1 weighting. The corresponding three-time correlation function is

$$S_{\text{bin},3}(t;t_f) = A \cdot \left\langle \frac{1}{N} \sum_{i=1}^{N} K_i(t_f,R) \cdot K_i(t,R) \right\rangle , \tag{5.20}$$

with $K_i(t,R) = 1$ if $|\vec{r}_i(t) - \vec{r}_i(0)| < R$ and $K_i(t,R) = 0$ if $|\vec{r}_i(t) - \vec{r}_i(0)| \geq R$. The length R is set to $(2\pi/24)$ nm, because with this choice $S_{\text{bin}}(t)$ is almost identical to $S_q(t)$ with $q = 22.7\ \text{nm}^{-1}$.

5.3.2 Conditional probability functions

In order to quantify back and forth dynamics, the following conditional probability function (CPF) can be defined [167],

$$\langle R(r_{01}) \rangle = \frac{1}{N} \sum_{i=1}^{N} [\langle r_{2,i} \rangle - \langle r_{1,i} \rangle] \tag{5.21}$$

with $\langle r_{1,i} \rangle$ as mean position of a particle i moving the distance r_{01} in the first time interval in a certain direction. This direction is chosen parallel to the movement of the particle and all motion is defined as projection onto this vector, see chapter 6.3 for the example of a particle trapped in a harmonic potential. $\langle r_{2,i} \rangle$ yields the averaged location of a particle, but corresponding to the second time interval. This CPF is also a three-time correlation function, but works very different compared with the previous function, see equation (5.20). Figure 5.4 illustrates the time intervals and locations. The reader is referred to chapter 6.3 for examples on how to use this CPF.

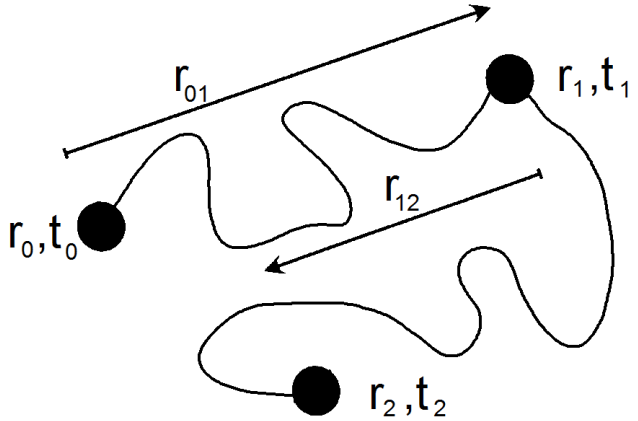

Figure 5.4: Illustration of time intervals and locations used for equation (5.21). This figure is adapted from [167].

5.3.3 Cluster and string analyses

Three-time correlation functions and the CPF probe motion related to heterogeneity. Establishing the notion *spatially* heterogeneous dynamics needs additional information about the distribution of fast or slow particles in space. The following quantities are suitable to reveal the clustering of fast molecules, $S_W(t)$, and to obtain insights into special string-like motion of fast particles, $L_W(t)$. Both functions yield information on the size of a cluster or string for randomly chosen particles, the weight-averaged size, as function of time t.
The analysis of clusters is performed by calculating the weight-averaged cluster size

$$S_W(t) = \frac{\sum_n n^2 \cdot P_S(n,t)}{\sum_n n P_S(n,t)} \tag{5.22}$$

with $P_S(n,t)$ the probability to find a cluster of size n given the time interval t and $\sum_n P_S(n) = 1$ [56]. Particles are considered as part of the same cluster if

their distance is smaller than the typical hydrogen-bond length, see Figure 5.2. The idea is to examine e.g. the 5% fastest particles with respect to the time interval t. If too many particles are considered there is only the trivial result of a large cluster comprising all particles. It turned out that investigating the 5% to 10% fastest molecules yields valuable information [57, 58]. Formal, the condition for particles to be part of a cluster reads

$$|\vec{r}_l(0) - \vec{r}_m(0)| < 0.35 \text{ nm} \tag{5.23}$$

with l, m restricted to a subensemble of fast particles, the 5% fastest with respect to the time interval t (no analyses for the dependence on the amount of fast particles had been performed).
Further, string-like motion is investigated,

$$L_W(t) = \frac{\sum_n n^2 \cdot P_L(n,t)}{\sum_n n P_L(n,t)}. \tag{5.24}$$

This is also only calculated for the fastest (as before 5%) particles. In this case, particles are considered to be part of a string if they move to the previous location of another fast particle. Then, both particles are assigned to the same string. Explicitly, the definition is

$$\min[|\vec{r}_i(0) - \vec{r}_j(t)|, |\vec{r}_j(0) - \vec{r}_i(t)|] < 0.11 \text{ nm}. \tag{5.25}$$

Note the different indices for particles in the latter equation, revealing when particles approximately move to the previous location of another one. As there is never a perfect jump to those previously occupied locations, the value 0.11 nm, roughly corresponding to the size of a water molecule, is used as a threshold.

6 Bulk water

The goal of this chapter is to thoroughly characterize the bulk system before moving to more complex confinement systems. In particular indications for the HDL to LDL transition and spatially heterogeneous dynamics of SPC/E will be discussed. Some essential quantities are introduced to lay the ground for the analyses of water in confinements. In particular, some of the quantities are revisited in chapter 8.4 using a complex theory, thus, a basic understanding of heterogeneity and energy landscapes is mandatory. This is imparted in the following.

6.1 Structure of supercooled water

The radial pair distribution function and the structure factor have already been discussed above, see Figure 2.1 and 5.3. Unfortunately, both are of limited use for describing the structure of water in confinements, because introducing a wall breaks the isotropy of the system. Therefore, this chapter starts with a discussion of other measures of the local order.

6.1.1 Hydrogen bonds and tetrahedral order

Water has the ability to form hydrogen bonds (HB). The number of HB per molecule is illustrated for SPC/E in Figure 6.1. Most molecules form four HB with neighbors and as temperature is lowered, the tail towards less than four HB vanishes and the distribution of HB per molecule becomes more narrow and symmetrically shaped with a mean of four. Therefore, the average number of HB, shown in the inset, increases from roughly 3.7 to almost 4.

Owing to the roughly four HB per molecule and the H-O-H bond angle, which is for SPC/E equivalent to the tetrahedral angle, water forms tetrahedral networks. This is probed by the tetrahedral order parameter, see equation (5.5), which will be extensively studied for characterizing the local structure of water in confinement.

Figure 6.2 shows the distribution of the tetrahedral order parameter, giving the probability for a molecule to be in an environment specified by Q_i. A perfect tetrahedral environment yields $Q_i = 1$ and the minimal value is $Q_i = -3$. The mean of the distribution $\langle Q_i \rangle$ has the limits 0 and 1, for random and perfect tetrahedral order of the system, respectively. The distributions in Figure

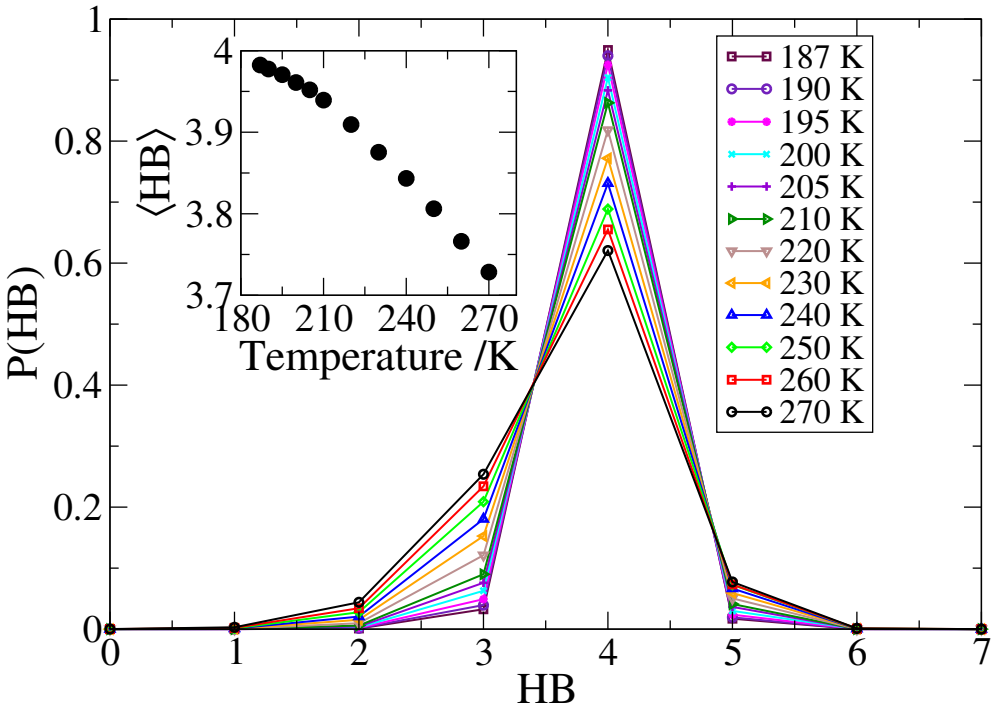

Figure 6.1: Probability distribution of the number of hydrogen bonds (HB) per molecule. The inset depicts the average number of HB as function of temperature.

6.2 exhibit a bimodal structure at high temperatures. Upon cooling, the peak located at $Q_i \approx 0.5$ vanishes but concurrently the second peak at $Q_i \approx 0.8 - 0.9$ increases and shifts towards 1. This behavior for SPC/E was first observed by *Errington* and interpreted as presumably related to a phase transition [128]. According to this, the first peak was attributed to a high-density liquid (HDL) coexisting with a low-density liquid (LDL) resulting in the second, ice-like peak. As the temperature is lowered, the HDL disappears and the remaining structure is that of LDL.

The inset in Figure 6.2 depicts the tetrahedral entropy, see equation (5.6), and the average of $P(Q_i, T)$, colored black and red respectively, as functions of temperature. According to the previous discussion, the mean value grows and strives towards the value of a perfect tetrahedral system $\langle Q_i \rangle = 1$. Accordingly, the tetrahedral entropy decreases in a continuous manner, no sharp change of structure is observed. Hence, relating to the LLCP or HDL to LDL transition scenario, no evidence for a first order phase transition is found for the bulk in the accessible temperature regime from 270 K to 187 K at $p = 1$ bar. This conjecture will be further detailed in chapter 7.

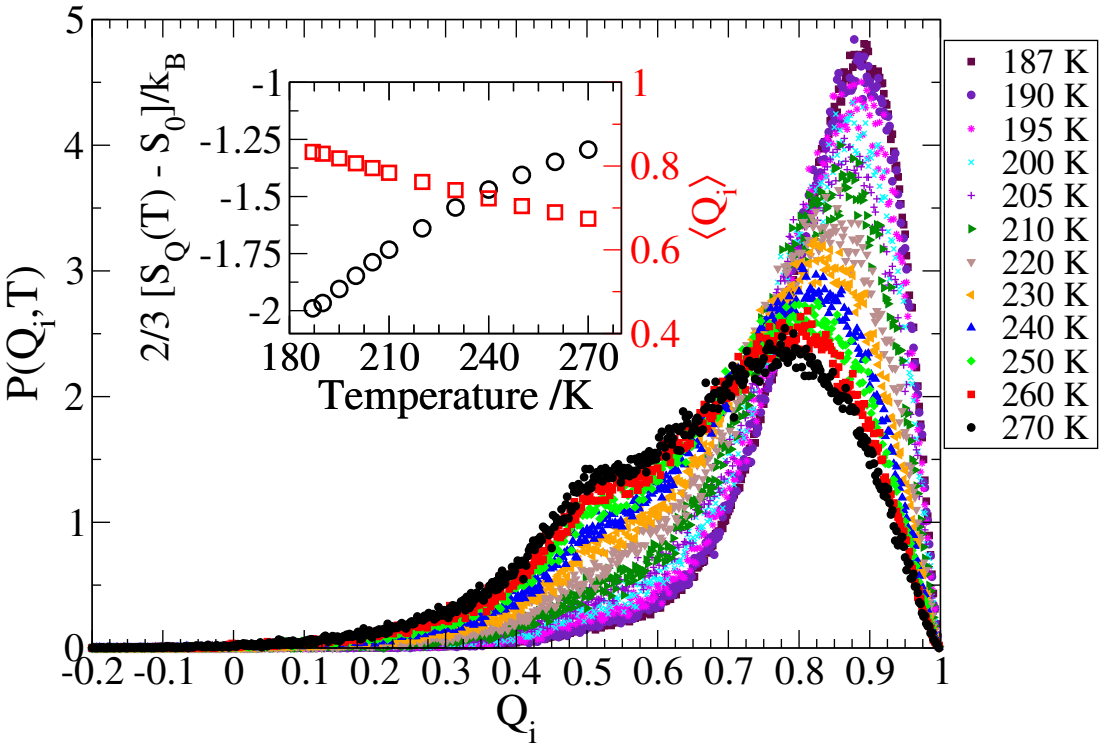

Figure 6.2: Probability distribution of the tetrahedral order parameter. The inset depicts the tetrahedral entropy (black) and the mean of the distribution (red) as function of temperature .

6.1.2 Final remarks on the structure and phase transitions

This chapter aimed at introducing the main quantities for probing structure and elucidating the structure of water, like the hydrogen bond network, giving rise to a tetrahedrally formed environment. This is quantified by the tetrahedral order parameter Q_i, which together with the tetrahedral entropy will be extensively used in the chapters dealing with water in confinements. The results are in agreement with previous studies on SPC/E, see [128].

Water exhibits a structure which is more complex than for other simple liquids of comparable molecular size [162]. Relating to this, a phase transition from HDL to LDL was discussed in chapter 2.7. For the bulk, no evidence for this transition was found for temperatures ranging from 270 K to 187 K at $p = 1$ bar. This statement is corroborated by Figure 2.3. There, the relaxation times were investigated. It was pointed out in chapter 2.7 that dynamics might be more suitable to detect a putative transition from HDL to LDL as a distinct

crossover, the FST, can be associated with the phase transition. However, one can readily observe that SPC/E does not exhibit this kind of transition in the investigated temperature regime at $p = 1$ bar (≈ 1 g/cm^3). *Brovchenko et al* claim to find indications of the FST in bulk simulations of SPC/E [111]. At a density of roughly 1 g/cm^3 the temperature for the phase transition is assumed to be at approximately 190 K, whereas at a slightly increased density, 1.08 g/cm^3, the transition temperature increases to 220 K. Interestingly, a putative transition was reported for SPC/E confined in silica pores at comparable densities ($\approx 1 \frac{\text{g}}{\text{cm}^3}$) and 220 K [17]. This rises the question whether confining water may shift the putative transition temperature to higher values, thus, the FST is revisited in chapter 7.

6.2 Slow dynamics and heterogeneity

In this subsection findings for the dynamics of supercooled SPC/E are detailed and spatially heterogeneous dynamics is addressed.

The first phenomenon, discussed in the context of Figure 2.2 and related text, was the emergence of a two-step decay of $S_q(t)$ at lower temperatures, replacing an apparently single-exponential decay. From the discussion of BM, it became clear that there is never a pure single-exponential decay on short length/time scales, because there is always ballistic motion and afterwards relaxation. To put it differently, it takes the system some time to fulfill conditions like (2.10). However, the origin of the two-step decay goes deeper. It is normally ascribed to a cage effect emerging for supercooled liquids [27]. Comparison of the MSD for oxygen atoms (Figure 2.4) with $S_q(t)$ at $t = 1$ ps (Figure 2.2 a)) shows that also in the case of SPC/E the step in the correlation function is presumably due to a local cage effect, $\sqrt{\langle \Delta r^2(t = 1 \text{ ps}) \rangle} \approx 0.1$ nm (compared with the next-neighbor distance ≈ 0.28 nm) [27].

Having clarified the first part of the two-step decay, the focus is now on the second part, the long-time decay. It was already stated in chapter 2.1 that usually a KWW function gives reasonable approximations for the long-time decay, e.g., of the incoherent intermediate scattering function for oxygen atoms $S_q(t)$,

[27] P-spin models also exhibit this kind of two-step decay without any real space. The explanation in those cases is that it takes the system some time to find the negative eigenvalues responsible for saddle-point diffusion in phase space. When there are only a few negative eigenvalues (deeply supercooled), it takes the system a while to find the negative ones. Meanwhile it explores the positive modes similar to the system being trapped in a potential. See Cavagna for details [27].

with $q = 22.7\ \mathrm{nm}^{-1}$. The approximations gave stretching exponents β_{KWW} in the range from 0.6 to 0.8, indicating deviations from a *simple* exponential decay, which was derived during the discussion on BM. Therefore, the question arises whether there is an underlying distribution of correlation times, giving rise to the stretched-exponential decay. Both scenarios have been introduced for supercooled liquids in general in chapter 2.2 as heterogeneous and homogeneous respectively. In experiments, the contributions were distinguished by employing three-time correlation functions, e.g. analogous to $S_{\mathrm{bin},3}$ (equation (5.20)).

Therefore, a similar analysis is performed. However, there is a very important subtle difference. In MD simulations, it is possible to define a binary filter for the motion of molecules. This means that all particles which moved farther than R during the time t_f are weighted with 0 and others with 1. This is usually not possible in experiments, and thus, great care must be taken when defining the limit of homogeneous dynamics, see [55].

Next, the two limiting cases are detailed. Homogeneous behavior yields by definition the factorization of $S_{\mathrm{bin},3}$ of contributions from the motions in the first (t_f) and second (t) time intervals, as both are perfectly uncorrelated. Due to the binary filter, the motion during t_f is simply weighted with 0 or 1 yielding

$$S^{\mathrm{hom}}_{\mathrm{bin},3}(t;t_f) = 1 \cdot S_{\mathrm{bin}}(t). \tag{6.1}$$

In this case, it is not possible to select a slow subset of particles. More precisely, *slow* is only a result of backward correlations. Particles can move during the time interval t_f and some of them move back, thus they are only slow with respect to the nature of the filter which simply compares the positions at two different times. The backward correlation intrinsically yields the stretched-exponential decay [54, 167].

In contrast, the perfect heterogeneous limit is the case where it is possible to select slow particles due to the distribution of correlation times without any homogeneous contribution. This means that it is possible to decompose the system into subensembles, where the particles show an exponential correlation function $e^{-\theta t}$ with a rate θ. θ depends on the subensemble. Regarding a single subensemble [55],

$$S_{3,\theta}(t;t_f) = S_{2,\theta}(t_f) \cdot S_{2,\theta}(t) = e^{-\theta(t_f+t)} = S_{2,\theta}(t_f+t), \tag{6.2}$$

with the first equality due to the fact that it is not possible to select fast and slow particles within a single subensemble. Therefore, the homogeneous case

applies and a factorization is allowed. Equation (6.2) is valid regardless of the chosen subensemble, and thus, the rate average gives the two-time correlation function. One can write [55],

$$S^{\text{het}}_{\text{bin},3}(t;t_f) = S_{\text{bin}}(t+t_f). \tag{6.3}$$

It is strongly emphasized that this is only valid if the filter times are not too large. The system is ergodic, hence, there must be a lifetime for heterogeneity (of truly fast or slow), which was found to be on the order of τ_α in experiments, see chapter 2.2. For $t_f \gg \tau_\alpha$ the limit of BM applies, which is trivially homogeneous due to ergodicity.

Figure 6.3 exhibits $S_{\text{bin}}(t)$ and $S_{\text{bin},3}(t)$ for oxygen atoms and filter times $t_f \approx \tau_{\alpha,\text{trans}}$, see equation 5.20. The solid line indicates the purely heterogeneous scenario. Both functions use a binary weighting ($K_i(t,R) = 1$ if $|\vec{r}_i(t) - \vec{r}_i(0)| < R$ and $K_i(t,R) = 0$ if $|\vec{r}_i(t) - \vec{r}_i(0)| \geq R$), as it is not convenient to mix a binary filter with a smooth weighting of dynamics owing to the freedom of choosing R. Therefore, R was set to $(2\pi/24)$ nm, because then, $S_q(t)$ with $q = 22.7\ \text{nm}^{-1}$ and $S_{\text{bin}}(t)$ are virtually identical.

Concluding from the data shown in Figure 6.3, the three-time correlation function is located between the limiting cases. Thus, bulk water exhibits a mixed heterogeneous and homogeneous character. This statement is valid for different temperatures too, but not depicted.

6.3 Backward correlation and energy landscape

The homogeneous or backward contribution to the translational motion is further detailed by employing conditional probability functions (CPF) for the oxygen atoms [167].

The CPF as defined in equation (5.21) consists of two parts. The first part $\langle r_{1,i}(r_{01})\rangle$ gives the expected location of the particle after moving into a particular direction and by passing a distance r_{01} in the first time interval t_{01}. It is of paramount importance for the understanding of this quantity that the reference direction is always chosen parallel to the direction of movement in the first interval and the motion in the second interval is projected onto this vector, see the example of a particle in a harmonic potential below. The second part yields the averaged location of particles $\langle r_{2,i}\rangle$ at the end of the second time interval t_{12} which passed the distance r_{01} in the first interval. The difference

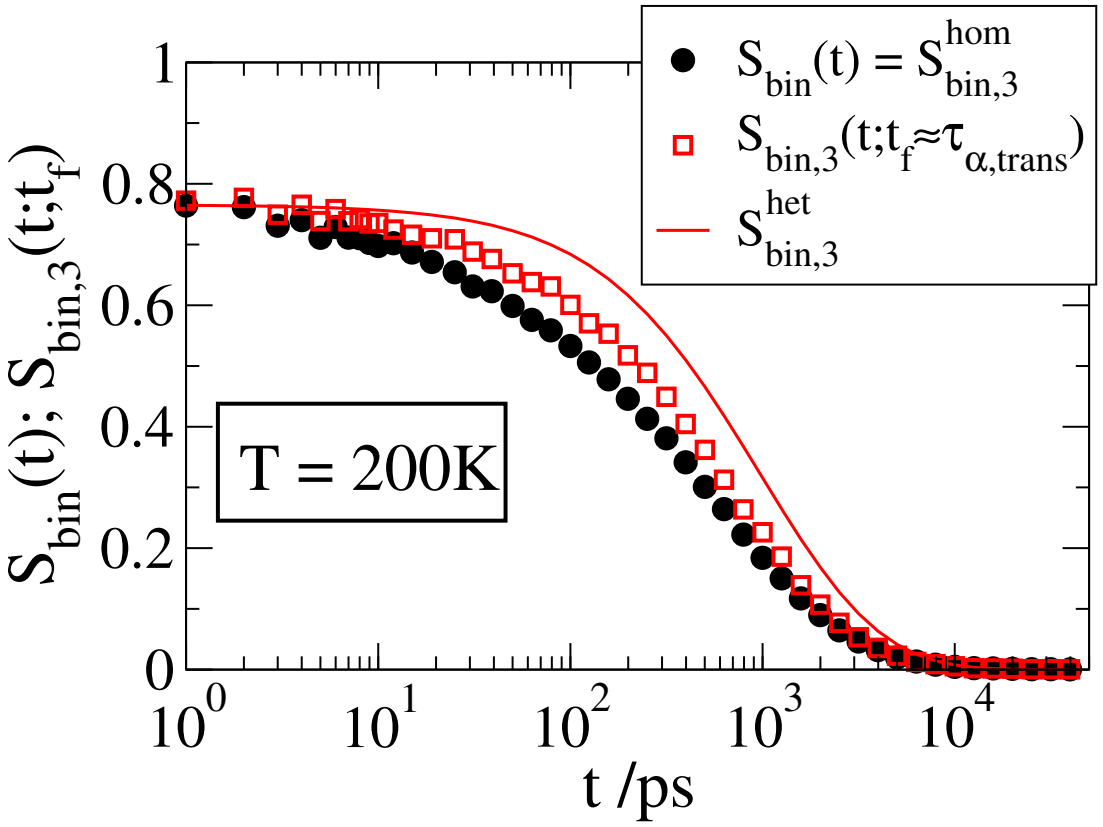

Figure 6.3: Two-time and three-time correlation functions for oxygen atoms (equation (5.20)). Both types of functions make use of a binary weighting of motion, see text for explanation why this is necessary. The filter time is $t_f \approx \tau_{\alpha,\text{trans}}$. The solid line indicates the purely heterogeneous case consistent with t_f, see equation (6.3).

between both parts $\langle R(r_{01})\rangle = \langle r_{2,i}\rangle - \langle r_{1,i}(r_{01})\rangle$ yields information on forward ($\langle R(r_{01})\rangle > 0$) or backward ($\langle R(r_{01})\rangle < 0$) correlations based on the underlying energy landscapes.

Before this concept is employed to investigate bulk dynamics, the simple one-dimensional example of a particle trapped in a harmonic potential $f(x) = -\kappa x$ will be scrutinized. This example gives intuitive insights into the meaning of the CPF, see [167].

The system is assumed to be equilibrated, thereby, the relevant motion is diffusion within the potential. Then, the average position of the particle is given as $\langle x\rangle = 0$ at the initial time. Now, the particle moves a distance r_{01}. There are two possible locations for the particle, $x(t_{01}) = -r_{01}$ and $x(t_{01}) = r_{01}$ and both have

equal probability. Hence, straightforward calculation yields $\langle r_{1,i}(r_{01})\rangle = 1/2 \cdot r_{01}$ for the probability to move in the particular direction the particle did. The second time interval is supposed to be very large, therefore, the average location of the particle at the end of the second interval is 0, thus, $\langle r_{2,i}\rangle = 0$. For the CPF, both contributions yield $\langle R(r_{01})\rangle = \langle r_{2,i}\rangle - \langle r_{1,i}(r_{01})\rangle = -1/2 \cdot r_{01}$. The negative value indicates backward correlation, as trivially expected for a particle which moves out of the equilibrium position and is then forced back towards the potential minimum.

Turning to the bulk, the panels of Figure 6.4 depict $\langle R(r_{01})\rangle$ for time intervals $t_{01} \approx \tau_{\alpha,\mathrm{trans}}$ and $t_{12} \approx n \cdot \tau_{\alpha,\mathrm{trans}}$ dependent on the distance r_{01} passed during the first time interval. For the left panel $t_{12} \approx 2 \cdot \tau_{\alpha,\mathrm{trans}}$ was chosen and the right panel shows the results for fixed temperature $T = 190$ K but various time intervals t_{12}. Dashed lines indicate the long-time limit for a particle trapped in a harmonic potential, see the example above. It is evident that the values $\langle R(r_{01})\rangle$ are strictly negative, yielding backward correlation. They initially decrease according to the harmonic expectation, regardless of temperature [28]. Thus, pertaining to the two-step decay, the statement of molecules being trapped in cages is corroborated as particles always probe a local effective harmonic potential. This will be very important with respect to the ECNLE approach, which is used to describe dynamics in chapter 8.4.

For high temperatures and at distances $r_{01} > 0.2$ nm, $\langle R(r_{01})\rangle$ seems to level off whereas for low temperatures it increases. The deviation from the harmonic expectation at larger distances is due to the crossing of finite energy barriers. Molecules which crossed the barrier arrive at a new position which is again a local minimum. Therefore, the constant values of $\langle R(r_{01})\rangle$ at high temperatures reveal that *all* sufficiently large steps during the first time interval lead to new minima and $\langle r_{2,i}\rangle$ averages out during the second time interval. This means that there is no static energy landscape on time scales $t_{01} \approx \tau_{\alpha,\mathrm{trans}}$ and $t_{12} \approx 2 \cdot \tau_{\alpha,\mathrm{trans}}$. The opposite is true at lower temperatures as $\langle R(r_{01})\rangle$ increases at $r_{01} > 0.2$ nm. Presumably, $\langle r_{2,i}\rangle$ increases with decreasing temperature due to the presence of a static energy landscape for fast molecules[29]. This is sys-

[28] Here, the values for $\langle R(r_{01})\rangle$ usually never rise to 0 when there is a sufficiently well defined initial minimum. $\langle R(r_{01})\rangle = 0$ is obtained only for finite barrier heights and if considering very long times t_{01} and t_{12}, because then particles do not recall the initial minimum and thus, $\langle r_{1,i}(r_{01})\rangle = 0$ as well as $\langle r_{2,i}\rangle = 0$. In contrast to that, forward correlations can be obtained for instance in cases of very rigid static energy landscapes with different minima and finite barriers [167].

[29] The fact that the curve for $T = 270$ K is located in between the curves for $T = 260$ K and $T = 230$ K is owing to the discrete time step times the output rate and not to an increased $\langle r_{2,i}\rangle$. The correlation times are obtained by interpolation of the incoherent intermediate

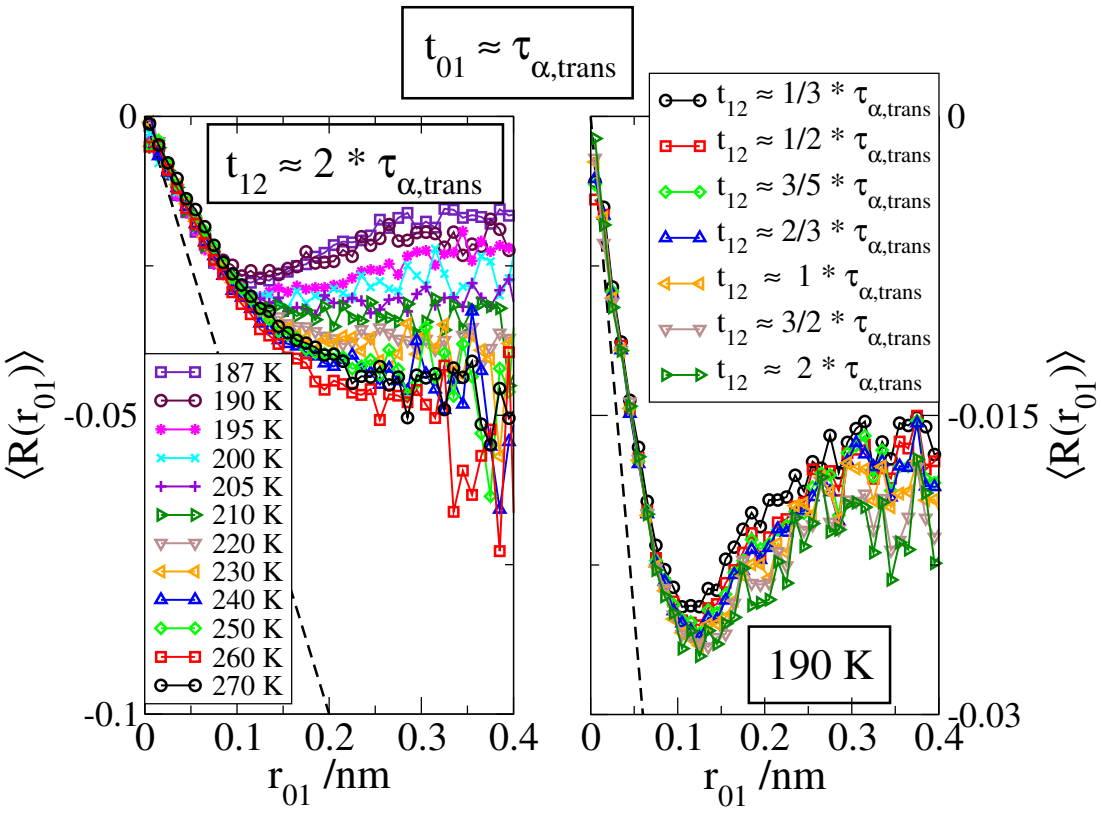

Figure 6.4: Conditional probability function for oxygen atoms of bulk water. The left panel shows $\langle R(r_{01})\rangle$ with $t_{01} \approx \tau_{\alpha,\text{trans}}$ and $t_{12} \approx 2 \cdot \tau_{\alpha,\text{trans}}$ for various temperatures. The panel on the right exhibits data at a temperature of 190 K with $t_{01} \approx \tau_{\alpha,\text{trans}}$ but for various time intervals $t_{12} \approx n \cdot \tau_{\alpha,\text{trans}}$. In both panels, dashed lines denote the prediction for motion within a harmonic potential.

tematically investigated by changing the second time interval t_{12} at $T = 190$ K, see the panel on the right hand side of Figure 6.4. For a small time interval t_{12}, $\langle R(r_{01})\rangle$ is large. With rising t_{12}, $\langle R(r_{01})\rangle$ decreases. This means that fast molecules arrive at a well defined minimum and explore it during the second time interval. Upon increasing of t_{12} the entire energy landscape changes due to motion of slower particles and therefore $\langle r_{2,i}\rangle$ tends to small values and eventually to zero yielding the plateau for $\langle R(r_{01})\rangle$ discussed for high temperatures. Therefore, using the same relative time scales $t_{01} \approx \tau_{\alpha,\text{trans}}$ and $t_{12} \approx 2 \cdot \tau_{\alpha,\text{trans}}$ reveals that the extent of changing the energy landscape is not identical. The time scale of the relaxation of the energy landscape seems to decorrelate from

scattering function to the point in time when it decreased to $1/e$ yielding decimal digits. The resulting deviations are largest at high temperatures and very small correlation times compared to the output rate.

$\tau_{\alpha,\text{trans}}$, what might give a first hint on collective behavior.

6.4 Heterogeneous contribution

The heterogeneous contribution to the data shown in Figure 6.3 is investigated using a real space picture of dynamics. Therefore, the backward Fourier-transformed $\mathfrak{F}\left\{S_q(t)\right\} = G(r,t)$ the so-called van Hove correlation function (VHF) is studied for the oxygen atoms. Results are depicted in Figure 6.5 for an evolution time $t \approx \tau_{\alpha,\text{trans}}$.

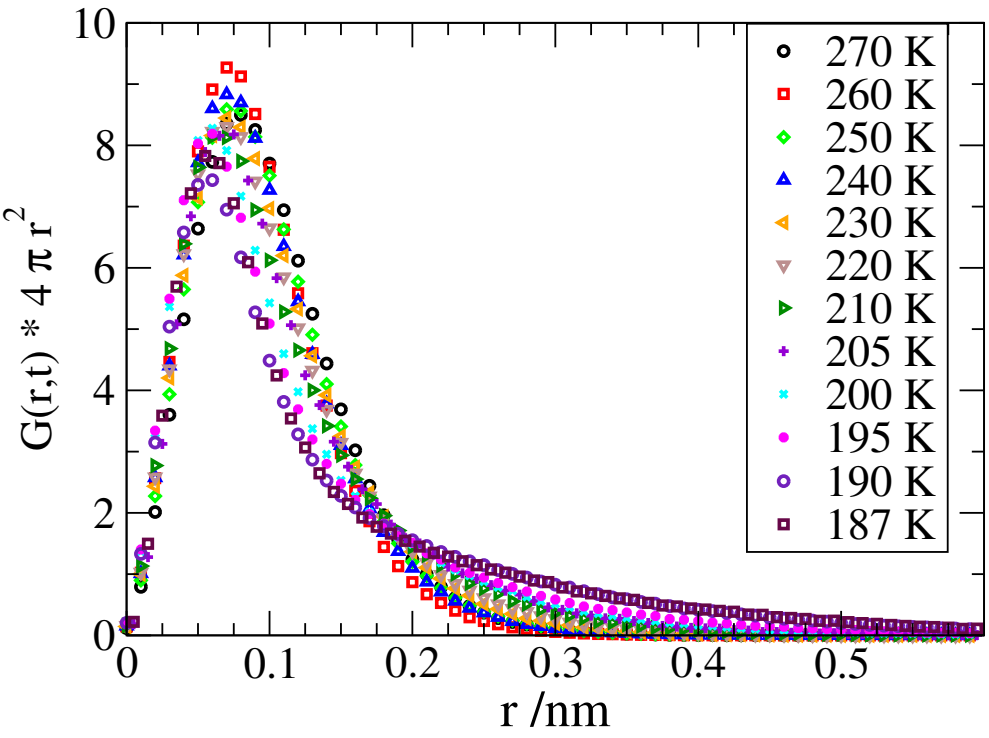

Figure 6.5: Self-part of the van Hove correlation function for oxygen atoms of bulk water at various temperatures. The time interval for detecting dynamics is set to $t \approx \tau_{\alpha,\text{trans}}$.

At high temperatures, a distribution with a peak at $r \approx 0.1$ nm is observed [25, 51, 87]. Lowering temperature results in a more stretched distribution as the peak shifts towards smaller displacements and narrows, and additionally, skewness and curtosis increase. In the limit of BM (high temperatures or very long evolution times) the distribution of particle displacements is Gaussian-shaped, cf. equations (2.13) or (2.16), with an additional weighting factor $4\pi \cdot r^2$ for considering the modulus of the displacements in three dimensions

[25, 51].

It has been shown in chapter 6.2 that there is a heterogeneous contribution to translational motion[30]. Therefore, the terms fast or slow have a true meaning. Hence, one can conclude that at low temperatures, the pronounced skewness is due to a considerable fraction of very fast particles as previously described for SPC/E by *Sciortino* [25]. A static energy landscape with well defined minima and barriers would imprint further peaks on the distribution similar to a hopping process with given jump length [89]. Such behavior is not observed for the bulk regardless of the chosen evolution time. Thus, CPF seem to be more sensitive and suitable to investigate energy landscapes than VHF.

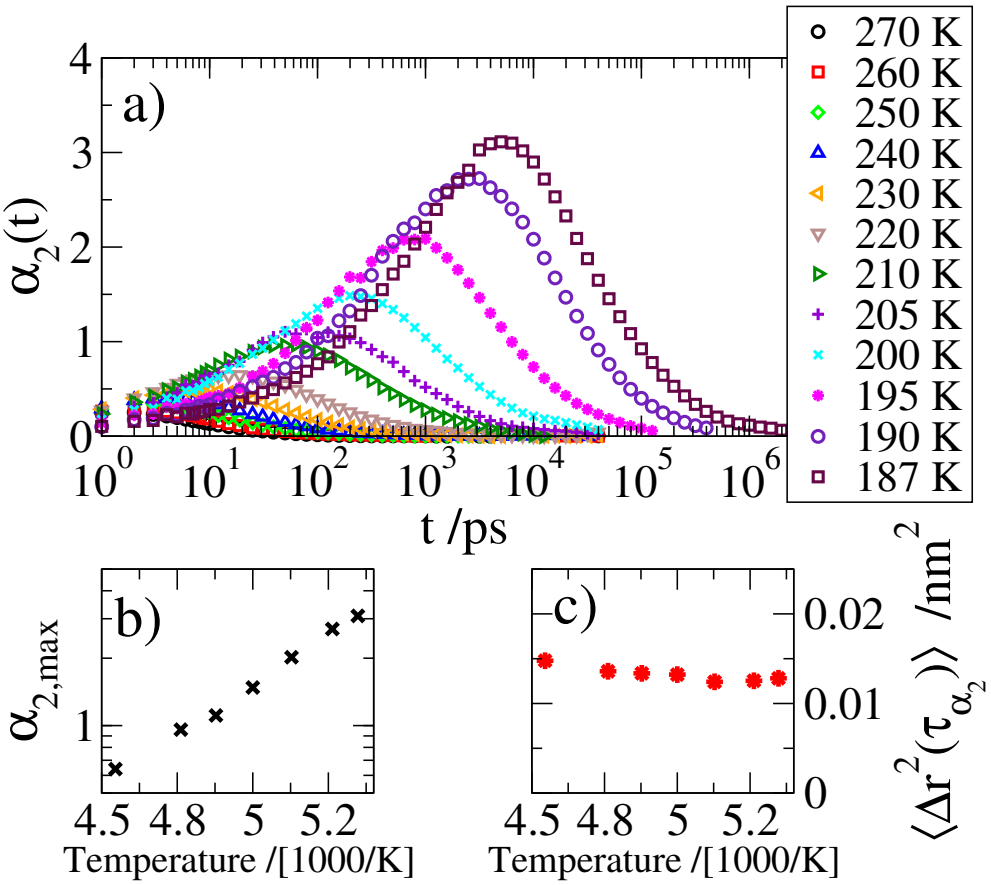

Figure 6.6: a) Non-Gaussian parameter $\alpha_2(t)$ for oxygen atoms. The parameter probes the deviation from an ideal Gaussian-shaped distribution of displacements. b) shows peak values of α_2 for temperatures ranging from $T = 240$ K to 187 K. c) depicts the mean square displacement at time τ_{α_2}, when α_2 is a maximum.

[30] This is valid for rotational motion too, but not shown.

In order to measure the deviations of the VHF from the ideal Gaussian-shaped behavior, the so-called classic non-Gaussian parameter (NGP), α_2 is commonly used [25, 51, 87, 168], cf. equation (5.10)[31]. Figure 6.6 a) shows the results for the displacements of oxygen atoms as a function of time. A perfectly Gaussian-shaped distribution of displacements yields $\alpha_2 = 0$. It is striking that the results can be parted into the three regimes illustrated in Figure 2.4. The NGP is small for time intervals $t \approx 1$ ps corresponding to vibrational motion. In the intermediate or subdiffusive regime $\alpha_2(t)$ exhibits a distinct peak, at least at low temperatures, and in the diffusive regime α_2 is 0 again. This behavior is usually observed for supercooled liquids and especially for SPC/E [25, 59, 87]. Further, the peak height is an increasing function of temperature, illustrated in panel b). This can be rationalized with the VHF, see Figure 6.6. The lower the temperature, the more narrow is the peak at ≈ 0.1 nm. Hence, the contrast between particles leaving their local cage and particles still trapped becomes larger, and leads to strong deviations from Gaussian motion. Panel c) depicts the value of the MSD for the time τ_{α_2} when $\alpha_2(t)$ is a maximum as function of inverse temperature. The time τ_{α_2} is often referred to as the time of maximum heterogeneity of the system [169]. It is located in the so-called late-β or early-α regime [25, 59][32]. In terms of an initial non-equilibrium mean free-energy landscape, like in Figure 2.6, where all particles have to overcome the same barrier, the values for the MSD at time τ_{α_2} can be thought of as the point of maximum restoring force [87]. This is shown in Figure 6.6 c), supporting the previous statement that particles are trapped in very local potentials.

Above, the increasing peak height of α_2 was related to the more distinct contrast between particles, which are still caged and those, which have already escaped at lower temperatures. In fact, appraising the increasing peak height while lowering the temperature in more detail is a difficult task, because the NGP strongly weights the fast particles due to the $\langle r^4 \rangle$ term. Therefore, it is necessary to investigate the mechanisms for fast dynamics. This is related to the key feature of supercooled liquids to have no random distribution of highly mobile particles over the system, but rather a clustering of fast and slow particles, see chapter 2.2 [56, 172, 173].

[31] In fact there are several non-Gaussian parameters $\alpha_n(t)$, see *Sciortino* [25] and the so-called new non-Gaussian parameter $\gamma(t)$ introduced by *Flenner* [59].

[32] Here and in the cited literature β regime denotes the time regime ranging from the beginning of the plateau in correlation functions due to the two-step decay and leaving the plateau with the onset of relaxation processes, according to the mode-coupling theory [72, 170, 171].

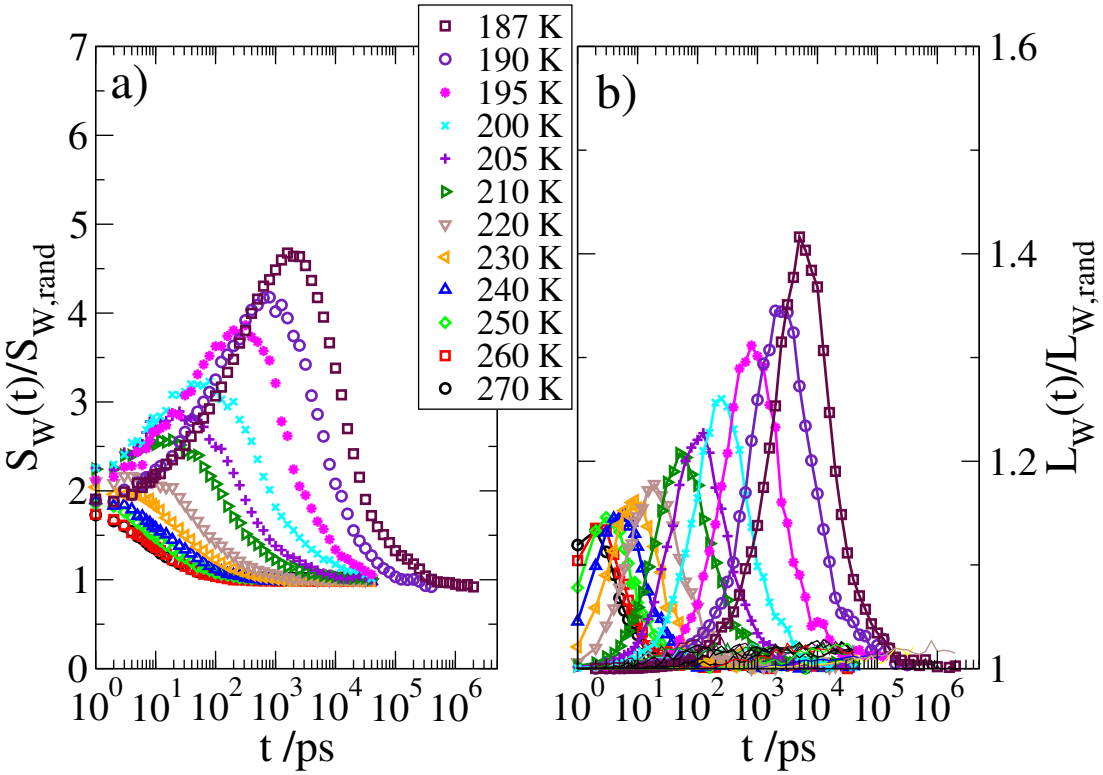

Figure 6.7: The motion of the 5% oxygen atoms with the largest displacements was analyzed. a) Weight-averaged cluster size $S_W(t)$ for various temperatures. b) Weight-averaged string size $L_W(t)$ for various temperatures. In both cases the data were normalized by a randomly chosen ensemble of oxygen atoms of equal size (5% out of all oxygen atoms).

Figure 6.7 illustrates weight-averaged cluster sizes for the 5% fastest oxygen atoms. The data were normalized by the weight-averaged cluster size for a randomly chosen subset of oxygen atoms of equal size (5% out of all oxygen atoms) in order to account for *statistical* clusters. In panel a) data for the weight-averaged cluster size $S_W(t)$, see equation (5.22) is shown. In essence, the time interval t is used to select a subensemble of particles, highly mobile oxygen atoms (45 atoms out of 895), and then clusters are determined based on the spatial distribution of this subensemble at the initial time, see equation (5.23) for the condition of belonging to a cluster. Hence, changing the time interval only alters the subensemble for which clusters are ascertained. The increasing peak height indicates that water dynamics becomes increasingly spatially heterogeneous when lowering the temperature.

The weight-averaged string size $L_W(t)$, see equation (5.24), is obtained in a

similar way as only the 5% (45 atoms out of 895) most mobile oxygen atoms are considered. However, rather than determining a cluster based on the initial distribution of particles, only particles moving in a string-like way, see equation (5.25), are considered. Similar to $S_{\mathrm{W}}(t)$, the peak height of $L_{\mathrm{W}}(t)$ rises. Hence string-like cooperative motion becomes more important for the motion of fast water molecules upon cooling.

It is evident that $S_W(t)$ and $L_W(t)$ show a behavior similar to that of the NGP, in accordance with several reports [50, 51, 168]. As stated above, quantities like $\alpha_2(t)$ are thought to be related to dynamic heterogeneity [174]. However, α_2 takes into account motion on all length scales and it is dominated by the fast particles. Therefore, it is not permissible to draw the conclusion that increasing peaks of α_2 are ultimately due to rising heterogeneity of the structural relaxation of the system, as different markers of heterogeneity, for instance the previously mentioned stretching parameters $\beta_{\mathrm{KWW}}(T)$, seem to level off at low temperatures rather than declining further, see Figure 6.8 [58].

In conclusion, spatially heterogeneous dynamics is found for the motion of oxygen atoms of SPC/E. This was also reported for different water models like the TIP5P or ST2 models [175, 176] and can be considered as one of the most intriguing findings for supercooled liquids in general, see chapter 2.2. In chapter 8.4, an approach will be used which presumably answers the questions about the importance of SHD for vitrification and about the origin of SHD in water. As the presented results are typical for several supercooled liquids, this immediately implies that the approach in chapter 8.4 might be of significant relevance for the entire research on supercooled liquids and not only for SPC/E.

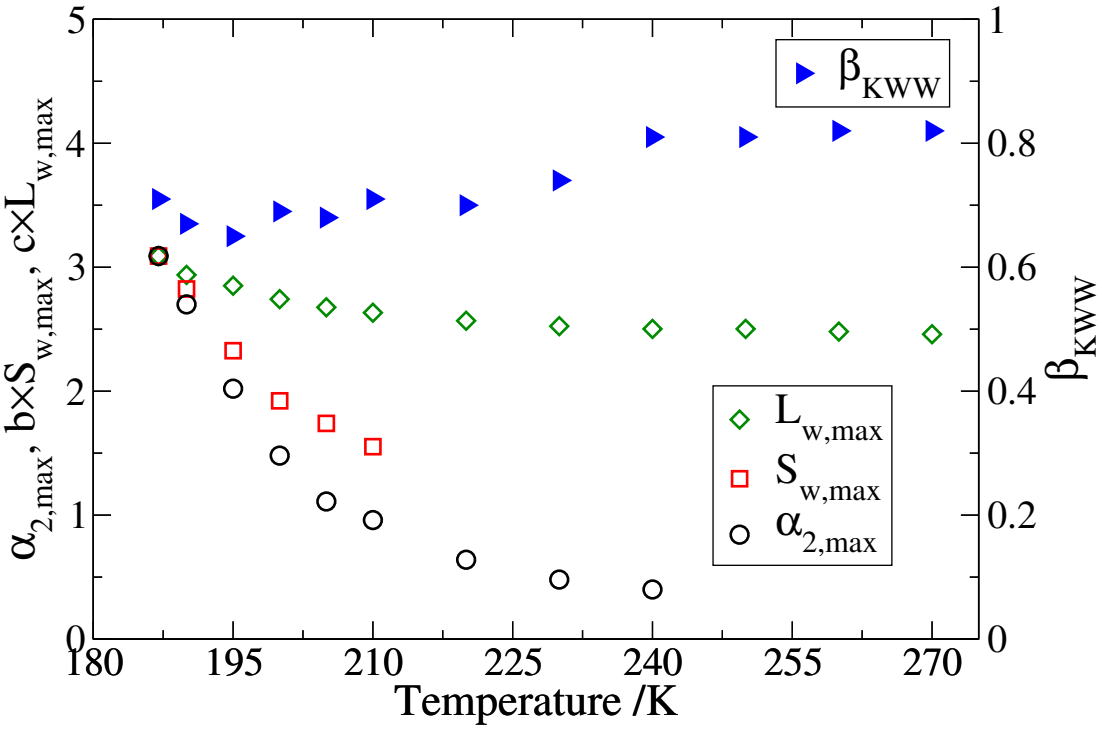

Figure 6.8: Maximum of $\alpha_2(t)$, $S_w(t)$ and $L_w(t)$ on the left y-axis compared with β_{KWW} on the right-hand side as functions of temperature. By way of comparison, $S_w(t)$ and $L_w(t)$ are scaled with constants b and c to the point defined by $\alpha_{2,\text{max}}$ at $T = 187$ K.

6.5 Time scales and correlation lengths

It was already shown that time scales are important for investigating properties of supercooled liquids. For very long times, BM is recovered, hence, it is again emphasized that the focus of the present work is on intermediate time scales characterized by τ_α obtained from correlation functions using the condition $C(\tau) = 1/e$. The first part of this subsection is meant to elucidate the relevance of that particular condition.

The idea is that until τ_α supercooled liquids look similar to systems with quenched disorder, but the disorder is self-induced [177]. Therefore, the structural relaxation process may be imagined as similar to a dynamical phase transition [177]. In terms of fluctuations, it is expected that in the case of a real dynamical phase transition the fluctuations of a quantity related to density fluctuations should diverge [177]. A possible choice to probe fluctuations is the variance of the incoherent intermediate scattering function $S_q(t)$ given by χ_4, cf. equation (5.18). Figure 6.9 a) illustrates the response function $\chi_4(t)$ as

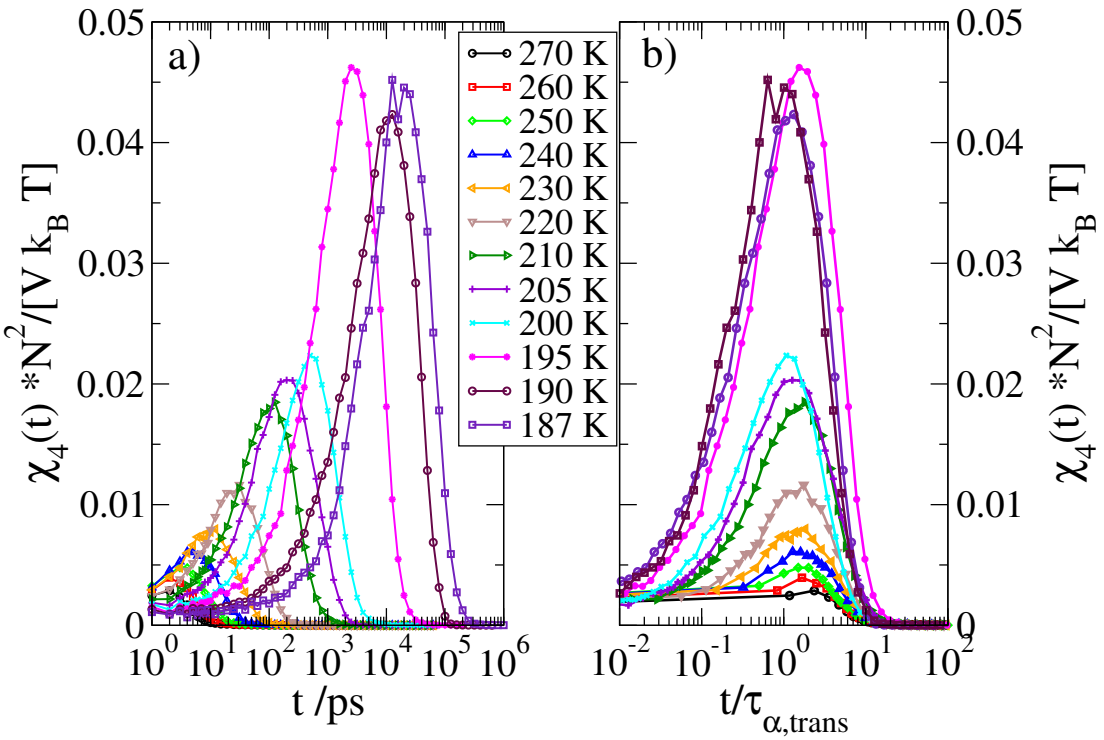

Figure 6.9: Panel a) depicts $\chi_4(t)$ for oxygen atoms with a chosen length scale $q = 22.7\ \mathrm{nm}^{-1}$. Panel b) shows the same data like panel a) but the x-axis was scaled with $\tau_{\alpha,\mathrm{trans}}$.

a function of the time interval t for the translational motion of oxygen atoms

probed on a length scale $q = 22.7\,\mathrm{nm}^{-1}$. Panel b) shows the same data for a time axis scaled with $\tau_{\alpha,\mathrm{trans}}$. The curves rise with increasing time interval up to a single peak and then decline to zero. This is expected as there exists no real phase transition and hence the divergence is avoided. As the temperature is lowered the peaks increase and except for the curve for $T = 195$ K this behavior appears to be strictly monotonic. The reason for the non-monotonic peak heights, obtained below $T = 200$ K is not clear, but increasing or reducing the number of averages to obtain the curves shows that χ_4 is highly sensitive to the number of averages. The trajectory length in units of $t/\tau_{\alpha,\mathrm{trans}}$ is probably not sufficient for $T = 195$ K, but in fact, a physical origin can not be ruled out. Recent research on theories like the MCT revealed that a diverging peak height is predicted at a specific temperature T_c [75]. This is directly related to the discussed RFOT transition. In real systems the divergence is assumed to smear out due to finite dimensions and activated events, not captured by the mean-field-like theory, dominating the relaxation process at lower temperatures [18, 27, 70]. The temperature $T = 195$ K is near the proposed transition temperature for SPC/E at $T_c \approx 200$ K [49]. However, this is the only finding supporting the MCT transition idea and is therefore more likely related to averaging.

Panel b) shows that the peaks for all temperatures occur roughly at the same time $t \approx \tau_{\alpha,\mathrm{trans}}$, therefore the ad hoc definition $C(\tau) = 1/e$ is indeed appropriate to capture the time scale of a relaxation process on a given length scale q.

Without employing any theory and simply based on the definition of χ_4, the rising peak heights upon cooling are usually attributed to an increasing dynamical correlation of particles, specified by a correlation length, and thus giving a measure for spatially heterogeneous dynamics (SHD). But as pointed out by *Berthier*, great care must be taken to draw this conclusion [61, 62]. Rather than governed by growing correlations also growing local fluctuations can yield rising peak heights. In chapter 8 further approaches to obtain correlation lengths are used.

An interesting issue, first tackled by *Bormuth* and *Henritzi*, is how the time scales of heterogeneity as probed by α_2, L_W, S_W and χ_4 compare [57, 58]. In order to address this, the times, when the respective functions which probe heterogeneity of oxygen dynamics are at maximum, are plotted as function of $\tau_{\alpha,\mathrm{trans}}$, obtained from $S_q(t)$ for oxygen atoms on next-neighbor length scales ($q = 22.7\,\mathrm{nm}^{-1}$). This is depicted in Figure 6.10 a). A power-law dependence is found for SPC/E in agreement with the results for an abundance of glass-forming liquids [57, 58]. The continuous lines are power laws $\tau_i = \tau_i \propto \tau_{\alpha,\mathrm{trans}}^{\gamma}$ and they describe the data well. This result is called *hyperscaling* [57, 58]. The

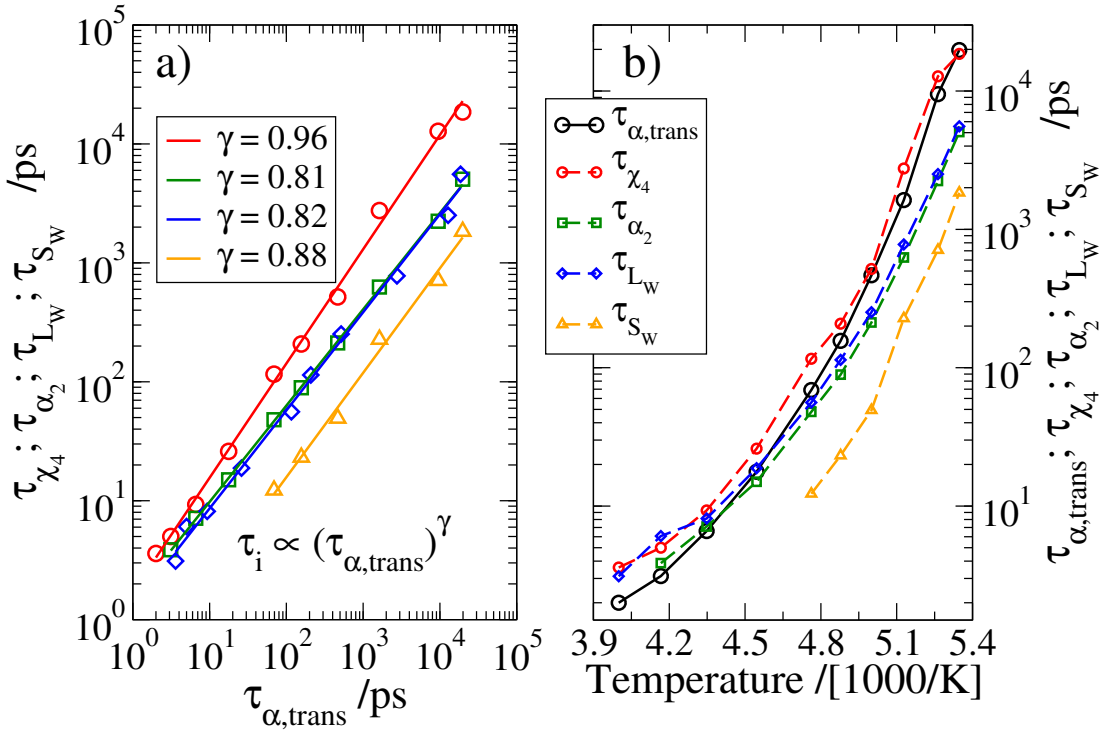

Figure 6.10: Panel a) depicts τ_{α_2}, τ_{L_W}, τ_{S_W} and χ_4 defined by the time when α_2, L_W, S_W and χ_4 for oxygen atoms and in case of χ_4 with a chosen length scale $q = 22.7$ nm^{-1}, is at maximum as a function of $\tau_{\alpha,\text{trans}}$ obtained from the incoherent intermediate scattering function for oxygen atoms using $q = 22.7$ nm^{-1}. Panel b) shows the same data like panel a) but plotted against the inverse temperature. The continuous lines in panel a) are functions according to $\tau_i \propto \tau^{\gamma}_{\alpha,\text{trans}}$. The dashed lines in panel b) are guides for the eye.

value of γ characterizes to what extent the translational correlation time and the time scales of heterogeneity spread when lowering the temperature. The exponent γ is largest for χ_4 and lowest for α_2 meaning that τ_{χ_4} almost scales like $\tau_{\alpha,\text{trans}}$ as was qualitatively shown in Figure 6.9 b), whereas L_W, S_W and α_2 decorrelate from $\tau_{\alpha,\text{trans}}$. Panel b) of Figure 6.10 illustrates the various time scales as function of the inverse temperature and underlines the previous statement. Additionally, it is evident that the difference between τ_{α_2} and τ_{L_W} is very small, further supporting the results of the last subsection that fast molecules and string-like motion, given the small amplitude of L_W in Figure 6.7 at least to some extent, are responsible for the non-Gaussian behavior at intermediate times, consistent with results by *Bormuth* [57]. The hyperscaling behavior will be elucidated using the ECNLE approach, see chapter 8.4.3.

6.6 Stokes-Einstein breakdown

In the previous subsections spatially heterogeneous dynamics (SHD) were investigated. A putative consequence of this heterogeneity is the so-called breakdown of the Stokes-Einstein law [178]. The Stokes-Einstein law relates the self-diffusion constant D, with the shear viscosity η, reading

$$D \cdot \frac{\eta}{k_\mathrm{B} T} = C \tag{6.4}$$

[86, 178, 179]. It is very difficult to directly probe the shear viscosity in MD simulations, thus usually the correlation time $\tau_{\alpha,\mathrm{trans}}$ is applied. For this work, the modification is done by the substitution $\tau_{\alpha,\mathrm{trans}} \propto \frac{\eta}{k_\mathrm{B} T}$, yielding the BM result, see the text explaining equation (2.16).

It was argued that the breakdown can be understood in terms of a distribution of correlation times [86, 180], which is related to a distribution of activation energies. The hopping diffusion over the barriers is governed by the rate average $\langle \tau^{-1} \rangle$, whereas $\tau_{\alpha,\mathrm{trans}}$ is determined by the mean escape time $\langle \tau \rangle$. If there is only one correlation time, and hence, a single activation energy like in the case of BM, or if there is a distribution of correlation times and upon cooling the distribution is only shifted, then $\langle \tau^{-1} \rangle \langle \tau \rangle = \mathrm{const}$. However, usually a so-called fractional Stokes-Einstein relation is found for supercooled liquids [58, 179],

$$D \cdot \tau_{\alpha,\mathrm{trans}}^{\theta} = C. \tag{6.5}$$

Figure 6.11 shows the diffusion constant as function of $\tau_{\alpha,\mathrm{trans}}$ and $\tau_{\alpha,\mathrm{trans}}/T$. The breakdown is characterized by the exponent $\theta \neq 1$. In earlier studies on SPC/E and on various other supercooled liquids a different replacement $\tau_{\alpha,\mathrm{trans}} \propto \eta$ was used, thus, in those cases $\tau_{\alpha,\mathrm{trans}}/T$ was investigated and is therefore also included in the Figure, revealing no substantial difference for θ [58, 179].

The results suggest a continuing broadening of an underlying distribution of correlation times, because even if there were a constant distribution of activation energies, the correlation times distribution would broaden upon cooling. This further supports the idea that the NGP peak times, also decorrelating from $\tau_{\alpha,\mathrm{trans}}$ like the diffusion constant, are a measure for the roughly 5% to 10% fastest molecules. In chapter 8, a possibility to obtain a distribution of effective activation energies is demonstrated and the breakdown of the Stokes-Einstein law is revisited.

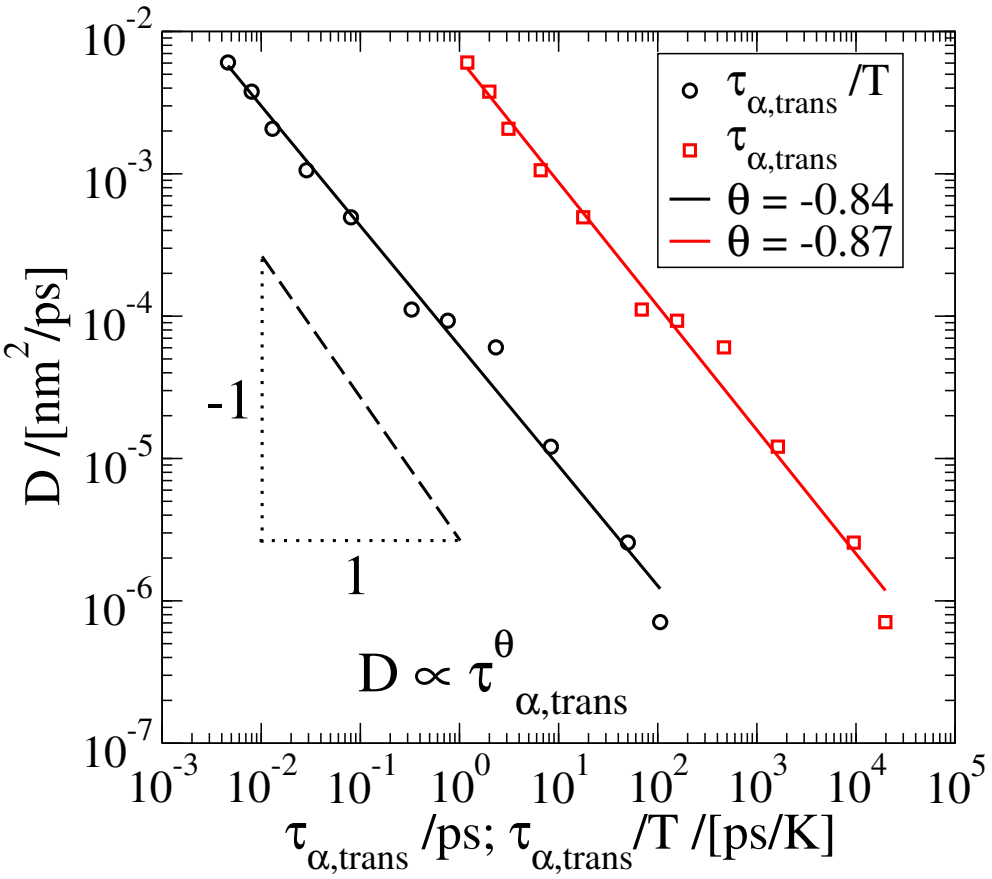

Figure 6.11: Diffusion constant D as function of $\tau_{\alpha,\text{trans}}$ and $\tau_{\alpha,\text{trans}}/T$. The solid lines are fits according to $D \cdot \tau^{\theta}_{\alpha,\text{trans}} = C$

6.7 Conclusion for the bulk system

The first part focused on structure, therefore, hydrogen bonds and tetrahedral order were examined. Also the question about a possible phase transition from HDL to LDL, detailed in chapter 2.7, was addressed, but no evidence for the transition was observed. It is highlighted that no HDL to LDL transition is expected for SPC/E in the investigated temperature range and pressure [111]. However, at increased density, $\approx 10\%$ to the density of the examined bulk system, the transition for SPC/E is predicted to occur at roughly 220 K. Hence, it is interesting to scrutinize the origin of a claimed phase transition behavior for SPC/E in silica pores [17] at almost the same temperature, $T = 220$ K, but at a density of ≈ 1 g/cm^3, which is virtually identical to the density of the presented bulk system. As no transition was found for the bulk, one can speculate that confining water might increase the HDL to LDL transition temperature. Settling this issue is one of the main motivations of the present study, therefore, structure and dynamics of SPC/E in these confinements will be thoroughly examined and a different explanation for the claimed HDL to LDL transition will be given, see chapter 7. It is stated that the results related to the HDL to LDL phase transition depend on the explicit water model. For example, it was claimed that the TIP5P water model exhibits indications for crossing the Widom line at roughly 250 K ($p = 1$ bar) [159].

Next, dynamics was investigated. The goal of this part was to introduce some important aspects. First, the emerging two-step decay was attributed to local caging effects signaling the entering of the supercooled regime. Therefore, on short times and sufficiently low temperatures, particles are caged in local potentials. The entire analyses of chapter 8.4 will make use of this finding.

Second, the stretched-exponential decay was discussed referring to the concepts of homogeneous and heterogeneous motion. Three-time correlations illustrated a mixed homogeneous/heterogeneous character for the motion of oxygen atoms on next-neighbor length scales. In order to disentangle both contributions, CPFs were employed and indicated backward correlations and the presence of a fluctuating energy landscape. The concept of energy landscapes will be crucial to understand some of the main findings for SPC/E in confinements, like Cole-Cole relaxation patterns.

Third, the heterogeneous part was investigated by studying the non-Gaussian parameter (NGP) and cluster and string related quantities for fast particles. The NGP strongly suggested, in terms of BM, the presence of an anomalous large amount of fast motion and together with the cluster and string analyses the pic-

ture of spatially heterogeneous dynamics was established. This concept will be important as the investigated confinement systems show an imposed dynamic heterogeneity.

Fourth, the relevance of correlation times, obtained by the definition $C(\tau) = 1/e$, was demonstrated by examination of χ_4. This measure also yielded a first hint for a growing cooperative length scale. The discussed theories, RFOT and ECNLE, make use of length scales. One of the main new scientific results will be the analysis of those proposed length scales, in particular the elastic length scale, using the neutral confinement systems, see chapter 8.

Fifth, the breakdown of the Stokes-Einstein law gave hints for a broadening distribution of correlation times, also supporting the idea that the NGP is basically sensitive to the motion of the fastest molecules, what explains the decorrelation of associated time scales τ_{α_2}, τ_{L_W}, τ_{S_W} from $\tau_{\alpha,\text{trans}}$. In chapter 8.4, distributions of effective energy barriers will be obtained and directly used to calculate the decorrelation coefficient of the fractional Stokes-Einstein relation.

So far, diverse dynamical properties of supercooled liquids and SPC/E have been discussed. The question of how all these properties are related and especially, what drives fragile behavior is addressed in chapter 8. There, a new approach the ECNLE theory will be used to describe many results which were discussed in this chapter. Using the approach from chapter 8.4 to explain the findings from the bulk is presumably appropriate for various other supercooled liquids, as the presented results are in agreement with previous studies on supercooled water [25, 51, 111], and are typical for various other supercooled liquids [58]. Therefore, the following chapters might be of general importance for the understanding of supercooled liquids, and not only for SPC/E.

7 Water in silica confinements

This chapter deals with SPC/E in silica confinements. The motivation for this is rooted in the approaches of experimentalists to proof or disproof theories, which attempt to explain the anomalies of water, see chapter 2.7. For this purpose, water in confinements is used to enter the discussed *No man's land*. Results have been partially published [148, 181] or submitted for publication [182].

7.1 Structure

As pointed out in chapter Systems, three pore fillings for the small silica pore (SSP) are used. Figure 7.1 depicts the density distribution as function of the distance $(x^2 + y^2)^{1/2}$ from the pore axis (z is the symmetry axis of the pores).

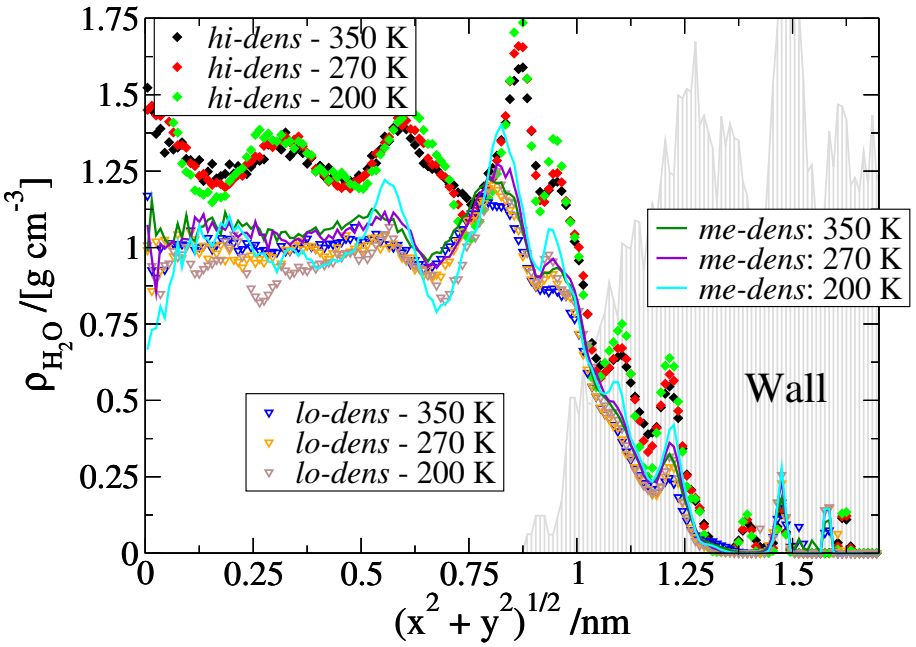

Figure 7.1: Density distribution of water in the small silica pore. The distance from the center of the pore is plotted on the horizontal axis (symmetry axis points in z-direction). Three different pore fillings are compared. The gray area illustrates the wall and is arbitrarily scaled to fit the density regime of water.

The pore wall is marked by the gray area. As observable in Figure 7.1, the densities for the pore fillings are: high density (*hi-dens*) ≈ 1.3 g/cm^3, medium

density (*me-dens*) $\approx$ 1.1 g/cm^3, and low density (*lo-dens*) $\approx$ 1.0 g/cm^3. For the high-density system (*hi-dens*) the density and layering effects are largest. Here, the layering appears to be almost independent of temperature. There is a pronounced peak located near the pore surface at $(x^2+y^2)^{1/2} \approx 0.87$ nm. The medium-density and low-density fillings (*me-dens* and *lo-dens*) exhibit layering too, with a distinctive peak at $(x^2+y^2)^{1/2} \approx 0.82$ nm, but only surface water seems to be affected at high temperatures. Lowering the temperature yields more distinct peaks. The peak pattern for the latter systems is shifted to smaller values, suggesting a lower pressure for these systems compared to the high-density one. The results agree with previous MD studies on confined water [17, 183].

Compared with the average density, the most prominent peak is about $\approx$ 30% higher for the *hi-dens* system and about $\approx$ 25 % for the other pore fillings. Further, water molecules appear to penetrate into the wall, which is illustrated by the gray area (the density was scaled and a running average was performed to smooth the curve), regardless of temperature or pore filling. This behavior can be also attributed to a rough pore surface, which is investigated below, but before, water in the large silica pore (LSP) will be characterized.

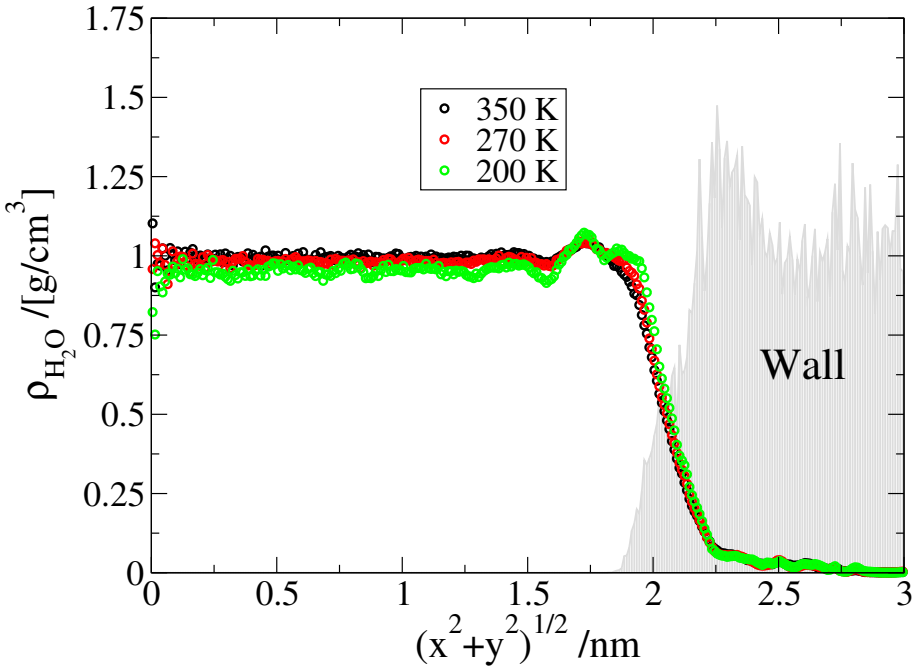

Figure 7.2: Density distribution of water in the large silica pore. The distance from the center of the pore is plotted on the horizontal axis (symmetry axis of the pores points in z-direction). The gray area illustrates the wall and is arbitrarily scaled to fit the density regime of water.

For the large silica pore (LSP), the findings are similar to that for the small pore, see Figure 7.2. However, the main peak is less distinct than in the small pore for comparable density at the pore center and the density distribution indicates weaker layering near the wall surface with density variations of about 10%. Presumably, this is owing to the larger curvature of the SSP wall and the slightly larger number of silanols per area ($\approx 2-3$ for the LSP compared with ≈ 3 for the SSP). Even given the same amount of silanols per surface area, a water molecule near a bended wall has a larger surface area accessible than near a plane wall, effectively increasing the hydrophilicity. A second peak closer to the wall than the first one emerges upon lowering the temperature, also observed for the small silica pore. Concurrently to the appearance of this second peak, the overall density farther away from the surface slightly decreases.

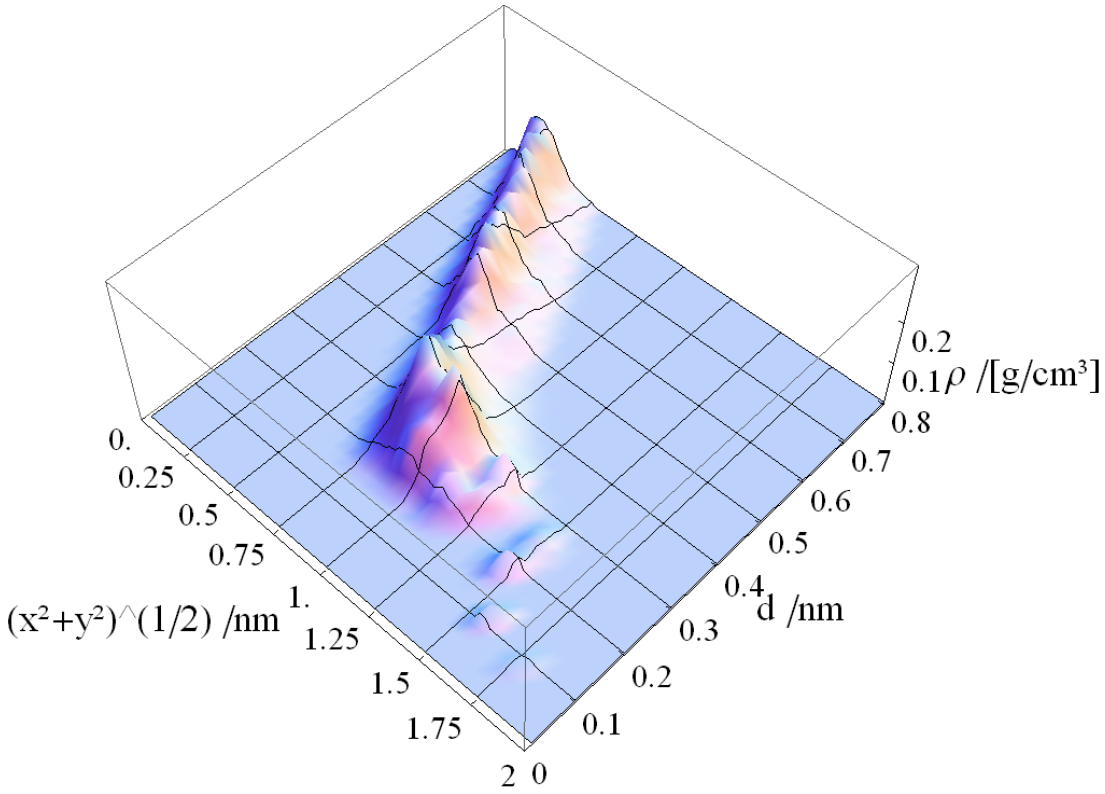

Figure 7.3: Density distribution of water in the small silica pore with the *lo-dens* filling at 240 K. Plotted are the distance from the pore axis, the distance d to the pore wall and the density.

Like for the small pores, some molecules penetrate the wall, which is indicated by the gray area. The large amount of water, which appears to intrude

the pore-surface area, suggests a rough pore surface for the small silica pore and for the large silica pore. This is examined in Figure 7.3 for the *lo-dens* system of the SSP, but is valid for different fillings and the larger pore, too. The plot shows the distance from the pore axis, the density and the distance d to the wall atoms. A perfectly smooth surface would yield a simple linear mapping of $(x^2 + y^2)^{1/2}$ onto d. This is obviously not the case as for instance the value $d = 0.3$ nm can be assigned to a broad distribution of $(x^2 + y^2)^{1/2}$. In order to account for the roughness, the following analyses are based on the distance d to the pore wall, see also the prelude of chapter 5 for details.

Owing to the density fluctuations inside the silica pores, the question arises how the local structure is affected. To address this, the tetrahedral order parameter or the number of HB can be used. Figure 7.4 a) depicts the tetrahedral order-parameter distribution for the *lo-dens* system at 230 K. Water molecules in the immediate vicinity ($d = 0.225$ nm) and at some distance from the wall ($d = 0.525$ nm) are investigated.

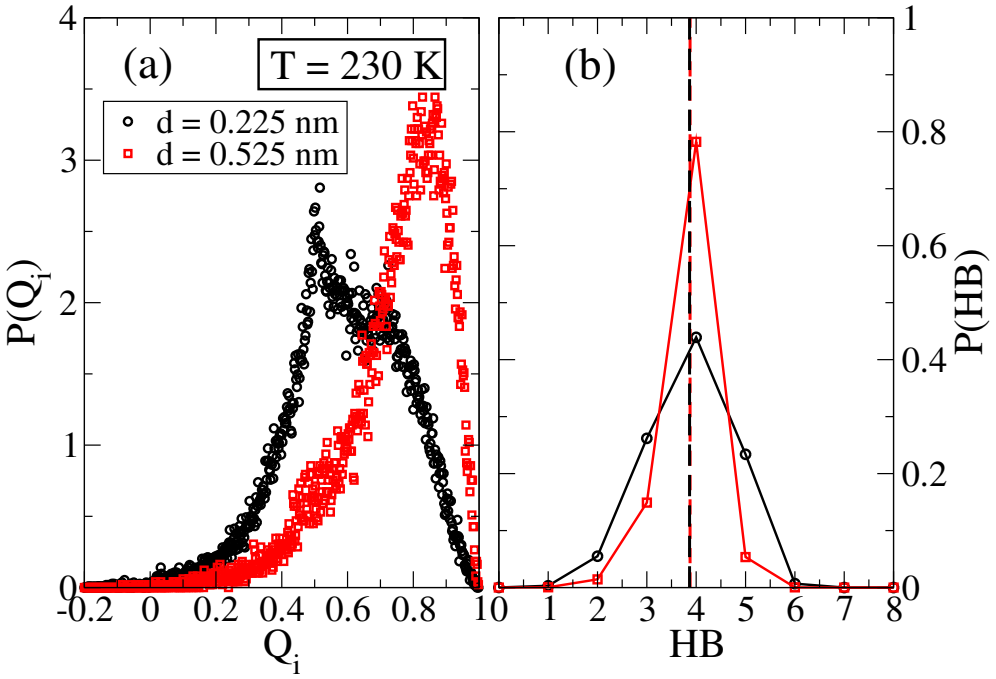

Figure 7.4: Distribution of the tetrahedral order parameter (a) and the distribution of hydrogen bonds per molecule (b) for the low-density system (small silica pore) at 230 K. The vertical lines in panel (b) mark the average number of hydrogen bonds per molecule for both distributions.

Albeit the distance between the chosen subensembles roughly corresponds to only a single water layer, the curves are very different. Adjacent to the surface, the tetrahedral order is suppressed, discernible from the peak location at $Q_i \approx 0.5$, whereas the peak shifts towards $Q_i \approx 0.8$ at larger distances, indicating a tetrahedrally ordered environment. In a previous study on supercooled water, peaks at those locations were interpreted as HDL and LDL related, see also chapter 6.1 [128]. Interestingly, panel b) reveals that the distribution of HB per molecule for the two subensembles differ in width, but not in average, see the vertical lines marking the averages, which are virtually identical for both distributions. Thus, despite the very different local environments, the number of HB is on average the same.

Rather than showing all distributions of the tetrahedral order parameter as function of temperature and distance to the pore wall, the tetrahedral entropy is used as characteristic quantity. The top row in Figure 7.5 depicts the tetrahedral entropy and the bottom row the number of HB per molecule for all silica-pore systems, with (a) *hi-dens*, (b) *me-dens*, (c) *lo-dens* and (d) the large silica pore. The strong density layering for the high-density system is neither mirrored by the tetrahedral entropy nor by the average number of HB, cf. panel (a).

As pointed out during the discussion of the data for Figure 7.4, the local structure in the vicinity of the wall is disturbed compared with water farther away from the surface. The tetrahedral entropy illustrates this behavior too, as the values for water near the wall are larger, suggesting low tetrahedral order, compared with values away from the pore. This is found for all investigated silica pores, showing almost the same values for the entropy near the walls at a given temperature, regardless of density.

In contrast, the extent of structural change during cooling is dependent on the pore fillings. This is accompanied by the difference between surface water and core water, which becomes increasingly more pronounced for lower temperatures and lower pore fillings. The first water layer up to distances $d \approx 0.4$ nm appears affected at high temperatures, but it is remarkable that there is no clear plateau value visible for core water of the *me-dens* and *lo-dens* systems at 200 K. The data for the larger silica pore (d) suggest that the plateau is obtained at larger distances from the wall than the pore size of the small silica pore. Therefore, the influence of the wall on the confined water depends on the density and the temperature and increases in range if one of these parameters is reduced. For completeness, the values of the tetrahedral entropy for the bulk system are indicated by large plus symbols. The density of the bulk system, ≈ 1 g/cm^3, is similar to that of the low density system (small silica pore) and to the

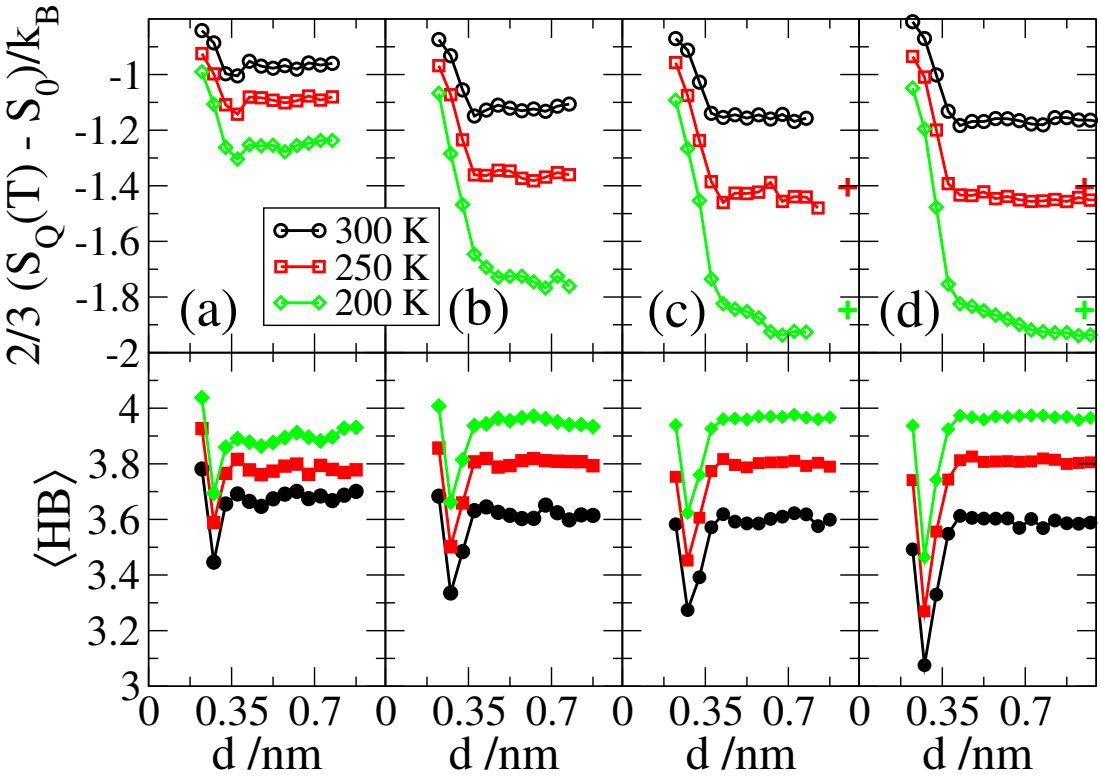

Figure 7.5: The tetrahedral entropy (top row) and average number of hydrogen bonds per molecule (bottom row) for the (a) *hi-dens* system (SSP), (b) *me-dens* system (SSP), (c) *lo-dens* system (SSP) and (d) the LSP. d denotes the distance to the pore wall. In panel (c) and (d), the large plus symbols mark the value of the tetrahedral entropy for the bulk system at the respective temperature.

density in the large silica pore. At 250 K, there is a good agreement with the values of the pore system at some distance to the wall, but at lower temperatures, there is a pronounced deviation.

The behavior of the average number of HB, shown in the bottom row of Figure 7.5, is different from the behavior of the tetrahedral entropy. As before, the same area is affected by the surface, but in this case almost independent of the filling and radius of the pores. Therefore, the number of hydrogen bonds appears to be less appropriate to detect the influence of the wall. The sharp drop of ⟨HB⟩, occurring in the disordered area, indicates that there may exist no trivial hydrogen-bond network spanning from the surface towards the pore center.

The results point to a so-called *core/shell* behavior, which has been found or

used to explain phenomena in various simulations and experiments on confined water [184–188]. Regarding tetrahedral order, the description seems appropriate at high temperatures, but as the temperature is reduced an intermediate regime emerges and thus more complex behavior prevails.

The results obtained for the structure of water inside the pores reveal imposed disorder in terms of tetrahedral order. In a more general approach, the structure of surface water is examined by projection of the density of a certain layer near the wall ($d = 0.325$ nm) onto a cylindrical surface. Other water layers near the wall show essentially the same behavior, but in the immediate vicinity of the wall, $d < 0.325$ nm, there are molecules which penetrated the wall, see Figure 7.3. Those molecules yield a pattern of four peaks along the z-direction in the density projection due to the fact that the pore was elongated 4 times along the z-direction.

The projection is shown in Figure 7.6 for the *lo-dens* system at 200 K, with z the direction of the symmetry axis of the pore and ϕ as the angle, which together with z determines the position of the atoms on the surface. The density distribution shows no simple structuring, therefore assuring that the wall does not induce the appearance of an ice-like phase, not captured by the tetrahedral order parameter, but rather imposes disorder. Hence, the lack of signs for crystallization of water in confinements is putatively attributable to the induced disorder for water adjacent to the wall and the size of the disordered area was shown to grow upon cooling.

Next, the proposed liquid-liquid phase transition will be addressed. It was mentioned that the FST is related to a distinct change in structure and dynamics, so it should be traceable if present. For this purpose the tetrahedral entropy is examined as function of temperature at different locations within the pore, see Figure 7.7. The left panel shows data for water near the surface ($d = 0.225$ nm) and the right panel at a larger distance to the wall ($d = 0.625$ nm).

In the vicinity of the wall the change of structure is small and very similar for all silica-pore systems, thus the induced disorder harldy depends on water density or pore size. In contrast, the curves in the right panel are steeper, especially for the low-density fillings. The latter are additionally similar to the bulk curve (dashed line) obtained for $p = 1$ bar yielding approximately a density of $1 \frac{\mathrm{g}}{\mathrm{cm}^3}$, similar to the low density system and the large silica pore.

The high-density and medium-density systems exhibit no kink or unexpected

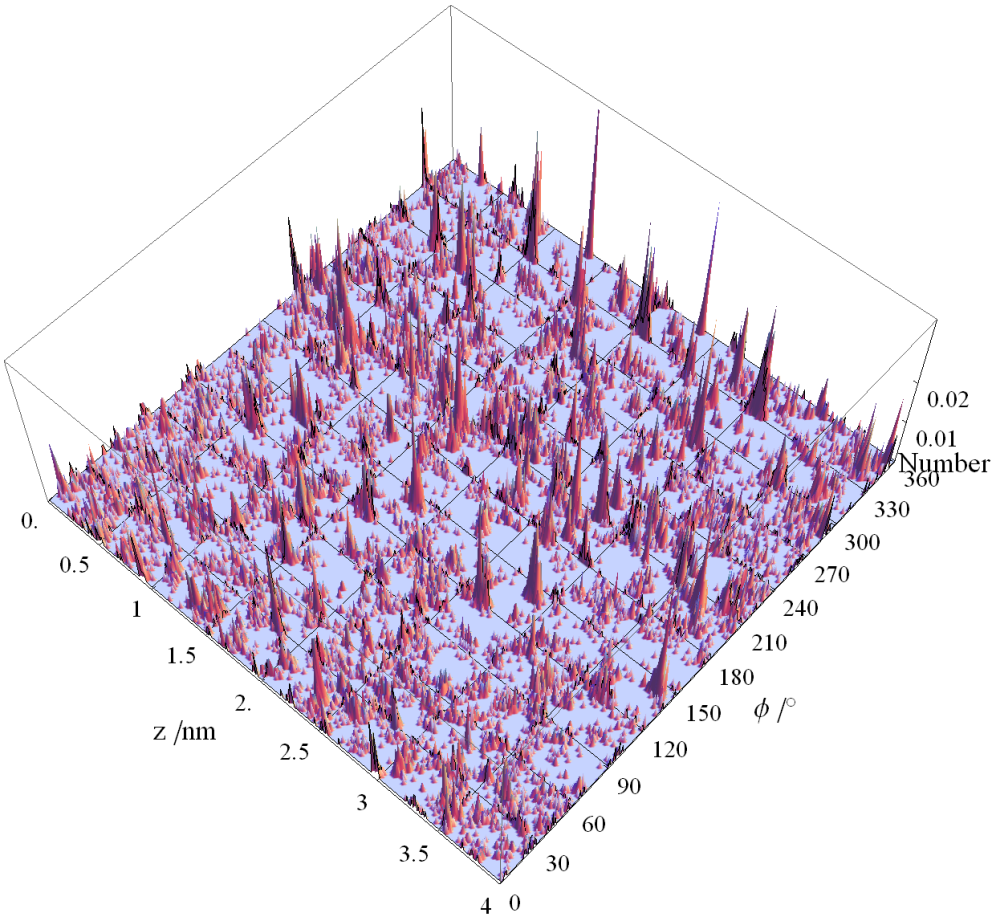

Figure 7.6: Density projection of an oxygen-atom layer near the pore wall ($d = 0.325$ nm) onto a cylindrical surface. z denotes the cylindrical symmetry axis along the pore, and ϕ is the polar angle. The data stem from the *lo-dens* system at 200 K.

behavior reflecting a phase transition. For the *lo-dens* system and the large silica pore the curves are very similar. Several kinks are observable, but evidentially, they are not located at the same temperature and both curves appear to be only slightly shifted compared to the bulk curve, where no kinks are found. This suggests that no distinct change of structure is observed for these systems and that the visible kinks are related to unsufficient statistics. Hence, a HDL to LDL transition is lacking in the investigated temperature range. This result corroborates the findings from the bulk system, where also no indication for the HDL to LDL transition was found. Again, it is emphasized that no transition is expected for the low-density systems and for the bulk. However, for the high density systems, the transition temperature should be in the region of ≈ 220 K, and therefore within the investigated temperature range [111]. In chapter

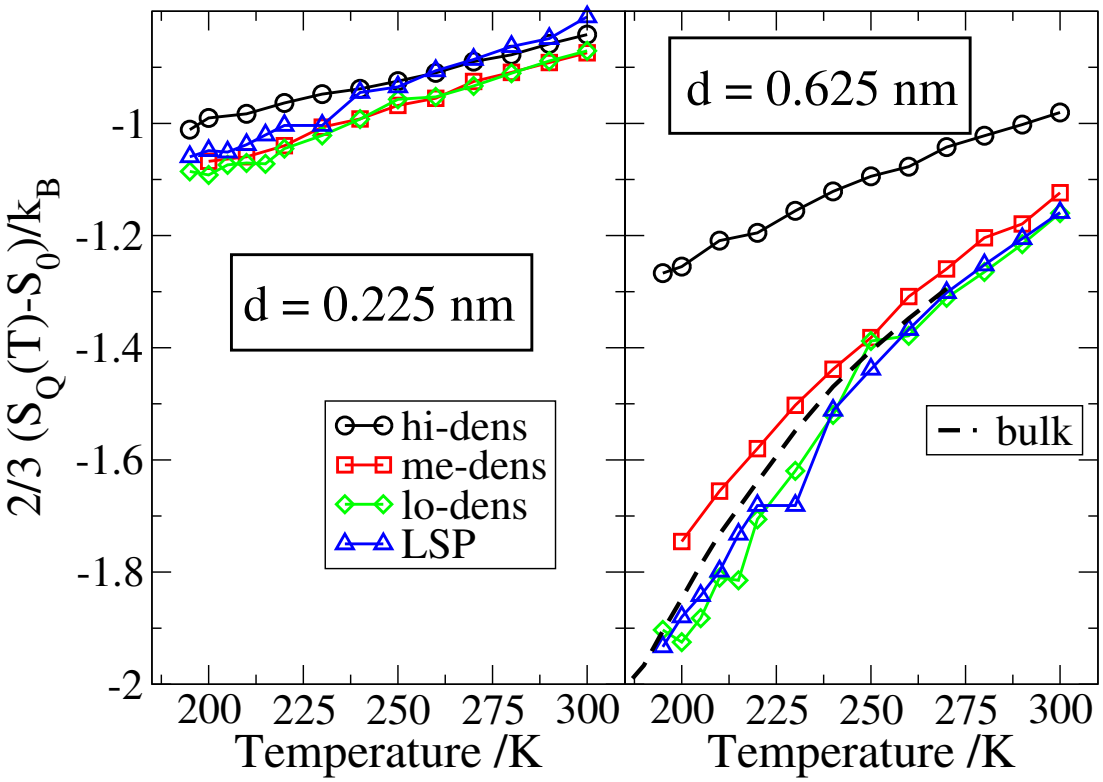

Figure 7.7: Tetrahedral entropy as a function of temperature. The left panel shows data for water adjacent to the pore wall ($d = 0.225$ nm). The panel on the right depicts data for water with larger distance to the surface $d = 0.625$ nm. The dashed line marks bulk data at $p = 1$ bar.

2.7, it was argued that dynamics is maybe more suitable to detect the putative transition from HDL to LDL than the structural quantities used in this chapter. Thus, the next subsection will characterize dynamics within the pore and afterwards, the liquid-liquid phase transition is investigated in terms of dynamics.

7.2 Dynamics

In this subsection dynamic properties of water confined in silica pores are studied. First, the entire water in the pores is investigated using correlation functions which are accessible in experiments. For this purpose the ISF, $S_q(t)$ with $q = 22.7\ \mathrm{nm}^{-1}$, and orientational autocorrelation functions $F_1(t)$ for dipole reorientation and $F_2(t)$ for $\vec{\mathrm{OH}}$ bond reorientation are analyzed. These functions are probed by neutron scattering, DS or NMR, respectively. Afterwards, a position resolved analysis will be performed. The details are discussed using the *lo-dens* system, and then the water dynamics for all pores will be compared.

Some of the findings of this chapter have been submitted for publication [182].

7.2.1 Comparison to experiments

Experiments usually probe dynamics averaged over the entire system. Hence, all water molecules inside the pores are considered for the analyses in this part. The ISF for oxygen atoms of the *lo-dens* system is shown in Figure 7.8 on the left side and the rotational correlation function $F_2(t)$ probing $\vec{\mathrm{OH}}$ bond reorientation on the right side [33]. The bottom row shows the same data as the top row but the time axis is scaled as $t/\tau_{\alpha,\mathrm{trans}}$ or $t/\tau_{\alpha,F_2}$ respectively.

Translational and rotational dynamics are somewhat different. The continuous line in the upper panels is a stretched-exponential function. The initial part of the long-time decay for translational motion can be well fitted, but at a certain point, see the black arrow in the upper-left panel, dynamics is slower than expected by the KWW function. This suggests that the fraction of slow particles is larger than for the bulk, where a KWW function gave reasonable interpolations. It is emphasized that the long-time tails of the decreasing correlations are well approximated by a Mittag-Leffler function (equation (2.2)), see Figure 7.9 [34].

[33] For calculating $S_q(t)$, the isotropic condition was used. Figure 12.1 shows that this assumption is valid also for calculations in confinement. The average over particles in different layers yields that the presence of the wall, which can be imagined as excluded volume, gives a preferred direction for motion but cancels out pairwise.

[34] The Mittag-Leffler function can be approximated by a stretched exponential if $\alpha \leq 1$ and short times, or equivalently the limit of very large τ_{MLF}, is considered [39]. The obtained values for τ_{MLF} are smaller than 1000 ps, hence, ensuring that the Mittag-Leffler and the KWW fits are not accidentally identical. The fit corresponds to a single-mode description, for more informations on that see [64, 66, 67].

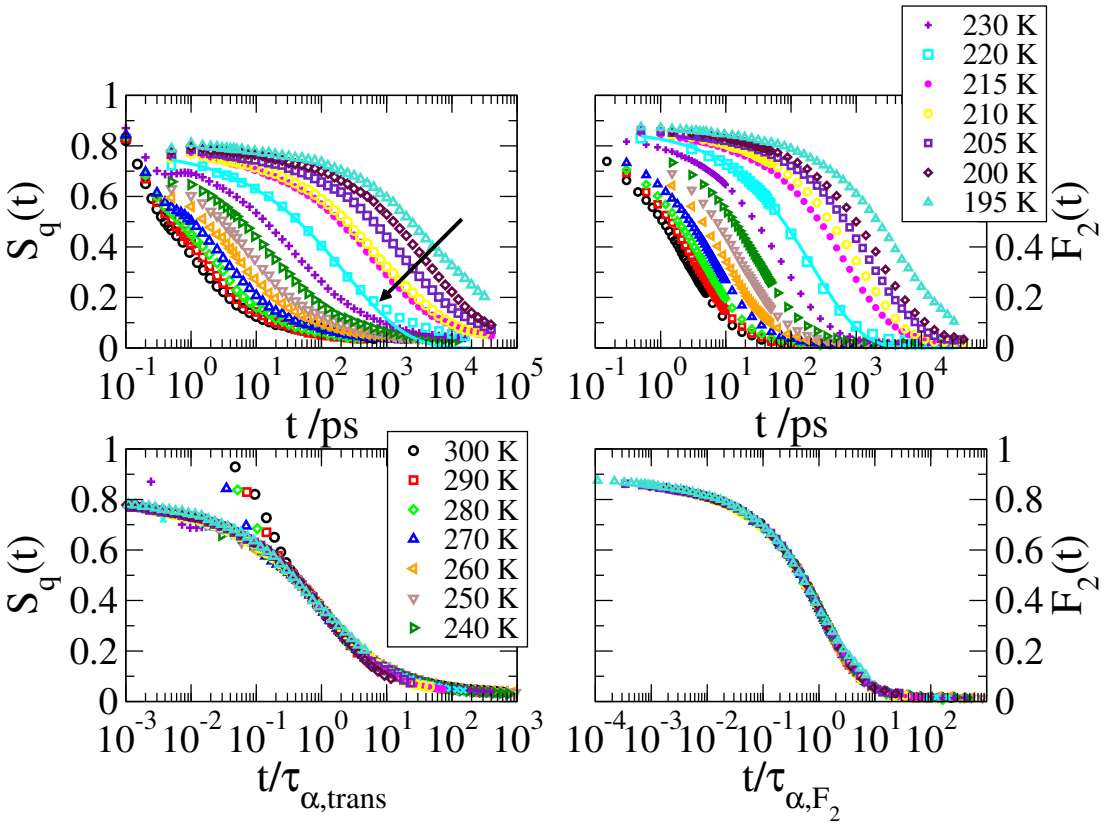

Figure 7.8: Characterization of dynamics for water of the *lo-dens* system at various temperatures. The left panels show the incoherent intermediate scattering function $S_q(t)$ ($q = 22.7\,\mathrm{nm}^{-1}$) for oxygen atoms. The right panel displays $F_2(t)$ probing the $\vec{\mathrm{OH}}$ bond reorientation. The bottom row depicts the same data as shown in the top row but the time axis is scaled by $t/\tau_{\alpha,\mathrm{trans}}(T)$ or $t/\tau_{\alpha,F_2}(T)$.

On the contrary, a KWW function reasonably well describes most of the decay of $F_2(t)$.

Further, the validation of the time-temperature superposition (TTS) principle is checked, see the bottom row in Figure 7.8. It basically probes how the shape of correlation functions change upon cooling. Bulk SPC/E exhibits the TTS scaling property, as can be readily concluded from the mild dependence of β_{KWW} on temperature depicted in Figure 6.8 [49]. The rotational motion of water in silica confinements shows the feature too, scaling the data to a master curve is valid, thus dynamics slow down but the mechanism for the decorrelation is not significantly altered. However, for the translational motion, deviations from the master curve can be observed, but they appear rather small. This behavior

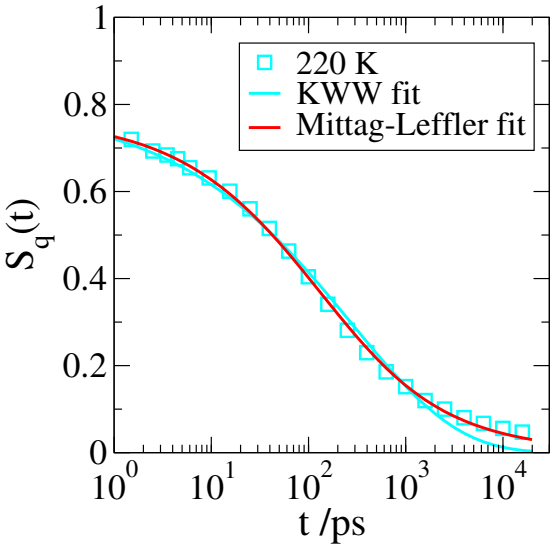

Figure 7.9: The ISF, $S_q(t)$ ($q = 22.7$ nm^{-1}), for oxygen atoms at 220 K. The data are the same as in the previous Figure, but is intended to highlight the difference between the Mittag-Leffler function (red line) and a usual KWW function (cyan line).

might be unexpected, because the influence of the wall on the structure was shown to grow significantly upon cooling in chapter 7.1, and thus, a significant change for the mechanism of motion was assumed, resulting in strong deviations from a master curve.

In order to further study the discrepancy between translational and rotational dynamics regarding the form of the decay, Figure 7.10 juxtaposes the susceptibilities corresponding to $S_q(t)$ in panel a), $F_1(t)$ in panel b), and $F_2(t)$ in c). The solid lines are fits to the CC and the dashed lines to the CD relaxation pattern, see equations (2.3) and (2.4). All shown data points were considered for the fits. Further, notice that the Mittag-Leffler approach, equation (2.2), yields exactly a Cole-Cole relaxation pattern for the imaginary part of the susceptibility [38].

Evidently, the CC approximation fits $\chi''_{S_q(t)}$ and $\chi''_{F_1(t)}$, whereas a CD approach does not successfully describe the data. The opposite holds for $F_2(t)$ where a CD yields a better approximation for the data. As will be shown below, the CC behavior is characteristic for interfacial water. The reason why $F_2(t)$ is less appropriate to detect signs of this shell water points to an additional decorrelation mechanism for $\vec{\text{OH}}$ bond reorientation, recently proposed for water near protein surfaces, the so-called π-*flip* motion [125]. This will be investigated in

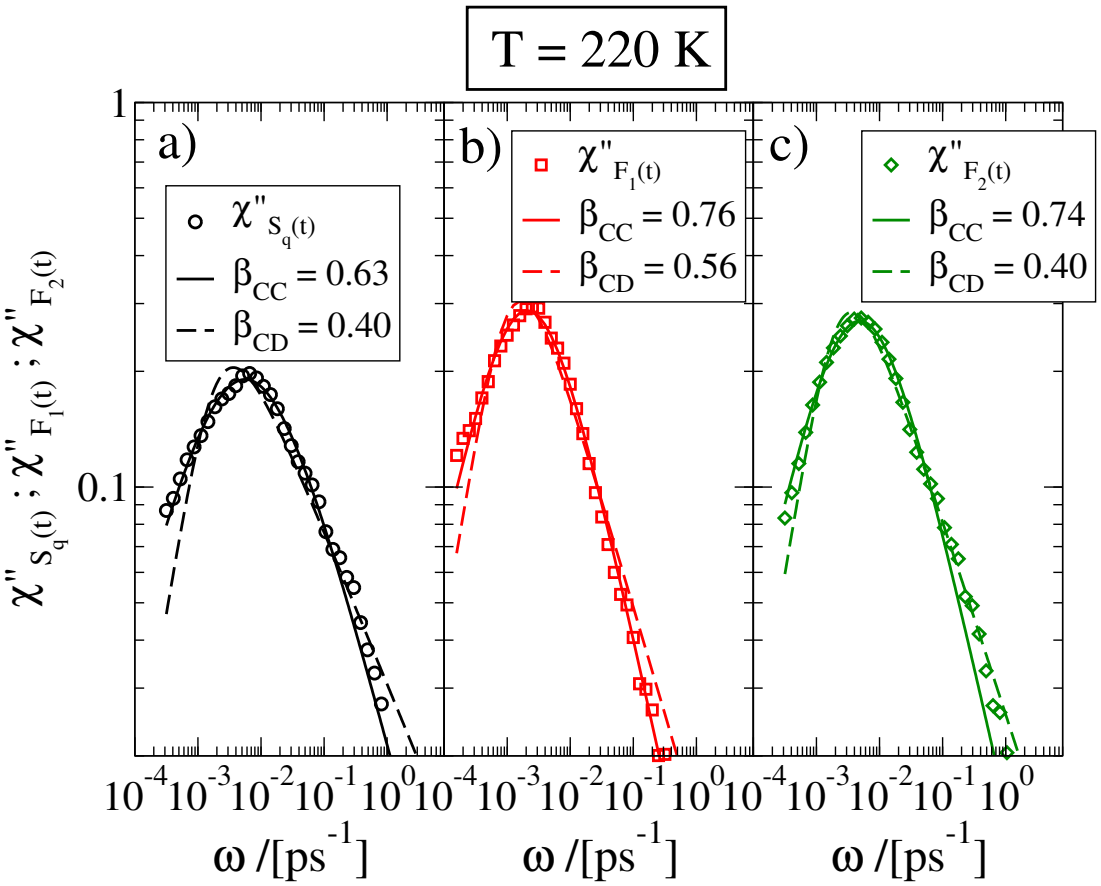

Figure 7.10: Susceptibilities corresponding to, a), $S_q(t)$ ($q = 22.7\,\mathrm{nm}^{-1}$) for translational motion of oxygen atoms, b), $F_1(t)$ for dipole reorientation, and c), $F_2(t)$ for $\vec{\mathrm{OH}}$ bond reorientation. The data stem from the low density system (small silica pore). The solid lines are functions according to the Cole-Cole (CC) relaxation pattern and dashed lines to the Cole-Davidson (CD) pattern. All shown data points were considered for the fits.

more detail in chapter 9. The dependence of the form of the decay on the pore size will be discussed in the next subsection.

MD studies on nanoconfined water found a power-law decay (large-time approximation of equation (2.2) yields a power-law [38]) for the reorientation of $\vec{\mathrm{OH}}$ bonds employing $F_2(t)$ [189]. The results presented here show that this is an almost negligible effect for the $\vec{\mathrm{OH}}$ bond reorientation as considerable deviations from the CD approach are only visible at very small frequencies compared with the peak location. Instead, the proposed effect is characteristic for translational motion and dipole reorientation.

The findings are further detailed using spatially resolved analyses in the following.

7.2.2 Spatially resolved analyses

In chapter 7.1 it was found that the wall strongly affects the structure of water adjacent to the pore surface. As studies (and theories like MCT [171]) propose a connection between structure and dynamics [190], it is convenient to examine dynamics as function of the distance to the pore wall, d.

Figure 7.11 illustrates the spatially resolved autocorrelation function $F_1(t)$ on the left, probing the reorientation of the dipole moment of water. The right panels depict the respective susceptibilities, which are probed in DS [191]. The data shown here stem from the low density system (small silica pore). This system is first characterized before turning to the other systems.

The top row in Figure 7.11 depicts the decay considering all water molecules of the system, the middle row water molecules near the pore wall ($d = 0.225$ nm), and the bottom row water at a distance of $d = 0.525$ nm. If the entire water in the pore or the water near the pore wall are considered the susceptibilities exhibit a symmetric behavior (CC like). Further, the values for β_{CC} are very similar. This gives a clear indication that the long-time tails have a significant contribution from the molecules in the immediate vicinity to the surface.

In contrast, for water far away from the pore wall, the decorrelation appears to be asymmetrically shaped (CD like). CD approaches are very similar to KWW ones and are thus used as synonyms in this context, see also chapter 2.1. The results from Figure 7.11 are interesting because there is a transition from CC behavior for interfacial water to CD behavior for water at the center of the pore. Supercooled bulk water also exhibits CD relaxation patterns, therefore, the finding can be understood as approach to bulk behavior.

The reason for this result is presumably rooted in how the wall affects the confined liquid. As stated in the previous subsection, the surface imposes disorder, proposing a static contribution to the energy landscape. In order to proof this in terms of dynamics, conditional-probability functions are used, like in section 6.2, but there is an additional restriction for the motion of oxygen atoms in

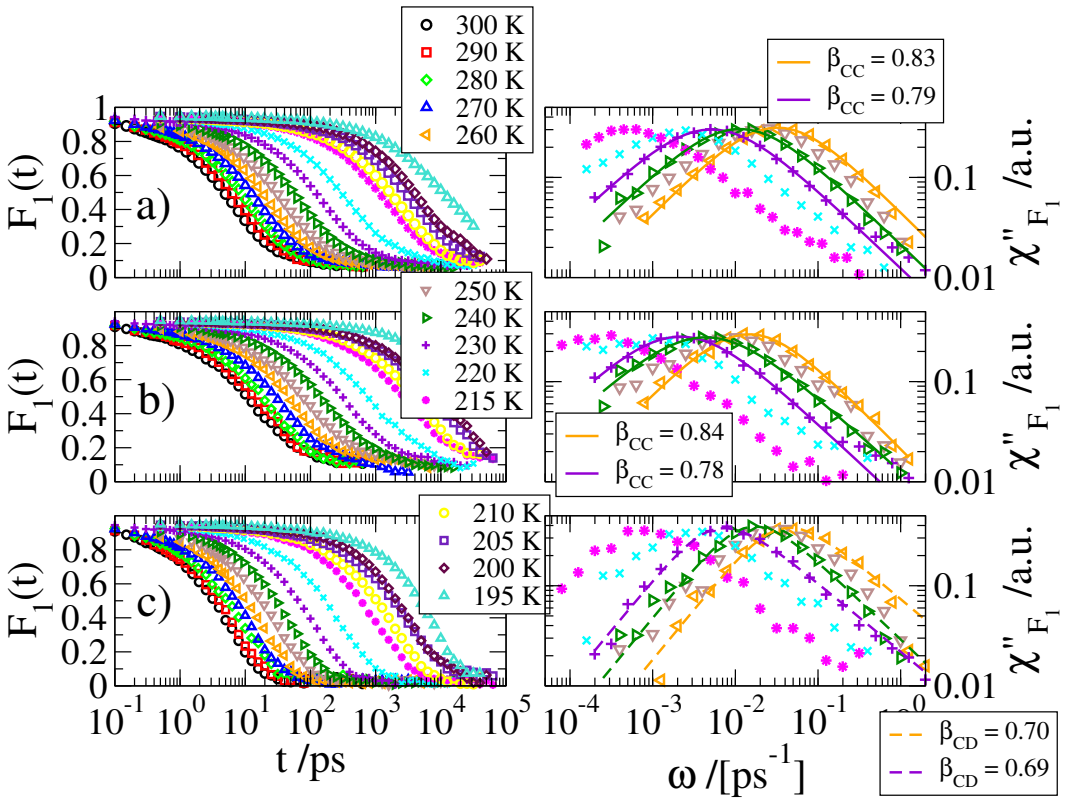

Figure 7.11: Orientational correlation function $F_1(t)$ probing the reorientation of the dipole vector for water molecules of the *lo-dens* system. Every row depicts $F_1(t)$ on the left, and the corresponding susceptibility on the right. Only susceptibilities in the temperature range from 260 K to 215 K are shown. The top row, a), shows $F_1(t)$ for all molecules of the system, b) depicts data only for water molecules near the pore wall ($d = 0.225$ nm), and the bottom row, c), illustrates $F_1(t)$ and $\chi''_{F_1(t)}$ for water molecules distant to the wall ($d = 0.525$ nm). Solid lines are interpolations using a Cole-Cole (CC) and dashed ones a Cole-Davidson (CD) relaxation pattern.

this case[35]. The goal is to describe the energy landscape for a given layer of molecules, therefore, the condition is applied that the particles are still in the layer after the time interval t_{01}. Figure 7.12 depicts $\langle R(r_{01})\rangle$ for interfacial oxygen atoms ($d = 0.225$ nm) of the *lo-dens* system at 220 K. It is emphasized that comparing bulk and interfacial water is only allowed if an average over the en-

[35] A different but much simpler way to gather information about energy landscapes is given in chapter 8.

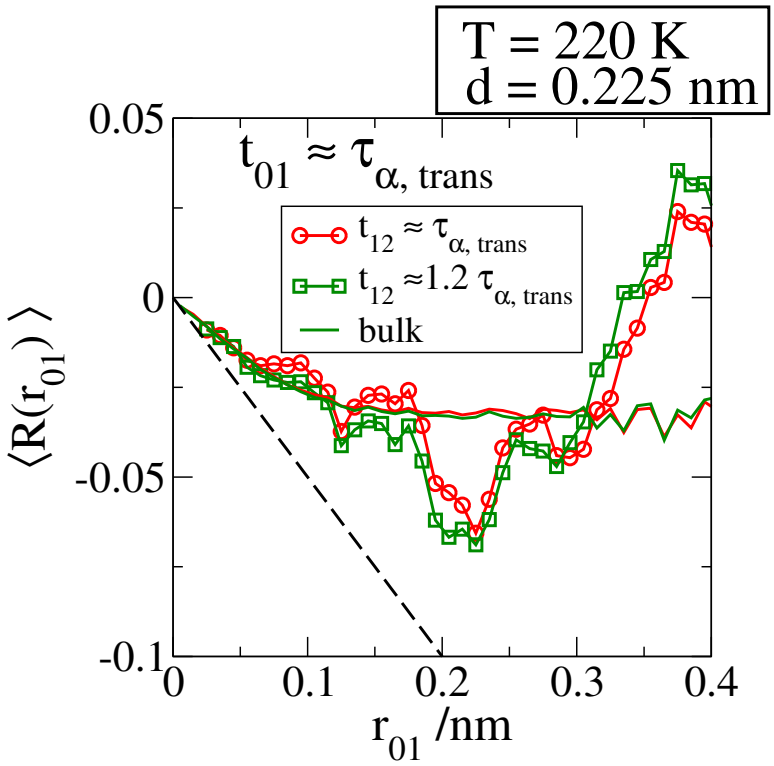

Figure 7.12: Conditional-probability function for interfacial oxygen atoms (d = 0.225 nm) of the *lo-dens* system at 220 K. The first time interval is $t_{01} \approx \tau_{\alpha,\text{trans}}$ and the second time intervals are $t_{12} \approx c \cdot \tau_{\alpha,\text{trans}}$ with c specified in the Figure. The solid lines correspond to the same time intervals but for the bulk, see the respective color. The dashed line marks the large-time harmonic-potential approximation. Running averages (5 points) had to be performed to smooth the curves.

tire roughness of the cylindrical surface[36] has been conducted. Water molecules which move parallel to the local surface in the first time interval are obviously more likely to move to the pore center in the second interval as the wall can be imagined as excluded volume. Thus, only for an appropriate average, the trivial contribution to $\langle r_{2,i} \rangle$ owing to the very presence of the wall itself is presumably averaged out, what is assumed in the following.

For small r_{01} the bulk and the interfacial water behave similar but major deviations occur for larger r_{01}. On length scales $r_{01} < 0.3$ nm the backward correlation can be concluded from the negative values of $\langle R(r_{01}) \rangle$, but on larger

[36] This point is extremely important. The average has to be done in a way to average out trivial contributions from the wall. In case of a slit geometry, the average has to be performed over both sides of the wall.

lengths a sharp rise is visible, which is not observed for the bulk. This increase of $\langle R(r_{01})\rangle$ to larger values than 0 is interpreted as evidence for a static energy landscape, where roughly the next-neighbor distance between hydrogen atoms of the silanols at the surface, ≈ 0.2 nm, indicates the inflection point of a local minimum and the transition to positive values at $\langle R(r_{01})\rangle = 0$ corresponds to forward correlation due to a different local minimum, similar to the hypothesized case of a sine potential in [167]. See also the discussion in chapter 6.2. Based on this, the picture of a specific energy landscape near the pore wall is established, which is still present on time scales $\tau_{\alpha,\mathrm{trans}}$. This means, that even if all water molecules near the surface rearrange, the energy landscape is not entirely relaxed, similar to what fast molecules explore in the bulk in the deeply supercooled regime, implying long-resting correlations or a broad distribution of correlation times or both.

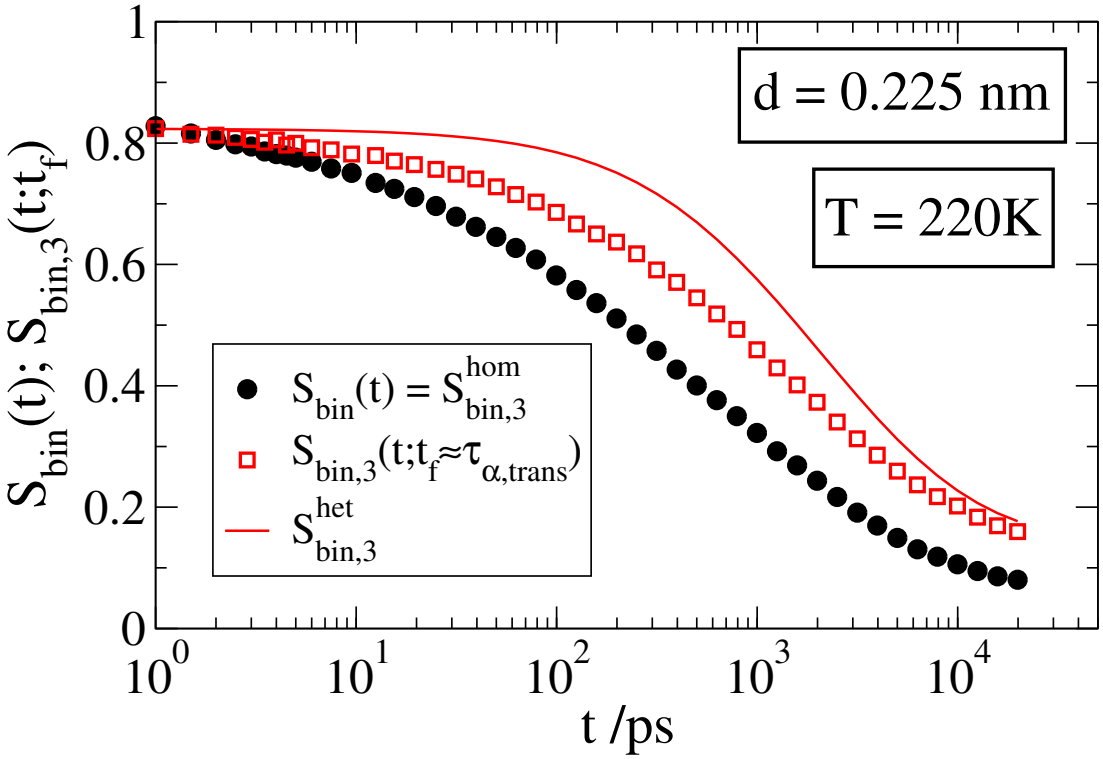

Figure 7.13: Two-time and three-time correlation function for oxygen atoms of water in the low density system (small silica pore), see equation (5.20). The solid line is the prediction for purely heterogeneous behavior.

Figure 7.13 depicts the modified three-point correlation function $S_{\mathrm{bin},3}(t)$ (oxygen atoms, $q = 24\ \mathrm{nm}^{-1}$) for interfacial water ($d = 0.225$ nm) of the low

density system (small silica pore). This is the same function and q value used for the bulk, see Figure 6.3. The modified correlation function was necessary to avoid a non-trivial forth-and-back jump contribution, which alters the prediction for the ideal homogeneous case in a complex way [55].

It is evident that a strong heterogeneous component is present as the deviation from the homogeneous expectation $S_{\text{bin}}(t)$ is large compared to bulk, cf. Figure 6.3. This indicates a broader distribution of correlation times compared to that of the bulk. The finding can be understood as in the bulk, or for water molecules far away from the surface, the energy landscape changes completely on time scales τ_α due to the motion of the particles, see chapter 6.3. This means that slow particles move faster than expected because their environment has changed. This yields a faster decorrelation for slow molecules and presumably gives rise to the CD-like decay $\propto \omega^1$ at low frequencies. For molecules near the surface, the energy landscape is never completely changed, due to the imprint of the wall. Therefore, motion near the wall exhibits larger heterogeneity as the environment for the slow molecules changes only to a certain extent and thus, the correlation times distribution is not *cut* at large times unlike in the bulk.

This interpretation is in agreement with attempts to motivate the use of CC relaxation patterns which propose power-law waiting time distributions, resulting from a very diverse energy landscape [192]. Details on that point can be found in chapter 10.

Now, the behavior of water for the other silica pores is investigated. Figure 7.14 shows the ISF, $S_q(t)$ with $q = 22.7\ \text{nm}^{-1}$ on the left and $F_2(t)$ on the right for the other silica pores. Basically, the discussed behavior is observed again, but data from the LSP, panels e) and f), show significantly less pronounced long-time tails, simply due to the fact that the amount of water adjacent to the surface is small compared to the bulk-like water. The found behavior strongly depends on the numbers of water molecules at the pore walls and in the pore center, respectively, complicating the analyses. Hence, experiments performing an ensemble average, like DS and NMR experiments, should be sensitive to the pore size and to the degree of filling of the pores. In general, the results reveal some fundamental differences how NMR studies, which probe F_2, and DS, probing F_1, perceive the influence of the wall, thus comparing results from both methods is a challenging task.

Next, dynamics throughout the pore is assessed by employing position-dependent correlation times obtained from autocorrelation functions. Figure

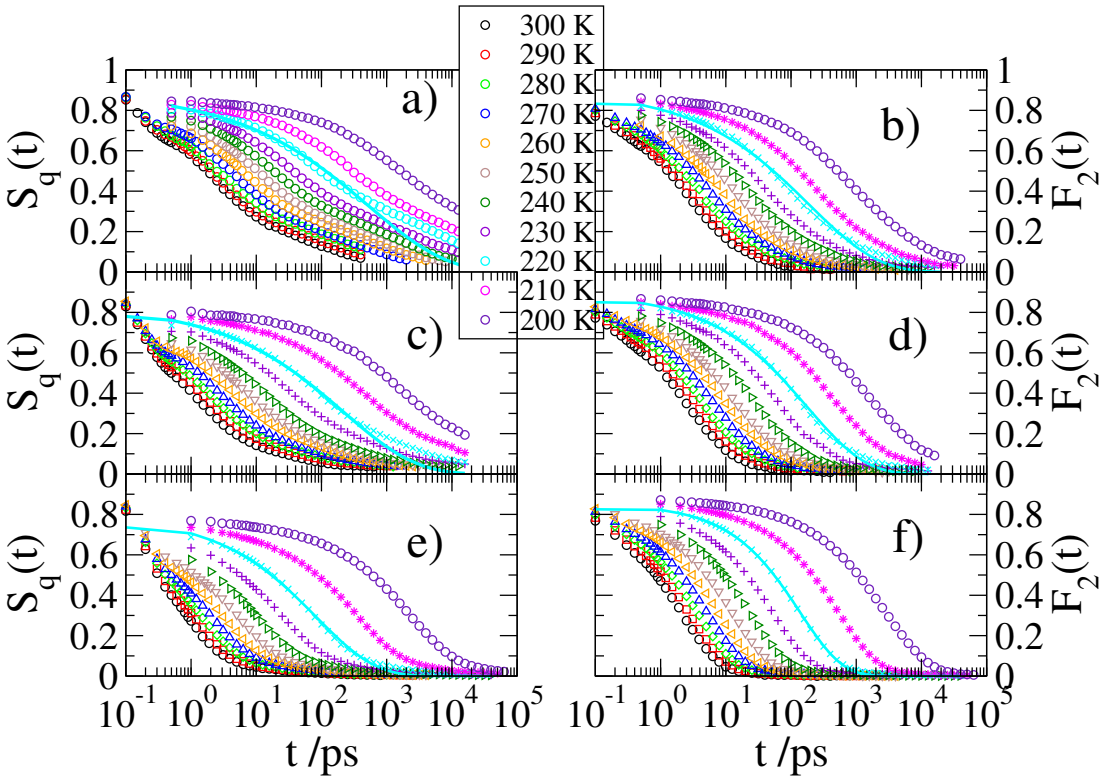

Figure 7.14: ISF, $S_q(t)$ with $q = 22.7\ \mathrm{nm}^{-1}$, and orientational correlation function $F_2(t)$ probing $\vec{OH}$ bond reorientation are depicted. a) and b) show data for the *hi-dens* system, c) and d) for the *me-dens* system and e) and f) for water in the large silica pore. Solid lines are KWW functions.

7.15 illustrates the dependence of dynamics on the distance to the pore wall, a) showing data for the *hi-dens* system, b) for the *me-dens* system, c) for the *lo-dens* system (a) to c) correspond to the small silica pore), and d) for the large silica pore.

The water dynamics exhibits a weak dependence on the water density or pore size. There is a region ($d < 0.4$ nm), previously identified as the structurally affected region, see Figure 7.5, where dynamics is slowed by one to two orders of magnitude. The region beyond the interfacial area is characterized by a plateau at high temperatures, but different effects are observed at lower temperatures. In panels a) and b) the motion speeds-up as monotonic function of increasing distance to the wall. For panels c) and d) there seems to be a minimum at $d = 0.4$ nm and beyond that point the motion of particles becomes slower again, see the dashed line as guide for the eye in panels c) and d). These complex trends are not mirrored in the structure, cf. Figure 7.5.

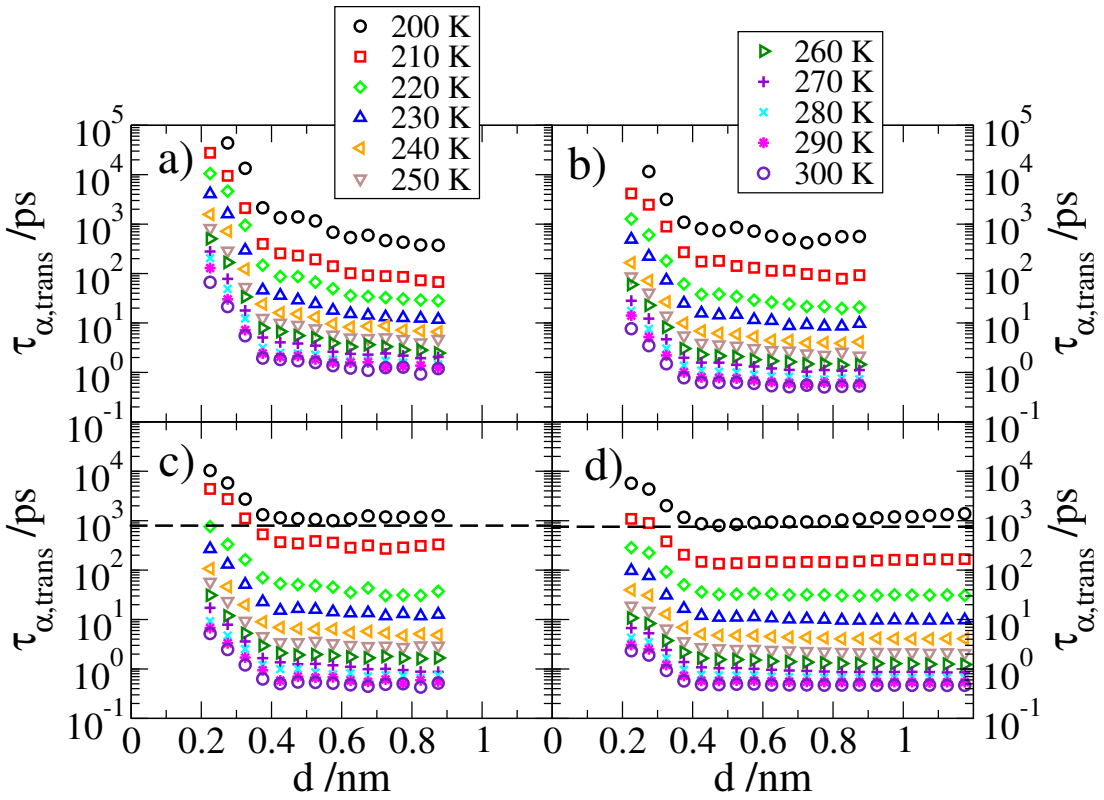

Figure 7.15: Dynamic profiles. The correlation time $\tau_{\alpha,\text{trans}}$ of $S_q(t)$ with $q = 22.7\ \text{nm}^{-1}$ for oxygen atoms of different systems as function of the initial distance d to the pore wall. a) shows the profile for the *hi-dens* system, b) for the *me-dens* system, c) for the *lo-dens* system (a) to c) correspond to the small silica pore), and d) the large silica pore. The dashed line is a guide for the eye, see text.

Moreover, the increasing range of induced disorder for the low-density systems (c) and d)) is not observable, in agreement with the small deviations from the time-temperature superposition principle for those systems.

The slowdown of dynamics near silica walls is one of the key results of the present thesis. This implies that the long-time tails found for ensemble-averages are attributable to the inherent CC behavior for interfacial water and additionally to the slowing when approaching the pore wall. The latter can be imagined as imposed heterogeneity.

MD studies on water confined in smooth pores led to the conclusion that the slowdown is mainly attributable to HB with the wall, yielding the predominant contribution to the static energy landscape [182]. One can rather speculate on

the reason why motion in the large silica pore becomes slower beyond $d \approx 0.4$ nm for low temperatures. This might be related to the temperature independent structure of the pore surface. At sufficiently low temperatures, the barriers in the bulk might become larger than the barriers imposed by the wall, e.g. due to disturbed structure of interfacial water. The inflection point in the region $d \approx 0.4$ nm presumably marks the transition from an interfacial hydrogen bond network to the bulk-like hydrogen bond network, which was discussed for Figure 7.5.

At the beginning of this chapter $S_q(t)$, $F_1(t)$, and $F_2(t)$ were compared and the lack of CC-like decays for $F_2(t)$ was shown. Hence, it is interesting to see if this is different in terms of slowing of dynamics.

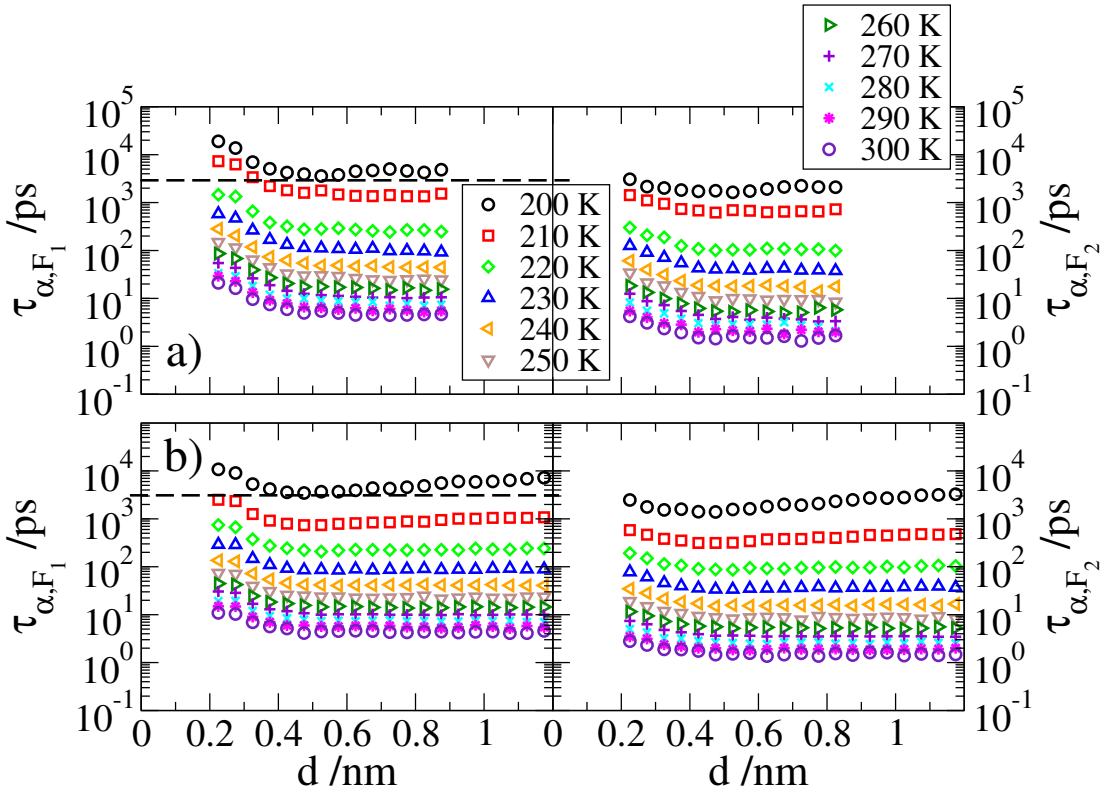

Figure 7.16: Dynamic profiles. The correlation times τ_{α,F_1} and τ_{α,F_2} are juxtaposed. The top row shows data for the *lo-dens* system and the bottom row for the large silica pore. The dashed lines are a guide for the eye, see text.

Figure 7.16 juxtaposes the correlation times τ_{α,F_1} and τ_{α,F_2}, with panel a) referring to the *lo-dens* system and b) to the large silica pore. Consistent with

the CC relaxation pattern, the correlation times τ_{α,F_1} show increasing values for water near the surface, similar to the results from $S_q(t)$. In contrast, τ_{α,F_2} is essentially flat, highlighting the statement that $F_2(t)$ might be sensitive to an additional process. Obviously, probing translational motion on next-neighbor length scales provides the best possibility to study the spatial heterogeneity of structural relaxation. This is a trivial statement as assigning dynamics to a certain layer is based on the idea that motion also occurs in that area. This is valid for translational motion, but not necessarily for rotational motion. Nontheless, $F_1(t)$ reveals the surface influence, therefore supporting the idea of $F_2(t)$ tracking an additional decorrelation process, interfering with the observation of a slowdown of structural relaxation and of CC-like decays near the surface.

So far, the imposed energy landscape yields CC behavior and a slowdown of dynamics. Those effects were found for interfacial water near the silica surface, where also a drastic change in structure was observed. Chapter 8 will address the question about the relation of dynamical properties to the altered structure.

7.3 Is there a liquid-liquid transition in pores?

From a structural point of view, no clear-cut evidence for a HDL to LDL transition was observed. Now, the focus is on dynamics and, hence, on a possible FST.

Gallo and co-workers performed MD simulations on SPC/E in silica pores, very similar to the ones used for this work, and claim to find a FST by investigation of translational dynamics for core water (distance to the pore wall > 0.5 nm) [17]. Therefore, the same analysis was conducted and the results are depicted in Figure 7.17. The correlation times are obtained from $S_q(t)$ with $q = 22.7$ nm^{-1}.

All investigated systems exhibit VFT behavior in the moderately supercooled regime ($T \approx 250$ K). For the medium density system (*me-dens*) and the high density system (*hi-dens*), this behavior continuous to lower temperatures similar to the bulk. However, the data for the low density system (*lo-dens*) deviates significantly from a simple VFT function. In the temperature regime from roughly 300 K to 215 K a VFT function describes the data (dashed line), but then a sudden kink occurs at ≈ 215 K which is followed by Arrhenius behavior (solid line). The location of the distinct kink is at the same temperature as found in the study by *Gallo*, see the green triangles. It should be noted that the occurrence of the kink is not restricted to core water but is found for all layers within the pore albeit less distinct. Opposite to this, $\tau_{\alpha,\mathrm{trans}}$ from the large silica pore exhibits no kink and a VFT function describes the temperature

dependence.

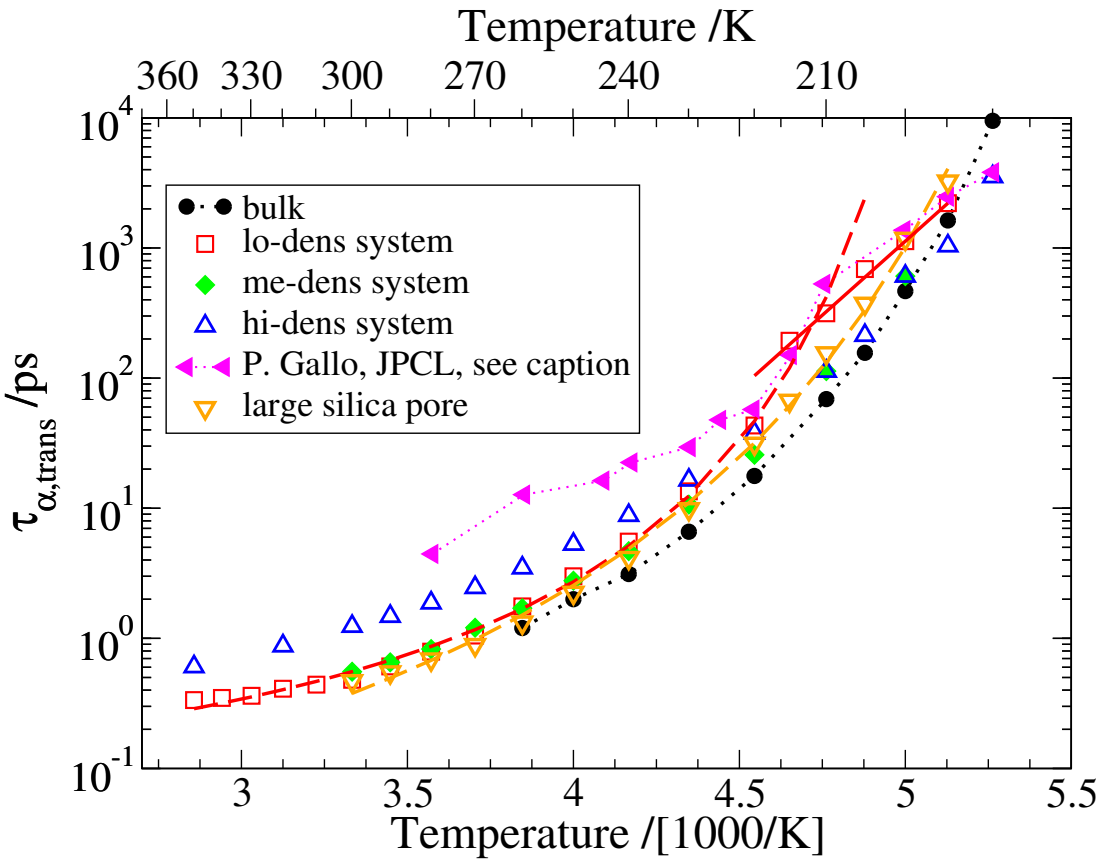

Figure 7.17: Temperature dependence of the translational correlation times. Only core water ($d \geq 0.5$ nm) was considered for the analyses. The dashed lines starting at high temperatures are VFT functions, whereas the solid line is an Arrhenius function. The dotted lines are guides for the eye. The magenta colored data stem from the paper by *P. Gallo*, JPCL, 2010 [17].

There is no obvious reason why the alleged FST should only occur for the small pore at low densities and not for the larger pore, which exhibits similar local structure and average density. Therefore, the found behavior strongly suggests that the kink is related to a very complex finite-size effect. A finite-size effect immediately implies the growth of length scales, as was observed for the imposed disorder. However, the reason why dynamics reveal no such increasing length is unclear, but a hypothesis is set out below.

One can assume that structural quantities are sensitive to the average position of minima whereas dynamics probe the intermediate energy landscape

between minima, explaining the mentioned discrepancy to detect the growing wall effect. Further, one can speculate that the position of the kink indicates the temperature where the imposed energy landscape gives the major contribution to the barriers for the entire system. This could also yield a smooth transition, but studies on supercooled liquids confined between narrow walls clearly find a nonlinear-feedback mechanism for dynamics depending on the separation of the walls [193].

Figure 7.18 underlines the conjecture. The correlation times for translational motion of oxygen atoms adjacent to the wall ($d = 0.225$ nm) are plotted dependent on temperature. The straight lines are Arrhenius functions and the orange triangles show the correlation times for the core water of the low density system (*lo-dens*) ($d \geq 0.5$ nm).

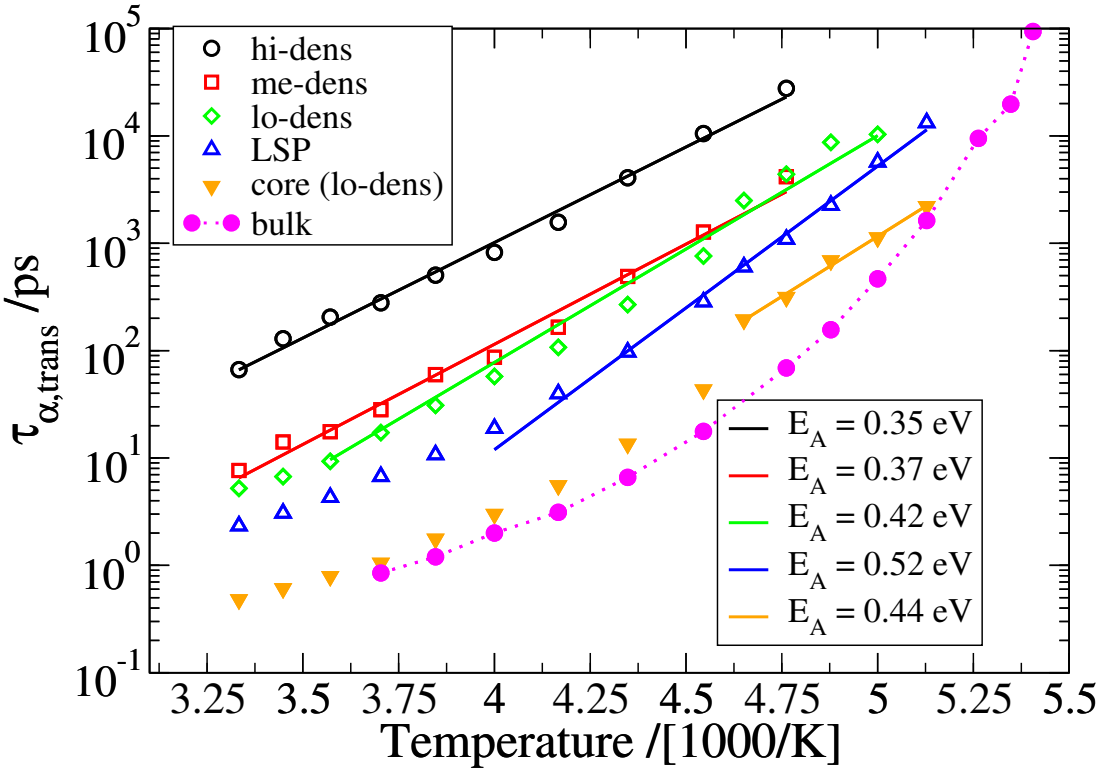

Figure 7.18: Temperature dependence of translational correlation times. Open symbols refer to surface water ($d = 0.225$ nm) for the different pore fillings. Orange triangles show data for the core water of the *lo-dens* sytem. The solid lines are Arrhenius functions, the respective activation energies E_A are mentioned in the legend. The dotted line is a guide for the eye.

Strikingly, the surface water obeys *strong* behavior, in contrast to the bulk. This kind of dependence on temperature is expected at low temperatures due to the static contribution to the energy landscape by the wall. At a certain temperature, this contribution is predominant and it does not change with temperature, so that the dependence of the correlation times on temperature is solely determined by the thermal energy of the system. The activation energy for crossing the barriers can be obtained from fits to an Arrhenius law and correspond to the breaking of roughly two hydrogen bonds [125]. Further, the activation energy increases with decreasing pore filling as dynamics becomes faster and approaches the curve for the bulk. Remarkably, the activation energies for the motion of surface oxygen atoms and for core water in the *lo-dens* system at temperatures below the kink appear to be similar. Hence, the kink is presumably attributable to the impact of the finite-size effect marking the change from bulk-like behavior at high temperatures to an interfacial or amorphous behavior for the entire water at low temperatures, but not to a HDL to LDL transition. Also mean-field calculations on water in silica pores performed by *Limmer* support this interpretation [194]. Therefore, a fragile-to-strong transition seems to occur when decreasing d, rather than the temperature.

7.4 Conclusion

A comprehensive characterization of structure and dynamics for water in silica pores was conducted.

A density layering, with at least one peak adjacent to the surface, was observed. Subsequently, the local order was examined and imposed disorder due to the presence of the wall was found for interfacial water by using an analysis which accounts for the roughness of the surface. Further, a growing range was observed for the influence of the wall on the local order of the confined molecules.

The investigation of dynamics revealed that the affected region coincides with the disordered region. The presence of an imposed energy landscape was elaborated for this area. Additionally, three key characteristics for interfacial water, namely CC relaxation behavior, a pronounced slowdown of dynamics, and *strong* behavior were found for all pores and fillings. Implications on DS and NMR experiments have been discussed, this led to the hypothesis that $F_2(t)$ probes an additional decorrelation process if compared with $F_1(t)$ or $S_q(t)$.

Finally, the proposed HDL to LDL transition was addressed. It was expected

that there is an indication for the transition for the high density or medium density systems, as studies on bulk SPC/E proposed that for densities in the region of ≈ 1.1 g/cm^3 the HDL to LDL transition temperature is at roughly 220 K [111]. However, the local order exposed no clear-cut evidence for a drastic change in structure regardless of the system. For dynamics, the low-density system (SSP) exhibited a sharp kink at roughly $T = 215$ K coinciding with the proposed temperature for a FST, see Figure 2.9. But the large silica pore, which shows similar density profiles and similar dynamics down to 215 K if compared with the *lo-dens* system, exhibits no such kink. Also the other pore systems showed no indication for a FST. Therefore, the growing range of wall-induced disorder led to the hypothesis that the kink is attributable to finite-size effects and not to a FST. Other simulation studies on water in confinements propose that confining water decreases the temperature regime where transitions like the HDL to LDL transition occur [195], presumably explaining why no indication of the FST was observed for the systems with higher densities. However, this might depend on the water model.

Following these results, one should rigorously distinguish between MD simulations and experiments. The discussion on the disordered structure of water inside the pores revealed that only water near the silica surface is affected. As there must be a reason for the suppression of crystallization in experiments, the most plausible explanation is to attribute this to the imposed disorder near the wall, but then this raises a doubt on how to transfer those findings to the bulk. This interpretation is supported by *Swenson* and co-workers who showed in a recently published paper that due to the influence of the wall on the structure no glass transition temperature could be found [196]. Additionally, recent work by *Sattig*, performing NMR studies on confined water, also exposed a kink in the temperature regime at 230 K to 220 K and he ascribed it to the change from bulk-like to interfacial water [32, 197], what is in agreement with the presented results of this work.

In order to investigate the FST in MD simulations, it appears naive to use silica walls for confining water, building a very complex system, given the fact that there is no consensus on the presence of this transition in simpler bulk systems. But, simulations on this topic seem to be well suited to aid the interpretation of experimental results.

8 Water in neutral confinements

The chapter dealing with water in silica pores revealed many concurring effects, namely finite-size effects, surface effects, and density effects. At all, those systems are extremely complex, thus, neutral confinements are employed to reduce the complexity as the wall-liquid interaction is identical to the liquid-liquid interaction. The goal is to introduce a wall without altering the structure of the confined liquid with respect to the bulk. Those systems are somewhat artificial, so they are only investigated by MD simulations or Monte-Carlo approaches, but turn out to give a unique opportunity to investigate fundamental issues of supercooled liquids.

As pointed out in chapter 4.2.3, several geometries and radii are used as confinements. A slit geometry (SL) with 5 nm spacing between the confining walls, cylindrical pores (CP) with radii R $= \{0.5; 1.5; 2.5\}$ nm, and a random-pinned geometry (RP) where various fractions, $f = \frac{N_{\text{fixed}}}{N_{\text{all}}}$, of oxygen atoms are pinned.

It was detailed in chapter 4.2.3 that all neutral-pore systems are equilibrated to a pressure $p = 1$ bar, identical to the presented bulk simulations. Thus, for the neutral confinements, data and results are directly compared with the bulk.

The findings illustrated below have been partially published [181, 198, 199].

8.1 Structure

In this subsection, the structure of the confined water is examined, employing the same methods like for the characterization of the silica pores.

The starting point is again the density distribution of oxygen atoms inside the pores, see Figure 8.1. From left to right, the distributions belong to the CP systems with radii $R = 25$ Å (CP-25), $R = 15$ Å (CP-15) and $R = 5$ Å (CP-05). The data are normalized by the bulk values at the respective temperature. Further, the red and blue curves are shifted up by 0.2 and 0.4, respectively. It is striking that for the large pore density fluctuations are small, expressed numerically, below 4% for the small peak adjacent to the wall if compared to the average density in the pores. The $R = 15$ Å system exhibits the same characteristics like the $R = 25$ Å pore, but the smallest pore is different. At high temperatures the density profile shows two peaks which become distinct at lower temperatures.

These peaks are expected because the introduction of the pore walls imme-

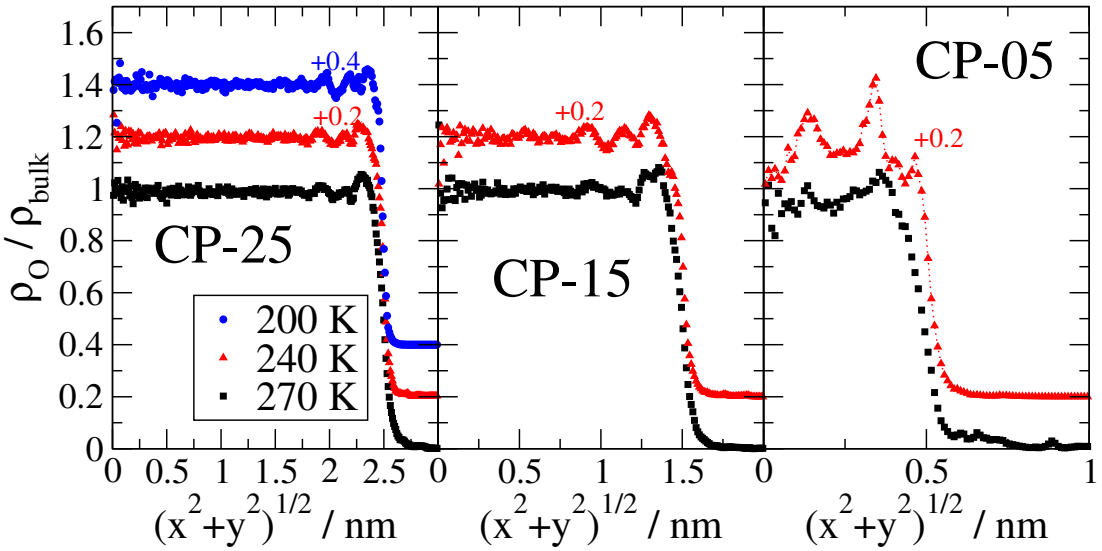

Figure 8.1: Density distribution of oxygen atoms inside CP. From left to right: the distributions for the CP systems with radii $R = 25$ Å, $R = 15$ Å and $R = 5$ Å are depicted. For clarity, the red and blue curves are shifted up by 0.2 and 0.4 respectively.

diately yields the breaking of the continuum description for the density near the boundary. Thus, the effect can be thought of like probing the radial pair distribution functions $g_{OO}(r)$, cf. Figure 2.1 c), and $g_{HO}(r)$ at short distances in a reversed way by substituting r with the distance d [37]. This is verified in Figure 8.2. The panels illustrate the density distribution as a function of d and $(x^2 + y^2)^{1/2}$, the liquid-wall distance and the liquid to pore-center distance respectively. The distribution in panel a) stems from the $R = 25$ Å and in b) from the $R = 5$ Å cylindrical pore, and only the interfacial regions are shown.

Strikingly, both pictures look almost identical, with the left panel being the smoothed version of the right panel. Further, a peak region at $d < 0.2$ nm is clearly separated from the remaining distribution, which starts at a well known distance $d \approx 0.27$ nm. The interpretation is straightforward. The first peak corresponds to the first peak in the oxygen-hydrogen radial pair distribution and the second to the next-neighbor peak of the oxygen-oxygen radial pair distribution, cf. Figure 12.2 on page 178. Therefore, the pronounced layering in the CP-05 pore is attributed to the short-range order of the liquid and additionally to the small number of particles involved, what also prevents from going to the continuum case.

[37] At short distances only, owing to the disparate radial summation compared to the calculation of d. The distance d takes into account all wall atoms, therefore, $g_{HO}(r)$ is important.

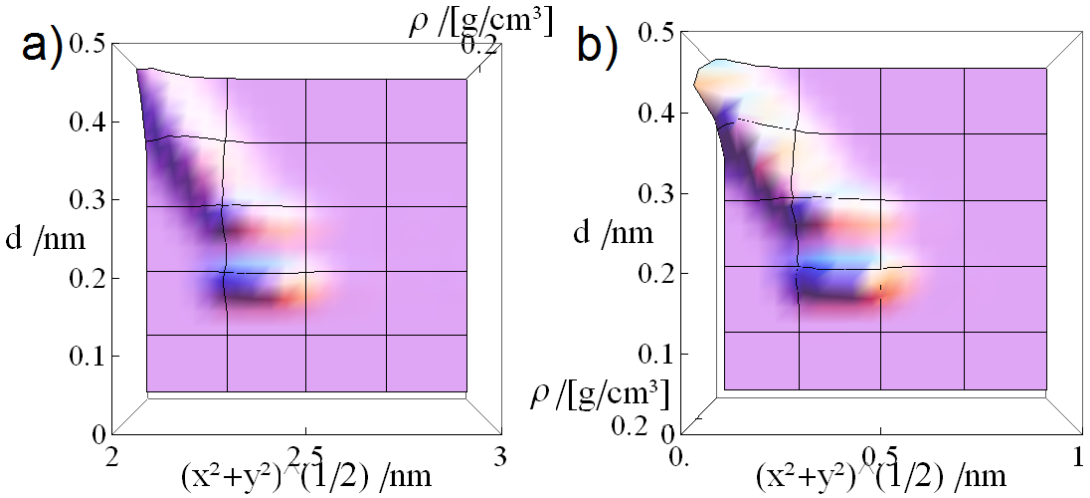

Figure 8.2: Density as function of distance to the pore wall d and the pore center $(x^2+y^2)^{1/2}$ for oxygen atoms confined to a cylindrical pore (CP). Panel a) depicts data for the pore with radius $R = 25$ Å and panel b) for $R = 5$ Å.

It is emphasized that this kind of layering is profoundly different from the one discussed for the silica pores. For the latter pores, the wall-liquid and the liquid-liquid interaction are disparate and thus give conflicting contributions to the preferred position of oxygen atoms adjacent to the wall. Hence, the layering should smear out and vanish if the breaking of the continuum description is the only mechanism under consideration.

Further, the distributions in Figure 8.2 reveal that the surface is rugged. Hence, the following analyses will take into account the roughness of the surface by segmenting the systems in subensembles with the distance d to the surface.

In a next step, the local order is scrutinized. To do so, the tetrahedral order parameter, Q_i, and the tetrahedral entropy are employed. Figure 8.3 depicts two distributions of Q_i for water adjacent to the surface of the CP systems and for the bulk at 240 K. The distributions appear to be virtually identical with the bulk result and thus support the interpretation of the layering as merely due to the short-range order of the liquid. Additionally, this is valid regardless of temperature.

In order to examine the local structure throughout the entire pores the tetrahedral entropy dependent on d will be used, see Figure 8.4. The top row shows data for the CP systems and the bottom row for the slit pore and the random-

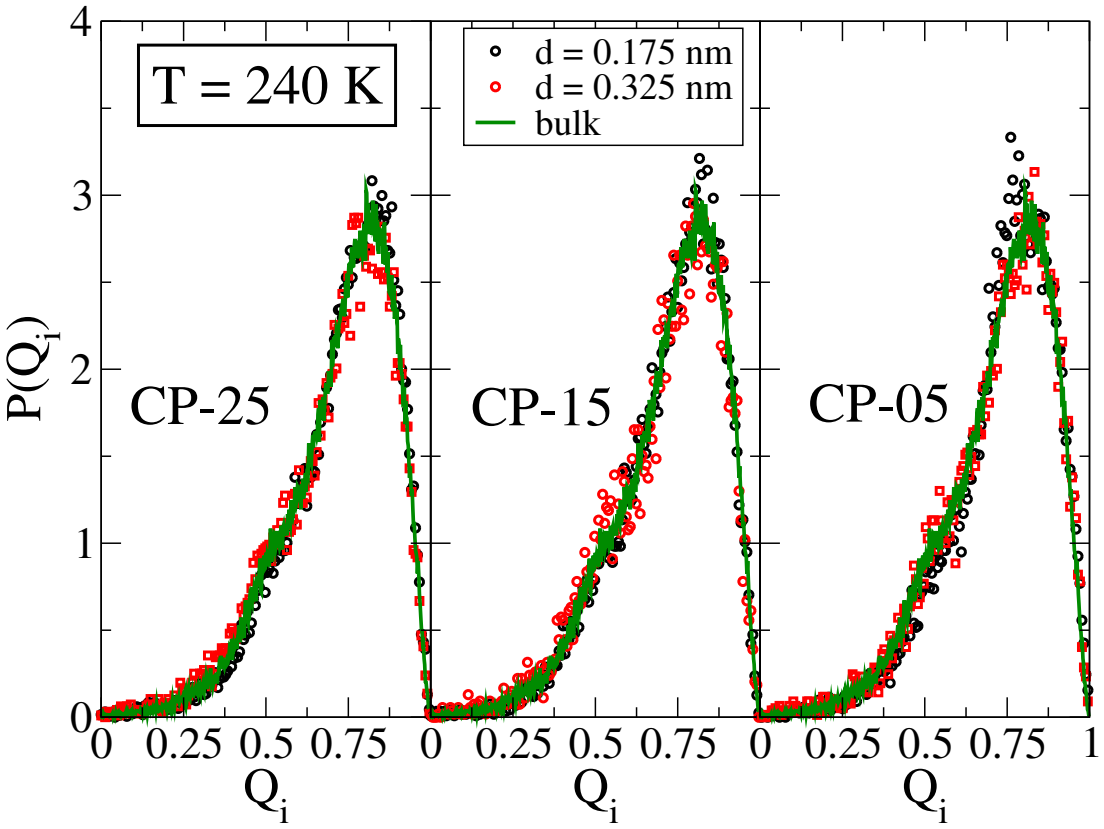

Figure 8.3: Distribution of the tetrahedral order parameter for two water layers adjacent to the wall of the cylindrical pores (CP) at 240 K. The green curve shows the bulk distribution.

pinned geometry. Evidently, the curves are in good agreement with the bulk value at a given temperature, but a pronounced deviation is visible for water in the immediate vicinity to the wall.

During the previous discussion on layering in the pores, it became clear that the peaks for the density distribution are owing to the breakdown of a continuum description for the density. The same will be shown to hold for the tetrahedral entropy.

Figure 8.5 illustrates the dependence of the tetrahedral entropy on d for various confinements and for the bulk. In the latter case, d denotes the oxygen atoms which have a distance of $[d-0.025, d+0.025]$ nm to at least one hydrogen or oxygen atom and to all remaining atoms a larger distance. That is precisely the definition to determine d for the confinement systems, but without the presence of a wall. The results exhibit a good agreement for the tetrahedral entropy of

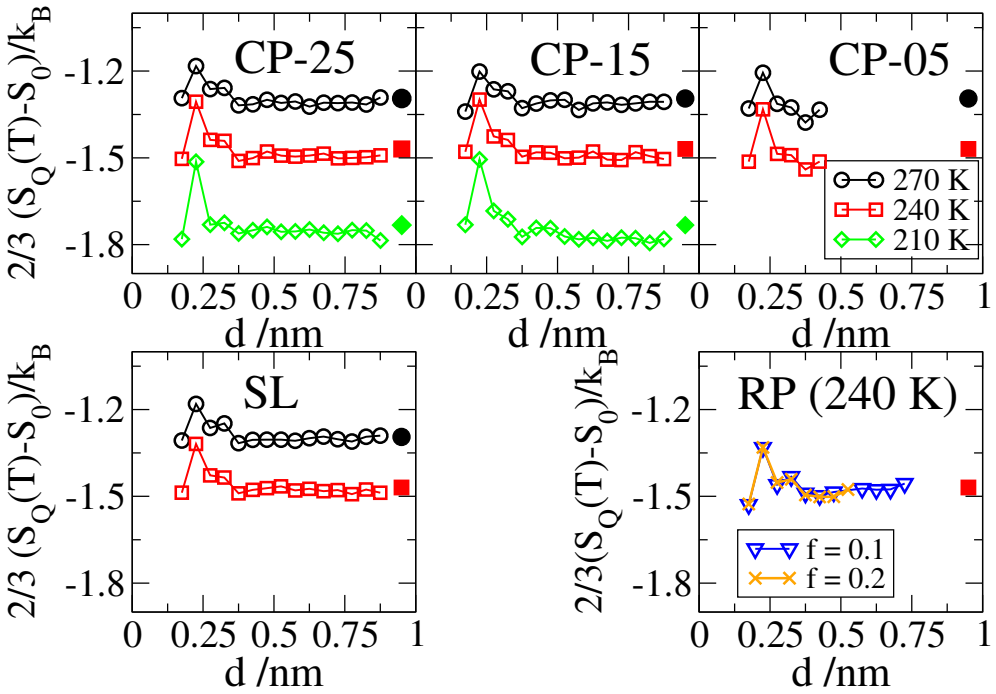

Figure 8.4: Tetrahedral entropy dependent on temperature and distance to the pore wall d. The top row depicts data for the CP systems, the bottom row for the SL and RP systems. The filled symbols denote bulk values, with the color and symbol corresponding to the particular temperature.

the bulk and various pore systems at 240 K, but this is valid at different temperatures too. Therefore, the observed deviations of the curves from the average bulk value are due to the short-range order of the liquid, like for the density.

In conclusion, it was shown that the density layering and the apparent deviations of the tetrahedral order dependent on d from the bulk average are simply the result of the short-range order of the liquid itself. Therefore, the neutral confinement provides the unique possibility to investigate dynamics within the pores without changing the structure.

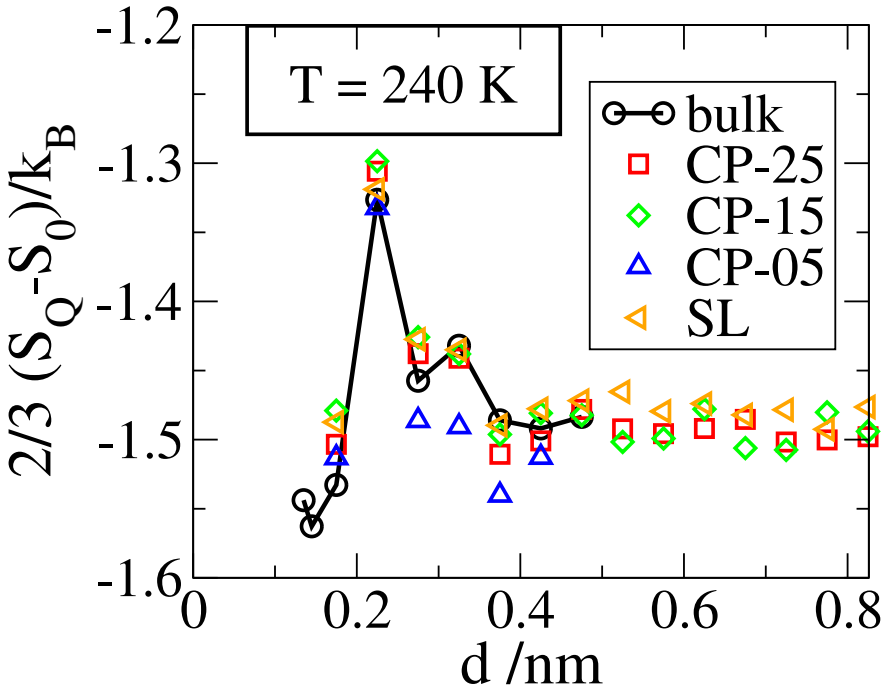

Figure 8.5: Tetrahedral entropy dependent on the distance to the wall for various confinement systems and for the bulk. See text for the notion d for the bulk in this context.

8.2 Dynamics

The focus for this subsection is mainly on translational motion. First, dynamics of water in the CP-25 pores is scrutinized, then the findings are generalized to the remaining systems.

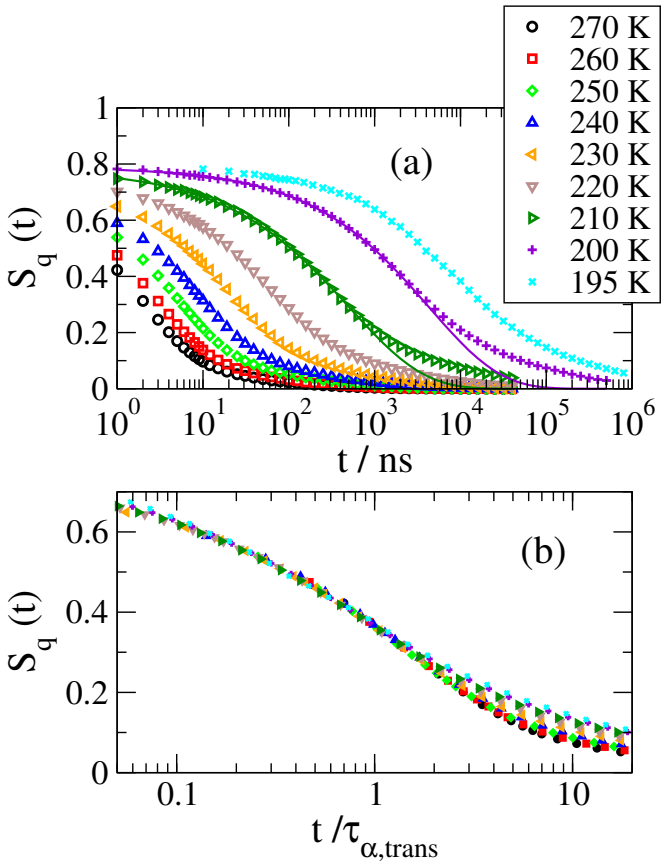

Figure 8.6: Incoherent intermediate scattering function, $S_q(t)$ with $q = 22.7\ \mathrm{nm}^{-1}$, for oxygen atoms in CP-25 confinement. Panel (b) shows the data from panel (a) but the time axis is scaled as $t/\tau_{\alpha,\mathrm{trans}}$.

Figure 8.6 shows $S_q(t)$ with $q = 22.7\ \mathrm{nm}^{-1}$ for oxygen atoms in the CP-25 confinement at various temperatures[38]. The solid lines in panel (a) are KWW functions. As for the silica pores, a pronounced long-time tail is observed, thus, the KWW functions are only able to describe the first part of the decay. Panel (b) depicts the same data but the time axis is scaled as $t/\tau_{\alpha,\mathrm{trans}}$. Here, scaling the data to a master curve is clearly not possible. This deviates from the

[38] The isotropic condition was used for calculation. See Figure 12.3 in the appendix for the legitimacy of this condition in neutral pores.

findings for water in the low density silica pore and strongly suggests that the mechanism of decorrelation changes upon cooling.

Next, the susceptibilities for $S_q(t)$, $F_1(t)$, and $F_2(t)$ are compared for the CP-25 pore, see the panels in Figure 8.7 in the same order from left to right.

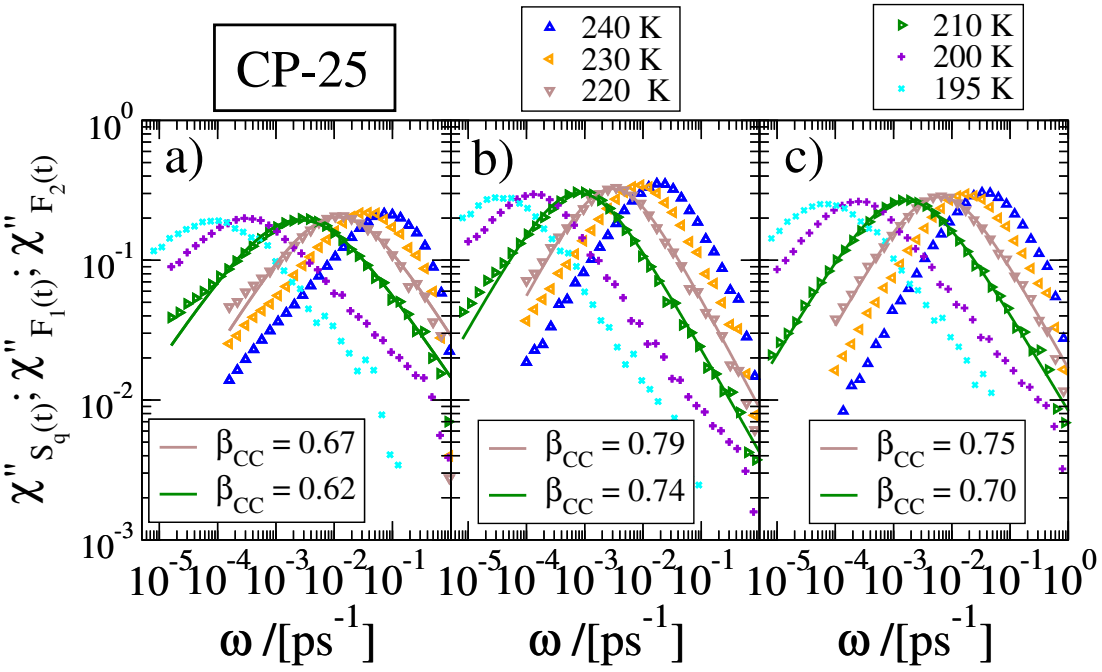

Figure 8.7: From left to right: a) Susceptibilities for $S_q(t)$ ($q = 22.7$ nm^{-1}) considering oxygen atoms, b) $F_1(t)$ for dipole reorientation, and c) $F_2(t)$ for $\vec{\text{OH}}$ bond reorientation in the CP-25 pore. Solid lines are Cole-Cole functions.

All dynamic quantities show a broad and symmetrically shaped response function corresponding to the long-time tails visible in Figure 8.6. The behavior is quantified by the solid lines, which correspond to the symmetrical Cole-Cole functions (for the definition, see equation (2.3) on page 8). It is remarkable that even the $\vec{\text{OH}}$ bond reorientation exhibits this kind of dynamics. This was not found for the silica pores. There, only $S_q(t)$ and $F_1(t)$ showed Cole-Cole like relaxation patterns and this was ascribed to an additional relaxation process for the $\vec{\text{OH}}$ bond reorientation near the surface, the *pi*-flip motion. In chapter 9, it will be shown that also for the neutral pores the π-flip motion is present. Therefore, one can speculate that the impact of the effect driving the CC-like behavior appears to be much larger for the neutral pores than for the silica pores. This is scrutinized below, but before, the transition from Cole-Cole

to KWW (or Cole-Davidson like in this context) relaxation patterns, found for the silica pores is examined.

To do so, spatially resolved analyses are performed. Figure 8.8 shows the susceptibilities for oxygen atoms of the CP-25 systems in the immediate vicinity and at some distance from the surface, $d = 0.175$ nm and $d = 0.525$ nm respectively. Evidently, the curves for surface water are very broad and a description employing a CC relaxation pattern is valid (solid lines), whereas for the distant water molecules an approximation using the CD relaxation pattern gives reasonable results (dashed lines). Therefore, there exists again a transition from CC-like relaxation for water near the surface to CD-like relaxation for water at some distance to the pore, like for the silica pores.

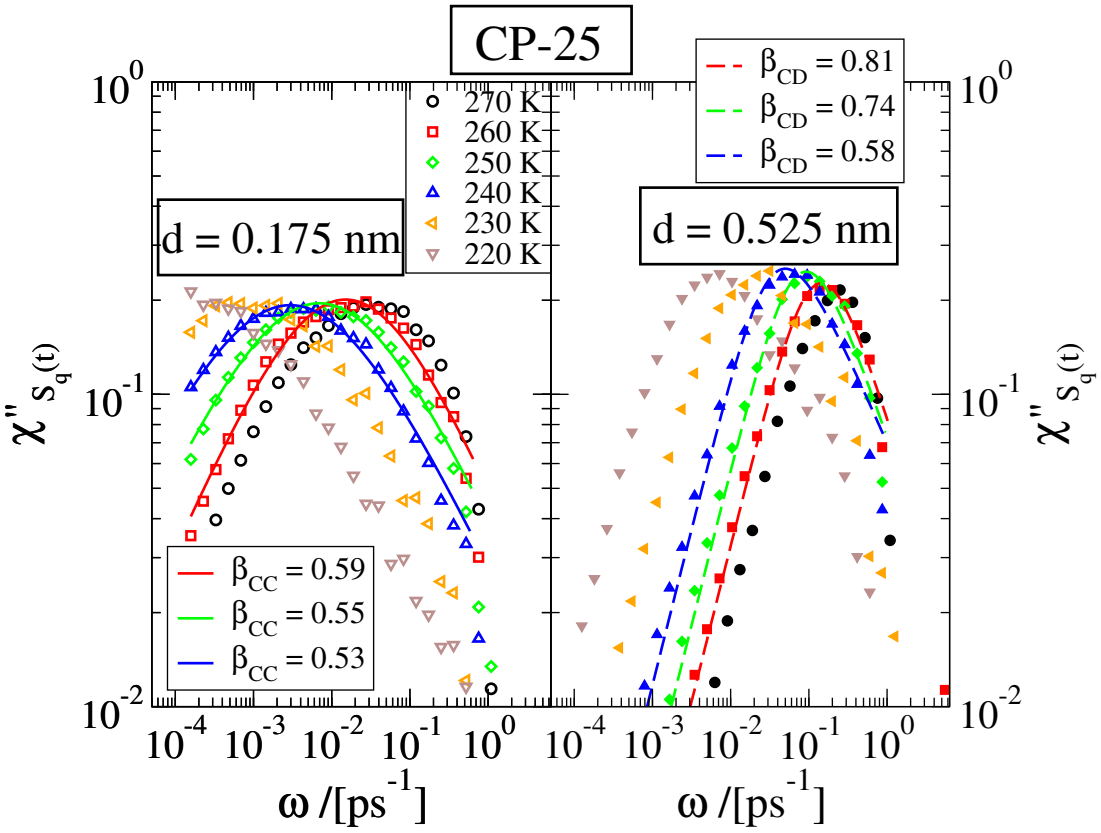

Figure 8.8: Susceptibilities for translational motion of oxygen atoms of the CP-25 system. The left panel shows data for surface water ($d = 0.175$ nm) and the right panel for water distant to the surface $d = 0.525$ nm. The solid lines are Cole-Cole functions and the dashed ones Cole-Davidson functions.

According to the findings in the previous chapter dealing with water in silica pores, CC behavior results from the presence of a static contribution to the energy landscape, which prevents the particles to entirely relax the energy landscape, even on very long time-scales. This will be also shown for the neutral confinements, but here van Hove correlation functions, $G(r,t)$, are employed, rather than conditional probability functions, see Figure 8.9.

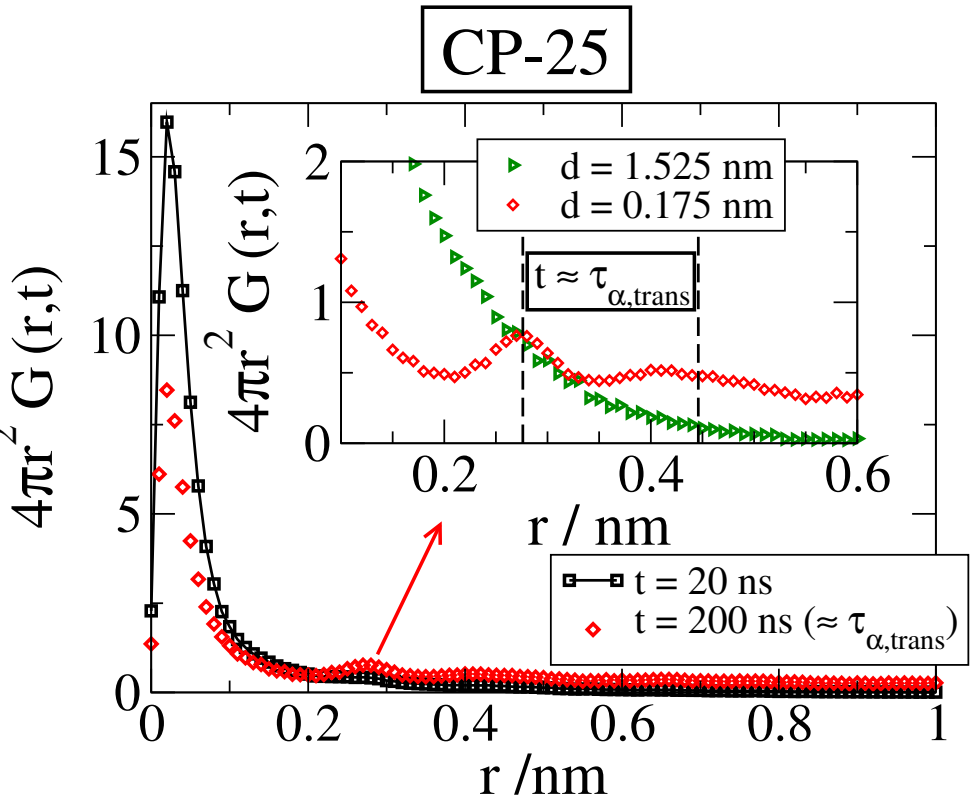

Figure 8.9: Van Hove correlation function for oxygen atoms of the CP-25 system at 200 K. The main graph shows the correlation function of a boundary layer ($d = 0.175$ nm) for two evolution times. The inset gives an enlarged view of the region of the secondary maximum at $r \approx 0.28$ nm and depicts the correlation function for two layers $d = 0.175$ nm and $d = 1.525$ nm. The dashed lines indicate the location of the first and second next-neighbor peaks for the oxygen-oxygen radial pair distribution function.

The main graph shows $G(r,t)$ for boundary oxygen atoms ($d = 0.175$ nm) of the CP-25 system for two evolution times at 200 K. For the very short evolution time ($t \approx \frac{1}{10}\tau_{\alpha,\mathrm{trans}}$) only one large peak, resulting from vibrations in the local cage is visible. Choosing $t = \tau_{\alpha,\mathrm{trans}}$ yields the emergence of a distinct

second peak. The inset depicts enlarged the region of the second maximum. Here, two water layers $d = 0.175$ nm and $d = 1.525$ nm with the same relative time scale $t = \tau_{\alpha,\text{trans}}$ are shown.

Water near the interface clearly exhibits a second maximum located at $r \approx 0.28$ nm. This perfectly matches the first next-neighbor peak for $g_{OO}(r)$, and additionally, a less pronounced peak is visible at the second next-neighbor distance (see the dashed lines). Water far away from the surface displays no such behavior. Due to the unchanged structure of the confined water compared to that of bulk, the spacing between minimums in the energy landscape must resemble the relative positions for oxygen atoms in the bulk, probed by $g_{OO}(r)$. Thus, the additional peaks strongly suggest the presence of a static energy landscape.

Next, the slowdown is examined.

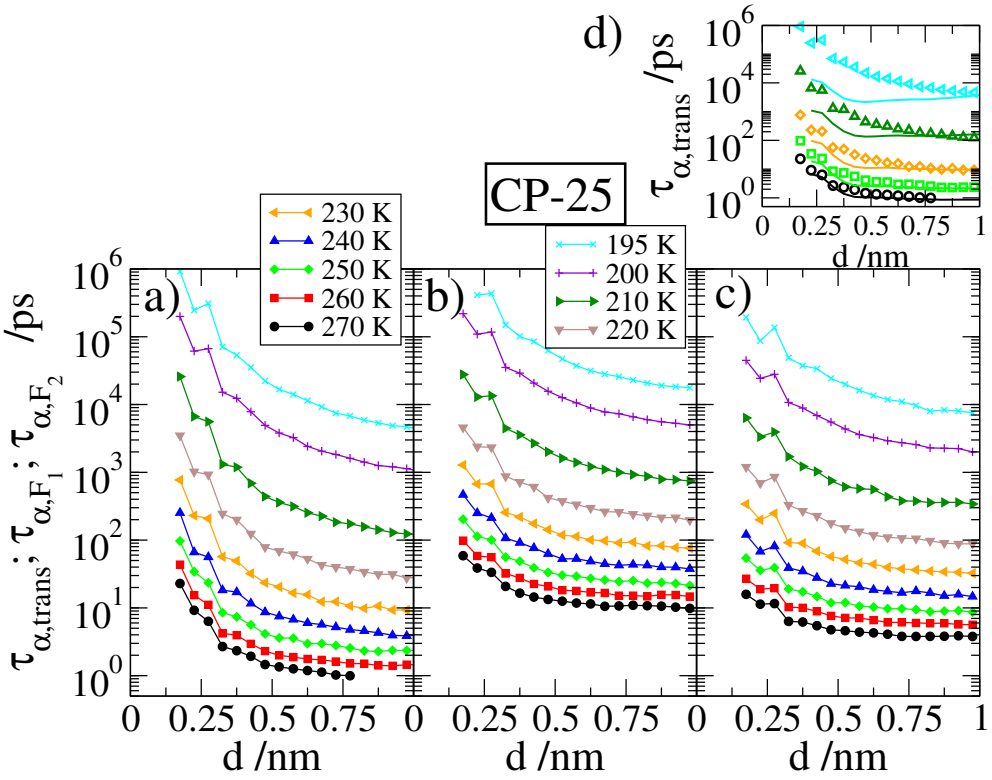

Figure 8.10: Correlation times dependent on the distance d to the pore wall of the CP-25 system. From left to right: a) $t = \tau_{\alpha,\text{trans}}$ (obtained from $S_q(t)$ with $q = 22.7$ nm^{-1}), b) $t = \tau_{\alpha,F_1}$, and c) $t = \tau_{\alpha,F_2}$. d) shows $t = \tau_{\alpha,\text{trans}}$ for oxygen atoms of the CP-25 pore and for oxygen atoms of the large silica pore (solid lines).

Figure 8.10 depicts correlation times for the translational and rotational motion of water in the CP-25 confinement. All have in common that dynamics slows down tremendously when approaching the pore wall. Therefore, the question how the slowing of dynamics in the silica pores is related to the induced disorder near the surface can be definitively answered. Even a pore wall which does not change the structure of the confined liquid yields a tremendous slowdown of dynamics. Further, the slowing is more pronounced for this pore than for the silica pores, see panel d), what was conjectured during the discussion on Figure 8.7. Thus, the influence of the neutral surface on dynamics appears larger than for the silica confinements and presumably explains why F_2 detects the slowing here but not for the silica walls. Nonetheless, this quantity is least capable to detect the slowing if compared with $S_q(t)$ and F_1.

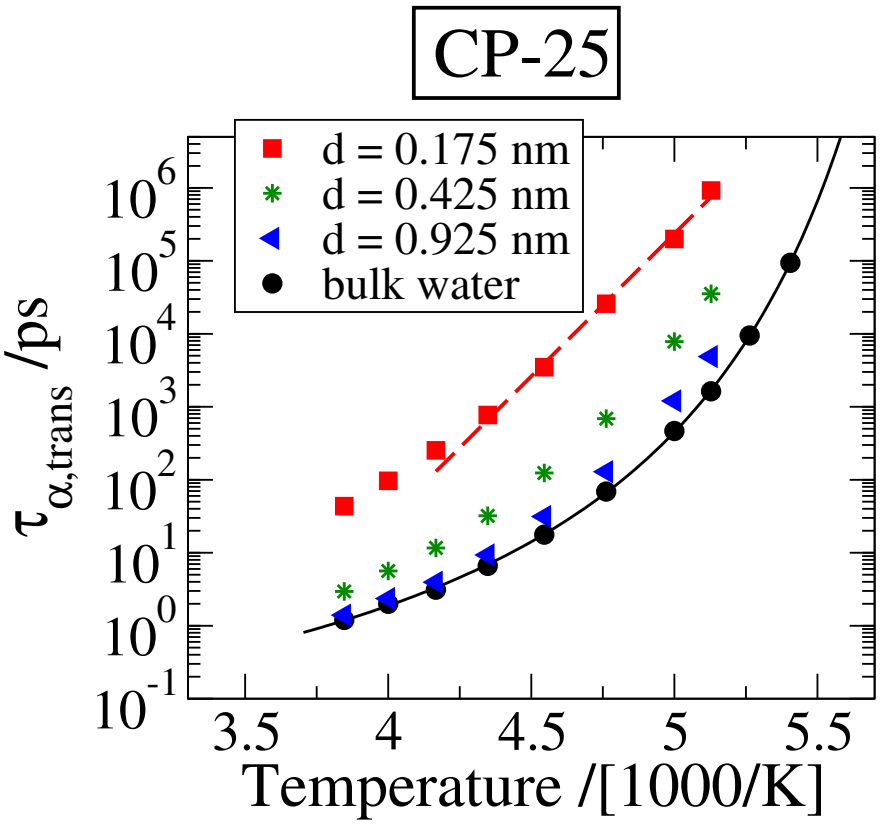

Figure 8.11: Correlation times $t = \tau_{\alpha,\mathrm{trans}}$ for oxygen atoms in the CP-25 confinement. Three different water layers are considered together with the bulk. The solid line corresponds to a VFT function. The dashed line shows an Arrhenius dependence on temperature.

The last feature of surface water, identified in the chapter dealing with silica pores as Arrhenius behavior, is examined in Figure 8.11. Translational corre-

lation times for three different water layers and for the bulk are illustrated. The solid line shows a VFT function and the dashed (straight) line indicates an Arrhenius temperature dependence for water in the vicinity of the surface. Therefore, interfacial water in neutral confinements shows similar characteristics for dynamics, namely CC relaxation patterns, *strong* behavior, and a distinct slowdown, as water in silica pores, but without imposed disorder. Thus, those effects appear to be general.

Figure 8.12 reveals that this statement is valid regardless of the geometry of the neutral pores. Panel a) shows $S_q(t)$ with $q = 22.7\ \mathrm{nm}^{-1}$ for oxygen atoms in various neutral confinements (all confined oxygen atoms considered). Distinct long-time tails are visible, corresponding to the CC behavior. Panel b) illustrates the slowdown of dynamics when approaching the pore wall. The much slower dynamics for the most narrow confinement, CP-05, is detailed in chapter 8.2.1. Panel c) illustrates the transition from *fragile* behavior for bulk water to *strong* behavior for interfacial water.

So far, the basic characterization of structure and dynamics for water in neutral confinements has been established. But neutral confinements allow for investigations, fundamentally related to fragility and processes driving the relaxation of supercooled liquids, because using the same bulk-like structure, only d determines the fragility and slowing of dynamics. A cornerstone for this will be the already mentioned breakdown of the time-temperature superposition (TTS) principle.

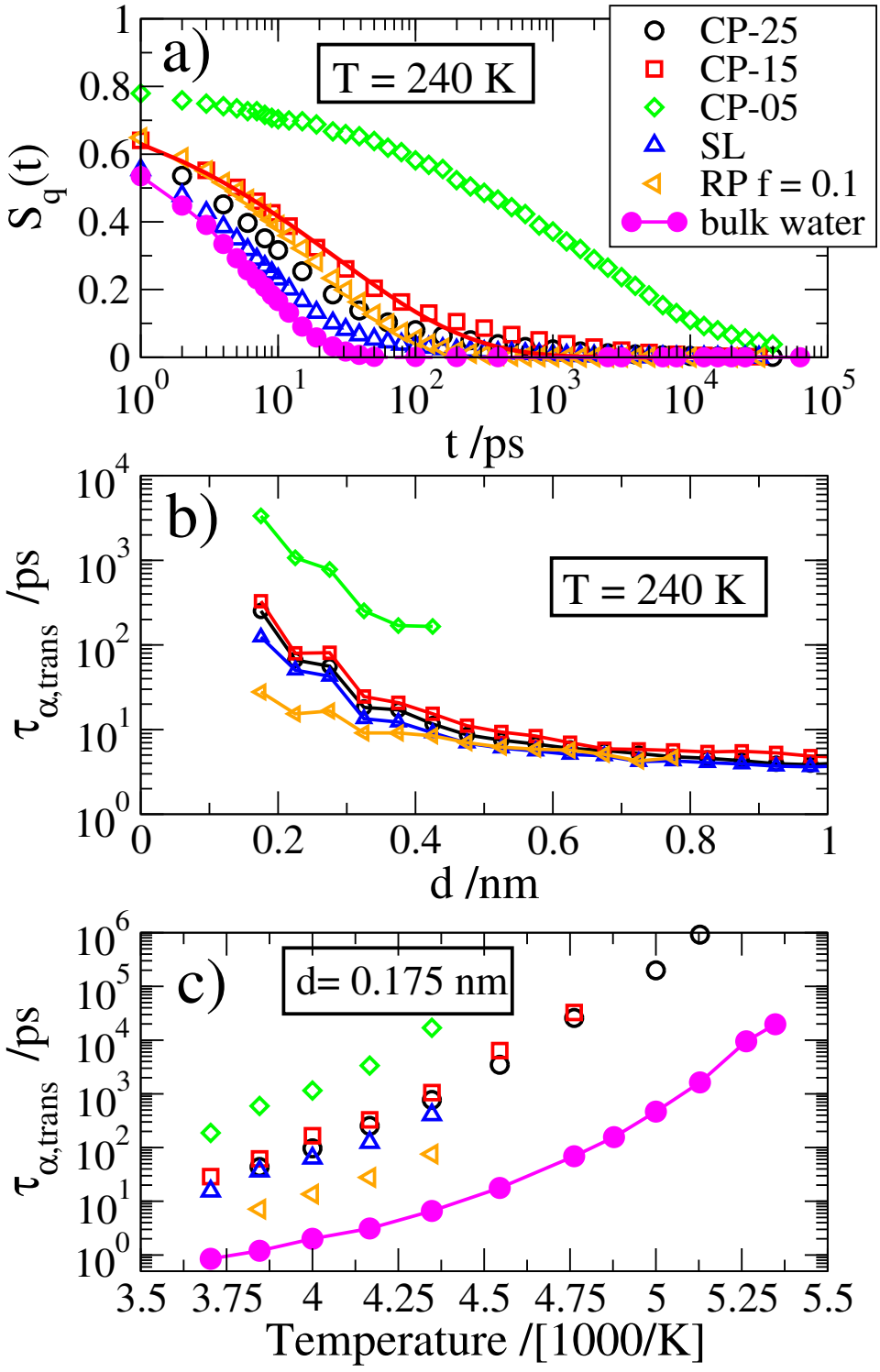

Figure 8.12: Comparing results from various geometries of neutral confinements. a) $S_q(t)$, with $q = 22.7\ \mathrm{nm}^{-1}$ for all oxygen atoms of the confined liquid. The solid line is a KWW function. b) Correlation time $\tau_{\alpha,\mathrm{trans}}$ dependent on the position d at 240 K. c) $\tau_{\alpha,\mathrm{trans}}$ for water near the surface ($d = 0.175$ nm) as a function of temperature.

8.2.1 Dynamic length scales

This chapter deals with dynamic length scales, referred to as ξ_d. These lengths are obtained from the range on which the surface affects the translational correlation times $\tau_{\alpha,\mathrm{trans}}$. In order to quantify this, an empirical equation is employed, see below, and dynamic profiles are investigated again, but this time, the representation of the vertical axis is changed. Figure 8.13 depicts the translational correlation times as $\ln(\tau_{\alpha,\mathrm{trans}})$ dependent on d for the cylindrical pores, from left to right for the $R = 25$ Å, $R = 15$ Å, and $R = 05$ Å pores.

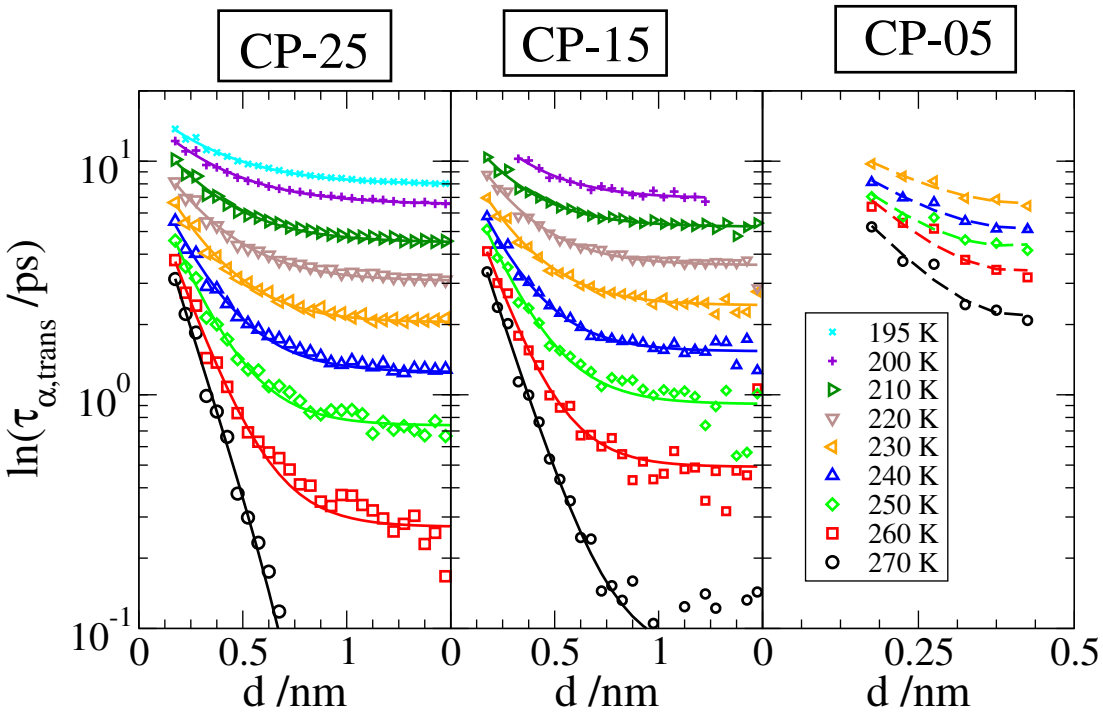

Figure 8.13: Dynamic profiles. Correlation times $\ln(\tau_{\alpha,\mathrm{trans}})$ dependent on d. From left to right: data for the CP-25, CP-15 and CP-05 systems. The solid lines are stretched-exponential functions, see equation (8.1) and dashed lines modified stretched-exponentials, see equation (8.2).

The solid lines are fits according to the empirical function

$$\ln\left(\frac{\tau_{\alpha,\mathrm{trans}}}{\tau_\infty}\right) \propto e^{-(d/\xi_d)}, \tag{8.1}$$

which was previously employed to describe data for a binary Lennard-Jones mixture [193]. The function comprises the distance to the pore wall d, a characteristic length scale ξ_d, which is proposed to be related to the dynamic length

scale of RFOT [18], and τ_∞, the value of correlation times far away from the surface. In very large pores, τ_∞ should equal τ_{bulk}, and indeed, τ_∞ is similar to τ_{bulk} for the large pore (CP-25), but the ratio $\frac{\tau_\infty}{\tau_{\text{bulk}}}$ deviates systematically for the CP-15 pore and the deviations increase as the temperature is reduced. This has been found to be attributable to an additive non-linear feedback mechanism, additionally slowing dynamics [193], reading

$$\ln\left(\frac{\tau_{\alpha,\text{trans}}}{\tau_\infty}\right) \propto A \cdot e^{-(d/\xi_d)} + B \cdot e^{-(R-d)/\xi_d}, \tag{8.2}$$

with the second term on the right-hand-side accounting for the absence of bulk-like behavior in the system, $B > 0$, and R the radius of the pores. The dashed lines for the CP-05 data show approximations using the latter equation. To do so, ξ_d and τ_∞ from the CP-25 pore were employed. The weighting factors A and B reveal an increasing impact of the second term upon reducing the temperature. Hence, suggesting the reason for the much slower dynamics for oxygen atoms in the CP-05 pores, see also Figure 8.12 [39]. This restricts the analyses to systems where the confinement effect is assumed to be not too strong, namely CP-25, CP-15, SL and the RP systems with $f = 0.1$. Otherwise, to many free parameters prevent a proper approximation.

Figure 8.14 shows the dynamic profiles for the RP geometries. Panel a) depicts the RP $f = 0.1$ system and the solid lines are functions according to equation (8.1). Panel b) illustrates a different approach for the RP systems. Here, an averaged confining length was defined according to $\langle d \rangle = 1/2(v/f)^{1/3}$, with v the average volume per particle. This was recently proposed in the literature [18] and the systems are denoted as $\langle$RP$\rangle$. For both approaches, τ_∞ was set to τ_{bulk}, see the circles at larger distances marking τ_{bulk}.

It is striking that the exponential functions describe the data for all neutral confinements, thus in a next step, the obtained dynamic length scales ξ_d are scrutinized.

The absence of the TTS principle, cf. Figure 8.6, indicates a growing length scale which changes the size of the influenced region [40]. The length scales

[39] It turns out that the equations from [193] can be used almost without modification. This is surprising due to the different geometries, slit vs cylindrical. For the CP-05 pore an effect due to the curvature of the surface was expected but seems to be small.

[40] To the best knowledge of the author, this statement is only valid for confinement systems. MCT predicts an increasing length scale and TTS, but for the confinement systems, an increasing length alters the affected volume of the finite system and hence the statement can be made.

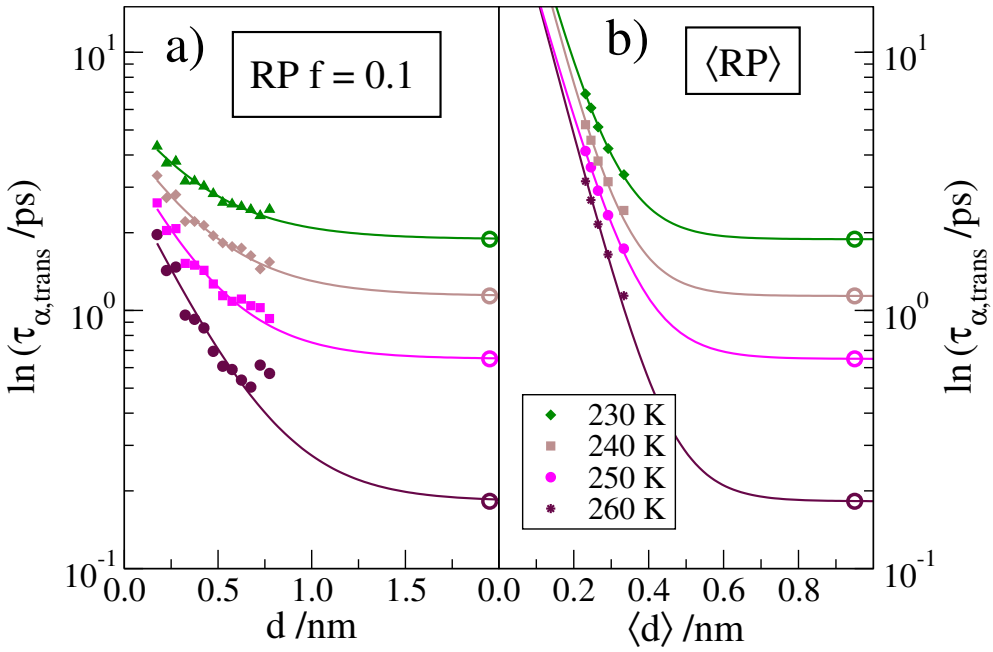

Figure 8.14: Correlation times $\tau_{\alpha,\text{trans}}$ as a function of distance to the wall for various geometries. ⟨RP⟩ denotes a different approach to obtain a confining length $\langle d \rangle$. In this particular case $\langle d \rangle = 1/2(v/f)^{1/3}$, with v the average volume per molecule [18, 199]. The circles mark the correlation times for the bulk.

ξ_d for various confinement geometries are shown in Figure 8.15. An increasing length is found for the CP-25, CP-15 and SL confinements, additionally, the manner appears to be a linear function of inverse temperature and the values for these confinements are almost identical. For the RP $f = 0.1$ pore, ξ_d increases too, but for the ⟨RP⟩ system ξ_d appears constant.

As stated in the theory section, RP geometries with a low fraction of pinned particles yield contributions to dynamics which are not related to a deeper physical meaning for supercooled liquids. This was shown by *Szamel* who performed MCT calculations on RP geometries and found that for these systems a non-vanishing term in the memory kernel, due to the presence of the wall atoms, mediates an additional interaction between mobile particles which governs the low pinning regime [84]. This might explain the deviating length scales for the RP $f = 0.1$ system. Unfortunately, it is not possible to use much larger pinning fractions and perform the same analysis like for the RP $f = 0.1$ confinement, because the slowing of dynamics is dramatic due to the impact of the finite-size effect, see the second term on the right-hand side of equation (8.2). This renders such analyses beyond the capability of computer resources.

The findings for the ⟨RP⟩ approach are in agreement with other studies on RP systems [200]. However, the results for the CP-05 pore indicate that employing an averaged distance to the pore wall $\langle d \rangle$ and using equation (8.1) is not suitable. This can be understood using equation (8.2). Due to the changing impact of the non-linear feedback introduced by a more narrow confinement, a comparison between the different $\langle d \rangle$ or fractions f of pinned particles is not convenient as these systems should be governed by different parameters A and B. Also the change with temperature for the parameters might be non-linear and dependent on f.

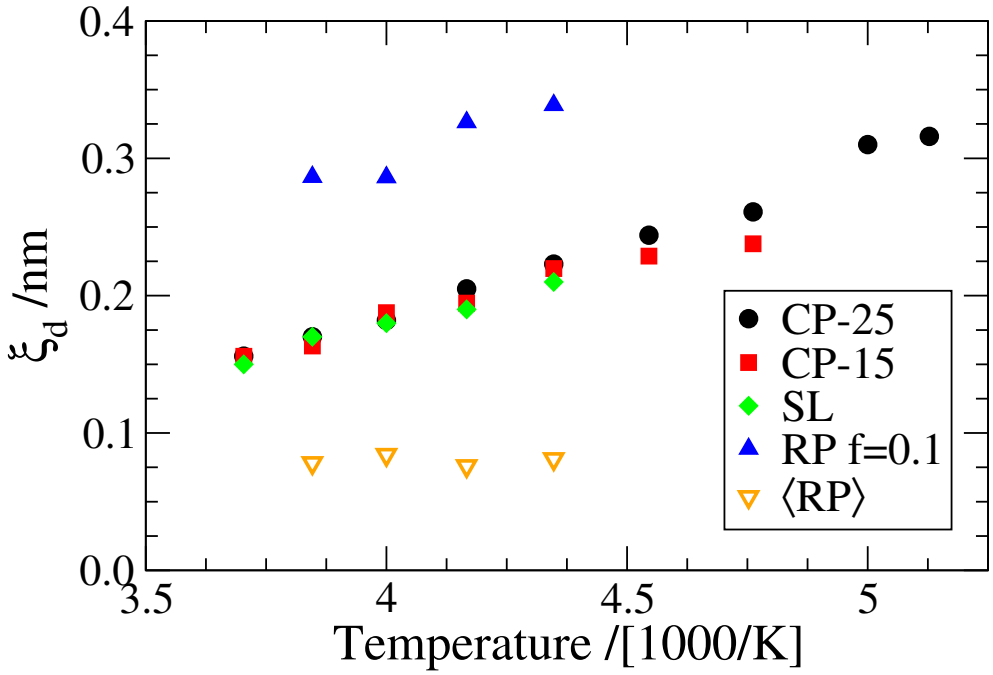

Figure 8.15: Correlation length ξ_d as a function of temperature for various geometries. ⟨RP⟩ denotes a different approach to obtain a confining length d. In this particular case $\langle d \rangle = 1/2(v/f)^{1/3}$, with v the average volume per molecule [18, 199].

Concluding, all confinements, apart from the ⟨RP⟩ approach, yield a monotonically increasing dynamical length scale ξ_d upon cooling. As mentioned above, ξ_d was proposed to be related to the dynamic length scale of the MCT approach ξ_{MCT} [18], which was introduced during the discussion of the RFOT theory in chapter 2.4. The MCT length scale gives a measure on how dynamics is correlated on times τ_α. So, one can establish a connection between ξ_d and ξ_{MCT}: The maximum of four-point correlation functions can be used to

determine ξ_{MCT}, however, it was stated in chapter 6.5 that this is a complex task due to local fluctuations, which hamper the analyses. Instead, the peaks of the four-point correlation functions were used to establish τ_α as structural correlation time. According to the coincidence of the peak of four-point correlations and τ_α, one can speculate that both length are related as ξ_d is based on structural correlation times, too. Following this, one can state, that at least in the investigated temperature regime, no clear indication for a transition to activated dynamics is present as ξ_d exhibits no peak behavior.

8.2.2 Static length scales

Next, the static length scales are examined. It is emphasized that the way how the static length scale was determined is not identical to the idea by *Bouchaud* and *Biroli*, see chapter 2.4. For the present study, a self overlap $Q(t)$, see equation (5.19), is computed as function of the distance to the pore wall, and no point-to-set correlation with the wall. Figure 8.16 illustrates the main idea. Panel a) shows a system, with particles marked by the red circles. Then, panel b), the position of the particles below the red line is locked, see the red-shaded area. This is the initial configuration. In c), time evolves and all particles can move to different places. If one of the red-shaded areas is occupied by a particle, regardless of which one, the overlap function counts this cell as 1 and 0 otherwise. Hence, this quantity probes to what extent configurations can change.

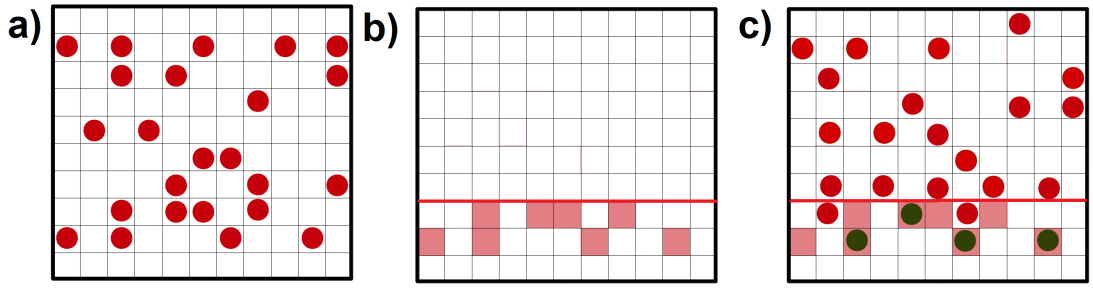

Figure 8.16: Schematic illustration for the definition of overlap functions. See text for explanation. The figure is adapted from [58].

One important aspect is that it is possible to probe different configurations for a certain ensemble of particles, like all particles below the red line in panel b) of Figure 8.16. This will be used to select particles in a certain distance to the pore wall.

Following *Charbonneau* and co-workers, it is valid to use this self-overlap ap-

proach, and the static length obtained this way is presumably proportional to the point-to-set length scale for most of the temperature regime accessible in the present study [201]. Figure 8.17 illustrates $Q(t)$ and $S_q(t)$ with $q = 22.7$ nm^{-1} for oxygen atoms at 240 K. The data stem from the SL, CP-15 and CP-25 confinements. Every row shows data for one of the mentioned systems. $S_q(t)$ depicts the previously detailed long-time tails if compared with the bulk, but $Q(t)$ is different.

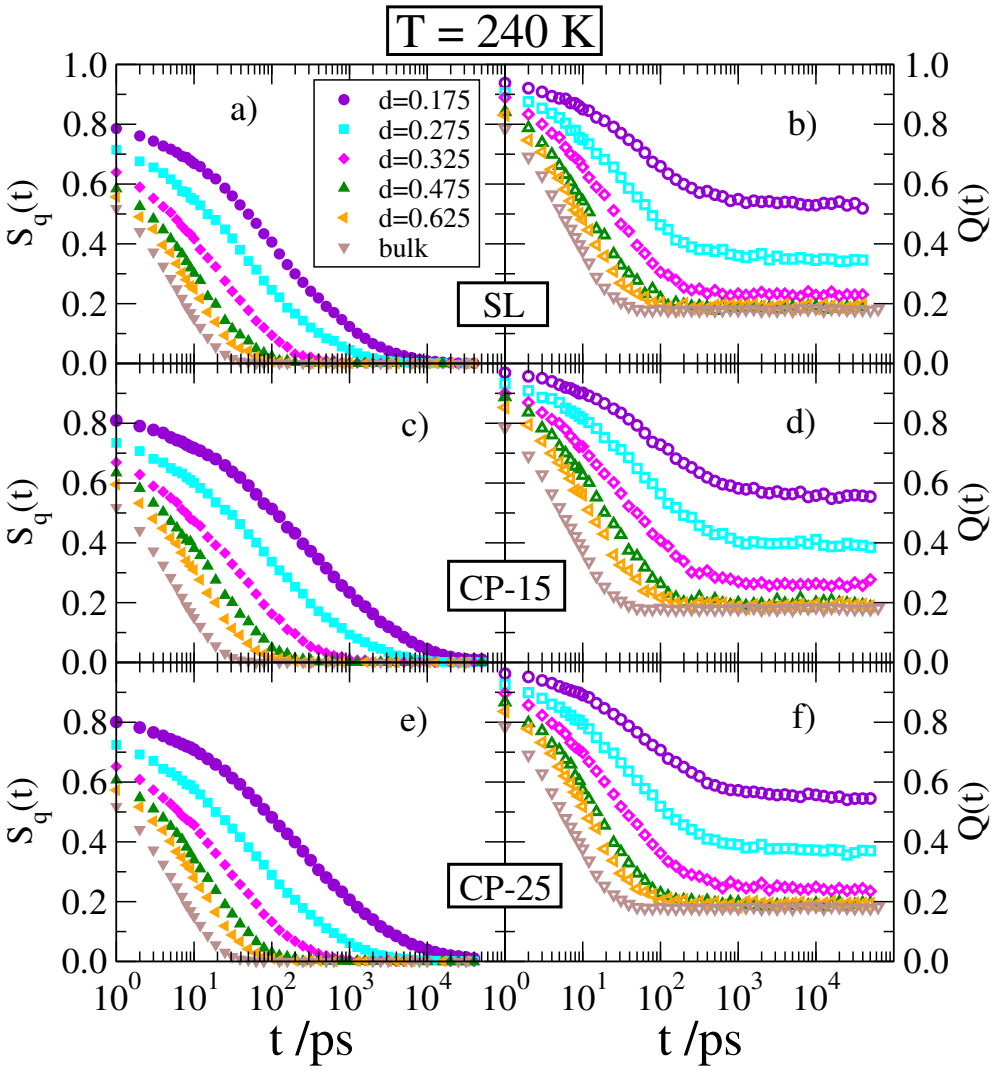

Figure 8.17: Comparison between $S_q(t)$ with $q = 22.7$ nm^{-1} (left column) and overlap function $Q(t)$ (right column) for oxygen atoms in several confinements at 240 K. The top row shows data for the SL confinement, the middle row for the CP-15 pore and the bottom row for the CP-25 system.

First, there is also a stretched-exponential decay, but then a plateau value is reached. The focus of the following discussions is on the long-time plateau, referred to as Q_∞. The plateau for the bulk, denoted Q_{rand}, is simply due to the finite density of the liquid, hence, the initial configurations can not decorrelate to an arbitrary small extent. The plateau height is also a function of the size of the cells, which is set to a fixed value of 0.11 nm radius, cf. chapter 5.2.7. It is very important to realize that $Q_{\text{rand}}(T)$ gives the lower boundary for all neutral confinements, because they are equilibrated in the NpT ensemble and yield the average density and structure of the bulk. Further, Q_∞ is also a function of the distance to the wall. Therefore, $Q(t)$ is ascertained as function of d, see Figure 8.18.

Strikingly, Q_∞ is strongly dependent on temperature and distance to the pore wall d for the CP-25 and SL confinements. The solid lines are stretched-exponential functions in agreement with equation (2.31), with L substituted by d, reading

$$Q_\infty(d,T) = (1-A)\cdot e^{-\left(d/\xi_S\right)^\phi} + A. \tag{8.3}$$

A refers to Q_{rand} and is almost identical to it (deviation ≈ 0.004 at 240 K), but due to statistical issues concerning the small bulk system and thus large fluctuations for Q_{rand}, A was chosen as a free parameter. The compressing parameter ϕ rises from ≈ 1 to ≈ 2 for the lowest temperatures, in general agreement with the literature [80]. Additionally, the curves for the CP-25 and SL confinement are similar.

The results for the CP-25 and SL confinements suggest that the wall imposes a static energy landscape which becomes more pronounced as the temperature is reduced. In contrast to previous approaches to detect static or at least long-resting contributions owing to the energy landscapes, this approach gives the opportunity to precisely determine the range, ξ_S, and strength, $Q_\infty(d,T)$, of this effect, and additionally yields a straightforward comparison between different geometries owing to the common boundary Q_{rand}.

Figure 8.19 illustrates $Q_\infty - A$, with A determined by fits to data from the CP-25 system at 240 K, see Figure 8.18. The CP-25, CP-15 and SL geometries show similar behavior. Data for the CP-05 confinement is not presented as the slow-down of dynamics is too strong to observe proper plateau values for $Q(t)$. The RP $f = 0.1$ confinement exhibits a very weak dependence on d, consequently, it was not possible to describe the data by employing equation (8.3). In contrast, the $\langle\text{RP}\rangle$ approach reveals a steeper dependence on $\langle d\rangle$ than the CP and SL

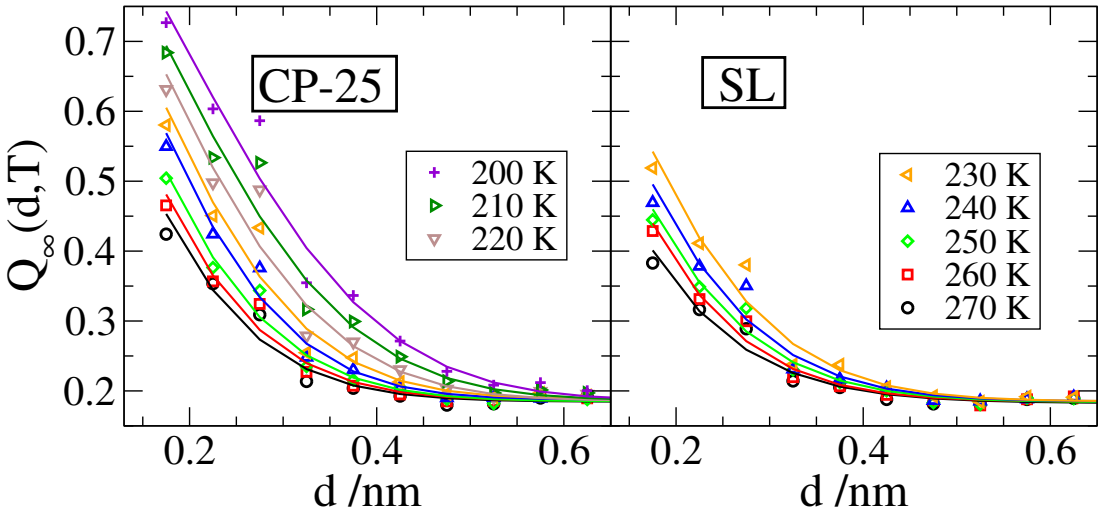

Figure 8.18: Q_∞ dependent on d and temperature. The left panel shows data for the CP-25 system. The right panel for the SL geometry. The solid lines are fits using equation (8.3).

confinements, but a description with equation (8.3) is suitable, see orange line.

The reason why the RP $f = 0.1$ system shows this peculiar behavior can be rationalized with the statement given during the discussion on dynamic length scales. *Charbonneau* and *Szamel* set out in their publications that in the limit of a small fraction of pinned particles a rather trivial contribution to Q_∞ prevails, which is only related to trivial two-point correlations and thus is not appropriate to detect configurations contributing to S_C, as this is the very idea of employing Q_∞ [83, 84]. Nonetheless, this system is very valuable and the data is depicted, because it illustrates the *simple* contribution, and one can therefore assume that the SL, CP and ⟨RP⟩ confinements are not in the low-pinning limit.

Further, the static length scales ξ_S are examined, see Figure 8.20 b). Panel a) shows the dynamic length scales discussed above as comparison. Like the dynamic lengths the static ones increase upon cooling. Additionally, all systems for which ξ_S could be obtained reveal a very similar dependence on the temperature. It might appear puzzling why the ⟨RP⟩ approach gives similar length scales like the CP and SL confinements in this case, however, for the dynamical lengths, the approach was ruled out based on finite-size effects. In contrast to this, the thorough analysis of Q_∞ by *Biroli* revealed no additive impact for very narrow pores, compare equation (8.3) with (8.2) [80]. This can be understood regarding the long-time limit for Q_∞ which does not account for bulk-like fluctuations. The missing of these fluctuations in very narrow confinements is at

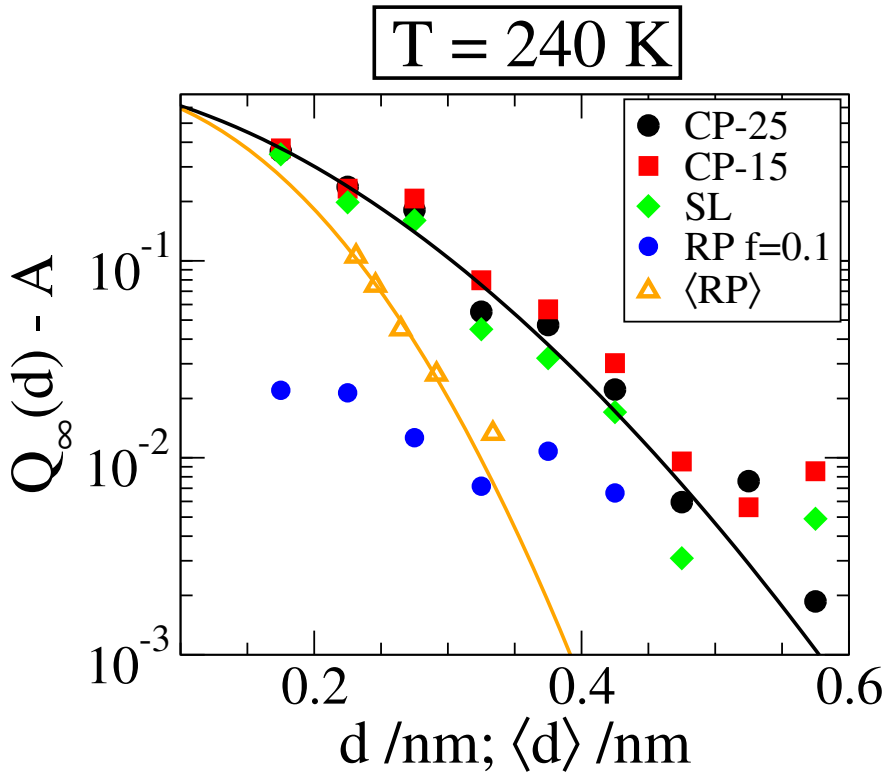

Figure 8.19: $Q_\infty - A$ dependent on d for various confinement geometries at 240 K. A was obtained from fits according to equation (8.3) for the CP-25 confinement at 240 K, see the black line. For the ⟨RP⟩ approach, the distance to the pore wall is defined as $\langle d \rangle = 1/2(v/f)^{1/3}$, with v the average volume per molecule [18, 199], and the orange line is a fit using equation (8.3).

the bottom for introducing the second term in (8.2).

Furthermore, the straight dashed lines are a linear regression for ξ_S of the CP-25 system. The approach approximates the temperature dependence of ξ_S and also of the dynamic length scales, apart from the RP systems. This is surprising given the very different ways the length scales have been defined and suggests an unknown relation between them.

In conclusion a monotonic increase of the static length scales was observed. It was argued that the increase is indeed related with the balance between ΔF_{surf} and ΔF_{vol} as the low-pinning limit, presumably given by the RP $f = 0.1$ confinement, exhibited very different behavior for Q_∞, making it impossible to properly derive a static length scale.

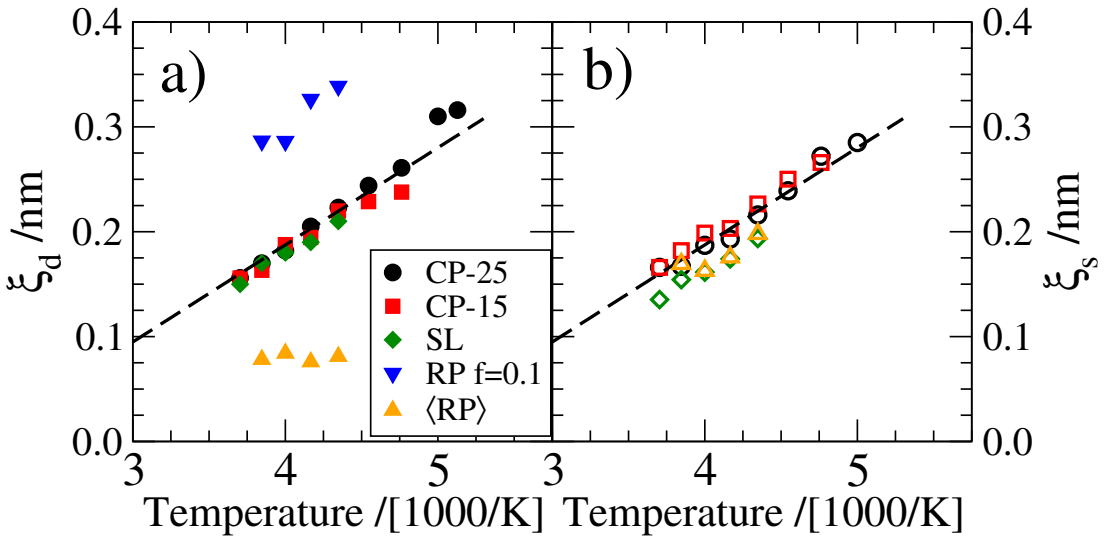

Figure 8.20: Panel a): dynamic length scales, the same as in Figure 8.15. Panel b): Static length scales obtained from fits according to equation (8.3). The dashed lines show a linear regression for ξ_S of the CP-25 confinement.

8.2.3 Fragile behavior and RFOT

The increasing static length suggests a fragile behavior for water as the size of amorphous order or droplets increases and therefore the free-energy barrier too. Hence, the next step is to transfer the findings from the pore to the bulk system. This is done by relating ξ_S directly with $\tau_{\alpha,\mathrm{bulk}}$. The correlation times for the bulk are explicitly denoted $\tau_{\alpha,\mathrm{bulk}}$ to highlight the very important transfer from findings for the neutral pores to the bulk system and are obtained from $S_q(t)$ for oxygen atoms with $q = 22.7\ \mathrm{nm}^{-1}$. The main problem hampering this approach is that it was presumably possible to get a length scale were the surface tension and the entropy contribution balance, but the exponent ψ is not known, see equation (2.30). In previous studies, the exponent ψ was found to vary between 1 and 2, what would maybe yield a fractal surface of the droplets [82, 202].

Figure 8.21 depicts both length scales, ξ_d and ξ_S as function of $\tau_{\alpha,\mathrm{bulk}}$. For water, it turned out that an exponent $\psi = 2$ gives reasonable results for both length scales from the SL and CP confinements, see the dashed lines which indicate a linear dependence of $\ln(\tau_{\alpha,\mathrm{bulk}})$ on $\xi^2_{d;S}$. An exponent $\psi = 2$ would first yield a surface with dimensionality $\theta = 2$, and in this case, the droplets were

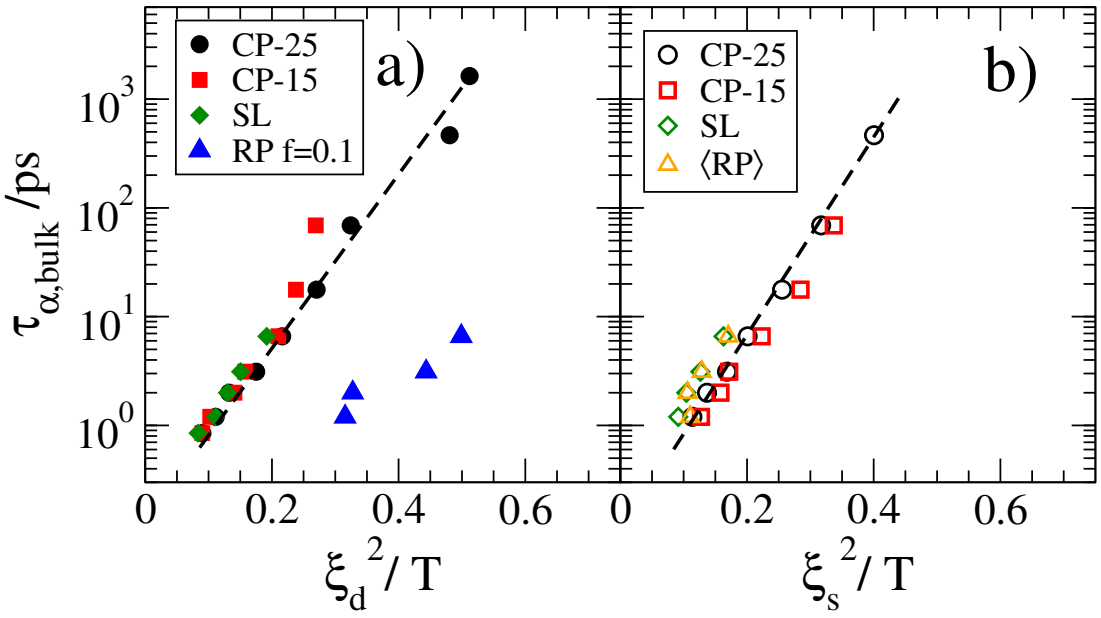

Figure 8.21: Length scales $\xi^2_{d;S}/T$ as function of $\tau_{\alpha,\mathrm{bulk}}$. Panel a) shows the results for the dynamic length scale ξ_d, panel b) for the static length scale ξ_S. The dashed lines indicate a linear correlation for $\xi^2_{d;S}/T$ with $\tau_{\alpha,\mathrm{bulk}}$.

simple and compact objects. Second, the temperature dependence of $\tau_{\alpha,\mathrm{bulk}}$ would not be identical to a VFT approach, as this follows for $\psi = 3/2$, see chapter 2.4.

For the RP $f = 0.1$ geometry, ξ_d seems to deviate from the $\psi = 2$ dependence. The reason for this behavior was detailed in the last two subsections, and is arguably owing to the low-pinning limit. In contrast, ξ_S from the ⟨RP⟩ approach is virtually identical to the static length scale from the SL and CP confinements.

Despite this success in finding a relation between the correlation times and the length scales obtained from pores, the questions are still which of these two length scales is dominating the slowdown and fragility and specifically is there a transition from non-activated to activated dynamics? Studies of supercooled SPC/E estimated $T_C \approx 200$ K [49]. The performed simulations for neutral confinements cover the temperature regime from 270 K down to 195 K, thus, evidence for the transition should be within range, but was not observed. To finally answer these questions for SPC/E, lower temperatures have to be achieved what is not possible with the current computer resources. Instead, using silica as confined liquid in neutral silica pores would possibly be fruit-

ful due to the known transition from fragile to strong behavior for this system [56, 203]. For this system, the temperature regime was accessible more than 10 years ago, thus, nowadays computer resources should not limit the analyses and the changing temperature dependence should, according to RFOT, be reflected in a growing or constant static length scale. Therefore, this could be used as test for the theory.

As no clear-cut evidence supporting the transition idea of RFOT could be found, the next analyses will focus on the changed fragility and the slowdown of dynamics near the pore wall.

8.3 Assessing the slowdown of dynamics

It was pointed out that dynamics slows down for water near silica walls and near the neutral surface. Additionally, it was stated that this is due to an energy landscape imposed by the surface. Therefore, one can ask what will happen if the wall-liquid interaction is changed by altering the HB strength between the surface and the liquid?

This can be done by changing the charges on the wall atoms while the net charge of every molecule is still zero and the charges of the liquid part of the system are not modified. Increasing the polarization of the wall atoms yields stronger HB with the liquid and vice versa. For the following analyses, the polarization is characterized by the charge on the oxygen atoms of the wall q_{M}. The more negative, the more polarized are the wall molecules.

Given the statements above, it is expected that the structure of water molecules adjacent to the wall is affected by changing the polarization of the surface, as this is no longer a neutral confinement. Additionally, the slowing should be reduced for low wall polarization and enhanced for increased wall polarization, because the imposed effects on water molecules near the surface should be weaker or stronger, respectively.

In order to investigate the effect of the changed wall polarization, the CP-25 confinement at $T = 240$ K was used. No new equilibration was conducted, but rather, the wall polarization was changed and new production runs in the NVT ensemble were carried out for a single temperature $T = 240$ K. Five different polarizations are investigated.

Figure 8.22 shows the density distribution dependent on the distance to the

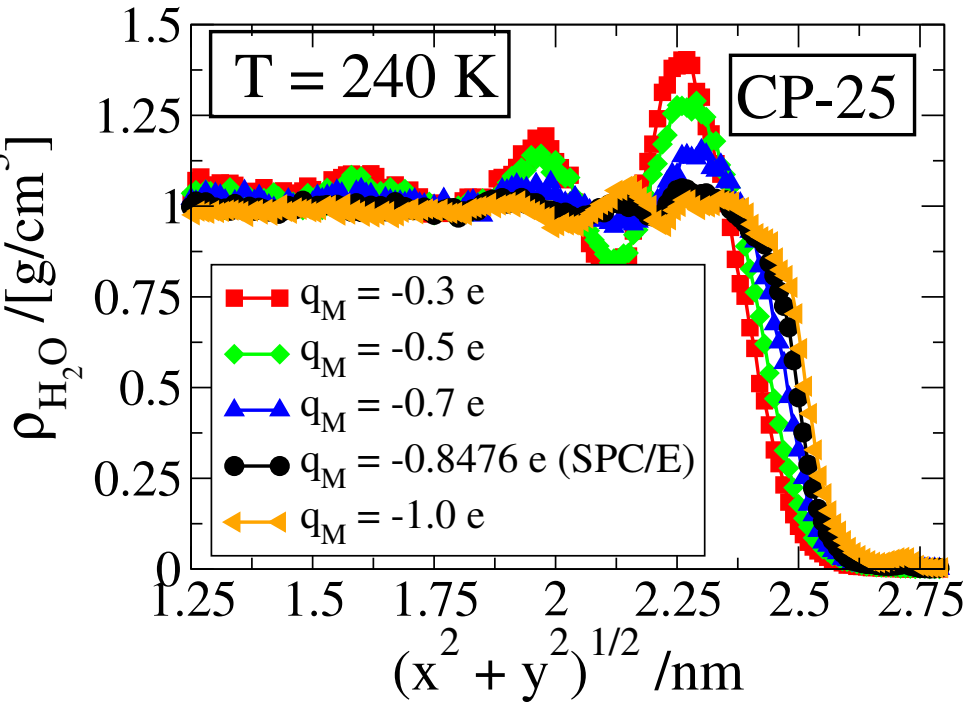

Figure 8.22: Density distribution dependent on the distance to the pore center for various wall polarizations of the CP-25 pore at 240 K. q_M denotes the charge on the wall oxygen atom. $q_M = -0.8476$ e corresponds to the neutral pore. The charges of the liquid are not changed and the net charge of all water molecules is zero.

pore center. $q_M = -0.8476$ e corresponds to the neutral CP-25 pore. Evidently, density layering becomes significant upon lowering the polarization. Reducing the polarization by ≈ 18% (the blue curve) yields a peak adjacent to the surface, but increasing the polarization by roughly the same amount (the orange curve) gives a smaller peak, which is not in the immediate vicinity to the wall, at ≈ 2.125 nm. For low wall polarizations, the water molecules are repelled and the density distribution shifts to the left. On the contrary, for enhanced polarization, water molecules are attracted towards the wall and the density distribution shifts to the right. This behavior is expected as the original CP-25 confinement is no longer a neutral one, because the wall-liquid interaction is increased or reduced compared to that of the liquid-liquid interaction.

So far, it has been shown that the structure within these pores is changed with respect to the bulk or neutral pores, but how about dynamics? Figure 8.23 illustrates the dynamic profiles for the various wall polarizations. As before, d is the distance to the pore wall and the vertical axis shows $\ln(\tau_{\alpha,\text{trans}})$

(obtained from $S_q(t)$ for oxygen atoms and $q = 22.7$ nm^{-1}).

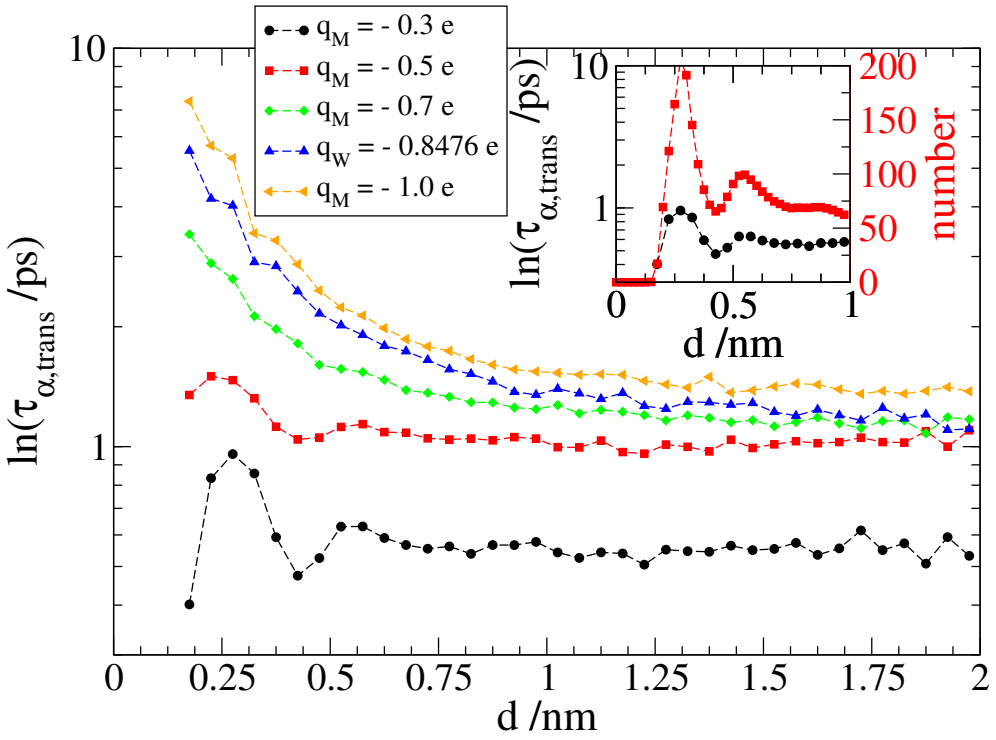

Figure 8.23: Dynamic profiles. Correlation times $\tau_{\alpha,\text{trans}}$ (obtained from $S_q(t)$ for oxygen atoms, with $q = 22.7$ nm^{-1}) dependent on the distance to the surface d for different wall polarizations of the CP-25 pore at $T = 240$ K. q_M denotes the charge on the wall oxygen atom. $q_\text{M} = -0.8476$ e corresponds to the neutral pore. The charges of the liquid are not changed and the net charge of all water molecules is zero. The inset depicts $\tau_{\alpha,\text{trans}}$ as function of d, together with the number of molecules found in the layers defined by d for the polarization $q_\text{M} = -0.3$ e.

Strikingly, the more pronounced the polarization, the stronger is the slowdown of dynamics when approaching the wall. For low wall polarizations, the slowdown is reduced and for $q_\text{M} = -0.3$ e vanishes completely. Instead, complex layering effects are mirrored in the dynamic profile for the latter polarization, see the inset. Large particle number, and slower dynamics coincide. Further, the entire dynamics throughout the pore is changed, which is clearly visible for the black curve, which is below the other curves. Thus, dynamics is much faster, even far away from the pore wall. This effect is presumably attributable to the specific behavior of water dynamics as function of pressure. As stated above, the low polarization wall effectively repels the liquid. Therefore,

the density and, thus, the pressure are increased at the pore center, because the original pore corresponds to a volume yielding an overall pressure of $p = 1$ bar. In essence, the pressure of the confined liquid is increased owing to the repulsion, resulting in faster dynamics for water [190].

In general, these analyses corroborate the previous statements about the slowdown of dynamics, which was attributed to a static energetic contribution by the pore wall. The dependence on the polarity of the water molecules, and, thus, on their capability for HB shows that the static contribution is explicitly due to HB between the wall and the confined liquid.

8.4 Free-energy model

In the last chapter, the origin of the slowdown was resolved. In this part, the goal is to find a theory that allows to rationalize the slowdown of dynamics in neutral confinements.

For this purpose, it is essential to find other quantities than τ_α, which change also as a function of the distance to the pore wall d. A close inspection of $S_q(t)$ dependent on d, see Figure 8.17, reveals that also the vibrational plateau at 1 ps changes significantly as a function of d. Therefore, dynamics on this time scale will be investigated using the CP-25 pores in the following.

This is done by employing the van Hove autocorrelation functions $G(\mathrm{x}, t = 1\ \mathrm{ps})$ and $G(\mathrm{z}, t = 1\ \mathrm{ps})$, see equation (5.9). Here, the van Hove functions separately describe the displacements in x and z direction [41].

Figure 8.24 depicts $G(\mathrm{x}, t = 1\ \mathrm{ps})$ and $G(\mathrm{z}, t = 1\ \mathrm{ps})$ for oxygen atoms in the CP-25 pore as a function of d. The chosen temperature is $T = 250$ K. $G(\mathrm{x}, t = 1\ \mathrm{ps})$ and $G(\mathrm{z}, t = 1\ \mathrm{ps})$ describe the probability for oxygen atoms to move a distance x,z within this time interval in the respective directions. It is found that the short time dynamics in both directions are very similar. Therefore, no dependence of the short time dynamics on the direction of motion within the pore can be found, corroborating the statement on the isotropic motion for $S_q(t)$ in the pores, see Figure 12.3 in the appendix.

However, a strong dependence of $G(\mathrm{x}, t = 1\ \mathrm{ps})$ and $G(\mathrm{z}, t = 1\ \mathrm{ps})$ on the

[41] Averaging over all molecules within a layer gives an average over motion within the x-y-plane, as the symmetry axis of the cylindrical pores points in z-direction. Hence, x and y yield the same information.

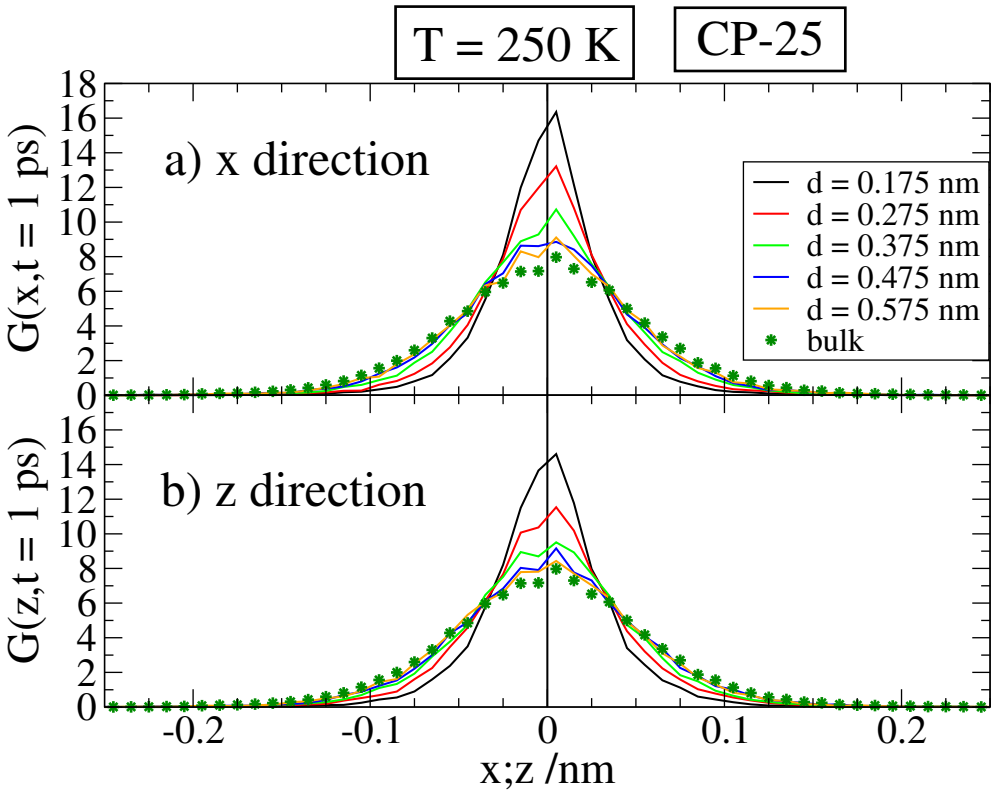

Figure 8.24: Probability $G(x, t = 1\text{ ps})$ and $G(z, t = 1\text{ ps})$ for oxygen atoms to move a distance within 1 ps depending on the distance to the pore wall d. The data stem from the CP-25 confinement at $T = 250K$ and from the bulk at this temperature. Panel a) depicts motion in x-direction and panel b) motion in z-direction (the symmetry axis of the cylindrical pore is in z-direction).

distance to the pore wall is visible. In the immediate vicinity to the wall, the distribution is very narrow (black curve), and with increasing d, the curves approach the bulk distribution. This is valid for different temperatures too. In order to quantify the findings, the variance of the distributions is used, which is given by $1/3\langle\Delta r^2\rangle$ at 1 ps, see equation (5.7).

Figure 8.25 illustrates the variance of the distributions from Figure 8.24 a) (only x direction). As was pointed out before, the distributions become very narrow near the wall. Furthermore, the curves look like the dynamic profiles, see Figure 8.13, however, turned upside down.

Before examining the relation between the short time MSD and the correlation times of the dynamic profiles, the short time motion is detailed. For

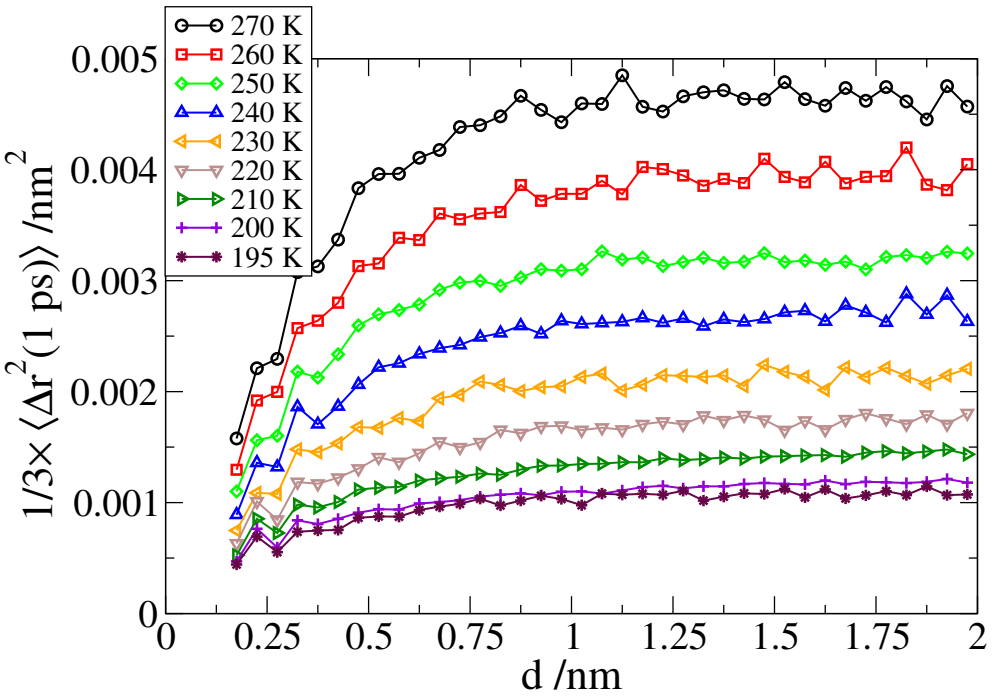

Figure 8.25: Short time mean squared displacement for the motion of oxygen atoms (only x direction) at $t = 1$ ps depending on temperature and d in the CP-25 confinements. The data was obtained from the variance of the distributions in Figure 8.24.

this purpose, the velocity autocorrelation function (VAC) $C_v(t)$, see equation (5.13), and the vibrational density of states (VDOS) $Z(\omega)$, see equation (5.14), are used. Both quantities allow for an investigation of short time dynamics and yield information about vibrational modes.

Figure 8.26 illustrates $C_v(t)$ and $Z(\omega)$ for the CP-25 pore at $T = 200$ K. It is striking that $C_v(t)$ exhibits a very different behavior for water molecules in the immediate vicinity to the wall compared to that of water molecules at some distance to the surface. $Z(\omega)$ reveals two peaks. According to *Balucani*, the peaks are allegedly related to transversal (trans) and longitudinal (long) modes propagating through the system [204]. Following this interpretation, one can speculate that the VDOS for oxygen atoms adjacent to the wall shows a shift of transversal modes to higher frequencies.

In general, $C_v(t)$ decorrelates on a 1 ps time scale, therefore, the MSD for this time is dominated by vibrations within local cages. This is of paramount importance for the following discussion, because this will be used in the following ECNLE approach, see chapter 2.5. It is stressed that there are further

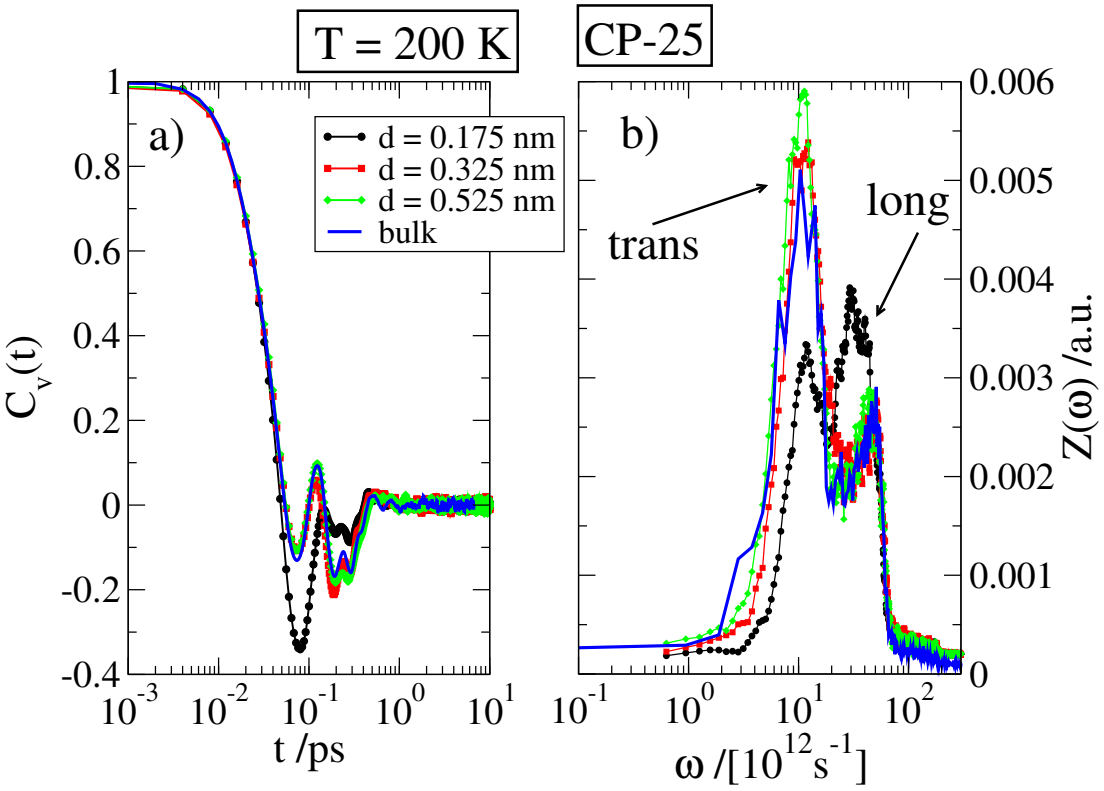

Figure 8.26: Panel a): Velocity autocorrelation function $C_v(t)$ for oxygen atoms as a function of d for the CP-25 confinement at 200 K. Panel b): the corresponding vibrational density of states $Z(\omega)$ for the data from panel a). The arrows indicate two peaks, which are presumably attributable to transversal (trans) and longitudinal (long) modes [204].

relaxation-like contributions to $\langle \Delta r^2(t = 1 \text{ ps}) \rangle$ at higher temperatures, especially in the non-supercooled regime, which may yield a different behavior. Also, there might be a relation to the Boson peak, however, this was not investigated in detail [81, 205]. Further studies may focus on this topic when trying to establish a connection to the RFOT theory, similar to the procedure proposed in [81, 82].

The findings can be rationalized by bringing up to mind the way the wall was produced. The oxygen atoms of the wall are trapped within very steep harmonic potentials. Owing to the lack of density fluctuations originating from the wall, molecules near the surface are trapped in more narrow potential minima. Additionally, following the ECNLE theory, the water molecules in the vicinity of the wall perform a cage-expansion motion and probe the very stiff trapping

potential of the wall and neighbors, which is the key idea for the derivation of the elastic contribution to the barriers. Hence, the particles near the surface appear to be more strongly localized compared to the bulk, as indicated by the smaller MSD, see Figure 8.25. This localization can be associated with a changed shear modulus G, see equation (2.39). Thus, the main assumption is to attribute the slowdown when approaching the pore wall to the altered shear modulus G with respect to the bulk one. As the shear modulus is related to the shear waves, the presumably observed shift of transversal modes appears to support this approach [28].

The idea is the following: According to the ECNLE approach

$$\tau_{\alpha,\mathrm{trans}} = \tau_0 \cdot e^{\frac{F_\mathrm{B}+F_\mathrm{elastic}}{k_\mathrm{B}T}} = \tau_0 \cdot e^{\frac{F_\mathrm{B}+H(T)G(T)}{k_\mathrm{B}T}}, \tag{8.4}$$

with $F_\mathrm{elastic} = H(T) \cdot G(T)$, see equation (2.37). Assuming that the contribution to $\langle \Delta r^2(t = 1\ \mathrm{ps}) \rangle$ is mainly due to vibrations and the fraction of transversal and longitudinal modes is constant (see chapter 2.5), gives

$$\tau_{\alpha,\mathrm{trans}} = \tau_0 \cdot e^{\frac{A}{\sqrt{\langle \Delta r^2(t=1\ \mathrm{ps}) \rangle}} + \frac{B \cdot \xi^2_\mathrm{elastic}(T)}{\langle \Delta r^2(t=1\ \mathrm{ps}) \rangle}} \tag{8.5}$$

with A, B and τ_0 as fit parameter. This equation can be further transformed to account for the slowdown relative to the bulk-like behavior at some distance to the pore wall. The idea is to split the shear modulus into two parts,

$$G(d,T) = G(T)_\mathrm{bulk} + G(d,T)_\mathrm{W}, \tag{8.6}$$

with $G(T)_\mathrm{bulk}$ as the bulk shear modulus, approached at distances far away from the surface, and $G(d,T)_\mathrm{W}$ the additional contribution from the wall. Transforming equation (8.5) yields

$$\tau_{\alpha,\mathrm{trans}} \approx \tau_0 \cdot e^{\frac{F_\mathrm{B}+H(T)\cdot\left[G(T)_\mathrm{bulk}+G(d,T)_\mathrm{W}\right]}{k_\mathrm{B}T}} \approx \tau_\mathrm{b} \cdot e^{\frac{\sqrt{G(d,t)_\mathrm{W}}+H(T)\cdot G(d,t)_\mathrm{W}}{k_\mathrm{B}T}}, \tag{8.7}$$

with τ_b as free parameter which accounts for the *bulk-like* dynamics far away from the wall. For the last transformation, $\sqrt{G(d,T)} = \sqrt{G(T)_\mathrm{bulk} + G(d,T)_\mathrm{W}} \approx \sqrt{G(T)_\mathrm{bulk}} + \sqrt{G(d,T)_\mathrm{W}}$. This is motivated by the fact that $G(d,T)_\mathrm{W}$ is assumed to be much larger than $G(T)_\mathrm{bulk}$ and the parameter A is adjusted to handle the approximation. Thus,

$$\tau_{\alpha,\mathrm{trans}} \approx \tau_\mathrm{b} \cdot e^{\frac{A}{\sqrt{\langle \Delta r^2_W(t=1\ \mathrm{ps}) \rangle}} + \frac{B \cdot \xi^2_\mathrm{elastic}(T)}{\langle \Delta r^2_W(t=1\ \mathrm{ps}) \rangle}}. \tag{8.8}$$

As stated above, it is assumed that the dependence of the shear modulus on the distance to the pore wall d is completely determined by the short time MSD. Therefore, $\xi^2_{\text{elastic}}(T)$ is supposed to be only dependent on temperature (and structure, but this was shown to be unchanged within the neutral pores). The following list compiles the basic assumptions:

- The influence of the wall leads to activated dynamics over barriers.
- The pores are large enough so that there is bulk-like behavior at some distance to the wall.
- $\langle \Delta r^2(t = 1\text{ ps}) \rangle$ is dominated by vibrations. Additionally, the fraction of longitudinal modes to shear modes it assumed to be constant, yielding a clear relation to the shear modulus [28].
- The shear modulus accounts for the dependence on the distance to the pore wall. All other quantities are constants for a fixed temperature.

Figure 8.27 illustrates the dynamical profile, the translational correlation times for oxygen atoms. The solid lines are fits according to equation (8.8), with the exponent A, $B \cdot \xi^2_{\text{elastic}}(T)$ and τ_{b} as fit parameters. It is stated that τ_{b} is very similar to τ_{bulk} but not identical.

Evidently, using an approach based on the ECNLE theory well describes the data. This is surprising because one can speculate that for oxygen atoms near the wall, the assumption that $\langle \Delta r^2(t = 1\text{ ps}) \rangle$ is due to a constant fraction of transversal to longitudinal modes should break down, as this is based on a single force constant for the interaction with the environment. In the vicinity of the wall, there is the interaction with the wall and the surrounding liquid which should yield two force constants. Further studies may focus on examining transversal modes directly and calculate the respective shear modulus without using the short time MSD. However, it is emphasized that this three parameter approach is able to describe the slowdown over several decades reasonably well.

An interesting and important question is: is it possible to split the data and attribute a part of the slowdown to the growth of the elastic barrier and another part to F_{B}, the localization? An approach to this question is shown in Figure 8.28. Notice, the vertical axis shows $\tau_{\alpha,\text{trans}}$.

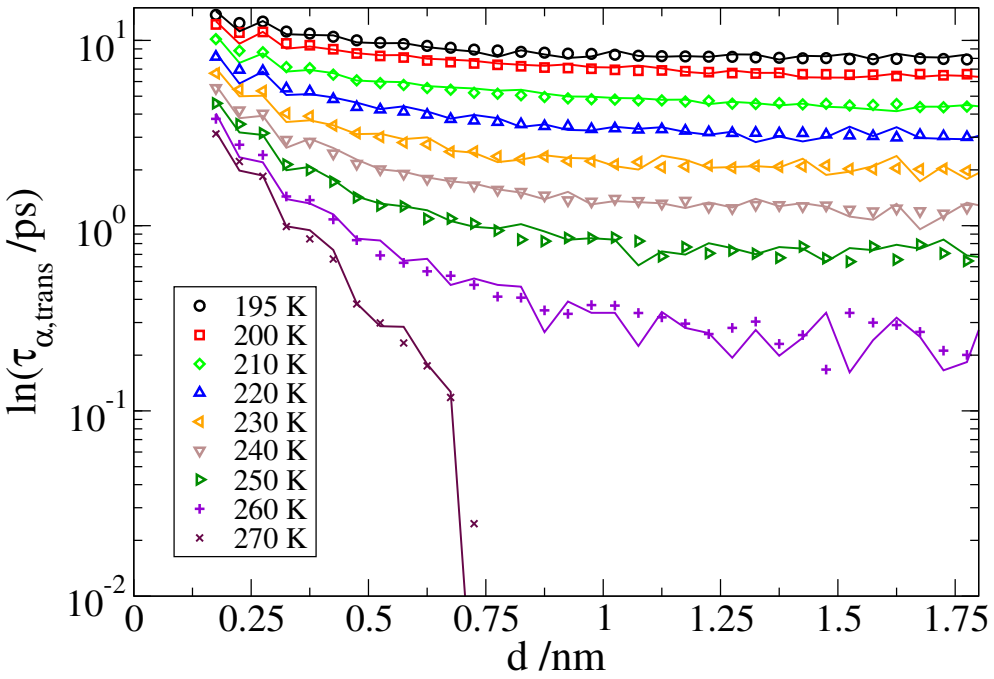

Figure 8.27: Dynamic profile. The translational correlation time (obtained from $S_q(t)$ for oxygen atoms with $q = 22.7\ \mathrm{nm}^{-1}$) as a function of d in the CP-25 confinement. The solid lines are fits according to equation 8.8.

In Figure 8.28, only the elastic part to the energy barrier in equation (8.8) was used. Strikingly, it is possible to fit the high temperature data, but at lower temperatures, the fit significantly deviates from the data. In order to test the hypothesis set out above, the dashed lines for $T = 200$ K and $T = 195$ K show fits using again only the elastic contribution but in this case, the data points in the immediate vicinity to the pore were omitted. Evidently, the fit approximates the data for $T = 200$ K and $T = 195$ K very well and only deviates for $d < 0.3$ nm. This clearly points towards a change of the relaxation process, elastic for bulk-like motion and dominated by localization near the pore wall. This argument will be at the heart to explain fragile behavior of supercooled liquids and is revisited below.

Next, the focus is on the elastic length ξ_{elastic}. The key to determine ξ_{elastic} is to propose that B is not temperature dependent and only depends on the properties of the wall, like the stiffness of the wall. Unfortunately, $\langle \Delta r_W^2(t = 1\ \mathrm{ps}) \rangle$ is very small and noisy, thus, taking the inverse worsens the description. Therefore, it is not possible to determine the square (ξ^2_{elastic}) of an allegedly small

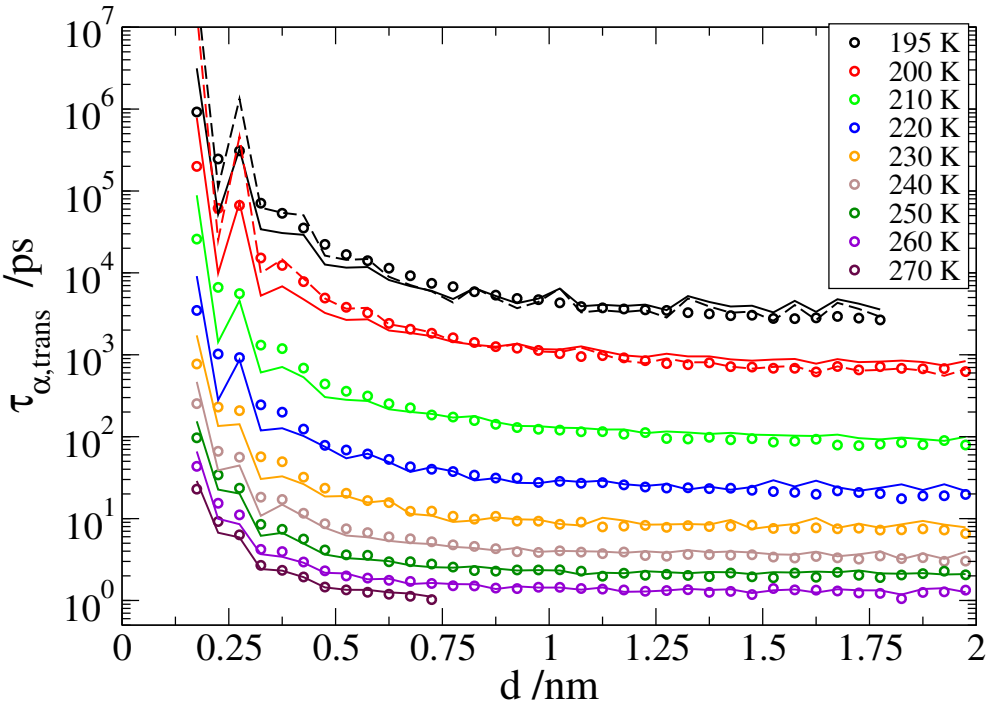

Figure 8.28: Dynamic profile. The translational correlation time (obtained from $S_q(t)$ for oxygen atoms with $q = 22.7$ nm^{-1}) depending on d in the CP-25 confinement. The solid lines are fits according to the elastic part (second term in the exponent) of equation 8.8. The dashed lines indicate a fit as for the solid lines, but the first three data points corresponding to oxygen atoms in the immediate vicinity to the wall had been omitted.

length scale, relative to the particle size [21], from the fits in Figure 8.27.

Given the arguments above, a different approach is chosen to estimate ξ_{elastic}. In chapter 8.2.1, an empirical equation (8.1) was used to describe the slowdown and a dynamic length scale was obtained. In Figure 8.27, the slowdown was transformed to a change of $\langle \Delta r^2(t = 1\ \mathrm{ps}) \rangle$. Thus, it is straightforward that the length scale obtained from equation (8.1) must be incorporated in $\langle \Delta r^2(t = 1\ \mathrm{ps}) \rangle$. It was discussed that this length scale might be appropriate to describe the MCT length scale, but here, the idea is to relate it to the cage expansion process.

At this point the crucial assumption for this part of the thesis is made: It was reasoned that the contribution F_{B} is only significant at low temperatures and near the pore wall. Therefore, the tremendous slowdown of dynamics is proposed to be mainly attributable to the elastic part of the barriers, and the

dynamical length scale gives an estimate of the cooperative volume. At higher temperatures, the volume is smaller, thus the slowdown is moderate when approaching the surface, but, at lower temperatures, the volume increases and yields a stronger coupling between molecules giving a slower decay to bulk-like dynamics upon increasing distance to the pore wall.

This idea is corroborated by analyzing the reduced fragility for particles adjacent to the wall. Figure 8.29 illustrates $\tau_{\alpha,\text{trans}}$ as function of temperature and d for oxygen atoms in the CP-25 pore and for comparison $\tau_{\alpha,\text{trans}}$ for the bulk system. The solid lines are approximations to equation (8.8), but in this case, $\tau_\text{b} = \tau_\text{bulk}$.

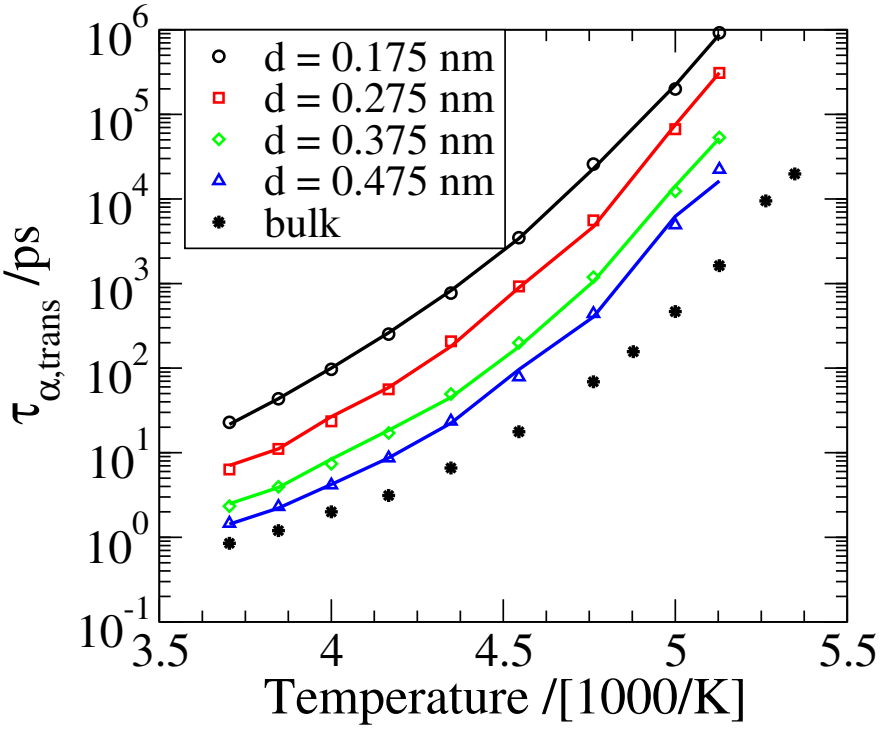

Figure 8.29: Structural correlation times $\tau_{\alpha,\text{trans}}$ dependent on temperature and distance to the pore wall d in the CP-25 confinement. $\tau_{\alpha,\text{trans}}$ was obtained from $S_q(t)$ for oxygen atoms with $q = 22.7\ \text{nm}^{-1}$. The solid lines are fits according to equation (8.8).

The temperature dependence is fitted well, however, the fit parameters A, B point towards a complex description of dynamics, see Table 6. The parameter A, which weights the contribution of F_B becomes increasingly less important as the particles are farther away from the surface. On the contrary, the parameter B which weights the elastic contribution increases by a factor more than 10.

Fit parameters	d = 0.175 nm	d = 0.275 nm	d = 0.375 nm	0.475 nm
A	0.154	0.135	0.091	0.060
B	0.0005	0.0015	0.0438	0.0696

Table 6: Fit parameters A and B, see equation (8.8), for the solid lines in Figure 8.29.

According to the parameters, fits without using ξ_{elastic} work for the correlation times of particles in the immediate vicinity to the pore, but not for particles at some distance to the pore wall.

A possible explanation for this behavior is the following idea: For particles far away from the surface, relaxation events are jumps to new positions. To do so, the elastic contribution is appropriate to describe the energy barrier which is necessary to deflect neighboring molecules in order to get to a new position. Near the surface this is different. There, the static contribution of the wall yields fixed positions for the molecules, as was shown during the discussion on the static length scale. Thus, the contribution to deflect molecules in their local cage to jump to a new minimum is small as the particles can only move to positions which were previously occupied by other ones. This is the reason why the van Hove function for particles in the immediate vicinity to the wall exhibits a peak at the next-neighbor distance, see Figure 8.9. Thus, the elastic contribution, which was clearly motivated as probing small displacements of the neighboring particles, is not important. The barrier is mainly determined by the increased localization and the attempt to jump to a different well defined minimum in the energy landscape.

Using this hypothesis, it is straightforward to explain the reduced fragility. As stated in chapter 2.5, the elastic part is responsible for fragile behavior, whereas the localization part F_{B} should only give an Arrhenius-like behavior. Thus, the parameters A and B precisely determine the fragility. If $A/B \gg 1$, the temperature dependence is assumed to be less fragile as compared to the case where $B/A \gg 1$. Hence, the hypothesis set out above is appropriate to explain the findings.

An interesting question concerning the different fragilities is: is there an intersection between the bulk correlation times and the correlation times for water adjacent to the surface. Following the laid out mechanism for motion of the molecules, it seems reasonable to suppose a crossing of the curves. At a sufficiently low temperature, and given that the dynamic heterogeneity rises upon lowering the temperature, fast molecules are assumed to perceive the

interaction with slow molecules as similar to the presence of a neutral wall. Thus, particles in the vicinity of the wall should behave like fast molecules in the bulk. This might aid the understanding of secondary relaxation processes and neatly explains the presence of spatially heterogeneous dynamics. Fast molecules which probe the static energy landscape imposed by the slow particles jump to the position of another fast molecule. This gives rise to string-like motion, see chapter 6.4, which in this sense should be the ultimate measure for the mechanism of motion. This yields a trivial reason for the clustering of fast molecules: Fast molecules have to cluster as they mainly jump to previously occupied positions. This should be strictly valid in tightly packed systems without a large number of *defects*. Therefore, a free place in the neighborhood of an oxygen atom determines if it is fast with respect to the average structural correlation time.

A further check of the hypothesis is performed by varying the softness of the wall.

Given the arguments above, the stiffness of the wall should only contribute to the absolute amplitude of the slowdown and should not change the dynamic length scale. This is investigated in Figure 8.30.

Figure 8.30 depicts the dynamical profile for translational motion dependent on the force constant κ in the CP-25 pore at 240 K. The force constant κ of the wall was introduced in chapter 4. It determines the harmonic potential which was used to trap oxygen atoms in order to produce walls. The unit of the force constant is in *Gromacs* units kJ/(mol nm^2). All data for neutral pores which have been shown so far were obtained from confinement systems using $\kappa = 10^6$. From panel a), it is evident that for all investigated force constants, a slowdown is observable. The solid lines are fits to equation (8.1). Panel b) shows the same data but the axes have been rescaled. For the rescaling, the dynamic length scale for $\kappa = 10^6$ was used. If the dynamic length changes upon reducing the wall stiffness, a master curve is ruled out. Additionally, it is necessary to account for the amplitude of the slowing $A(\kappa)$ (the proportionality constant in equation (8.1)).

Evidently, panel b) reveals that a master curve can be obtained and, thus, the dynamic length scale is not dependent on the wall stiffness, in contrast to the amplitude of the slowdown. Increasing the softness of the wall should reduce the localization part and if ξ_{elastic} is an inherent length of the liquid, let the elastic contribution unchanged. This is exactly the result, thus the finding corroborates the notion that the dynamic length scale might be associated with

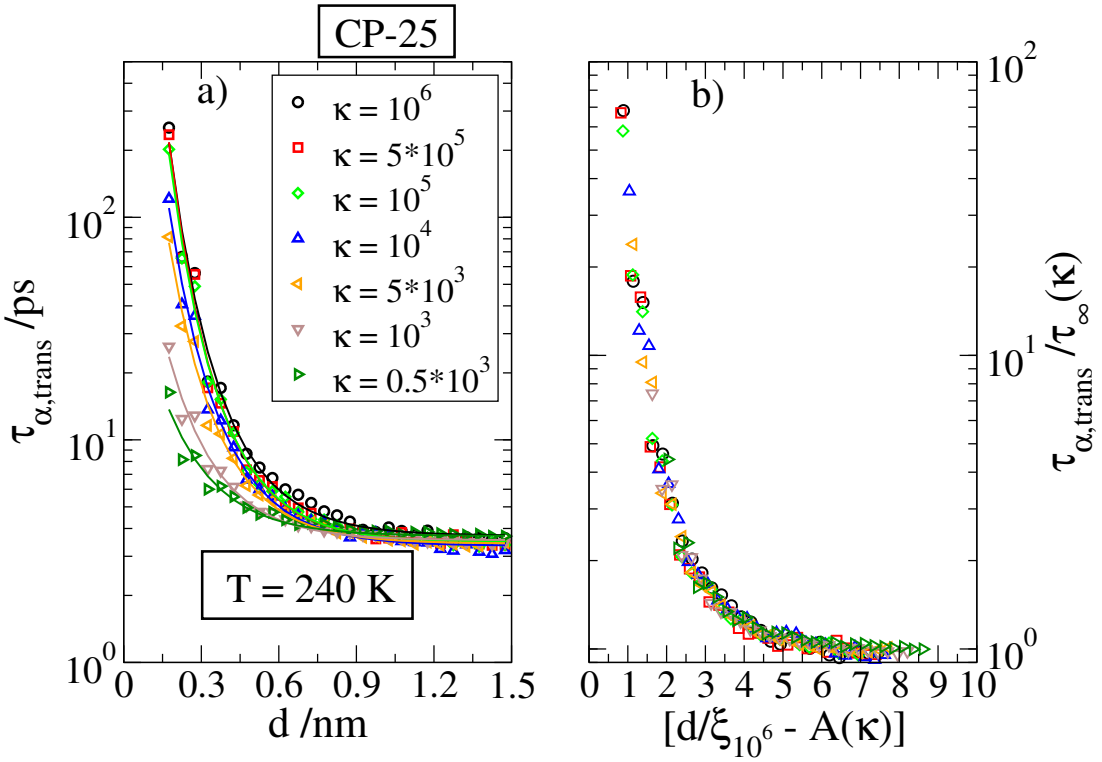

Figure 8.30: a) Dynamic profile. The translational correlation time (obtained from $S_q(t)$ for oxygen atoms with $q = 22.7$ nm^{-1}) as function of d in the CP-25 confinement. The temperature is set to 240 K and several values for the stiffness of the wall κ are examined. See the text for further information. The solid lines are fits according to equation (8.1). b) Rescaling of the horizontal and vertical axes yields a master curve.

ξ_{elastic}. Further studies might proof this for different temperatures, which was not pursued for this study.

8.4.1 Dynamic heterogeneity in neutral pores

Dynamic heterogeneity is one of the main features of supercooled liquids, see chapter 2.2. In this part, the ECNLE theory will be used to shed light on this important topic.

In the previous chapter, the ECNLE approach was used to describe the tremendous slowdown of dynamics. Before that, it was shown that the wall imposes a static contribution to the energy landscape, which induces additional hetero-

geneity of the system as a function of the distance d, but also within a given layer. This behavior will be scrutinized for the CP-25 pore by calculating a distribution of effective energy barriers, which is another way to estimate heterogeneity, than in the previous chapters.

The starting point is the idea that $\langle \Delta r^2(t = 1\text{ ps}) \rangle$ is averaged over the ensemble. So, in a next step, the distribution of $\langle \Delta r_i^2(t = 1\text{ ps}) \rangle$ for single molecules is calculated. Together with fit parameters A, B for the solid lines in Figure 8.27, this yields a distribution of effective energy barriers for the structural relaxation depending on the distance to the pore wall d. Notice, the fits were conducted by using equation (8.8).

Figure 8.31 shows the distribution of effective energy barriers, due to the wall, for the temperature $T = 270$ K (This approach can be used for different temperatures too, and the key assertions do not change).

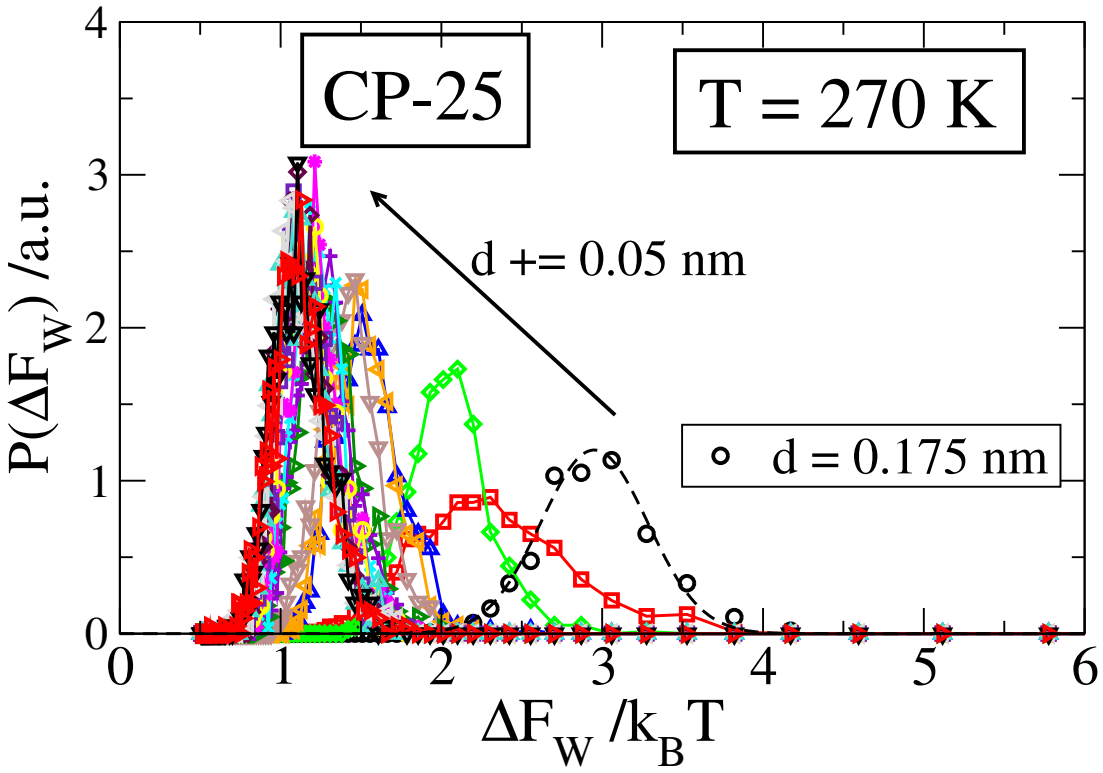

Figure 8.31: Energy barrier ΔF_W based on the structural relaxation of oxygen atoms as a function of d. The data stem from the CP-25 confinement at 270 K. The solid lines are a guide for the eye. The dashed line is a Gaussian approximation.

First, the mean of the distribution of energy barriers shifts to larger barriers when approaching the pore wall. This is in agreement with the discussed slow-down of dynamics. Additionally, the width of the distributions increase upon approaching the wall. The idea to transform the short time MSD into a distribution of effective barriers is intrinsically related to a one-step picture of dynamics. A fraction of particles is still in the local cage and a fraction has crossed the barriers. Thus, this approach is a projection onto an effective distribution of correlation times, but, backward correlation is incorporated due to the definition of $\tau_{\alpha,\mathrm{trans}}$. Only due to the latter argument, the statement is valid that this strongly supports the results from chapter 7.2.2. There, a stronger heterogeneous contribution was found for the motion of oxygen atoms in the immediate vicinity to the silica pore by applying a three-time correlation function. Here, this is indicated by the increased width of the distributions. Further, one can observe that the distributions are symmetrically shaped. The dashed black line indicates a Gaussian approximation, which describes the data.

8.4.2 Describing bulk dynamics with the ECNLE approach

Next the focus is on bulk dynamics. One can try to describe the structural corre-

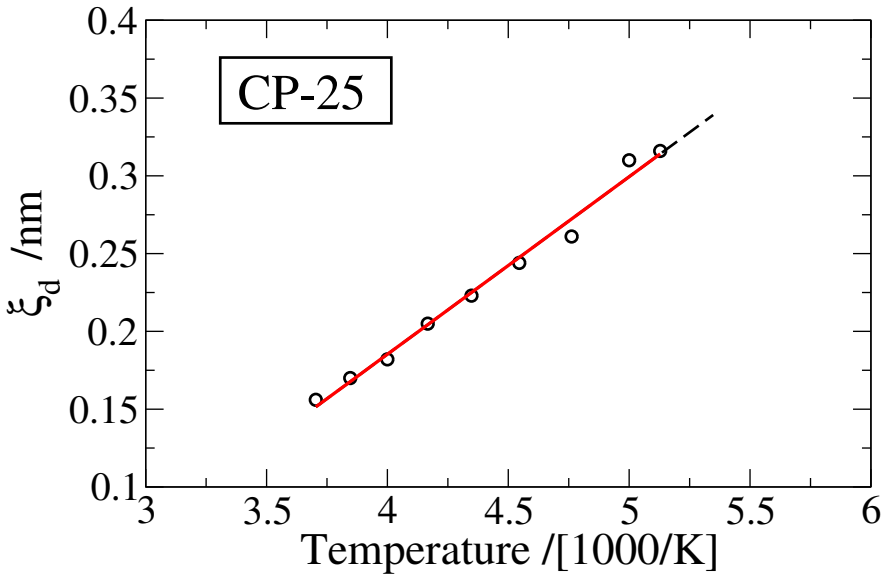

Figure 8.32: Dynamic length scale ξ_d for the CP-25 confinement. The red line shows a linear approximation for the data. The dashed black line illustrates the area of extrapolation, namely, for two temperatures $T = 190$ K and $T = 187$ K.

lation times for the bulk according to equation (8.5). To do so, an extrapolation

for the dynamic length scale ξ_d, which is assumed to be identical to ξ_{elastic}, is used to fit the entire temperature regime of the bulk. For the CP-25 confinement, the lowest achievable temperature was 195 K and for the bulk 187 K. Therefore, an extrapolation is necessary, which is illustrated in Figure 8.32. The red line is a linear fit, and the dashed black line indicates the area of extrapolation. Due to the small extent of extrapolation, it appears convenient to use this approach.

This extended length scale is used to describe the bulk data. Figure 8.33 shows $\tau_{\alpha,\text{trans}}$ as a function of inverse temperature.

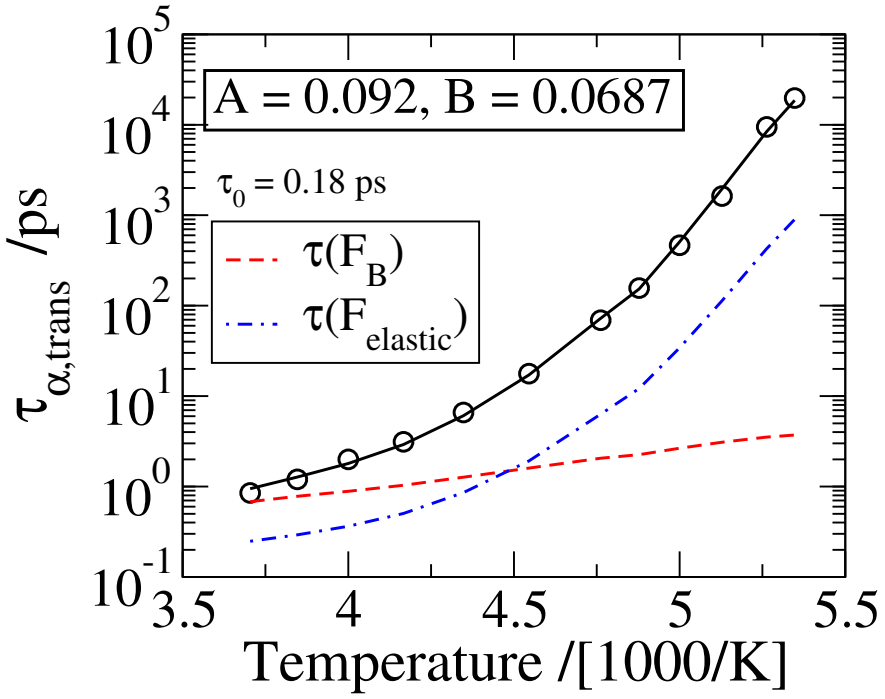

Figure 8.33: Structural correlation times $\tau_{\alpha,\text{trans}}$ as a function of temperature. The solid line is a fit to equation (8.5). A linear extrapolation was used to obtain ξ_{elastic} at the temperatures 190 K and 187 K, see Figure 8.32. The red dashed line illustrates the estimated contribution from F_{B} and the blue dashed line from F_{elastic}.

Strikingly, using equation (8.5) describes the data. It is emphasized that effectively only two free parameters A and B were necessary for the fit. The dashed lines reveal that the contribution from F_{B} is important at high temperatures, and at low temperatures F_{elastic} dominates. This is in agreement with the theory, which attributes the fragile behavior at low temperatures to the elastic

contribution. It is emphasized that it was assured that an appropriate fit is not possible if

- only the F_{B} part is used,
- only F_{elastic} but with constant ξ_{elastic} was employed,
- both parts are used, but with a fixed elastic length scale,
- only the elastic part, but with $\xi_{\mathrm{elastic}}(T) = \xi_d(T)$ (in this case the low temperature data is well approximated).

This highlights the relevance of F_{B} and F_{elastic} and especially of ξ_{elastic} for the fits.

In analogy to the analysis for the CP-25 pore, a distribution of effective activation energies can be calculated using the fit parameters from Figure 8.33. This is shown in Figure 8.34.

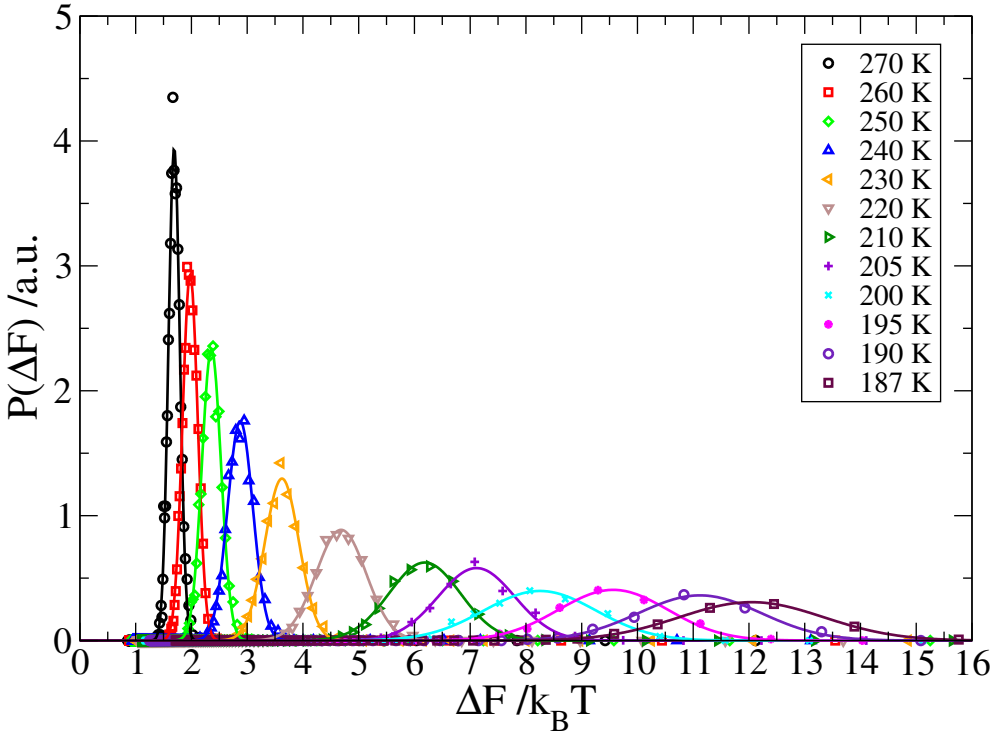

Figure 8.34: Distribution of effective activation energies for structural relaxation, probed by $S_q(t)$ for oxygen atoms with $q = 22.7\ \mathrm{nm}^{-1}$. The distribution was calculated according to the fit parameters in Figure 8.33. The solid lines are Gaussian approximations.

Trivially, the mean of the barriers increases as the temperature is reduced. More important, the width also increase and, as for the distribution of effective activation energies in the CP-25 pore, the distributions are Gaussian shaped, see the solid lines. The Gaussian approximations are used to calculate correlation times for particles which have to overcome barriers of height $\Delta F_k = \langle P(\Delta F) \rangle \pm n \cdot \sigma$, e.g. -2σ from the mean barrier. The results are illustrated in Figure 8.35.

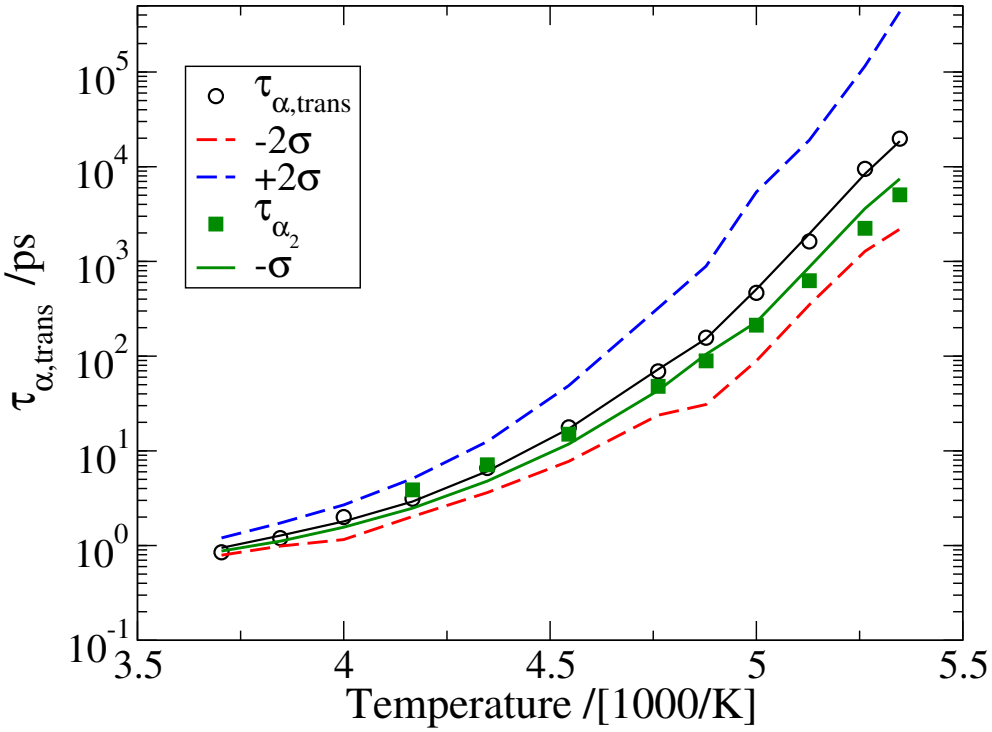

Figure 8.35: Correlation times for the bulk based on the distribution of effective barriers, see Figure 8.34. The structural correlation times $\tau_{\alpha,\text{trans}}$ for the bulk are approximated by the mean of the distributions (identical to the solid line in Figure 8.33), see the black solid line. The red and the blue line correspond to barriers at $-2\cdot\sigma$ and $+2\cdot\sigma$ from the mean barrier, respectively. The green solid line depicts the effective correlation times for an energy barrier according to $-\sigma$ from the mean. The green data points show the time when the non-Gaussian parameter α_2 is at maximum.

The black solid line depicts correlation times associated with the mean of the barrier distribution. This is identical to the fit of the bulk data in Figure 8.33. The red and blue curves show correlation times, corresponding to barriers $\pm 2\cdot\sigma$. A pronounced decoupling of these correlation times is visible. This is due to the already mentioned increased width of the distributions, indicating a

broader distribution of effective correlation times. Interestingly, the correlation times for barriers determined at $-\sigma$ from the mean, are very similar to the time τ_{α_2}. This corroborates the statement from chapter 6.4 that τ_{α_2} is sensitive to the motion of the roughly 10 to 15 % *fastest* particles in the system.

8.4.3 Hyperscaling

Further, the calculations in the previous chapter are presumably suitable to explain the scaling of time scales like τ_{α_2} with $\tau_{\alpha,\text{trans}}$. This feature was denoted as *hyperscaling* [57, 58].

Following the considerations of the previous chapter, the barriers calculated at $-\sigma$ from the mean describe τ_{α_2} reasonably well. Hence, it is straightforward that $\tau_{\alpha_2} \propto e^{a \cdot \frac{\Delta F}{k_\text{B} T}}$, with ΔF determined by the fit of equation (8.5) to $\tau_{\alpha,\text{trans}}$. The prefactor a is given as $a = 1 - \frac{\sigma}{\Delta F}$, with σ the standard deviation of the effective energy distribution. This yields

$$\ln(\tau_{\alpha_2}) = a \cdot \ln(\tau_{\alpha,\text{trans}}). \tag{8.9}$$

A simple linear scaling between τ_{α_2} and the structural correlation times is, thus, only achieved for $a = 1$. In order to describe *fast* dynamics, $a < 1$, and this trivially describes the decorrelation of related time scales from the structural correlation time. The situation becomes more complex when there is a broadening of the distribution of effective activation energies, because $a = a(T)$. This might result in deviations from the hyperscaling behavior. For the present case a can be calculated from Gaussian fits to the distributions in Figure 8.34 yielding $a \approx 0.89$ at temperatures below 210 K. This is similar to the hyperscaling exponent $a = 0.81$ of $\tau_{\alpha,\text{trans}}$ and τ_{α_2} obtained in chapter 6.5.

8.4.4 Fractional Stokes-Einstein law

In chapter 6.4, a presence of spatially heterogeneous dynamics and a breakdown of the Stokes-Einstein law were observed for bulk water. Here, this breakdown is revisited. Specifically, based on the reasonable assumption of a Gaussian distribution of barriers, the Stokes-Einstein breakdown is analytically scrutinized.

As mentioned in chapter 6.6, the Stokes-Einstein law relates the diffusion constant D to the viscosity, or in this case, to the structural correlation time $\tau_{\alpha,\text{trans}}$.

The important fact is that $D \propto \langle \tau^{-1} \rangle$, whereas $\tau_{\alpha,\text{trans}} = \langle \tau \rangle$ [86]. Using the Gaussian assumption for the distribution of barriers yields

$$D \approx e^{-\langle \Delta F \rangle + \sigma^2/2} \tag{8.10}$$

and

$$\tau_{\alpha,\text{trans}} \approx e^{+\langle \Delta F \rangle + \sigma^2/2} \tag{8.11}$$

with $\langle \Delta F \rangle$ the mean and σ^2 the variance of the barrier distribution [86]. Thus, some calculus yields the fractional Stokes-Einstein law [86],

$$D = A * \tau_{\alpha,\text{trans}}^{-\gamma}, \tag{8.12}$$

with $\gamma = \frac{1-\frac{\sigma^2}{2\langle \Delta F \rangle}}{1+\frac{\sigma^2}{2\langle \Delta F \rangle}}$. The parameter γ, which determines the slope in a double log representation, was calculated from the Gaussian approximations in Figure 8.34. Figure 8.36 shows D depending on $\tau_{\alpha,\text{trans}}$ and on $\tau_{\alpha,\text{trans}}/T$. The solid lines are fits to equation (8.12), with only A as free parameter. They well describe the data sets. Thus, the proposed approach appears appropriate to rationalize the decorrelation of rate averaged quantities and time averaged ones.

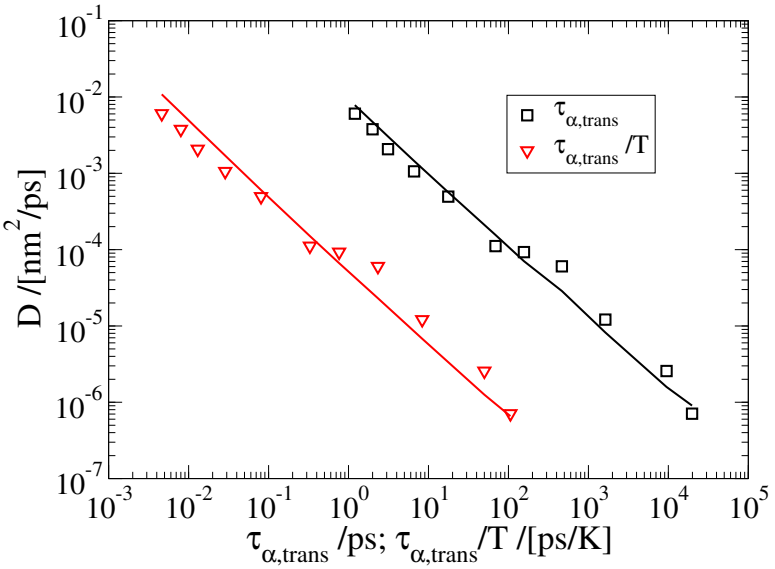

Figure 8.36: Fractional Stokes-Einstein law. The diffusion constant D as a function of $\tau_{\alpha,\text{trans}}$ and $\tau_{\alpha,\text{trans}}/T$. The solid lines are approximations comprising a single free parameter A, see equation (8.12). γ is calculated from the Gaussian fits to the distributions in Figure 8.34.

8.5 Conclusion

It was shown that neutral pores are suitable to confine a liquid without changing the structure. The investigation of dynamics within those pores revealed effects, which were also found for dynamics of water in the silica pores, namely, CC-like relaxation patterns, a tremendous slowdown of dynamics near the wall, and a reduced fragility adjacent to the wall. Therefore, these effects seem to be generic for atomistic pores, and also basically independent of the geometry of the confinement. The effects were attributed to a static contribution to the energy landscape mainly due to hydrogen bonds to the wall.

Afterwards, the slowdown was detailed. To do so, an empirical equation was used and it turned out that the approximation conveniently describes the slowdown for all investigated geometries. From those approximations, a dynamic length ξ_d was obtained. A close inspection revealed an increasing length upon lowering the temperature. One geometry gave a constant length, but this analysis was found to be inappropriate due to important non-linear feedback effects prevailing in very narrow confinements.

This length scale was related to different theoretical approaches which try to explain dynamics of supercooled liquids. The RFOT approach predicts a diverging dynamical length scale at the transition temperature from non-activated to activated dynamics, T_C. In finite dimensions, this sharp transition is assumed to smear out. Consequently, a peak behavior is proposed to mark T_C. Previous studies settled T_C for SPC/E at $T_C \approx 200$ K [49]. The analysis of ξ_d reveals a linear increase as a function of inverse temperature down to $T = 195$ K, without any indication for a peak of ξ_d.

Additionally, overlap functions were employed to obtain static lengths, which are supposed to describe the activated regime below T_C. The idea is that this length, ξ_S, gives the size of amorphous order and determines the minimal size of relaxation events. The analyses revealed an increasing static length, similar in value and temperature dependence to the dynamic length. The square of both length was found to scale with $\ln(\tau_{\alpha,\text{trans}})$ from the bulk, suggesting a spherical geometry for the amorphous regions. The growing length scales were related to the fragile behavior of supercooled water.

The drawbacks of this approach are clearly related to the questions which of the introduced length scale is related to fragility and what is the relevance of them as there is no indication for a transition from non-activated to activated dynamics. Thus, a different approach, the ECNLE theory, was adopted to ratio-

nalize the findings.

This approach assumes two contributions. The first part deals with single particle jumps out of a local potential minimum. The second part relates the motion within local minima to displacements of adjacent molecules. Both effects yield contributions to the effective energy barriers via the shear modulus, with the barriers distinguished into F_{B} for the single particle jumps, and F_{elastic} for the elastic displacement of neighboring molecules. A simplified connection between the shear modulus and the vibrational MSD was used to approximate the slowdown of dynamics when approaching the wall. Near the wall, the molecules probe a static energy landscape. This yields predefined locations for the molecules, and thus, at low temperatures, only jumps to previously occupied positions are possible. This contribution was shown to be directly related to the first contribution of the barriers. The second one was shown to be responsible for most of the slowdown when approaching the surface. Thus, the previously denoted dynamic length, ξ_d, was associated with the elastic length, on which particles induce displacements of neighboring molecules. In order to describe the reduced fragility for particles in the immediate vicinity of the wall, both contributions were used to approximate the temperature dependence of the correlation times. Weighting factors, introduced for the fit procedure, revealed that near the wall, the first part of the theory, dealing with single particle jumps, is the origin of the reduced fragility for those molecules. At some distance to the wall, the elastic contribution rose significantly compared to that adjacent to the wall, and the fragile behavior was clearly related to the increasing elastic length and changed shear modulus. The same approach was used to describe the bulk correlation times by effectively using only two parameters. This fit gave a very good description of the data.

These findings motivated the following picture for dynamics in supercooled water: At short times, fast molecules probe the static energy landscape provided by the slow molecules. Hence, the mechanism of motion for the fast molecules should be closely related to the findings for motion in the immediate vicinity to the wall. There, single particle jumps to adjacent locations, which were previously occupied by other molecules determine the correlation times. This explains the clustering of fast molecules, as a jump event has to take place in the neighborhood of an oxygen atom in order to be fast. Following the jumps of fast molecules, the energy landscape begins to change, as the fluctuations smear out the previously well defined locations for a jump event. Hence, on time scales of structural relaxation, the main mechanism for motion is supposed to be related to the breaking of the local cages. Therefore, no hopping motion is relevant, but rather to push neighboring molecules out of the way.

This is a collective motion. The energy barrier for this mechanism is, thus, directly related to the approximation of elastic displacements induced by adjacent molecules. The latter mechanism yields fragile behavior and dominates at low temperatures.

Following those considerations, distributions of effective energy barriers were calculated for the bulk. The mean and width of those Gaussian-shaped distributions were shown to increase upon lowering the temperature. These findings were used to access a decoupling of rate and time averages, in agreement with the fractional Stokes-Einstein law. It was possible to relate the decoupling to the distributions of effective energy barriers for the bulk system. This again highlights the relevance of confinement system for the general understanding of supercooled liquids.

In conclusion, some of the questions raised in chapter 2.6 can be answered within the framework of the ECNLE approach. First, this study shows no evidence that spatially heterogeneous dynamics (SHD) are the driver of vitrification. Here, SHD are probably only a side effect of broad distributions of correlation times, as the main contribution to the slowing comes from the elastic part, whereas it was reasoned that SHD are presumably related to local jump events. Second, the elastic correlation length appears to be different than a simple coarse-graining length scale due to the explicit cooperativity of associated motion.

9 A possible secondary process in water

In this chapter, a possible secondary process for the reorientation of water molecules, the π-flip motion, is studied.

The motivation to discuss this process was given in chapter 7. There, and in chapter 8, some remarkable features of water near surfaces were introduced. In this context, it was found that the reorientation of the $\vec{\text{OH}}$ bonds appeared to differ significantly from the findings for the dipole reorientation, which gave results similar to that of translation motion. It turned out that the $\vec{\text{OH}}$ bond reorientation seemed to be less sensitive to a change of motion within the pores, and therefore, to the imprinted static energy landscape.

This finding can be rationalized by the observation of π-flip motion for water molecules. This means that the dipole vector points in the same direction before and after the flip, but the hydrogen atoms swapped places. There is an abundance of NMR studies on water in proteins and zeolites which found this process along with several MD simulation studies [125, 206–211]. Therefore, this process seems to be typical of water which is trapped or confined in a hardly changing environment.

In order to detect this kind of reorientation, the van Hove function is modified to account for angles ϕ, rather than for the displacement r, see equation (5.9). In contrast to $G(r,t)$, which was weighted by $4\pi r^2$, $G(\phi,t)$ is weighted by $\sin(\phi)$ and thus, the long-time limit for $G(\phi,t)$ is a $\sin(\phi)$-shaped distribution. As the π-flip is a swap of locations of the hydrogen atoms, a distinct peak of $G(\phi_{\text{OH}},t)$ at $\approx 109\,^\circ$ is expected for SPC/E due to the H-O-H angle of $109\,^\circ$. Additionally, the surface normal of the H-O-H plane should rotate by $180\,^\circ$. The angle between the surface normal at time t_0 and t is referred to as $\phi_\perp$.

Here, the process is called *secondary* process to distinguish it from structural relaxation. For molecules performing only π-flips, F_2 for the $\vec{\text{OH}}$ bond reorientation will not decay to zero, therefore, it is called *secondary* in this context.

Figure 9.1 illustrates $G(\phi_{\text{OH}}, t = \tau_{\alpha,\text{F}_2})$ in panels a) and c), and $G(\phi_\perp, t = \tau_{\alpha,\text{F}_2})$ in panels b) and d). The top row shows data for molecules in the immediate vicinity ($d = 0.225$ nm) of the silica wall in the low density system (*lo-dens*) and the bottom row for water molecules with a distance of $d = 0.175$ nm to the surface in the CP-25 confinement.

At high temperatures, there is in all cases only a vibrational peak at roughly

20 °. However, upon lowering the temperature, an additional peak emerges for all angles and systems. For ϕ_{OH}, the additional peak is located at ≈ 109 °, perfectly coinciding with the expectation for a swapping of locations of the hydrogen atoms. Additionally, the vector perpendicular to the H-O-H plane develops a peak at roughly 170 °. An exact 180 ° jump can not be found as the probability to detect this is zero, due to the sinusoidal weighting of the curve. Vibrations and inexact jumps yield a broadening of the peak which therefore appears at ≈ 170 °. Hence, these results strongly suggests that at low temperatures, molecules in the vicinity of the walls perform this kind of motion.

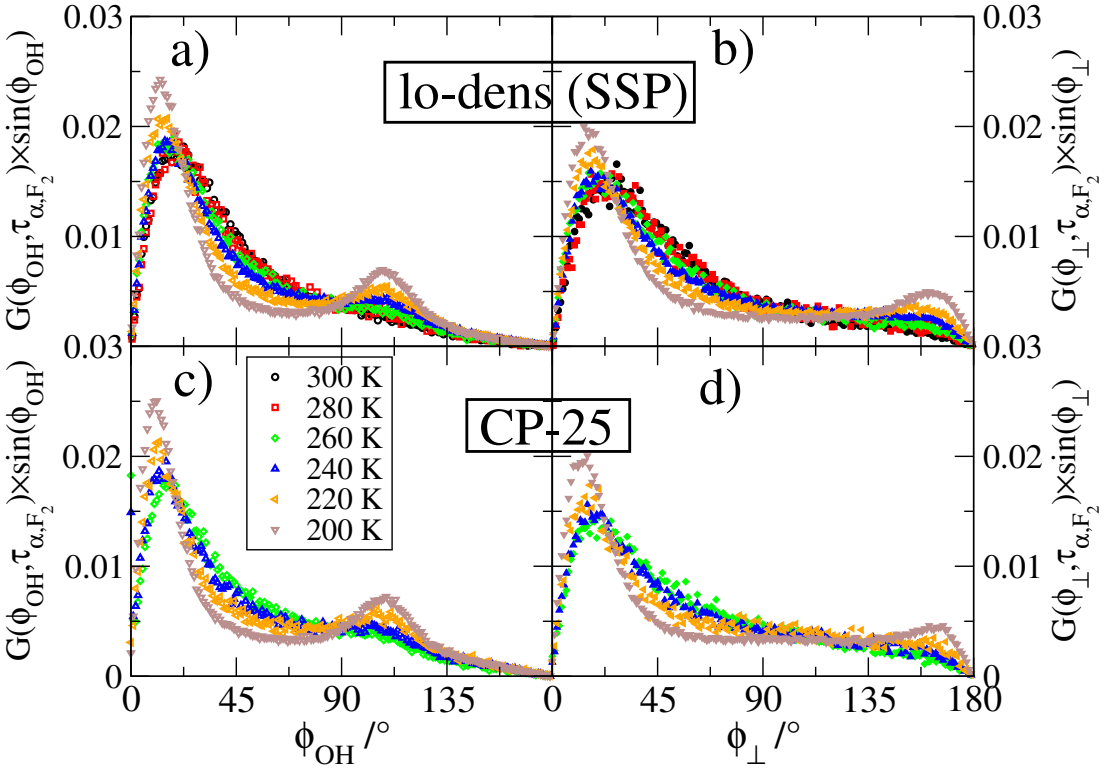

Figure 9.1: Van Hove orientational correlation function $G(\phi, t = \tau_{\alpha,F_2})$. Two different vectors or angles are considered. First, the $\vec{OH}$-bond reorientation, ϕ_{OH}. Second, the reorientation of the surface normal to the H-O-H plane, $\phi_{\perp}$. The top row depicts data for water molecules in the low density silica confinement (small silica pore), and the bottom row in the CP-25 confinement. The molecules have distances $d = 0.225$ nm to the silica wall and $d = 0.175$ nm to the neutral wall, respectively.

At some distance to the pore walls, $d = 0.975$ nm, the situation is different. Figure 9.2 shows $G(\phi_{OH}, t = \tau_{\alpha,F_2})$ in panel a) and c), and $G(\phi_{\perp}, t = \tau_{\alpha,F_2})$ in

panel b) and d). Here, only data for the CP-25 confinement are depicted, but this is valid for the other pore systems too. As before, a peak related to vibrational motion can be observed, but distinct additional peaks are absent, even at rather low temperatures. It is emphasized that this assertion is not changed for choosing time scales shorter than τ_{α,F_2}, see the bottom row where the evolution time is varied.

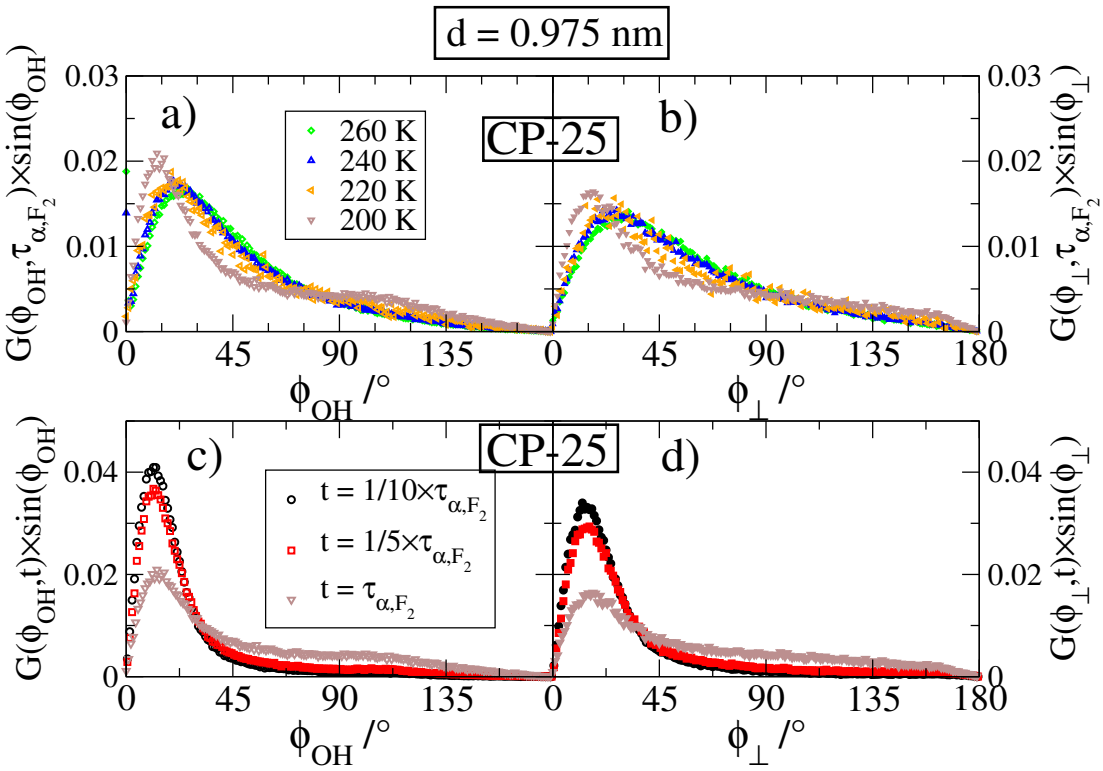

Figure 9.2: Top row: Van Hove orientational correlation function $G(\phi, t = \tau_{\alpha,F_2})$. Two different vectors or angles are considered. First, the $\vec{OH}$-bond reorientation, ϕ_{OH}. Second, the reorientation of the surface normal to the H-O-H plane, $\phi_\perp$. The data stem from the CP-25 confinement. Water molecules have a distance of $d = 0.975$ nm to the wall. Bottom row: time evolution, $t = n \times \tau_{\alpha,F_2}$ of the van Hove correlation functions for molecules at $d = 0.975$ nm to the CP-25 wall at 200 K.

As π-flips give an additional relaxation channel for the $\vec{OH}$-bond reorientation, dynamics is faster than without the appearance of this effect. Therefore, the effect presumably explains the significant difference in how F_1, F_2 and $S_q(t)$ probe the wall influence. Experimental studies, see the cited literature at the beginning of the chapter, found this process for water embedded in a slowly

varying environment without the possibility for translation motion. Thus, this also highlights the importance of the imprinted static contributions to the energy landscape by the wall atoms to explain the findings.

Next, the question of the presence of this process in the bulk is addressed. In order to obtain information about correlation times and the activation energy of the π-flips, a quantitative analysis will be performed.

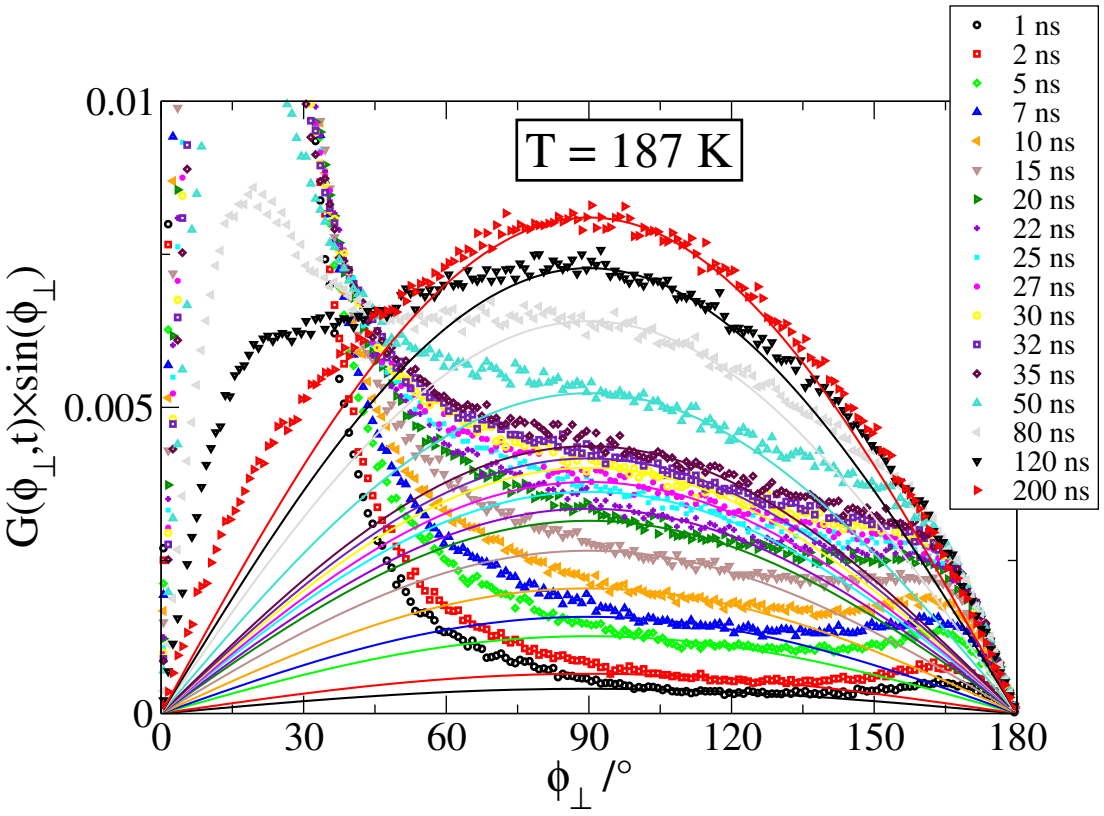

Figure 9.3: Van Hove orientational correlation function $G(\phi_\perp, t)$ for water molecules in the bulk system at 187 K. Various evolution times t have been considered. The solid lines are approximations for the isotropic contribution to $G(\phi_\perp, t)$ which governs the long-time limit.

For this purpose, $G(\phi_\perp, t)$ is examined in detail. Figure 9.3 illustrates $G(\phi_\perp, t)$ for water molecules in the bulk at 187 K. At times, $t < 30$ ns ($\tau_{\alpha,F_2} \approx 30$ ns), a peak can be observed at ≈ 170 °. At longer times , the distribution will ultimately approach the above mentioned sinusoidal distribution. The solid lines are approximations to account for the contribution of the isotropic part to the entire curves. The excess intensity at 170 ° is used to estimate the relevance of the π-flips. Thus, the area under the solid lines in the region, > 150 °, is

subtracted from the numerical integral of the data for $\phi_\perp > 150\,°$. The boundary $\phi_\perp > 150\,°$ is set to allow for distorted π-flips. The overall contribution of the isotropic motion is given by the entire area under the solid lines, and the π-flip contribution by the proposed excess intensity. The discussed analysis was performed for $T = \{200\,\text{K}, 195\,\text{K}, 190\,\text{K}, 187\,\text{K}\}$. At higher temperatures, the π-flip is virtually indistinguishable from the isotropic reorientation.

Having obtained the different parts for separating $G(\phi_\perp, t)$, correlation times can be estimated, see Figure 9.4. The open symbols show the area, or contribution, for the isotropic process, denoted as α. The filled symbols show the estimated relevance of the π-flip process, referred to as β.

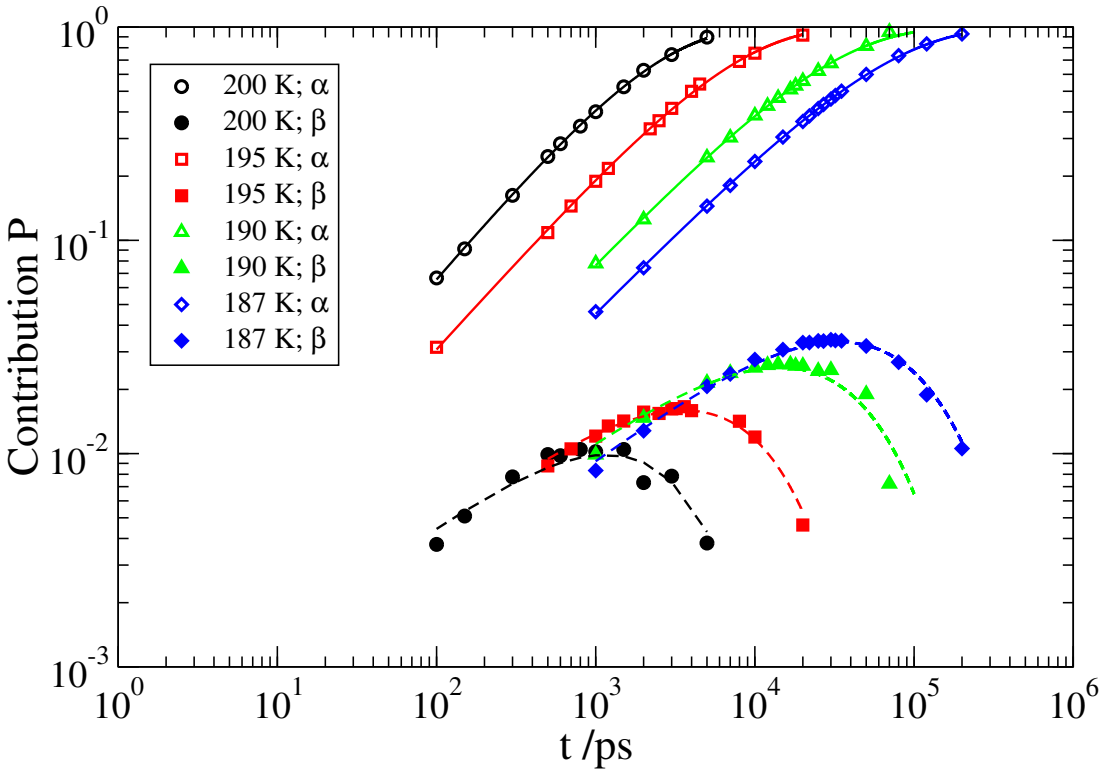

Figure 9.4: Contributions to $G(\phi_\perp, t)$. The isotropic process (open symbols), governing the long-time limit, is denoted as α and the secondary π-flip motion is referred to as β (filled symbols). The solid lines are fits according to equation (9.1) and the dashed lines to equation (9.2).

Analytic expressions for the α and β processes are based on considerations

outlined above and on general findings for processes in supercooled liquids. First, α governs the long-time limit, thus suggesting

$$P_\alpha = 1 - e^{-(t/\tau_\alpha)^\alpha}, \tag{9.1}$$

with P_α the contribution of this process and the second term motivated by the general KWW relaxation behavior. The solild lines are fits of the data to equation (9.1), yielding reasonable results.

Second, an equation describing the β process can be rationalized by assuming that the α process is absent and only π-flips are taking place. Then, the long-time limit for this process must equal 1/2 as the probability to find the hydrogen atoms at the time $t \to \infty$ swapped compared with the initial position is 50% (obviously, there are forth-and-back jumps and only the region beyond 150 ° is considered). However, the α process is present and cannot be omitted. Additionally, this process will dominate over all other processes for long times. This motivates the following equation

$$P_\beta = (1/2 - 1/2 \cdot E_\beta(-(t/\tau_\beta)^\beta) \cdot e^{-(t/\tau_\alpha)^\alpha}, \tag{9.2}$$

with P_β the contribution due to the π-flips, which eventually decays to zero due to the rising of P_α, and $E_\beta(-(t/\tau_\beta)^\beta)$ the Mittag-Leffler function (not to be confused with the generalized Mittag-Leffler function, β refers only to the term β as secondary process.). The Mittag-Leffler term is motivated by the fact that the secondary process cannot yield a relaxed energy landscape, thus, it appears convenient not to use an additional stretched exponential term describing a changing energy landscape allegedly giving rise to the asymmetric shape in frequency space. For the sake of completeness this was also considered and the results are depicted below.

Figure 9.5 illustrates the correlation times $\tau_{\alpha,\mathrm{F}_2}$ and τ_β as a function of temperature. Strikingly, the explicit expression for the second term, which was discussed above, appears to be irrelevant. Only for longer times, the difference between the Mittag-Leffler and the KWW-like approach should matter, however, the long-time contribution is entirely governed by the isotropic process, thus, results are virtually identical. It is evident that this secondary process is very slow and appears to obey an Arrhenius-like temperature dependence. The activation energy is $E_A = 0.44$ eV, corresponding to the breaking of roughly two hydrogen bonds [125].

Concluding, one should notice that experiments do not probe the π-flip contribution in the way it was derived here, but the correlation times are assumed

to give an estimation for the relevant temperature region of the process. This can be clearly settled at the glass transition temperature T_g of water due to the *strong* temperature dependence of τ_β. Further studies may focus on water models different from SPC/E to investigate this process, however, it should be present in MD simulations in general, due to the rigidity of the molecules. Therefore, *ab-initio* simulations may determine the relevance from a quantum mechanical point of view.

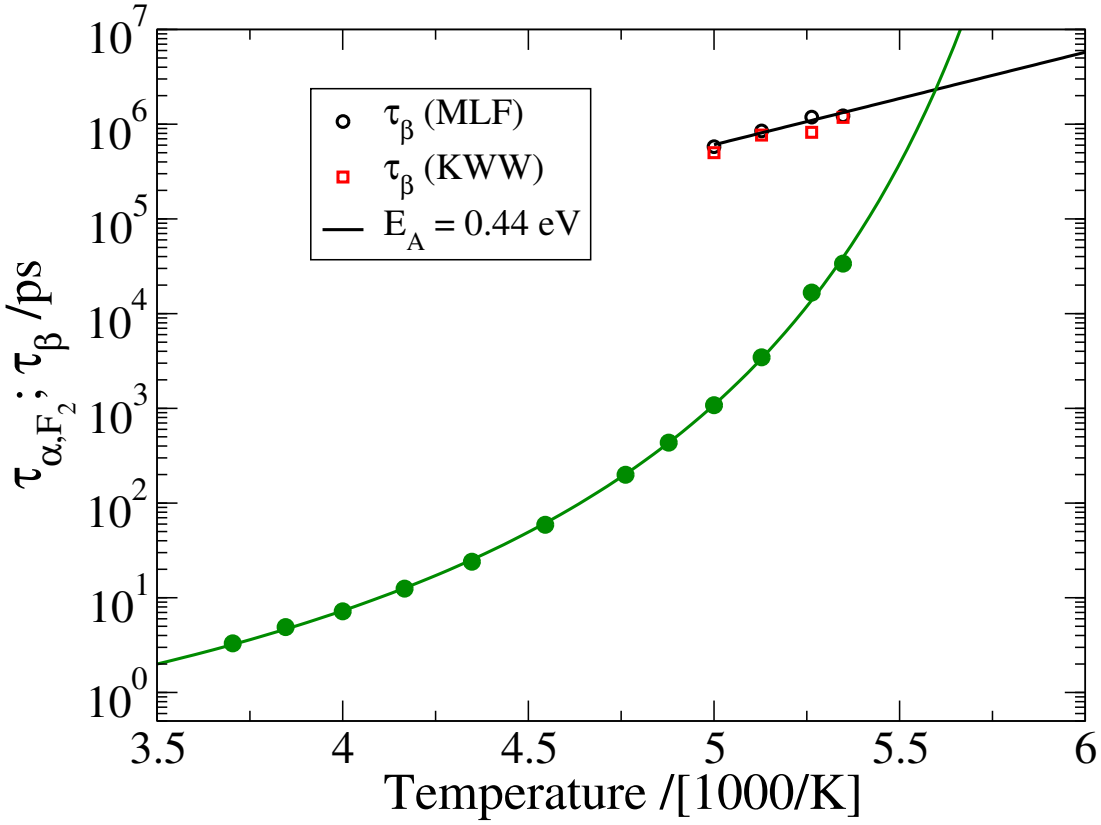

Figure 9.5: Correlation times τ_{α,F_2} and τ_β dependent on temperature. τ_β was obtained from equation (9.2). Two scenarios, KWW-like and Mittag-Leffler related ones, see text, are distinguished. The green solid line is a VFT fit to τ_{α,F_2}. The black solid line shows an Arrhenius approximation for the temperature dependence, yielding an activation energy of $E_A = 0.44$ eV.

10 Subdiffusive protein motion

In this chapter, protein dynamics will be studied. The system comprises eight peptide chains $(VPGVG)_{50}$ and 2732 water molecules, resulting in a hydration level of $h = 0.3$ g/g. The results presented in the following, and further simulation details, have been published and can be found in [212]. A complete overview over protein dynamics is beyond the scope of this thesis and only one peculiar regime of dynamics will be addressed.

Proteins are of great importance for metabolism in creatures and biology in general. Understanding dynamics of proteins yields insights into protein functions and related mechanisms. However, in the context of the present study, the focus is on describing internal protein dynamics. Thus, the question arises what is special about internal protein dynamics? Several experimental and MD simulation studies found a power-law decay of correlations for internal protein motion [66, 213, 214] (see also the literature in [212]). Figure 10.1 illustrates this behavior. In panel a), the intermediate scattering function $S_q(t)$ is depicted as function of time. Only nitrogen atoms of the protein-backbone have been considered for the analyses and the modulus of the scattering vector is set to $q = 22.7\ \mathrm{nm}^{-1}$. In panel b), the MSD for the same atoms is shown.

The findings for $S_q(t)$ can be separated into three different regimes, similar but maybe not identical to the regimes found for the MSD of bulk water, see Figure 2.4. First, there are vibrations. Then, there is an anomalous type of decay which is indicated by the black dashed lines. Third, a different relaxation process takes over. The MSD in panel b) exhibits that the anomalous decay of $S_q(t)$ is related to subdiffusive behavior. The slope is by far smaller than 1 as the MSD rises by less than one order of magnitude over more than 4 decades in time. Thus, this is subdiffusion, in contrast to diffusion where the MSD scales linearly with time, see the discussion on BM in chapter 2.3.

There are several open questions about this classification. There is an anomalous decay, compared to that of water described in the previous chapters, but, the small amplitude of decay does not allow for a clear verification of a power-law. Therefore, it is not clear if this effect is truly identical to what was found by e.g. neutron scattering experiments which clearly obtain a power-law decay [213]. Additionally, the origin of the final relaxation process, terminating the apparent power-law, is vague. This is partially due to the fact that simulations are by far to short to clearly observe this relaxation mechanism, see the curves in Figure 10.1 which only decay to values ≈ 0.5. Despite the open questions concerning the dynamics, the focus is only on the intermediate, anomalous,

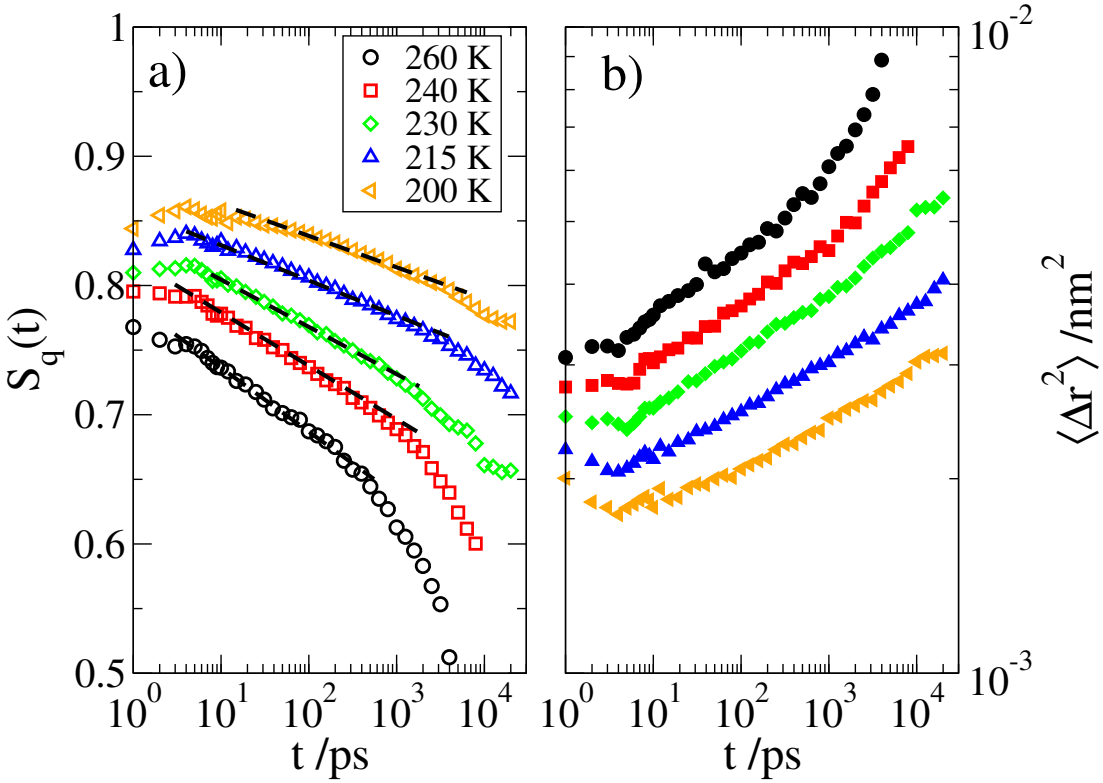

Figure 10.1: Panel a): Incoherent intermediate scattering function $S_q(t)$ with $q = 22.7\ \mathrm{nm}^{-1}$ for nitrogen atoms of the backbone of $(\mathrm{VPGVP})_{50}$. The dashed black lines are straight lines to indicate the *anomalous* decay behavior. Panel b): MSD for nitrogen atoms of the backbone.

regime, and a single approach to describe the results will be detailed below. Other aspects will not be investigated.

All literature for this part can be found in [66, 67, 215–220].

As stated above, the anomalous decorrelation is related to subdiffusive behavior. There are several approaches suitable to derive subdiffusion. Fractional Brownian motion models introduce a time dependent diffusion constant, fractional generalized Langevin-equation approaches assume a power-law dependence for the fluctuations and continuous time random walk models employ power-law waiting time distributions to model subdiffusive behavior. It is emphasized that all those approaches yield identical results for standard Brownian motion, but not for the subdiffusive regime. A thorough characterization of all models is beyond the scope of this thesis. Here, the fractional Fokker-Planck equation is used to describe the data in Figure 10.1. This equation can be derived from the continuous time random walk model if power-law waiting times

are considered. For the resulting master equation an expansion is done in leading order terms. This yields the fractional diffusion equation. The fractional Fokker-Planck equation (fFPE) is the phenomenological expansion of the latter equation to account for particles in an external field $V(x)$. It is possible to verify that the resulting probability densities are well defined and positive (which is not trivial as there are no conditions like the Pawula theorem stating that an expansion in moments M_n with $n \geq 3$ vanishes, like for the derivation of the *usual* Fokker-Planck equation (2.11)). The fFPE is given as,

$$W(x,t) - W(x,0) = {}_0D_t^{-\alpha} \left[-\frac{\partial}{\partial x} \frac{V(x)}{m\eta_\alpha} + K_\alpha \frac{\partial^2}{\partial x^2} \right] W(x,t), \tag{10.1}$$

with η_α a generalized friction constant, K_α a generalized diffusion constant and ${}_0D_t^{-\alpha}$, with $0 < \alpha < 1$, defined by

$${}_0D_t^{-\alpha} W(x,t) = \frac{1}{\Gamma(\alpha)} \int_0^t dt' \frac{W(x,t')}{(t-t')^{1-\alpha}}. \tag{10.2}$$

Thus, ${}_0D_t^{-\alpha}$ defines a weighted integral over the entire history of the system. Next, the relation ${}_0D_t^{1-\alpha} = \frac{\partial}{\partial t} {}_0D_t^{-\alpha}$ is important. It simply means that the derivative ${}_0D_t^{1-\alpha}$ (notice ${}_0D_t^{\epsilon}$: if ϵ is positive, this defines the derivative, and if negative an integral!) with respect to a non-integer value $1-\alpha$ is mathematically identical to the integral of order α and subsequent derivation with respect to t. Thus, it is possible to obtain an equation which is very similar to the usual Fokker-Planck equation, see equation (2.11),

$$\frac{\partial W(x,t)}{\partial t} = {}_0D_t^{1-\alpha} \left[-\frac{\partial}{\partial x} \frac{V(x)}{m\eta_\alpha} + K_\alpha \frac{\partial^2}{\partial x^2} \right] W(x,t). \tag{10.3}$$

Is is emphasized that this approach introduces a power-law memory, due to the power-law waiting times, which clearly defines a non-Markovian system. Equation (10.3), with $V(x) = \text{const.}$, yields very complex solutions in space x, but remarkably simple solutions for the incoherent intermediate scattering function $S_q(t)$

$$S_q(t) = E_\alpha(-K_\alpha q^2 t^\alpha). \tag{10.4}$$

Therefore, this approach yields a possible explanation for the Cole-Cole behavior discussed in the previous chapters.

The effective potential probed by the nitrogen atoms, for which the subdiffusive behavior was observed, see Figure 10.1, was found to be similar to a

harmonic potential $V(x) = \frac{1}{2}\kappa x^2$ [212]. Stochastic motion of particles in a harmonic potential is called Ornstein-Uhlenbeck process, therefore, the approach set out above corresponds to a fractional Ornstein-Uhlenbeck process. Here, only the final solutions are mentioned, a full calculation can be found in [66].

Solving equation (10.3) with $V(x) = \frac{1}{2}\kappa x^2$ yields for the MSD (assuming isotropy of the system)

$$\langle \Delta r^2 \rangle = 6 \cdot \langle x^2 \rangle_{\mathrm{st}} \left[1 - E_\alpha \left(- \left(\frac{t}{\tau} \right)^\alpha \right) \right] \tag{10.5}$$

with $\langle x^2 \rangle_{\mathrm{st}}$ the stationary MSD in x direction. For the incoherent intermediate scattering function, the following equation is obtained

$$S_q(t) = e^{-q^2 \langle x^2 \rangle_{\mathrm{st}}} \sum_{n=0}^{\infty} \frac{q^{2n} (\langle x^2 \rangle_{\mathrm{st}})^n}{n!} E_\alpha \left(-n \left(\frac{t}{\tau} \right)^\alpha \right). \tag{10.6}$$

The result is basically similar to the non-fractional case where the Mittag-Leffler functions are replaced by exponential functions. The sum in equation (10.6) is due to a different representation of the Fokker-Planck equation. A Fokker-Planck operator for the harmonically bound particle can be defined. Following *Risken*, one can show that Hermite polynomials are eigenfunctions of this operator [64]. Thus, n in equation (10.6) denotes the n-th Hermite polynomial $H_n(x)$. Further, n is related to the eigenvalues γ_n which are linked to the correlation time via $\gamma_n = \frac{n}{\tau^\alpha}$. Hence, $n = 0$ corresponds to the stationary state and the larger n the faster is the decay towards this stationary state [42].

The physical picture of the fractional Ornstein-Uhlenbeck process is illustrated in Figure 10.2. The particles are harmonically bound with various trapping events taking place during the exploration of the potential. These trapping events yield the memory, which is related to the power-law waiting time distribution.

Figure 10.3 shows the calculation for $S_q(t)$ and the fits to the MSD of nitrogen atoms according to equations (10.6) and (10.5). For the fit, τ was set to $\tau = 400$ ps. First, the MSD was fitted. It is visible that the approximation gives

[42] It is emphasized that the spectral decomposition of the Fokker-Planck operator also works e.g. for the freely diffusing particle in the overdamped case. However, inserting the simple solution for the eigenfunctions (in principle the solution of the time-independent Schrödinger equation) in equation 3.41 in [66] to calculate $S_q(t)$ shows that only the solution $n = 1$ does not vanish (n=0 is not possible, there is no stationary state). Hence, there is **no**(!) such thing as a sum for $S_q(t)$ like $S_q(t) = \sum e^{-n(t/\tau)}$ in this case.

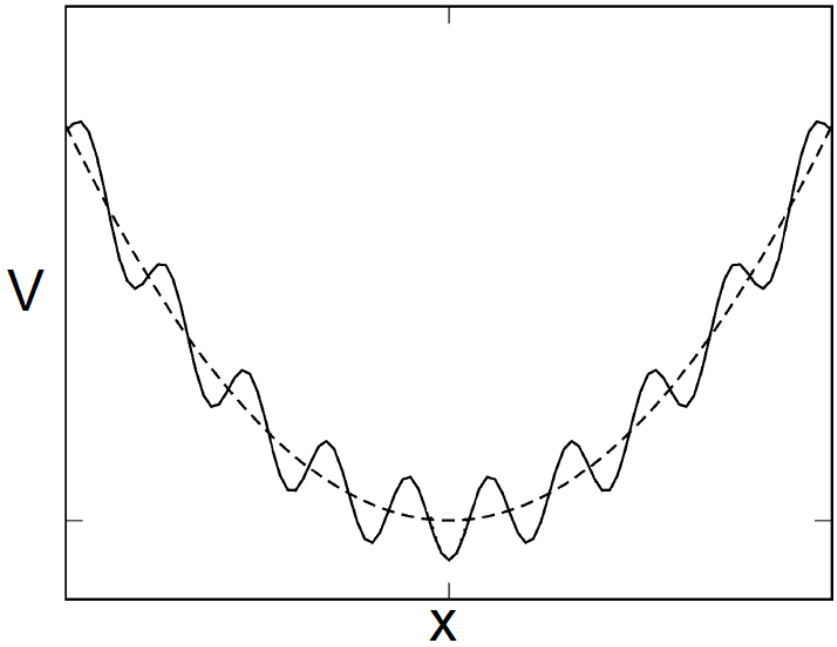

Figure 10.2: Illustration of the fractional Ornstein-Uhlenbeck approach. Particles are trapped in an effective harmonic potential, the dashed line, but, multiple small trapping events, the solid line, give rise to a slowly decaying memory.

good results. The stationary MSD is depicted in the inset and reveals a linear dependence on temperature. The parameter α is almost constant $\alpha = 0.16 \pm 0.02$. With these parameters $S_q(t)$ was calculated, not fitted. Evidently, the calculations yield a good approximation for the decay of $S_q(t)$ in the anomalous regime.

In conclusion, the data is well approximated by employing the fractional Ornstein-Uhlenbeck process, however, there are some subtleties which are discussed now. First, this approach is clearly a non-equilibrium process. Due to the power-law waiting time, a mean characteristic time is diverging, therefore, different models which also allow for studying subdiffusive motion may be more appropriate. Second, the presented approach is a high-level one, as complex dynamics is assumed, with only little knowledge on the origin of power-law waiting times or memories. According to *Kneller*, who related the memory to a complex model of beads and springs representing the protein, a deeper understanding on a particle level appears appropriate [66]. Such models also seem promising to yield valuable information on the connection of protein dynamics with polymer dynamics.

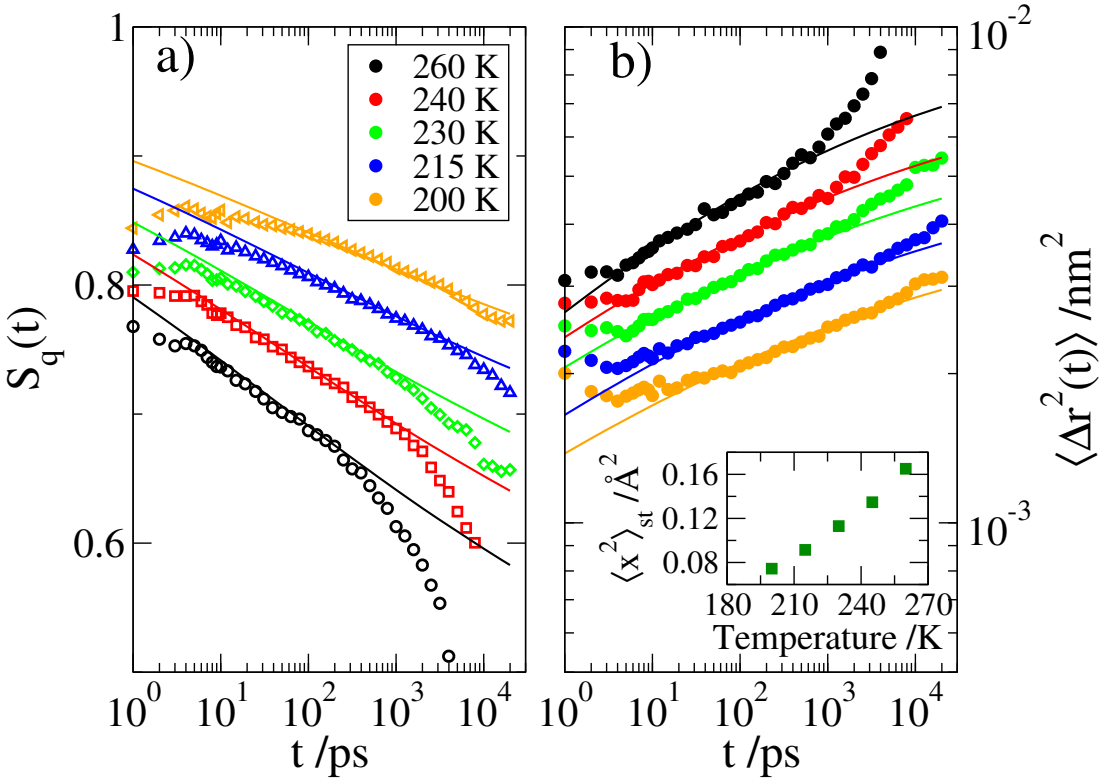

Figure 10.3: Panel a): $S_q(t)$ with $q = 22.7$ nm^{-1} for nitrogen atoms of the backbone of $(VPGVG)_{50}$. The solid lines in panel a) are calculations based on the fits to data from panel b). Panel b): MSD of nitrogen atoms of the backbone of $(VPGVG)_{50}$. The solid lines are fits to data according to equation (10.5). The inset shows the resulting stationary MSD as function of temperature.

11 Summary

In this thesis, several important results were presented. It was possible to distinguish finite-size, density and surface effects. Increasing the density in the silica pores resulted in a pronounced density layering throughout the pores. At lower densities, a single density peak was found in the immediate vicinity of the surface. Further, it was observed that the silica walls induce disorder for water molecules near the surface. The length on which the silica wall affects the structure of the confined liquid was found to be smaller at high densities and larger at lower densities and lower temperatures.

Together with the distorted structure near the silica walls, a static contribution to the energy landscape was observed which affects the motion of molecules adjacent to the wall. In contrast to the silica pores, it was verified that the structure of water in the neutral pores is not changed compared to that of the bulk. Despite this difference, similar effects for dynamics in both confinement systems were found, thus, it was shown that atomistic confinements impose a static contribution to the energy landscape. This results in a drastic change of the relaxation mechanism near the wall: from bulk-like Cole-Davidson patterns to Cole-Cole relaxation behavior, from bulk-like fragile behavior to a strong temperature dependence for the motion of water molecules, and a tremendous slowing of dynamics.

Additionally, the fragile-to-strong transition for motion in narrow silica pores was observed at low temperatures and low densities, in agreement with the literature [17]. However, in contrast to the literature, it was shown that the effect is presumably not due to the proposed phase transition of water, but rather to a finite-size effect, as a larger silica pore with the same density at the pore center and a very similar structure revealed no such transition behavior. This interpretation is further supported by findings from narrow neutral confinements. There, a non-linear feedback mechanism had a huge impact on dynamics due to the absence of bulk-like behavior in the pores.

The neutral confinements were further used to shed light on intrinsic length scales of SPC/E water. Two different length scales were obtained. The dynamic length scale characterizes the range on which dynamics is affected by the wall in the neutral pores. The static one is assumed to describe the range on which the wall hinders the sampling of amorphous configurations of the confined water. Both lengths are similar in value and exhibit a linear growth as a function of inverse temperature in the investigated temperature regime. According to the random first-order transition theory, the temperature depen-

dence of the static length should determine the fragility of bulk liquids at low temperatures. In this study, a simple relation between the structural correlation times of the bulk and the dynamic or static lengths from the neutral pores was observed. However, it remains vague which of these lengths dominates. Therefore, a novel theoretical approach was used, the elastically cooperative non-linear Langevin equation approach. The latter approach well describes the tremendous slowdown of dynamics in the neutral pores. Thus, a striking correlation between vibrational dynamics on a picosecond timescale with structural correlation times of up to several hundreds of nanoseconds is established, while effectively using only two fit parameters. This yields a detailed understanding of the mechanism of motion in the pores. Additionally, the dynamic length scale allowed to employ the ECNLE approach for the correlation times of the bulk liquid. As before, using effectively only two fit parameters is sufficient to entirely describe the fragile behavior of the bulk. Other features of supercooled liquids, e.g., the Stokes-Einstein breakdown were examined and can also be explained using this approach. It was shown that SPC/E exhibits several typical features of supercooled liquids, therefore, the presented approach may be of great importance for understanding supercooled liquids in general.

In addition to these main aspects of the thesis, two minor topics were investigated. First, π-flip motion was observed for water molecules adjacent to confinement walls. For water molecules in the bulk, a procedure to quantify this process was proposed and allowed to settle the relevance of this process for bulk water at near the glass transition temperature.

Second, internal protein motion was investigated. Subdiffusive behavior for internal motion in $(\mathrm{VPGVG})_{50}$ was found. The data can be described by assuming that the motion takes place in a harmonic potential with a power-law waiting time distribution. However, owing to the high-level character of the approach, further studies should focus on establishing a more particle based picture of dynamics.

12 Appendix

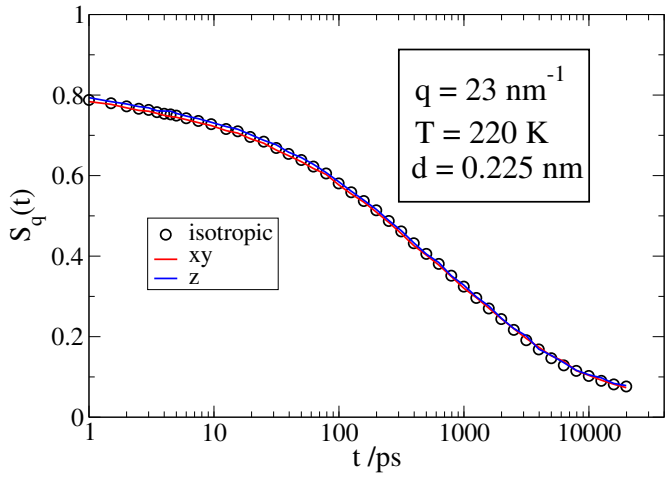

Figure 12.1: The ISF, $S_q(t)$ with $q = 23$ nm^{-1}, for oxygen atoms of the *lo-dens* silica pore at 220 K. Only atoms adjacent to the surface are considered ($d = 0.225$ nm). Calculations based on the isotropic assumption of equation (5.8) are shown together with the ISF for the xy direction and z direction.

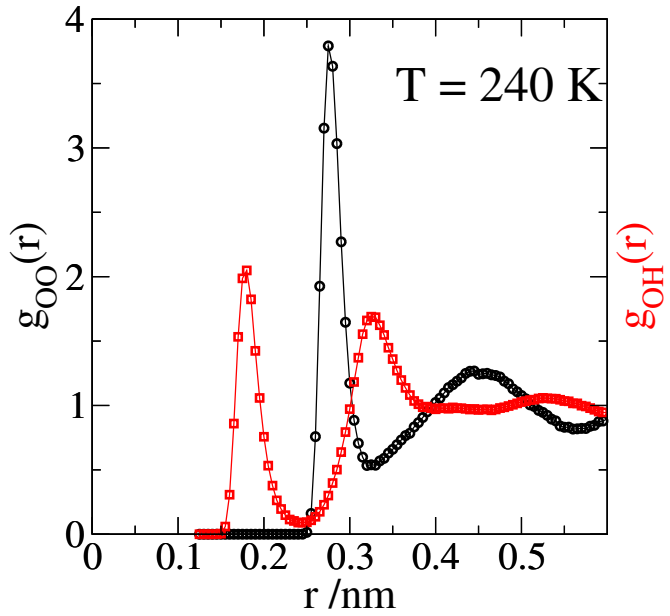

Figure 12.2: Radial-pair distribution function for oxygen-oxygen and for oxygen-hydrogen of the bulk system at $T = 240$ K. The intramolecular part for O-H is omitted.

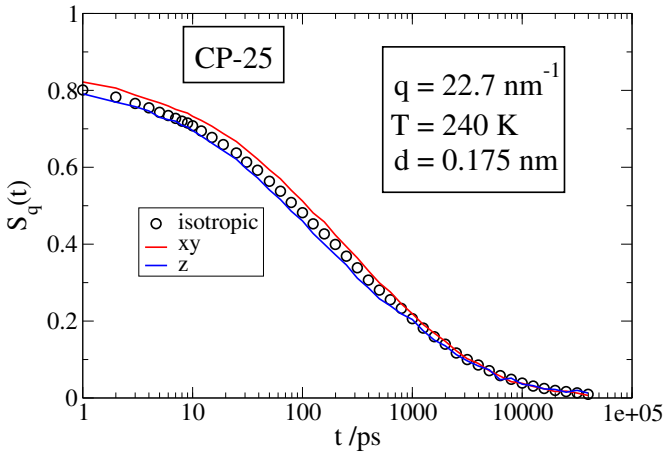

Figure 12.3: The ISF, $S_q(t)$ with $q = 22.7$ nm^{-1}, for oxygen atoms of the CP-25 system at 220 K. Only atoms adjacent to the surface are considered ($d = 0.175$ nm). Calculations based on the isotropic assumption of equation (5.8) are shown together with the ISF for the xy direction and z direction.

References

[1] B. Schmandt et al. “Dehydration melting at the top of the lower mantle”. In: *Science* 344 (2014), p. 1265.

[2] J. C. Rasaiah, S. Garde, and G. Hummer. “Water in Nonpolar Confinement: From Nanotubes to Proteins and Beyond”. In: *Annu. Rev. Phys. Chem.* 59 (2008), pp. 713 –740.

[3] N. E. Levinger. “Water in Confinement”. In: *Science* 298 (2002), p. 1722.

[4] P. H. Poole et al. “Phase behavior of metastable water”. In: *Nature* 360 (1992).

[5] C. A. Angell. “Insights into Phases of Liquid Water from Study of Its Unusual Glass-Forming Properties”. In: *Science* 319 (2008), pp. 582–587.

[6] S. Sastry et al. “Singularity-free interpretation of the thermodynamics of supercooled water”. In: *Phys. Rev. E* 53.6 (1996).

[7] F. Mallamace et al. “Role of the solvent in the dynamical transitions of proteins: The case of the lysozyme-water system”. In: *J. Chem. Phys.* 127 (2007), p. 045104.

[8] S. Cerveny et al. “Glass Transition and Relaxation Processes in Supercooled Water”. In: *Phys. Rev. Lett.* 93 (2004), p. 245702.

[9] S. Capaccioli, K. L. Ngai, and N. Shinyashiki. “The Johari-Goldstein β-Relaxation of Water”. In: *J. Phys. Chem. B* 111 (2007), pp. 8197 –8209.

[10] R. Schmidt et al. “Pore Size Determination of MCM-41 Mesoporous Materials by means of ’H NMR Spectroscopy, N2 adsorption, and HREM. A Preliminary Study”. In: *J. Am. Chem. Soc.* 117.14 (1995), pp. 4049 –4056.

[11] A. Schreiber, I. Ketelsen, and G. H. Findenegg. “Melting and freezing of water in ordered mesoporous silica materials”. In: *Phys. Chem. Chem. Phys.* 3 (2001), p. 1185.

[12] K. Morishige and H. Iwasaki. “X-ray Study of Freezing and Melting of Water Confined within SBA-15”. In: *Langmuir* 19 (2003), pp. 2808 –2811.

[13] H. J. C. Berendsen et al. *Interaction models for water in relation to protein hydration*. Springer, 1981, pp. 331–342.

[14] H. J. C. Berendsen, J.R. Grigera, and T.P. Straatsma. “The missing term in effective pair potentials”. In: *J. Phys. Chem.* 91 (1987), pp. 6269–6271.

[15] G. Cicero et al. “Water Confined in Nanotubes and between Graphene Sheets: A First Principle Study”. In: *J. Am. Chem. Soc.* 130 (2008), pp. 1871 –1878.

[16] S. R.-V. Castrillón et al. “Evolution from Surface-Influenced to Bulk-Like Dynamics in Nanoscopically Confined Water”. In: *Phase Transitions* 113 (2009), pp. 7973 –7976.

[17] P. Gallo, M. Rovere, and S.-H. Chen. “Dynamic Crossover in Supercooled Confined Water: Understanding Bulk Properties through Confinement”. In: *J. Phys. Chem. Lett.* 1 (2010), pp. 729 –733.

[18] W. Kob, S. Roldán-Vargas, and L. Berthier. “Non-monotonic temperature evolution of dynamic correlations in glass-forming liquids”. In: *Nature Physics* 8 (2011), pp. 164 –167. ISSN: 1745-2473.

[19] G. M. Hocky, T. E. Markland, and D. R. Reichman. “Growing Point-to-Set Length Scale Correlates with Growing Relaxation Times in Model Supercooled Liquids”. In: *Phys. Rev. Lett.* 108 (2012), p. 225506.

[20] L. Berthier and W. Kob. “Static point-to-set correlations in glass-forming liquids”. In: *Phys. Rev. E* 85 (2012), p. 011102.

[21] S. Mirigian and K. S. Schweizer. “Elastically cooperative activated barrier hopping theory of relaxation in viscous fluids. I. General formulation and application to hard sphere fluids”. In: *J. Chem. Phys.* 140 (2014), p. 194506.

[22] Günther Höhne, Wolfgang Hemminger, and H-J Flammersheim. *Differential scanning calorimetry*. Springer, 2003.

[23] C. A. Angell. “Supercooled Water”. In: *Annu. Rev. Phys. Chem.* 34 (1983), pp. 593 –630.

[24] L. A. Báez and P. Clancy. “Existence of a density maximum in extended simple point charge water”. In: *J. Chem. Phys.* 101 (1994), p. 9837.

[25] F. Sciortino et al. “Supercooled water and the kinetic glass transition”. In: *Phys. Rev. E* 54.6 (1996), pp. 6331 –6343.

[26] R. Shevchuk and F. Rao. “Note: Microsecond long atomistic simulation of supercooled water”. In: *J. Chem. Phys.* 137 (2012), p. 036101.

[27] A. Cavagna. “Supercooled Liquids for Pedestrians”. In: *arXiv* 0903.4264v1 (2009).

[28] J. C. Dyre. “Colloquium: The glass transition and elastic models of glass-forming liquids”. In: *Rev. Mod. Phys.* 78.64 (2006), p. 953.

[29] M. D. Ediger, C. A. Angell, and S. R. Nagel. “Supercooled Liquids And Glasses”. In: *J. Phys. Chem.* 100.95 (1996), pp. 13200 –13212.

[30] A-J. Dianoux and G. Lander. *Neutron data booklet*. 2nd ed. ocp science, 2003.

[31] P. Lunkenheimer and A. Loidl. "Dielectric spectroscopy of glass-forming materials:α-relaxation and excess wing". In: *Chem. Phys.* 284 (2002), pp. 205 –219.

[32] M. Sattig and M. Vogel. "Dynamic Crossovers and Stepwise Solidification of Confined Water: A 2H NMR Study". In: *J. Phys. Chem. Lett.* 5 (2013), pp. 174 –178.

[33] Sander Pronk et al. "GROMACS 4.5: a high-throughput and highly parallel open source molecular simulation toolkit". In: *Bioinformatics* (2013), btt055.

[34] R. Kubo. "The fluctuation-dissipation theorem". In: *Rep. Prog. Phys.* 29 (1966), p. 255.

[35] P. Lunkenheimer et al. "Glassy dynamics". In: *Contemp. Phys.* 41.1 (2000), pp. 15–36.

[36] I. Podlubny. *Mittag-Leffler function*. 2014. URL: `http://www.mathworks.com/matlabcentral/fileexchange/8738-mittag-leffler-function`.

[37] K. Weron and M. K. b. "On the Cole-Cole relaxation function and related Mittag-Lettter distribution". In: *Physica A* 232 (1996), pp. 180 –188.

[38] R. Metzler and J. Klafter. "From stretched exponential to inverse power-law: Fractional dynamics, Cole-Cole relaxation processes, and beyond". In: *J. Non-Cryst. Solids* 305 (2002), pp. 81 –87.

[39] N. Pottier. "Relaxation time distributions for an anomalously diffusing particle". In: *Physica A* 390 (2011), pp. 2863 –2879. ISSN: 0378-4371.

[40] A. Bello, E. Laredo, and M. Grimau. "Distribution of relaxation times from dielectric spectroscopy using Monte Carlo simulated annealing: Application to α-PVDF". In: *Phys. Rev. B* 60.18 (1999).

[41] T. Blochowicz. "Broadband Dielectric Spectroscopy in Neat and Binary Molecular Glass Formers Frequency and Time Domain Spectroscopy, Non-Resonant Spectral Hole Burning". PhD thesis. Bayreuth, 2003.

[42] C. P. Lindsey and G. D. Patterson. "Detailed comparison of the Williams-Watts and Cole-Davidson functions". In: *J. Chem. Phys.* 73.7 (1980), p. 3348.

[43] L. M. Martinez and C. A. Angell. "A thermodynamic connection to the fragility of glass-forming liquids." In: *Nature* 410.6829 (2001), pp. 663 –667.

[44] G. S. Fulcher. “Analysis of recent measurements of the viscosity of glasses”. In: *J. Am. Ceram. Soc.* 8 (1925), pp. 339–355l.

[45] G. Tammann and W. Hesse. “Die Abhängigkeit der Viscosität von der Temperatur bie unterkühlten Flüssigkeiten”. In: *Z. Anorg. Allg. Chem.* 156 (1926), pp. 245–257.

[46] M. Goldstein. In: *J. Chem. Phys.* 51 (1969), p. 3728.

[47] S. Sastry. “The relationship between fragility, configurational entropy and the potential energy landscape of glass-forming liquids”. In: *Nature* 409 (2001), p. 164.

[48] C. A. Angell. “Perspective On The Glass Transition”. In: *J. Phys. Chem. Solids* 49.8 (1988), pp. 863 –871.

[49] F. Sciortino et al. “Supercooled water and the kinetic glass transition. II. Collective dynamics”. In: *Phys. Rev. E* 56.5 (1997), pp. 5397–5404.

[50] N. Giovambattista et al. “Connection between Adam-Gibbs Theory and Spatially Heterogeneous Dynamics”. In: *Phys. Rev. Lett.* 90.8 (2003), p. 085506.

[51] N. Giovambattista et al. “Dynamic Heterogeneities in Supercooled Water”. In: *J. Phys. Chem. B* 108 (2004), pp. 6655 –6662.

[52] M. D. Ediger. “Spatially Heterogeneous Dynamics in Supercooled Liquids”. In: *Annu. Rev. Phys. Chem.* 51 (2000), pp. 99–128.

[53] H. Sillescu. “Heterogeneity at the glass transition: A review”. In: *J. Non-Cryst. Solids* 243 (1999), pp. 81 –108.

[54] A. Heuer and K. Okun. “Heterogeneous and homogeneous dynamics in a simulated polymer melt: Analysis of multi-time correlation functions”. In: *J. Chem. Phys.* 106 (1997), p. 6176.

[55] M. Vogel and T. Torbrügge. “Nonexponential polymer segmental motion in the presence and absence of ions: 2H NMR multitime correlation functions for polymer electrolytes poly(propylene glycol)-LiClO4”. In: *J. Chem. Phys.* 126 (2007), p. 204902.

[56] M. Vogel and S. C. Glotzer. “Temperature dependence of spatially heterogeneous dynamics in a model of viscous silica”. In: *Phys. Rev.* 70 (2004), p. 061504.

[57] A. Bormuth. “Untersuchung der Polymerdynamik in Abhängigkeit von Kettenlänge, Temperatur und Druck mit Hilfe von Molekulardynamik Simulationen”. PhD thesis. TU Darmstadt, 2012.

[58] P. Henritzi. “A Molecular Dynamics Simulation Study of Dynamic Processes in Molecular Glass-Forming Liquids”. PhD thesis. TU Darmstadt, 2014.

[59] E. Flenner and G. Szamel. “Relaxation in a glassy binary mixture: Mode-coupling-like power laws, dynamic heterogeneity, and a new non-Gaussian parameter”. In: *Phys. Rev. E* 72.1 (2005), p. 011205.

[60] L. Berthier. “Dynamic heterogeneity in amorphous materials”. In: *Physics* 4.42 (2011).

[61] L. Berthier et al. “Spontaneous and induced dynamic correlations in glass formers. II. Model calculations and comparison to numerical simulations”. In: *J. Chem. Phys.* 126 (2007), p. 184504.

[62] L. Berthier et al. “Spontaneous and induced dynamic fluctuations in glass formers. I. General results and dependence on ensemble and dynamics”. In: *J. Chem. Phys.* 126 (2007), p. 184503.

[63] M. Vogel. In: *Phys. Rev. B* 68.66 (2003), p. 184301.

[64] H. Risken. *The Fokker-Planck Equation, Methods of Solution and Applications*. 2nd ed. Springer, 1989.

[65] R. Zwanzig. *Nonequilibrium Statistical Mechanics*. 1st ed. Oxford University Press, 2001.

[66] G. R. Kneller. “Quasielastic neutron scattering and relaxation processes in proteins: Analytical and simulation-based models”. In: *Phys. Chem. Chem. Phys.* 7 (2005), pp. 2641 –2655.

[67] G. R. Kneller. *Stochastic dynamics and relaxations in simple liquids and proteins -Brownian dynamics and beyond-*. 1st ed.

[68] V. Ilyin, I. Procaccia, and A. Zagorodny. “Fokker-Planck equation with memory: The crossover from ballistic to diffusive processes in many-particle systems and incompressible media”. In: *Condens. Matter Phys.* 16.1 (2013), pp. 13004 –1 –18.

[69] V. Ilyin and A. Zagorodny. “Fokker-planck equations with memory: The cross over from ballistic to diffusive processes”. In: *Ukr. J. Phys.* 55.12 (2010).

[70] G. Biroli and J.-P. Bouchaud. “The Random First-Order Transition Theory of Glasses: A critical assessment”. In: *arXiv* 0912.2542v1 (2009).

[71] W. Götze. *Complex dynamics of glass-forming liquids, a mode-coupling theory*. 1st ed. Oxford University Press, 2009.

[72] D. R. Reichman and P. Charbonneau. “Mode-coupling theory”. In: *J. Stat. Mech.* 2005.05 (2005), P05013.

[73] T. Voigtmann. “Mode Coupling Theory of the Glass Transition in Binary Mixtures”. In: (2002).

[74] P. Wieth and M. Vogel. “Dynamical and structural properties of monohydroxy alcohols exhibiting a Debye process”. In: *J. Chem. Phys.* 140 (2014), p. 144507.

[75] G. Biroli and J.-P. Bouchaud. “Diverging length scale and upper critical dimension in the Mode-Coupling Theory of the glass transition”. In: *Europhys. Lett.* 67.1 (2004), pp. 21 –27.

[76] G. Biroli et al. “Inhomogeneous Mode-Coupling Theory and Growing Dynamic Length in Supercooled Liquids”. In: *Phys. Rev. Lett.* 97 (2006), p. 195701.

[77] J.-P. Bouchaud and G. Biroli. “On the Adam-Gibbs-Kirkpatrick-Thirumalai-Wolynes scenario for the viscosity increase in glasses”. In: *J. Chem. Phys.* 121.15 (2004), p. 7347.

[78] V. Lubchenko and P. G. Wolynes. “Theory of Structural Glasses and Supercooled Liquids”. In: *Annu. Rev. Phys. Chem.* 58 (2007), pp. 235 –266.

[79] T. R. Kirkpatrick, D. Thirumalai, and P. G. Wolynes. “Scaling concepts for the dynamics of viscous liquids near an ideal glassy state”. In: *Phys. Rev. A* 40.2 (1989), p. 1045.

[80] GBJP Biroli et al. “Thermodynamic signature of growing amorphous order in glass-forming liquids”. In: *Nature Physics* 4 (2008), pp. 771–775.

[81] S. Karmakar, E. Lerner, and I. Procaccia. “Direct estimate of the static length-scale accompanying the glass transition”. In: *Physica A* 391 (2012), pp. 1001 –1008.

[82] G. Biroli, S. Karmakar, and I. Procaccia. “Comparison of static length scales characterizing the glass transition.” In: *Phys. Rev. Lett.* 111 (2013), p. 165701.

[83] P. Charbonneau and G. Tarjus. “Decorrelation of the static and dynamic length scales in hard-sphere glass formers”. In: *Phys. Rev. E* 87 (2013), p. 042305.

[84] G. Szamel and E. Flenner. “Glassy dynamics of partially pinned fluids: An alternative mode-coupling approach”. In: *Euro. Phys. Lett.* 101 (2013), p. 66005.

[85] V. Krakoviack. “Mode-coupling theory for the slow collective dynamics of fluids adsorbed in disordered porous media”. In: *Phys. Rev. E* 75 (2007), p. 031503.

[86] K. S. Schweizer and E. J. Saltzman. “Activated Hopping, Barrier Fluctuations, and Heterogeneity in Glassy Suspensions and Liquids”. In: *J. Phys. Chem. B* 108.51 (2004), pp. 19729 –19741.

[87] E. J. Saltzman and K. S. Schweizer. “Non-Gaussian effects, space-time decoupling, and mobility bifurcation in glassy hard-sphere fluids and suspensions”. In: *Phys. Rev. E* 74 (2006), p. 061501.

[88] K. S. Schweizer and G. Yatsenko. “Collisions, caging, thermodynamics, and jamming in the barrier hopping theory of glassy hard sphere fluids”. In: *J. Chem. Phys.* 127 (2007), p. 164505.

[89] E. J. Saltzman and K. S. Schweizer. “Large-amplitude jumps and non-Gaussian dynamics in highly concentrated hard sphere fluids”. In: *Phys. Rev. E* 77 (2008), p. 051504.

[90] S. Mirigian and K. S. Schweizer. “Unified Theory of Activated Relaxation in Liquids over 14 Decades in Time”. In: *J. Phys. Chem. Lett* 4 (2013), pp. 3648 –3653.

[91] S. Mirigian and K. S. Schweizer. “Elastically cooperative activated barrier hopping theory of relaxation in viscous fluids. II. Thermal liquids”. In: *J. Chem. Phys.* 140 (2014), p. 194507.

[92] T. R. Kirkpatrick and P. G. Wolynes. “Connections between some kinetic and equilibrium theories of the glass transition”. In: *Phys. Rev. A* 35.7 (1987).

[93] J. C. Dyre and W. H. Wang. “The instantaneous shear modulus in the shoving model”. In: *J. Chem. Phys.* 136 (2012), p. 224108.

[94] K. Niss et al. “Connection between slow and fast dynamics of molecular liquids around the glass transition”. In: *Phys. Rev. E* 82 (2010), p. 021508.

[95] Ludovic Berthier et al. *Dynamical heterogeneities in glasses, colloids, and granular media*. Oxford University Press, 2011. Chap. An overview of the theories of the glass transition by G. Tarjus.

[96] H. E. Stanley et al. “The puzzling behavior of water at very low temperature Invited Lecture”. In: *Phys. Chem. Chem. Phys.* 2 (2000), pp. 1551–1558.

[97] P. H. Poole et al. “Effect of Hydrogen Bonds on the Thermodynamic Behavior of Liquid Water”. In: *Phys. Rev. Lett.* 73.12 (1994).

[98] L. Heckmann. “Thermodynamik und Phasenverhalten einfacher Modelle für Wasser”. PhD thesis. TU Darmstadt, 2013.

[99] O. Mishima and H. E. Stanley. “The relationship between liquid, supercooled and glassy water”. In: *Nature* 396 (1998), p. 329.

[100] S. Jähnert et al. “Melting and freezing of water in cylindrical silica nanopores”. In: *Phys. Chem. Chem. Phys.* 10 (2008), pp. 6039 –6051.

[101] L. Xu et al. “Relation between the Widom line and the dynamic crossover in systems with a liquid-liquid”. In: *Proc. Natl. Acad. Sci. USA* 102.46 (2005), pp. 16558 –16562.

[102] K. Ito, C. T. Moynihan, and C. A. Angell. “Thermodynamic determination of fragility in liquids and a fragile-to-strong liquid transition in water”. In: *Nature* 398 (1999), p. 492.

[103] G. Adam and J. H. Gibbs. “On the Temperature Dependence of Cooperative Relaxation Properties in Glass Forming Liquids”. In: *J. Chem. Phys.* 43 (1965), p. 139.

[104] H. Tanaka. “A new scenario of the apparent fragile-to-strong transition in tetrahedral liquids: Water as an example”. In: *J. Phys.: Condens. Matter* 15 (2003), p. 703.

[105] R. Bergman and J. Swenson. “Dynamics of supercooled water in confined geometry”. In: *Nature* 403 (2000), p. 283.

[106] R. Bergman et al. “Dielectric study of supercooled 2D water in a vermiculite clay”. In: *J. Chem. Phys.* 113.1 (2000), p. 357.

[107] J. Swenson, H. Jansson, and R. Bergman. “Relaxation Processes in Supercooled Confined Water and Implications for Protein Dynamics”. In: *Phys. Rev. Lett.* 96 (2006), p. 247802.

[108] S. Pawlus, S. Khodadadi, and A. P. Sokolov. “Conductivity in Hydrated Proteins: No Signs of the Fragile-to-Strong Crossover”. In: *Phys. Rev. Lett.* 100 (2008), p. 108103.

[109] S. Cerveny, Á. Alegría, and J. Colmenero. “Universal features of water dynamics in solutions of hydrophilic polymers, biopolymers, and small glass-forming materials”. In: *Phys. Rev. E* 77 (2008), p. 031803.

[110] K. L. Ngai, S. Capaccioli, and N. Shinyashiki. “The Protein “Glass” Transition and the Role of the Solvent”. In: *J. Phys. Chem. B* 112 (2008), pp. 3826 –3832.

[111] I. Brovchenko, A. Geiger, and A. Oleinikovac. “Liquid-liquid phase transitions in supercooled water studied by computer simulations of various water models”. In: *J. Chem. Phys.* 123 (2005), p. 044515.

[112] D. Paschek, A. Rüppert, and A. Geiger. “Thermodynamic and Structural Characterization of the Transformation from a Metastable Low-Density to a Very High-Density Form of Supercooled TIP4P-Ew Model Water”. In: *Chem. Phys. Chem.* 9 (2008), pp. 2737 –2741.

[113] L. Liu et al. “Pressure Dependence of Fragile-to-Strong Transition and a Possible Second Critical Point in Supercooled Confined Water”. In: *Phys. Rev. Lett.* 95 (2005), p. 117802.

[114] I. Brovchenko, A. Geiger, and A. Oleinikova. “Multiple liquid-liquid transitions in supercooled water”. In: *J. Chem. Phys.* 118.21 (2003), p. 9473.

[115] Y. Liu et al. “Liquid-liquid transition in ST2 water”. In: *J. Chem. Phys.* 137 (2012), p. 214505.

[116] P. Gallo and M. Rovere. “Mode coupling and fragile to strong transition in supercooled TIP4P water”. In: *J. Chem. Phys.* 137 (2012), p. 164503.

[117] P. Kumar et al. “Glass Transition in Biomolecules and the Liquid-Liquid Critical Point of Water”. In: *Phys. Rev. Lett.* 97 (2006), p. 177802.

[118] D. T. Limmer and D. Chandler. “The putative liquid-liquid transition is a liquid-solid transition in atomistic models of water”. In: *J. Chem. Phys.* 135 (2011), p. 134503.

[119] D. T. Limmer and D. Chandler. “The putative liquid-liquid transition is a liquid-solid transition in atomistic models of water. II”. In: *J. Chem. Phys.* 138 (2013), p. 214504.

[120] Michael P Allen. “Introduction to molecular dynamics simulation”. In: *Computational Soft Matter: From Synthetic Polymers to Proteins, Lecture Notes, Norbert Attig, Kurt Binder, Helmut Grubmuller, Kurt Kremer (Eds.), John von Neumann Institute for Computing, Julich* ().

[121] J.-P. Hansen and I. R. McDonald. *Theory of Simple Liquids (Third Edition)*. third. Elsevier, 2006.

[122] M. Rovere. “Lecture notes on Monte Carlo and Molecular Dynamics Simulations”. In: *School of Neutron Scattering "F. P. Ricci", Santa Margherita di Pula, 22 Sep.-3 Oct.* (2008).

[123] D. van der Spoel et al. “Gromacs User Manual version 4.5.6”. In: (2010).

[124] T. D. Kühne. “Ab-Initio Molecular Dynamics”. In: *arXiv* 1201.5945v2 (2013).

[125] M. Vogel. “Temperature-Dependent Mechanisms for the Dynamics of Protein-Hydration Waters: A Molecular Dynamics Simulation Study”. In: *J. Phys. Chem. B* 113 (2009), pp. 9386 –9392.

[126] T. Yan et al. “Molecular Dynamics Simulation of Ionic Liquids: The Effect of Electronic Polarizability”. In: *J. Phys. Chem. B* 108.32 (2004), pp. 11877 –11881.

[127] R. Richert and M. Yang. “Solvation dynamics of molecular glass-forming liquids in confinement”. In: *J. Phys.: Condens. Matter* 15 (2003), S1041 –S1050.

[128] J. R. Errington and P. G. Debenedetti. “Relationship between structural order and the anomalies of liquid water”. In: *Nature* 409 (2001), pp. 318–321.

[129] D. E. Shaw et al. “Anton, a special-purpose machine for molecular dynamics simulation”. In: *Comm. ACM* 51.7 (2008).

[130] J. M. Berg, J. L. Tymoczko, and L. Stryer. *Biochemie*. Vol. 5. Spektrum, 2003.

[131] S. Miyamoto and P. A. Kollman. “Settle: An analytical version of the SHAKE and RATTLE algorithm for rigid water models”. In: *J. Comput. Chem.* 13.8 (1992), pp. 952 –962.

[132] B. Hess, H. Bekker, and H. J. C. Berendsen. “LINCS: A linear constraint solver for molecular simulations”. In: *J. Comput. Chem.* 18.12 (1997), pp. 1463 –1472.

[133] J. E. Jones. “On the Determination of Molecular Fields. II. From the Equation of State of a Gas”. In: *Proc. R. Soc. Lond. A* 106 (1924), pp. 463–477.

[134] R. A. Buckingham. “The Classical Equation of State of Gaseous Helium, Neon and Argon”. In: *Proc. R. Soc. Lond. A* 168 (1938), pp. 264–283.

[135] W. F. Van Gunsteren and H. J. C. Berendsen. “A Leap-frog Algorithm for Stochastic Dynamics”. In: *Mol. Sim.* 1.3 (1988), pp. 173 –185.

[136] William G Hoover. “Canonical dynamics: Equilibrium phase-space distributions”. In: *Phys. Rev. A* 31.3 (1985), p. 1695.

[137] W. G. Hoover. “Canonical dynamics: Equilibrium phase-space distributions”. In: *Phys. Rev. A* 31.3 (1985), p. 1695.

[138] M. Parrinello and A. Rahman. “Polymorphic transitions in single crystals: A new molecular dynamics method”. In: *J. Appl. Phys.* 52 (1981), p. 7182.

[139] S. Nosé and M. L. Klein. “Constant pressure molecular dynamics for molecular systems”. In: *Mol. Phys.* 50.5 (1983), pp. 1055 –1076.

[140] P. Gallo, M. Rovere, and E. Spohr. “Supercooled Confined Water and the Mode Coupling Crossover Temperature”. In: *Phys. Rev. Lett.* 85.20 (2000).

[141] F. H. Stillinger and A. Rahman. “Improved simulation of liquid water by molecular dynamics”. In: *J. Chem. Phys.* 60.4 (1974), p. 1545.

[142] W. L. Jorgensen et al. “Comparison of simple potential functions for simulating liquid water”. In: *J. Chem. Phys.* 79.2 (1983), p. 926.

[143] M. W. Mahoney and W. L. Jorgensen. “A five-site model for liquid water and the reproduction of the density anomaly by rigid, nonpolarizable potential functions”. In: *J. Chem. Phys.* 112.20 (2000), p. 8910.

[144] J. L. F. Abascal and C. Vega. “A general purpose model for the condensed phases of water: TIP4P/2005”. In: *J. Chem. Phys.* 123 (2005), p. 234505.

[145] wikipedia entry. *Water model*. 2014. URL: `en.wikipedia.org/wiki/Water_model#mediaviewer/File:Water-2D-labelled.png`.

[146] A. C. T. van Duin et al. “ReaxFF: A Reactive Force Field for Hydrocarbons”. In: *J. Phys. Chem. A* 105 (2001), pp. 9396 –9409.

[147] A. C. T. van Duin et al. “ReaxFFSiO Reactive Force Field for Silicon and Silicon Oxide Systems”. In: *J. Phys. Chem. A* 107 (2003), pp. 3803 – 3811.

[148] C. Allolio et al. “Ab Initio H_2O in Realistic Hydrophilic Confinement”. In: *ChemPhysChem* (2014).

[149] William Humphrey, Andrew Dalke, and Klaus Schulten. “VMD – Visual Molecular Dynamics”. In: *Journal of Molecular Graphics* 14 (1996), pp. 33–38.

[150] A Brodka and TW Zerda. “Properties of liquid acetone in silica pores: Molecular dynamics simulation”. In: *J. Chem. Phys.* 104.16 (1996), p. 6319.

[151] A. Janz. “Molecular Dynamics Simulation of Water-Peptide-Systems using the Peptide VPGVG investigating the Strukture Dynamics Relationship”. In: (2012).

[152] J.-R. Hill and J. Sauer. “Molecular Mechanics Potential for Silica and Zeolite Catalysts Based on ab Initio Calculations”. In: *J. Phys. Chem.* 98 (1994), pp. 1238 –1244.

[153] F. Klameth. “Untersuchungen zu Myoglobin in Confinement mittels molekular-dynamischen Simulationen”. In: (2011).

[154] K. Kim, K. Miyazaki, and S. Saito. “Slow dynamics, dynamic heterogeneities, and fragility of supercooled liquids confined in random media”. In: *J. Phys.: Condens. Matter* 23 (2011), p. 234123.

[155] J. L. Yarnell et al. “Structure Factor and Radial Distribution Function for Liquid Argon at 85 K”. In: *Phys. Rev. A* 7.6 (1973), p. 2130.

[156] A. Luzar and D. Chandler. “Effect of Environment on Hydrogen Bond Dynamics in Liquid Water”. In: *Phys. Rev. Lett.* 76.6 (1996), p. 928.

[157] J. Martí, J. A. Padro, and E. Guàrdia. “Molecular dynamics simulation of liquid water along the coexistence curve: Hydrogen bonds and vibrational spectra”. In: *J. Chem. Phys.* 105.2 (1996), p. 639.

[158] R. M. Lynden-Bell and P. G. Debenedetti. “Computational Investigation of Order, Structure, and Dynamics in Modified Water Models”. In: *J. Phys. Chem. B* 109 (2005), pp. 6527 –6534.

[159] P. Kumara, S. V. Buldyrevb, and H. E. Stanleyc. “A tetrahedral entropy for water”. In: *Proc. Natl. Acad. Sci. USA* 106.52 (2009), pp. 22130 – 22134.

[160] T. Brückel et al. *Laboratory Course neutron Scattering; Schriften des Forschungszentrums Jülich Reihe Materie und Material*. Vol. 28, pp. I3–I4.

[161] L. Van Hove. “Correlations in Space and Time and Born Approximation Scattering in Systems of Interacting Particles”. In: *Phys. Rev.* 95.1 (1954).

[162] V. P. Voloshin et al. “Radial distribution functions of atoms and voids in large computer models of water”. In: *J. Struct. Chem.* 46.3 (2005), pp. 438 –445.

[163] P. J. Camp. “Dynamics in a two-dimensional core-softened fluid”. In: *Phys. Rev. E* 71 (2005), p. 031507.

[164] D. Caprion and H. R. Schober. “Vibrational density of states of selenium through the glass transition”. In: *J. Chem. Phys.* 114.7 (2001), p. 3236.

[165] R. Kubo. “Statistical-Mechanical Theroy of Irreversible Processes. I. General Theory and Simple Applications to Magnetic and Conduction Problems”. In: *J. Phys. Soc. Jap.* 12.6 (1957), pp. 570–586.

[166] H. Shimizu. “TimeCorrelation Function of Molecular Random Motion and Shape of Spectral Bands”. In: *J. Chem. Phys.* 43.7 (1965), p. 2453.

[167] A. Heuer et al. “Backward correlations and dynamic heterogeneities: A computer study of ion dynamics”. In: *Phys. Rev. B* 66 (2002), p. 224201.

[168] M. G. Mazza et al. “Relation between Rotational and Translational Dynamic Heterogeneities in Water”. In: *Phys. Rev. Lett.* 96.5 (2006), p. 057803.

[169] D. R. Reichman, E. Rabani, and P. L. Geissler. “Comparison of Dynamical Heterogeneity in Hard-Sphere and Attractive Glass Formers”. In: *J. Phys. Chem. B* 109.30 (2005), pp. 14654 –14658.

[170] M. Fuchs, W. Gotze, and M. R. Mayr. “Asymptotic laws for tagged-particle motion in glassy systems”. In: *Phys. Rev. E* 58.3 (1998), p. 3384.

[171] H. Z. Cummins. “The liquid-glass transition: A mode-coupling perspective”. In: *J. Phys.: Condens. Matter* 11 (1999), A95 –A117.

[172] W. Kob et al. In: *Phys. Rev. Lett.* 79.15 (1997), pp. 2827 –2830.

[173] M. Dzugutov, S. I. Simdyankin, and F. H. M. Zetterling. “Decoupling of Diffusion from Structural Relaxation and Spatial Heterogeneity in a Supercooled Simple Liquid”. In: *Phys. Rev. Lett.* 89.19 (2002), p. 195701.

[174] M. Vogel. “Conformational and Structural Relaxations of Poly(ethylene oxide) and Poly(propylene oxide) Melts: Molecular Dynamics Study of Spatial Heterogeneity, Cooperativity, and Correlated Forward-Backward Motion”. In: *Macromolecules* 41 (2008), pp. 2949 –2958.

[175] P. Kumar et al. “Relation between the Widom line and the breakdown of the Stokes-Einstein relation in supercooled water”. In: *Proc. Natl. Acad. Sci. USA* 104.23 (2007), pp. 9575 –9579.

[176] F. Sciortino, A. Geiger, and H. E. Stanley. “Effect of defects on molecular mobility in liquid water”. In: *Nature* 354 (1991), p. 218.

[177] L. Berthier and G. Biroli. “Theoretical perspective on the glass transition and amorphous materials”. In: *arXiv* 1011.2578v2 (2011).

[178] G. Tarjus and D. Kivelson. “Breakdown of the Stokes-Einstein relation in supercooled liquids”. In: *J. Chem. Phys.* 103 (1995), p. 3071.

[179] M. G. Mazza et al. “Connection of translational and rotational dynamical heterogeneities with the breakdown of the Stokes-Einstein and Stokes-Einstein-Debye relations in water”. In: *Phys. Rev. E* 76 (2007), p. 031203.

[180] M. Vogel et al. “Silver dynamics in silver iodide/silver phosphate glasses studied by multi-dimensional 109Ag NMR”. In: *Phys. Chem. Chem. Phys.* 4 (2002), pp. 3237 –3245.

[181] M. Rosenstihl et al. “Dynamics of interfacial water”. In: *J. Non-Cryst. Solids* (2014). ISSN: 0022-3093.

[182] M. Harrach et al. “The effect of the implementation of the pore wall on structure and dynamics of confined water”. In: ***SUBMITTED*** *to J. Chem. Phys.* ().

[183] M. Rovere et al. “A molecular dynamics simulation of water confined in a cylindrical SiO 2 pore”. In: *J. Chem. Phys.* 108.23 (1998), p. 9859.

[184] I. R. Piletic et al. “Testing the Core/Shell Model of Nanoconfined Water in Reverse Micelles Using Linear and Nonlinear IR Spectroscopy”. In: *J. Phys. Chem. A* 110 (2006), pp. 4985 –4999.

[185] N. Nandi and B. Bagchi. “Dielectric Relaxation of Biological Water”. In: *J. Phys. Chem. B* 101 (1997), pp. 10954 –10961.

[186] J. Faeder and B. M. Ladanyi. “Solvation Dynamics in Aqueous Reverse Micelles: A Computer Simulation Study”. In: *J. Phys. Chem. B* 105 (2001), pp. 11148 –11158.

[187] J. Faeder and B. M. Ladanyi. “Molecular Dynamics Simulations of the Interior of Aqueous Reverse Micelles”. In: *J. Phys. Chem. B* 104 (2000), pp. 1033 –1046.

[188] K. Ishikiriyama and M. Todoki. “Evaluation of water in silica pores using differential scanning calorimetry”. In: *Thermochi. Acta* 256 (1995), p. 213.

[189] D. Laage and W. H. Thompson. “Reorientation dynamics of nanoconfined water: Power-law decay, hydrogen-bond jumps, and test of a two-state model”. In: *J. Chem. Phys.* 136 (2012), p. 044513.

[190] R. Chopra, T. M. Truskett, and J. R. Errington. “On the Use of Excess Entropy Scaling to Describe the Dynamic Properties of Water”. In: *J. Phys. Chem. B* 114 (2010), pp. 10558 –10566.

[191] J. Hedström et al. “Does confined water exhibit a fragile-to-strong transition?” In: *Eur. Phys. J. Special Topics* 141 (2007), pp. 53 –56.

[192] H. Scher and E. W. Montroll. “Anomalous transit-time dispersion in amorphous solids”. In: *Phys. Rev. B* 12.6 (1975).

[193] P. Scheidler, W. Kob, and K. Binder. “The Relaxation Dynamics of a Supercooled Liquid Confined by Rough Walls”. In: *J. Phys. Chem. B* 108.21 (2004), pp. 6673 –6686.

[194] D. T. Limmer and D. Chandler. “Phase diagram of supercooled water confined to hydrophilic nanopores”. In: *J. Chem. Phys.* 137 (2012), p. 044509.

[195] P. Kumar et al. “Thermodynamics, structure, and dynamics of water confined between hydrophobic plates”. In: *Phys. Rev. E* 72 (2005), p. 051503.

[196] J. Swenson et al. “Why is there no clear glass transition of confined water?” In: *Chem. Phys.* 424 (2013), pp. 20 –25. ISSN: 0301-0104.

[197] M. Sattig et al. “NMR studies on the temperature-dependent dynamics of confined water”. In: *Phys. Chem. Chem. Phys.* 16 (2014), p. 19229. ISSN: 1463-9076.

[198] F. Klameth and M. Vogel. “Structure and dynamics of supercooled water in neutral confinements”. In: *J. Chem. Phys.* 138 (2013), p. 134503.

[199] F. Klameth, P. Henritzi, and M. Vogel. “Static and dynamic length scales in supercooled liquids: Insights from molecular dynamics simulations of water and tri-propylene oxide”. In: *J. Chem. Phys.* 140 (2014), p. 144501.

[200] R. L. Jack and C. J. Fullerton. “Dynamical correlations in a glass former with randomly pinned particles”. In: *Phys. Rev. E* 88 (2013), p. 042304.

[201] B. Charbonneau, P. Charbonneau, and G. Tarjus. “Geometrical Frustration and Static Correlations in a Simple Glass Former”. In: *Phys. Rev. Lett.* 108 (2012), p. 035701.

[202] F. W. Starr, J. F. Douglas, and S. Sastry. “The relationship of dynamical heterogeneity to the Adam-Gibbs and random first-order transition theories of glass formation”. In: *J. Chem. Phys.* 138 (2013), 12A541.

[203] M. Vogel and S. C. Glotzer. “Spatially Heterogeneous Dynamics and Dynamic Facilitation in a Model of Viscous Silica”. In: *Phys. Rev. Lett.* 92.25 (2004), p. 255901.

[204] U. Balucani, J. P. Brodholt, and R. Vallauri. “Analysis of the velocity autocorrelation function of water”. In: *J. Phys.: Condens. Matter* 8 (1996), pp. 6139 –6144.

[205] P. Kumar et al. “The Boson peak in supercooled water”. In: *Sci. Rep.* 3.1980 (2013).

[206] K. Larsson, J. Tegenfeldt, and A. Kvick. “NMR study of the motion of water molecules in the natrual zeolite bikitaite”. In: *J. Phys. Chem. Solids* 50.2 (1989), pp. 107–110.

[207] S. Fischer, C. S. Verma, and R. E. Hubbard. “Rotation of Structural Water inside a Protein: Calculation of the Rate and Vibrational Entropy of Activation”. In: *J. Phys. Chem. B* 102 (1998), pp. 1797 –1805.

[208] V. P. Denisov and B. Halle. “Protein hydration dynamics in aqueous solution”. In: *Farauday Discuss.* 103 (1996), pp. 227 –244.

[209] S. A. Lusceac, M. R. Vogel, and C. R. Herbers. “2H and 13C NMR studies on the temperature-dependent water and protein dynamics in hydrated elastin, myoglobin and collagen”. In: *BBA - Proteins and Proteomics* 1804 (2010), pp. 41 –48. ISSN: 1570-9639.

[210] P. Demontis, G. Stara, and G. B. Suffritti. “Dynamical behavior of one-dimensional water molecule chains in zeolites: Nanosecond time-scale molecular dynamics simulations of bikitaite”. In: *J. Chem. Phys.* 120.19 (2004), p. 9233.

[211] J. Tritt-Goc and N. Piślewski. “The influence of the motion of water molecules on proton dipolar coupling tensors in Sr[Fe(CN)5NO]·4H2O”. In: *Mol. Phys.* 87.1 (1996), pp. 139 –149.

[212] K. Kämpf, F. Klameth, and M. Vogel. “Power-law and logarithmic relaxations of hydrated proteins: A molecular dynamics simulations study”. In: *J. Chem. Phys.* 137 (2012), p. 205105.

[213] W. Doster, S. Cusack, and W. Petry. “Dynamic instability of liquidlike motions in a globular protein observed by inelastic neutron scattering”. In: *Phys. Rev. Lett.* 65.8 (1990).

[214] H. Yang et al. “Protein Conformational Dynamics Probed by Single-Molecule Electron Transfer”. In: *Org. Lett.* 302 (2003), p. 262.

[215] G. R. Kneller and V. Calandrini. “Estimating the influence of finite instrumental resolution on elastic neutron scattering intensities from proteins”. In: *J. Chem. Phys.* 126 (2007), p. 125107.

[216] G. R. Kneller, K. Hinsen, and P. Calligari. “Communication: A minimal model for the diffusion-relaxation backbone dynamics of proteins”. In: *J. Chem. Phys.* 136 (2012), p. 191101.

[217] R. Metzler and J. Klafter. “The restaurant at the end of the random walk: Recent developments in the description of anomalous transport by fractional dynamics”. In: *J. Phys. A: Math. Gen.* 37 (2004), R161–R208.

[218] R. Metzler and J. Klafter. “The random walk:S guide to anomalous diffusion: A fractional dynamics approach”. In: *Physics Reports* 339 (2000), pp. 1 –77.

[219] J.-H. Jeon et al. “Anomalous diffusion and power-law relaxation of the time averaged mean squared displacement in worm-like micellar solutions”. In: *New J. Phys.* 15 (2013), p. 045011.

[220] I. Goychuk and P. Hänggi. “Anomalous Escape Governed by Thermal 1/f Noise”. In: *Phys. Rev. Lett.* 99 (2007), p. 200601.

A Publications by the author

List of papers published or submitted to peer-reviewed journals:

1) K. Kämpf, F. Klameth, M. Vogel (2012) [212]

2) F. Klameth, M. Vogel (2013) [198]

3) F. Klameth, P. Henritzi, M. Vogel (2014) [199]

4) M. Rosenstihl, K. Kämpf, F. Klameth, M. Sattig, M. Vogel (2014) [181]

5) C. Allolio, F. Klameth, M. Vogel, D. Sebastiani (2014) [148]

6) M. Harrach, F. Klameth, B. Drossel, M. Vogel (2014) **submitted** [182]

[In preparation for publication:]

- P. Henritzi, A. Bormuth, F. Klameth, M. Vogel (2014/15) (on the hyperscaling behavior)
- F. Klameth, M. Vogel (2014/15) (on the ECNLE approach in neutral confinements)

List of talks given on conferences (only those in English language):

1) AK Treffen Polen (2012)

2) DPG Tagung Regensburg (2013)

3) AK Treffen Wewelsburg (2014)

List of poster contributions:

1) DPG Tagung Berlin (2012)

2) GRC Conference Holderness School, New Hampshire, USA (2013)

3) Liquids Conference, Lisbon, Portugal (2014)

Date and place of Birth

26.04.1985 Erlenbach am Main

University Education

November 2011 - December 2014 Doctorate Physics
(TU Darmstadt)

October 2010 - February 2014 B.Sc. Economics and Business Administration
(Goethe University Frankfurt)

October 2009 - October 2011 M.Sc. Physics
(TU Darmstadt)

October 2004 - September 2009 B.Sc. Physics
(TU Darmstadt)

School Education

2004 Abitur

2001 - 2004 Oberstufengymnasium Bachgauschule Babenhausen

C Danksagung

Ich möchte mich bei allen bedanken die mich während meiner Zeit an der TU Darmstadt und der Goethe Uni-Frankfurt begleitet und unterstützt haben.

Besonderer Dank geht an Prof. Michael Vogel für die tolle Betreuung während der Masterarbeit und der Promotion, sowie dafür, mir viel freie Hand bei der Auswahl der Themen gegeben zu haben. Vielen Dank auch an Prof. Barbara Drossel für die Ideen während der wöchentlichen Simulationssitzungen und für das Übernehmen der Zweitkorrektur.

Desweiteren möchte ich mich bei der gesamten Arbeitsgruppe und besonders bei Kerstin Kämpf, Patrick Henritzi, André Bormuth und Patrick Wieth für die gute Zusammenarbeit, die interessanten Gespräche und die kurzweilige Zeit bedanken. Außerdem besonders bei Markus Rosenstihl, für seine große Hilfsbereitschaft bei Problemen mit dem Rechencluster.

Bedanken möchte ich mich bei meiner Familie und Freunden für die große Unterstützung und die Ermunterung meine Ziele zu verfolgen, sowie besonders bei Stefan Striegler der diese Doktorarbeit Korrektur gelesen hat.

Spezieller Dank geht an meine Freundin Anna Schmitt die immer dafür gesorgt hat mich auf andere Gedanken zu bringen und den Stress der letzten Wochen klaglos ausgehalten hat.